UNIVERSITY OF CALIFORNIA SAN DIEGO

Exploring Process-Structure-Property Relationships via Additive Manufacturing

A dissertation submitted in partial satisfaction of the
requirements for the degree Doctor of Philosophy

in

Materials Science and Engineering

by

Joshua Stephan Pelz

Committee in charge:

Professor Marc Meyers, Chair
Professor Javier Garay
Professor Olivia Graeve
Professor Falko Kuester
Professor Michael Tolley

2022

The Dissertation of Joshua Stephan Pelz is approved, and it is acceptable in quality and form for publication on microfilm and electronically.

University of California San Diego

2022

DEDICATION

To my family,
Rosalie, Carl, Katherine, and Clayton

Each of you is a constant source of light in my life. Mom and dad, you taught me from a young age that hard work does pay off and that every one of my dreams is attainable. It is through the privilege of having an incredibly supportive family that I am writing this dissertation on my doctoral research. I am eternally grateful to each one of you.

Love,
Joshua Pelz

TABLE OF CONTENTS

LIST OF FIGURES

LIST OF TABLES

ACKNOWLEDGEMENTS

The research presented in this proposal was sponsored by the CCDC Army Research Laboratory and was accomplished under Cooperative Agreement Number W911NF-19-2-0054. The views and conclusions contained in this document are my own and should not be interpreted as representing the official policies, either expressed or implied, of the CCDC Army Research Laboratory or the U.S. Government. The U.S. Government is authorized to reproduce and distribute reprints for Government purposes notwithstanding any copyright notation herein. Funding was supplemented by the UCSD Center for High Energy Density Science (UCOP LAB FEES GRANT ID: LFR-17-449059). This work was performed, in part, at the San Diego Nanotechnology infrastructure (SDNI) of UCSD, a member of the National Nanotechnology Coordinated infrastructure (NNCI), which is supported by the National Science Foundation (Grant ECCS-2025752). This dissertation, in part, is based on work supported by the US Army Corps of Engineers under research Cooperative Agreement W912HZ-17-2-0024, National Institute of Standards and Technology Award #70NANB17H211, as well as National Science Foundation award #CNS-1338192, MRI: Development of Advanced Visualization Instrumentation for the Collaborative Exploration of Big Data.

I would like to thank all the members of the Meyers Group at the University of California, San Diego, specifically Dr. Shiteng Zhao, Dr. Rachel Flanagan, Dr. Audrey Velasco-Hogan, Aomin Huang, and Isaac Cabrera for their

mentorship, helpful insights, and support through the many trials of graduate school. I want to thank my undergraduate student researcher Samuel Figueroa for his time helping to develop the DIW system. I want to thank Prof. Falko Kuester and Dr. Luca De Vivo Nicoloso for their mentorship and support, primarily on the topic of additively manufactured prosthetic limbs. I want to sincerely thank my advisor, Prof. Marc Meyers, for his mentorship during my doctoral work and for supporting my delve into a research direction new to his group. His support of my transition to a project of my own choosing allowed my creativity to blossom and me to find my passion in developing custom additive manufacturing systems. I want to thank my committee members, Prof. Javier Garay, Prof. Olivia Graeve, and Prof. Michael Tolley, for supporting my doctoral studies and providing invaluable insight about my research.

I would like to thank the members of the Ceramic and Transparent Materials Branch at the US CCDC Army Research Laboratory, Aberdeen Proving Grounds, MD, specifically Dr. Sidra Silton, Dr. Lionel Vargas-Gonzalez, Dr. Jeff Swab, Dr. Chris Meredith, Dr. Taylor Shoulders, Dr. Kris Behler, Dr. Matthew Guziewski, Dr. Steven Kilczewski, and Tucker Moore for their support and technical advice. I want to give a special thanks to Dr. Nicholas Ku for his endless patience, mentorship, support, and technical advice. A large part of the success of my research is due to the supportive environment at ARL, Aberdeen Proving Ground, and I want to sincerely thank everyone who took the time to support my numerous research endeavors.

I want to express my sincere gratitude to my undergraduate advisor Prof. Geoff Brennecka who started me on the path towards ceramic 3D printing more than 7 years ago. Half-way through my sophomore year at the Colorado School of Mines you accepted me into your research group and gave me a grant to purchase two Lulzbot Taz 4 3D printers. Your mentorship and support started the core of my dissertation research and has continued to play a huge role in my professional career. In fact, the experience I gained working with the Taz 4 printers is a big reason why I was able to create the prosthetics start-up that I plan to go into full time after graduation.

I want to thank Tammy and Joe Tumminello for taking me into their home and making the many trips to Maryland feel like I was at home. I want to thank Gran and Pappous for lending me their car for my trips to Maryland. The love and support I receive from each of you never ceases to amaze me.

I want to acknowledge the support of my grandmother Diane Pelz, my uncle Bart Sears, and my grandfather Stephen Ellen. Each of you supported my academic pursuits starting from undergrad and extending all the way through graduate school. Thank you for putting your trust in me. Knowing that my family believes in me is one of the biggest reasons I was able to achieve this important milestone.

Chapter 2, in full, is a reprint of material that has been published: J. Pelz, N. Ku, L. R. Vargas-Gonzalez, M. A. Meyers, “Additive Manufacturing of Structural Ceramics: A Historical Perspective,” Journal of Materials Research

and Technology, 2021. The dissertation author was the primary investigator and author of this paper.

Chapter 3, in part, is a reprint of material that has been published: J. Pelz, N. Ku, M. A. Meyers, L. R. Vargas-Gonzalez, “Additive Manufacturing Utilizing a Novel In-Line Mixing System for Design of Functionally Graded Ceramic Composites,” ARL-TR-8851, CCDC Army Research Laboratory, 2019. The dissertation author was the primary investigator and author of this paper.

Chapter 4, in part, is a reprint of material that has been published: J. Pelz, N. Ku, W. T. Shoulders, M. A. Meyers, L. R. Vargas-Gonzalez, “Multi-Material Additive Manufacturing of Functionally Graded Carbide Ceramics via Active, In-Line Mixing,” Additive Manufacturing, 2021. The dissertation author was the primary investigator and author of this paper.

Chapter 5, in part, is currently being prepared for submission for publication of the material. J. Pelz, N. Ku, W. T. Shoulders, L. R. Vargas Gonzalez, M. A. Meyers. The dissertation author was the primary investigator and author of this paper.

Chapter 6, in part, is currently being prepared for submission for publication of the material. J. Pelz, L. De Vivo, H. Barrack, and F. Kuester. The dissertation author was the primary investigator and author of this paper.

Chapter 6, in part, is a reprint of material that was submitted: J. Pelz, L. De Vivo, H. Barrack, F. Kuester “PCT/US22/11939 - UNIBODY ENDOSKELETAL TRANSTIBIAL PROSTHETIC DEVICES AND DIGITAL

FABRICATION WORKFLOW," Patent Council Treaty, 2022. The dissertation author is an inventor and the primary author of this patent.

Chapter 6, in part, is a reprint of material that has been published: L. De Vivo, J. Pelz, H. Barrack, F. Kuester, "Towards 3D Printing of a Monocoque Transtibial Prosthesis using a Bio-Inspired Design Workflow," Rapid Prototyping Journal, 2021. The dissertation author was the co-primary investigator of this paper and helped prepare the original and final article drafts.

VITA

2017 – B.S. Metallurgical and Materials Engineering – Colorado School of Mines

2019 – M.S. Materials Science and Engineering – University of California San Diego

J. Pelz, N. Ku, L. R. Vargas-Gonzalez, M. A. Meyers, “Additive Manufacturing of Structural Ceramics: A Historical Perspective,” Journal of Materials Research and Technology, 2021.

L. De Vivo, **J. Pelz**, J. Mendoza, H. Barrack, F. Kuester, “Towards 3D Printing of a Monocoque Transtibial Prosthesis using a Bio-Inspired Design Workflow,” Rapid Prototyping Journal, 2021.

J. Pelz, N. Ku, W. T. Shoulders, M. A. Meyers, L. R. Vargas-Gonzalez,“Multi-Material Additive Manufacturing of Functionally Graded Carbide Ceramics via Active, In-Line Mixing,” Additive Manufacturing, 2021.

J. Pelz, N. Ku, M. A. Meyers, L. R. Vargas-Gonzalez, “Additive Manufacturing Utilizing a Novel In-Line Mixing System for Design of Functionally Graded Ceramic Composites,” ARL-TR-8851, CCDC Army Research Laboratory, 2019.

B. M. Cox, **J. Pelz**, G. L. Brennecka, "Critical Evaluation of Multi-Material Additively Manufactured TiO2 & BaTiO3 Electrical Ceramics for Functionally Graded Materials Applications," Ceramic Interconnect & Ceramic Microsystems Technologies (CICMT) Proceedings, 2017.

Y. Zhang, T. Huang, D. M. Jorgens, A. Nickerson, L. Lin, **J. Pelz**, J. W. Gray, C. S. López, X. Nan, "Quantitating morphological changes in biological samples during scanning electron microscopy sample preparation with correlative super-resolution microscopy," PLOS ONE 12(5): e0176839, 2017.

ABSTRACT OF THE DISSERTATION

Exploring Process-Structure-Property Relationships via Additive Manufacturing

by

Joshua Stephan Pelz

Doctor of Philosophy in Materials Science and Engineering

University of California San Diego, 2022

Professor Marc Meyers, Chair

Additive manufacturing enables the exploration of process-structure-property relationships in ceramic and thermoplastic materials. The research presented in this dissertation is focused on tailoring function via structure, in terms of both geometry and composition. This methodology is applied to two

areas: (a) advanced ceramics for dynamic environments and (b) single-piece prosthetic limbs 3D printed in thermoplastic materials.

While advanced ceramics have many exceptional properties, their low damage tolerance remains a major challenge for real-world use, especially in dynamic environments. We propose that heterogeneous structuring will unlock extrinsic mechanisms that improve damage tolerance, which will enable the use of printed ceramic components for structural applications in the aerospace, defense, and energy sectors. Carbide specimens with composition gradients and layered structures are fabricated using a custom direct ink writing system. Sintering of multi-phase ceramics is found to generate residual stresses due to coefficient of thermal expansion mismatch. Printed specimens are characterized and mechanically tested in quasi-static and dynamic strain-rate regimes. Process-structure-property relationships are discussed with a focus on dynamic mechanical response.

Recent advances in 3D scanning and computer-aided design enable the creation of ultra-personalized medical devices based on a patient's 'digital twin' or computer-generated model from 3D scan data. Medical devices, such as prosthetic limbs and orthotic braces, can be designed around the patient's digital twin to optimize fit and function, leading to improved comfort and medical outcomes. The presented research explores the fused-filament fabrication technique to create an affordable, single-piece transtibial (below-knee) prosthetic limb. The effect of printing parameters and material selection on mechanical

strength are explored for several engineering-grade thermoplastic materials, with and without chopped fiber. Unfilled nylon is found to have an optimal balance of interlayer bonding strength and flexibility for prosthetic devices, while carbon-fiber filled nylon is shown to increase energy storage and release during the gait cycle. A patent-pending prosthesis is successfully developed and deployed in an underserved community of Ensenada, MX.

CHAPTER 1. INTRODUCTION

1.1. Advanced Ceramics and their Applications

Advanced ceramics are characterized by exceptional wear, corrosion, and temperature resistance. These materials can be biocompatible, electrically activated, and optically active. Applications for these materials span nearly every industry, with an emphasis in the aerospace, automotive, defense, and biomedical sectors. As depicted in Figure 1.1, engine components, body and vehicle armor, and load-bearing medical implants all rely on advanced ceramics.

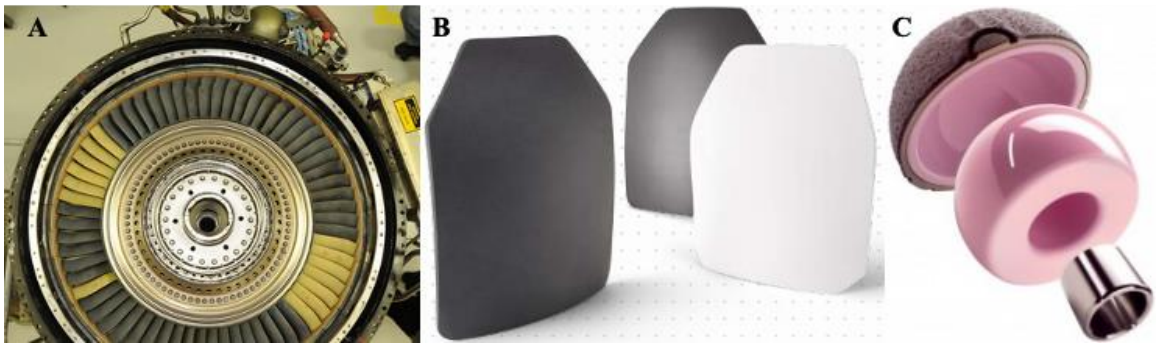

Figure 1.1. Three notable applications that use advanced ceramics for increased performance. (A) Ceramic matrix composite airplane turbine blades made from SiC, ceramic fibers, and ceramic resin increase thrust by 25% and decrease fuel consumption by 10% [geaviation.com]. (B) Ceramic body armor reduces weight and increases protection due to the high hardness and low density properties of boron carbide and silicon carbide [coorstek.com]. (C) Zirconia toughened alumina acetabular ball and cup joints greatly increase the service-life of total hip replacement implants [coorstek.com].

This proposal focuses on the application of ceramic body armor. Ceramic body armor has a long history in the U.S. Military and has been actively developed for many decades. A wide array of advanced ceramic materials has been explored, with boron carbide (B_4C) and silicon carbide (SiC) most often used due to their high hardness and low density [17]. This continuous effort has led to highly engineered, lightweight material systems with unparalleled

protective capabilities. However, while these monolithic ceramic specimens have approached the limits of hardness and strength, which are key properties for projectile defeat, cracking is eventually the dominant failure mechanism at higher projectile velocities [18]. As a result, the mode of fragmentation has the greatest effect on ballistic resistance [19]; the most effective way to improve ballistic performance is to increase the energy of fracture. Achieving full, theoretical density by reducing defects leads, generally, to superior mechanical properties [20]. Following this logic, traditional knowledge tells us to produce ceramic armor to be fully dense and of a single, monolithic material. While it is true that reducing defects, such as porosity, is vital to unlock the high hardness and compressive strength of ceramics, there is still the issue of penetration by fragmentation during ballistic events.

Carbide ceramics show exceptional ballistic performance, indicated by the cumulative mass of target fragments, for low to mid-range energy projectiles. However, studies on the impact resistance of boron carbide and silicon carbide plates using high-energy projectiles, such as armor piercing rounds, show much lower ballistic performance [1,17,21]. Figure 1.2 demonstrates the critical projectile velocity range above which ballistic performance is significantly reduced, as indicated by an increase in the fragmented mass. The reduced ballistic performance above 850 m/s suggests a lower shear strength and/or different fracture mechanisms at play. Fragments were collected from impact velocities of 793 m/s (20.3 GPa) and 907 m/s (23.3 GPa), in the sub- and

hypercritical velocity ranges respectively. It was shown that the decrease in performance at high pressures and strain rates can be attributed to localized, solid-state amorphous phase transformations in boron carbide and silicon carbide [1,22–25]. Studies reveal that intragranular amorphous bands form preferentially along specific crystallographic planes, showing similar directionality as crack paths [1]. Additionally, armor fragments show amorphous material on their fracture surfaces, verifying the conclusion that these localized amorphous bands are effectors of failure in boron carbide and silicon carbide armor.

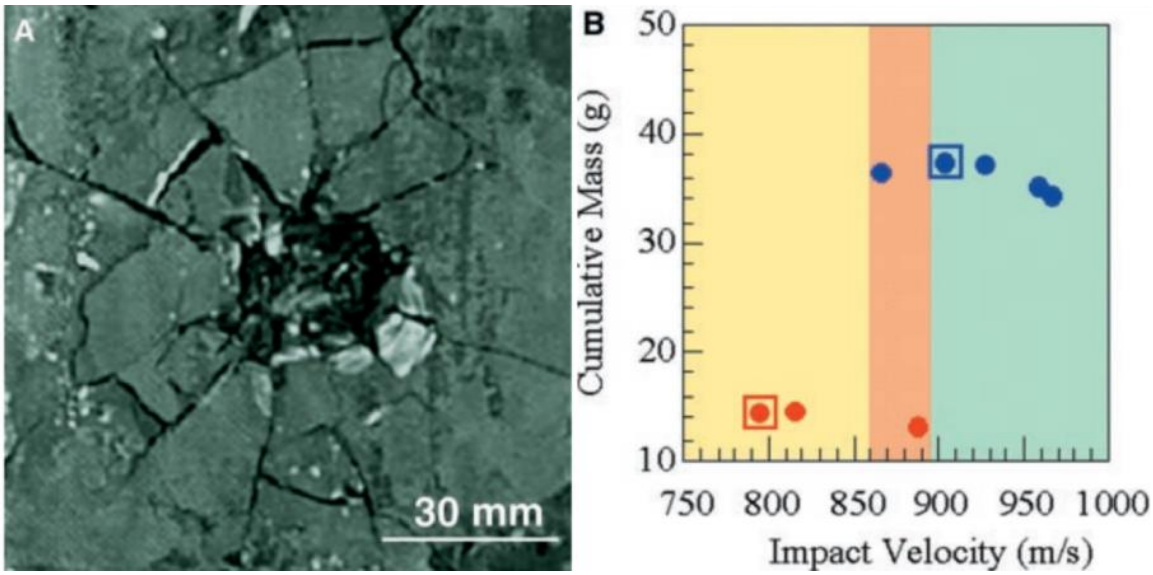

Figure 1.2. (A) Comminuted B4C plate from ballistic testing. (B) Plot of target fragment mass, for pieces less that 4 mm in size, versus impact velocity [1].

Recent studies have shown composites of boron carbide and silicon carbide to have increased ballistic performance due to various extrinsic toughening mechanisms [2,15,26]. Extrinsic mechanisms such as crack-tip deflection, blunting, and bridging increase the toughness of B_4C-SiC composites

over that of their intrinsic properties. Two of these mechanisms, crack-tip deflection and crack bridging, are shown in Figure 1.3.

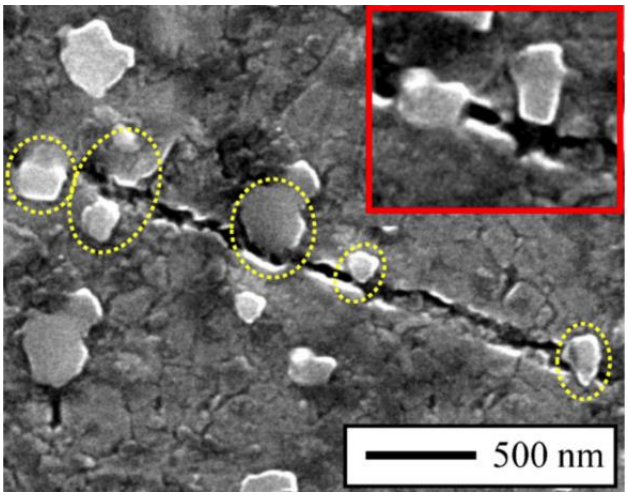

Figure 1.3. Scanning electron micrograph of a B_4C-SiC composite, a B_4C matrix with SiC inclusions, showing crack-tip deflection and crack bridging, which are two extrinsic toughening mechanisms [2].

The B_4C-SiC composite, with a B_4C matrix and second phase inclusions of SiC, illustrates the tortuous path a crack must take through composite parts due to extrinsic mechanisms. The crack must traverse around each SiC inclusion and is further hindered by SiC bridges. Each of these obstacles requires a certain amount of energy to overcome, which increases the toughness of composite B_4C-SiC parts by 65% over monolithic B_4C parts [2]. For these reasons, the state of the art for personal body protection devices employs B_4C-SiC composite ceramic plates. To drive further advancement, alternative methods of fracture mitigation must be explored to fully realize the exceptional properties of advanced ceramics.

1.2. Natural Design Motifs

Inspiration for alternative methods of fracture mitigation can be gained from nature, where biological structures derive superior mechanical performance using hierarchical structuring and composition gradients, with one typical example being the nacreous abalone shell. Nacre is a natural composite of calcium carbonate tiles and organic interlayers in a 'brick and mortar' microstructure with additional higher-scale organic mesolayers [27]. The structural organization of nacre at multiple length-scales leads to an 8-fold increase in fracture toughness over that of pure calcium carbonate [3]. Similarly, fish scales, such as those of the arapaima, use hierarchical structuring and mineralization gradients to increase toughness, strength, and ductility while remaining thin and lightweight [28,29]. Figure 1.4 highlights two biological design motifs, layering and mineral gradients, which are found in arapaima scales and the abalone shell. Figure 1.5 demonstrates the mineralization gradients present in the dactyl club of the mantis shrimp, which provide damage tolerance during the repeated dynamic loading of the club strikes.

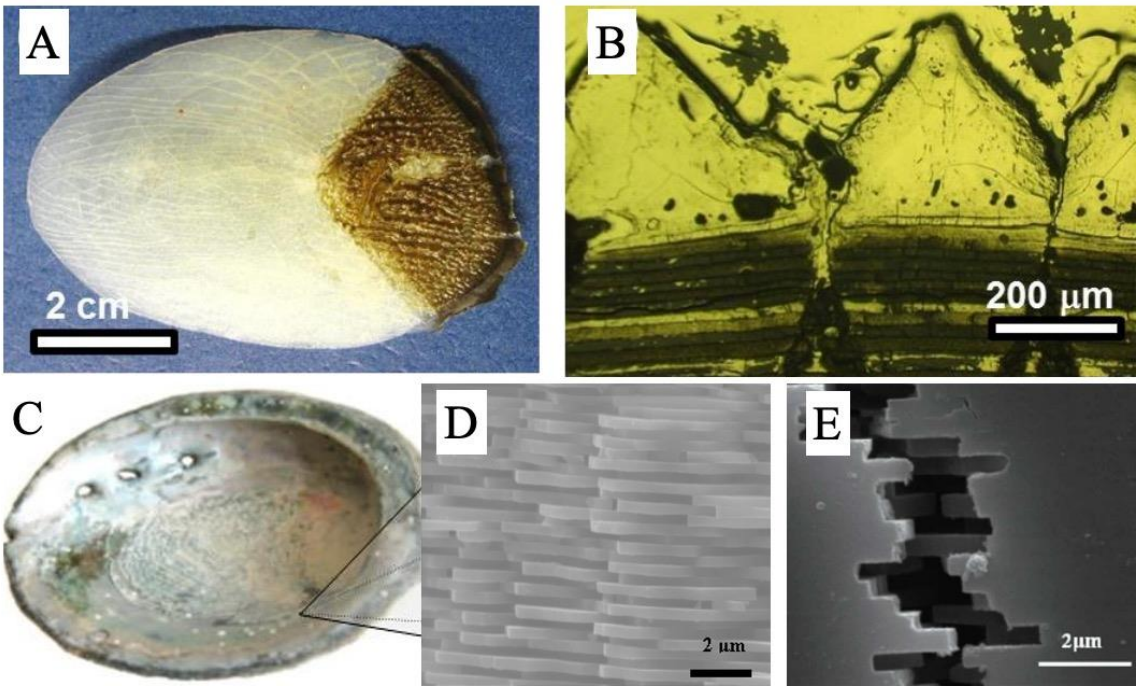

Figure 1.4. (A) The arapaima scale consists of a flexible base and hard, mineralized outer surface that inhibits penetration. (B) The mineralization gradient from the base layers to the hard, top surface arrests cracks that form in the arapaima scale during penetration events. (C) The abalone shell uses layering and hierarchical structuring to improve toughness over its weak constituent materials. (D) $CaCO_3$ tiles are arranged in a brick and mortar structure. (E) The tortuous crack path around aragonite tiles leads to an 8-fold increase in the toughness of nacre over pure $CaCO_3$ [3].

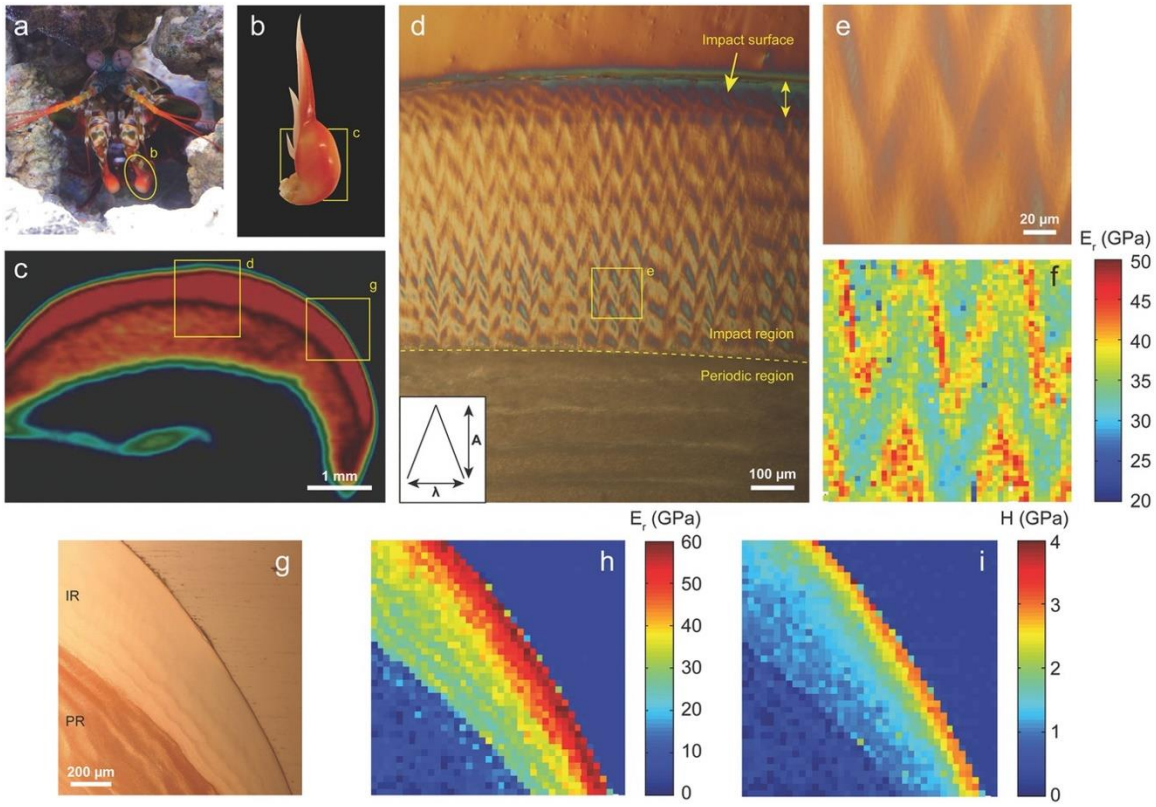

Figure 1.5. The mantis shrimp uses its club smash through the hard shells and feed on crustaceans. A-I) Overall structure with successively closer microscopy and accompanying nanoindentation maps demonstrating the composition gradient on the striking surface and in internal structures of the dactyl club. A combination of bouligand structuring and compositional gradients provide a high dynamic damage tolerance necessary for continued feeding.

Bioinspired design features can enhance performance if integrated into next-generation ceramic armor materials since they can provide greater strength, hardness, and toughness [30]. Indeed, recent studies have shown that ceramic specimens with second phase inclusions, layers, and multi-scaled organization show an increased toughness due to extrinsic fracture mechanisms that inhibit crack propagation [2,31–34]. Moshtaghioun et al. [2] observed two extrinsic toughening mechanisms, crack tip deflection and crack bridging, for a B_4C matrix with SiC inclusions shown in Figure 1.3. These extrinsic toughening mechanisms

led to a 65% increase in toughness compared with monolithic B_4C. Wang et al. [31] and Wilkerson et al. [32] demonstrated the toughening effect of using biomimetic nacre-like structures in ceramic composites. Rao et al. [33] and Lugovy et al. [34] increased the toughness of layered ceramic materials using thin compressive layers to deflect cracks at layer interfaces. These findings have catalyzed a major research effort to study the effects of composition, geometry, and multi-scaled structuring on mechanical performance in ceramic materials.

1.3. Fabrication Methods for Heterogeneous Structures

To manufacture these multi-phase materials, a processing technique is required that can produce complex, three-dimensional parts with material heterogeneity and organization across multiple length scales. Various ceramic forming technologies exist and are of commercial manufacturing scale, e.g. pressing, extrusion, slip casting, tape casting, and injection molding [35]. However, these techniques severely limit the available design space for variation of composition and geometry. Tape casting, without secondary layering steps, only allows control of the sheet thickness [35]. Pressing and extrusion produce parts of simple geometry such as disks, rods, and tubes [35]. Slip casting and injection molding afford the most geometric freedom, but do not enable material heterogeneity [36]. With the exception of layered tape-cast specimens, where layers may be of different materials [37], these techniques produce chemically homogenous parts.

Additive manufacturing (AM), on the other hand, enables the production of parts with complex, multi-scaled geometries, including internal structures [11,38,39]. Additionally, multi-material AM can support material heterogeneity by discrete layers and composition gradients [32,40]. The ISO/ASTM standard 52900:2015(E) defines the fundamental principle of AM processes as, “forming three dimensional parts by the successive addition of material” [4]. Additive manufacturing technology is based on fusing or bonding feedstock materials to build a part. The primary distinction between processes is the method of joining; this establishes seven families of AM technologies as shown in Figure 1.6: vat photopolymerization, powder bed fusion (PBF), binder jetting, material jetting, sheet lamination, material extrusion, and directed energy deposition.

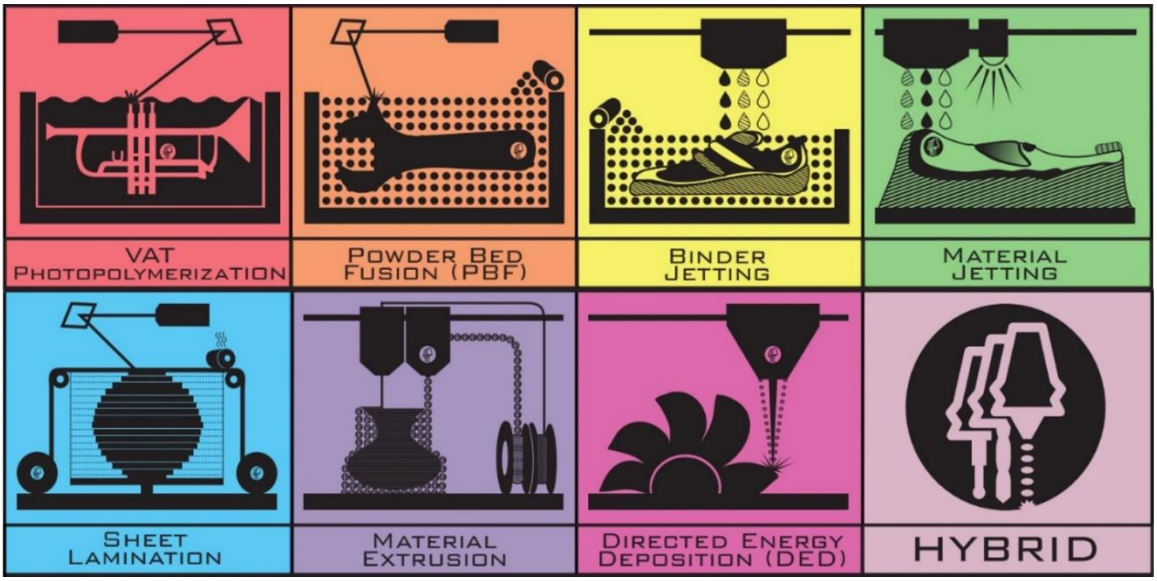

Figure 1.6. The families of additive manufacturing, including hybrid processing that combines two or more of the illustrated processes [4].

Metallic, ceramic, and polymeric materials have all been adapted for use in these AM processes, enabling the production of both prototypes and end-use

components. Additive manufacturing is best suited for low-volume production of complex geometries, because time and cost is independent of complexity in the plane normal to the build direction. A case study performed by E. Atzeni et al., whom found that the cost break-point for an aluminum aerospace component was a production volume of 42 pieces when comparing high-pressure die casting (HPDC) and powder bed fusion (PBF) processes [41]. Due to the high capital cost of the die and HPDC machine, production volumes below 42 pieces strongly favor the AM PBF process. The cost benefit of rapid prototyping techniques in the automotive industry has been extensively reported on [42]. Direct ink writing (DIW), a material extrusion AM technique [4] that allows multi-material and mixing capabilities [43–46], was chosen to fabricate multi-phase carbide specimens in this study. The DIW technique, also known as robocasting, involves extrusion of a line of highly-loaded colloidal suspension, termed 'ink', through a nozzle in a specific pattern layer-by-layer to produce a three-dimensional part [47]. This line of deposited material is known as a trace. The ink used for DIW relies on yield-pseudoplastic behavior to self-support following extrusion. Yield-pseudoplastic rheology enables the ink to retain structural integrity up to its yield stress, followed by shear-thinning behavior [48,49]. This behavior is critical for ink to both flow through a small nozzle (high-shear environment) and retain its shape post-extrusion (low-shear environment).

1.4. Ceramic Additive Manufacturing

Ceramic AM techniques are defined as indirect processes, because post-processing is required to densify printed green bodies [4]. A prerequisite of high sintered density is high green density; this requires high ceramic content and low binder/dispersant content [50]. The maximum density of loose, random packing for powder is approximately 60 vol.% [51], which effectively sets the upper-bound for ceramic content. Ink formulation in this study targets a ceramic content as close to 60 vol.% as possible without sacrificing yield-pseudoplastic rheology. Shrinkage occurs during sintering as a function of ceramic content and can impart significant residual stresses on densified parts. Residual stresses are the result of non-uniform shrinkage, which can arise from asymmetrical geometries and chemical heterogeneity. This effect is especially pronounced in parts with discrete composition changes, such as layered composites, where different coefficients of thermal expansion (CTE) produce compressive and tensile residual stresses that can lead to part failure [52]. Thus, a balance must be found between printability and post-print processing, namely sintering behavior.

Dense, complex oxide ceramic parts have been produced via AM techniques [53–57], whereas AM of dense carbides has faced challenges due to difficult colloidal dispersion and high sintering temperatures. Costakis et al. [58] produced B_4C parts via material extrusion, but obtained a theoretical density of just 82% through pressureless sintering. A higher theoretical density of 95% was achieved for extruded B_4C parts by Eqtesadi et al. [59], but required the use of

cold isostatic pressing and spark plasma sintering. These studies demonstrated the feasibility of AM for producing dense, geometrically complex carbide parts, but lacked investigation into material heterogeneity.

Several recent studies have attempted multi-material ceramic AM in order to develop functionally graded oxides. Functionally graded oxide ceramics were made using a material extrusion process with active mixing by Li et al. [44]. Similarly, a material extrusion system with mixing capabilities was designed by Smay et al. [43] to develop ternary mixtures for high-throughput characterization of oxide ceramics. Bioinspired ceramic-metal composites were demonstrated by Wilkerson et al. [32] with discrete “brick and mortar” structures mimicking the abalone nacre. These bioinspired $0.95Al_2O_3$-0.05Ni composites showed improved toughness compared with pure alumina based on their functional design. Studies on AM of functionally graded ceramics often use custom-built equipment due to the lack of commercial systems with multi-material and mixing capabilities [32,43,44]. Whereas multi-material ceramic AM of oxides has seen recent progress, fabrication of functionally graded carbides has remained elusive due to challenges with densification, ink formulation, and sourcing processing equipment.

This dissertation intends to fill the gap in processing technology for the development of advanced ceramic materials with tailored structural organization and material heterogeneity. High ceramic content B_4C and SiC inks are formulated with suitable rheology and their printability is evaluated. A custom,

low-cost DIW system is designed with active, in-line mixing capabilities for real-time control of material heterogeneity. Characterization and mechanical testing of multi-phase carbide specimens in both green and sintered states is performed to demonstrate and validate the effectiveness of this processing technique.

CHAPTER 2. HISTORY OF ADDITIVE MANUFACTURING

2.1. Introduction

Additive manufacturing (AM) has created a new era of digital manufacturing, where engineering practices, computer-aided design platforms, and part sourcing pipelines are dramatically changing. AM techniques are capable of producing plastic, metal, and ceramic components for both prototyping and end-use purposes.

The focus of Chapter 2 is the fabrication of dense, structural advanced ceramic components using the seven families of additive manufacturing. Initial studies on additive manufacturing of ceramic materials were reported just a few years after those of metal and plastic materials. However, industrial application of ceramic additive manufacturing is more than a decade behind metallic and plastic materials. Many of the challenges of ceramic AM can be traced back to the intrinsic difficulties of processing structural ceramic materials, including high processing temperatures, defect-sensitive mechanical properties, and poor machining characteristics. To mature the field of ceramic AM, future research and development should focus on expanding material selection, improving printing and post-processing control, realizing single-step processing, and unique capabilities such as multi-material and hybrid processing.

2.1.1. Preface

In this chapter, we detail the history, recent advances, and future directions for additive manufacturing (AM) of bulk, dense structural ceramics.

Advanced ceramics are attractive for use in structural applications due to their high hardness, wear resistance, and corrosion resistance. To achieve these properties, a relative density greater than 95% is necessary for structural ceramics, with many applications such as armor ceramics requiring above 98% relative density [60]. High hardness and wear resistance properties complicate machining processes; ceramic AM research is driven by the need for cost effective methods to manufacture complex components. Through our historical analysis of the development of ceramic AM, seminal works are highlighted to provide context for the lag in technology for ceramic AM compared with plastic and metal AM.

For readers interested in components with designed porosity such as lattice structures, several excellent reviews exist [61–63]. Specific applications for designed porosity include printing hydroxyapatite implants [64], bone scaffolds [65], and variable stiffness ceramic foams [66]. Bae [67] reviewed and investigated the use of direct ceramic casting using vat photopolymerization to create ceramic investment casting molds for applications like turbine blades with integrated cooling channels. Although the use of ceramic AM for creating molds is important, it is out of scope for this review. Several groups have used the additive manufacturing technique of direct energy deposition to develop ceramic coatings on titanium [68,69] and steel [70,71] to increase wear and corrosion resistance. Properties such as biocompatibility can also be improved by

deposition of ceramic coatings [72]. Although this is an important body of research, coatings are also out of scope for this review.

2.1.2. Advanced Ceramics and their Applications

Advanced ceramics are characterized by exceptional wear, corrosion, and temperature resistance. These materials can be biocompatible, electrically activated, and optically active. Applications span nearly every industry, with an emphasis in the aerospace, automotive, defense, medical, and energy sectors. Engine components, body and vehicle armor, and load-bearing medical implants all rely on dense, structural advanced ceramics [73].

Ceramic forming is a mature technology with several methodologies at a commercial manufacturing scale, e.g. pressing, extrusion, slip casting, tape casting, gel casting, and injection molding [74]. However, these traditional forming techniques often only allow two-dimensional design freedom, cannot create internal or multi-scaled features, and require complicated and expensive dies [38]. In addition, engineering of chemically heterogeneous structures is limited due to the stochastic nature of traditional powder mixing and processing. Tape casting, without secondary layering steps, only allows control of the sheet thickness. Pressing and extrusion produce parts of simple geometry such as disks, rods, and tubes [75]. Slip casting [76], gel casting [53,77], and injection molding [36] afford the most geometric freedom, but do not enable material heterogeneity. With the exception of layered tape-cast specimens, where layers may be of different materials [37], these techniques all produce chemically

homogenous parts. Furthermore, due to the exceptional wear resistance of advanced ceramics, machining is time consuming and expensive. In fact, machining of dense advanced ceramic parts can amount to more than 80% of the production cost [78].

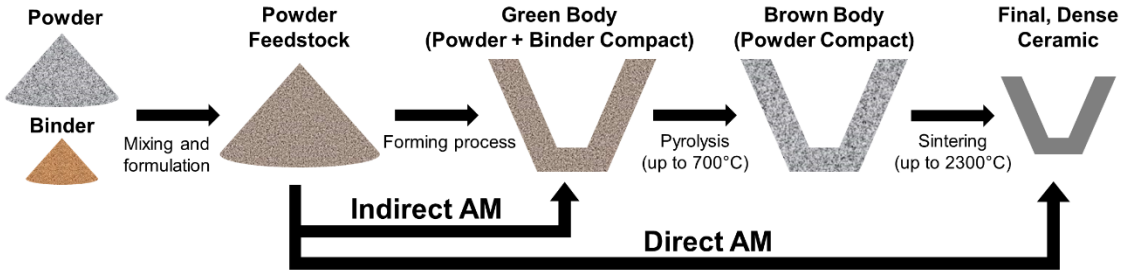

Figure 2.1. Direct additive manufacturing processes simultaneously produce a desired shape with final properties, whereas indirect processes require two or more steps to produce the desired geometry with final properties. For ceramic materials, pyrolysis and sintering are necessary to attain final properties after an indirect process is used to form a green body.

2.1.3. Additive Manufacturing

Additive manufacturing (AM), conversely, enables the production of parts with complex, multi-scaled geometries including internal structures [11,38,79]. Additionally, multi-material AM allows for tailored material heterogeneity by discrete layers and composition gradients [32,40,80]. The ISO/ASTM standard 52900:2015(E) defines the fundamental principle of AM processes as, “forming three dimensional parts by the successive addition of material” [4]. The primary distinction between additive processes is the method of joining, which establishes seven families of AM technologies: vat photopolymerization, powder bed fusion, binder jetting, material jetting, sheet lamination, material extrusion, and directed energy deposition [4]. These processes are described in Table 2.1, with information including material selection, special features, advantages and

disadvantages, and mechanical properties and microstructure. AM is achieved in either a single-step process (commonly called ‘direct’) or multi-step process (commonly called ‘indirect’) [4]. Figure 2.1 illustrates the difference between direct processes that simultaneously produce a desired shape with final properties and indirect processes that require two or more steps to produce the desired geometry with final properties. Metallic, ceramic, and polymeric materials have all been adapted for use in these AM processes, enabling the production of both prototypes and end-use components [73].

Additive manufacturing is best suited for low-volume production of complex geometries, because time and cost are weakly dependent on complexity; for masked AM processes, time and cost are fully-independent from complexity in the build plane [42]. A case study performed by Atzeni et al. [41] compared the cost of manufacturing an aluminum aerospace component using high-pressure die casting and powder bed fusion processes. Production volumes below 42 parts favor the AM powder bed fusion process, due to the high cost and long manufacturing time of the die. Further, AM affords the ability to make complex geometries that are impossible to create through subtractive manufacturing or forming processes.

It is important to note that mechanical properties are largely anisotropic for parts produced by AM, due to the layer-wise nature of the process [73]. In fact, the term ‘3D printing’ is a misnomer, as printing is a one- or two-dimensional process repeated layer-wise in the build direction. For this reason, mechanical

properties will differ depending on the testing orientation with respect to the build direction. Anisotropic mechanical properties arise from differences between inter-layer and inter-trace bonding strength, microstructure texturing, and other printing artifacts [81].

2.1.4. Challenges in Ceramic Additive Manufacturing

The commercial use of additive manufacturing to produce ceramic components is more than a decade behind that of polymeric and metallic materials. In addition, the adaptation of AM for ceramic materials occurred nine years after that of polymers [82]. This lag in technology is primarily due to the difficult processing conditions and quality requirements intrinsic to ceramic materials. For example, the lower melting temperatures of metallic and polymeric materials enables direct AM, wherein feedstock material is processed above its melting point, bonds to nearby material, and cools to maintain its desired shape with final properties, all within a single machine. In contrast, a majority of ceramic AM processes are indirect, wherein a green body is formed by the 3D printer using a binding agent to hold ceramic particles together and then several post-processing steps are required to attain final properties [48].

Table 2.1. The seven families of AM processes described for structural ceramic components. Material selection, special features, advantages, disadvantages, multi-material capability, and mechanical properties and microstructure are summarized for each ceramic AM technique.

Classification	Technique	Direct/Indirect	Multi-material Capable	Description	Feedstock Material
Vat Photo-polymerization	SL	Indirect	No	Stereolithography uses a laser to cure resin point-by-point.	Liquid vat of photocurable resin loaded with ceramic powder.
	DLP	Indirect	No	Digital light processing uses a light projector to selectively cure resin layer-by-layer.	
Powder Bed Fusion	SLS	Indirect	No	Selective laser sintering uses a laser to partially fuse or sinter ceramic powder point-by-point.	Ceramic powder bed; may contain a polymer binder.
	SLM	Direct	No	Selective laser melting uses a laser to fully sinter or melt ceramic powder point-by-point.	Ceramic powder bed
Binder Jetting	3DP	Indirect	No	Three-Dimensional Printing uses an inkjet head to selectively deposit liquid binder to fuse ceramic powder	Ceramic powder bed
Material Jetting	MJ	Indirect	Yes	Material jetting uses a inkjet head to rapidly eject droplets of photocurable or thermoplastic resin loaded with ceramic powder. Solidification happens by cooling or UV lamp curing.	Thermopolymer or photocurable ink loaded with ceramic powder
Sheet Lamination	LOM	Indirect	Yes, but only layer to layer	Layered object manufacturing uses a laser to cut two-dimensional profiles from a ceramic green tape, which are layered and fused through pressure and heat.	Tape cast polymer sheets loaded with ceramic powder
Material Extrusion	DW	Indirect	Yes	Direct write techniques extrude a ceramic slurry, point-by-point, that solidifies via rheological, temperature, or photocurable effects.	Slurry of ceramic powder, solvent, and binder
	FDC	Indirect	Yes	Fused deposition of ceramics extrudes thermoplastic filament loaded with ceramic powder from a heated nozzle, point-by-point.	Thermopolymer filament loaded with ceramic powder
Directed Energy Deposition	LENS	Direct	Yes	Laser engineered net shaping uses a high-powered laser to melt a jet of powder point-by-point in a process similar to welding.	Ceramic powder

Table 2.1. The seven families of AM processes described for structural ceramic components. Continued. Reference numbers tied to published review, not dissertation.

Classification	Minimum Required Binder Content [vol.%]	Minimum Feature Size [µm]	Maximum Density [%TD]	Average Flexural Strength [Mpa]	Challenges	Advantages
Vat Photo-polymerization	40 [61]	102 (x-y); 25 (z) [61]	97 (Al_2O_3) [61]	275 (Al_2O_3) [61]	Limited material selection (refractive index issues prevent the use of many borides, carbides, and nitrides).	Fast printing time; highest resolution; good surface finish; large part size
	55 [66]	40 (x-y); 25 (z) [66]	99.3 (Al_2O_3) [64]	427 (Al_2O_3) [64]		
Powder Bed Fusion	10 [83]	200 (x-y) [83]	89 (Al_2O_3) [82]	148 (Al_2O_3) [82]	Poor surface finish; low green body density	Overhangs are supported; wide material selection; good resolution
	0 [79]	100 (x-y); 100 (z) [79]	100 (Al_2O_3) [80]	500 (Al_2O_3) [80]	Severe thermal gradients cause part failure and limit size	
Binder Jetting	60 [100]	50 (x-y); 95 (z) [33]	98.5(ZTA) [98]	441 (ZTA) [98]	Poor surface finish; low green body density	
Material Jetting	65 [109]	20 (x-y); 10 (z) [106]	99 (PZT) [109]	Not reported	Low green body density	High resolution; multi-material capable
Sheet Lamination	44 [118]	190 (z) [118]	97 (Si_3N_4) [118]	700 (Si_3N_4) [118]	Defects and poor bonding at layer interfaces	Highest speed; layered composites
Material Extrusion	<10 [137]	1000 (x-y); 850 (z) [137]	98 (Al_2O_3) [137]	145.5 (Al_2O_3) [137]	poor resolution; difficult feedstock design	Low-cost process; multi-material capable; near-net shaping
	45 [136]	250 (x-y); 254 (z) [136]	>99 (Si_3N_4) [136]	908 (Si_3N_4) [136]	It is difficult to load filament with enough ceramic powder to facilitate full densification	low-cost process; multi-material capable
Directed Energy Deposition	0 [152]	400 (x-y); 500 (z) [152]	98 (Al_2O_3) [145]	Not reported	Severe thermal gradients cause part failure and limit size	direct processing; multi-material capable

Post-processing steps include pyrolysis (up to 700°C) and sintering (up to 2300°C), which are necessary to remove binders from the green body and

consolidate the ceramic powder into its final geometry with final properties. Green bodies formed by AM machines contain, at a maximum, 65-72 vol.% ceramic powder [48]. Post-processing to full density will result in dimensional shrinkage exceeding 30% [83], which can lead to warping, cracking, and poor dimensional control.

The mechanical properties of ceramic materials are defect-dominated due to their brittle nature and low damage tolerance. The hardness of alumina increases by more than 30% for a change in relative density from 92% to 98% [84]. This correlation between mechanical properties and flaw content dramatically increases the necessity of accurate processing control. Unfortunately, limited standardization exists for material feedstock production, process parameters, and post-processing, which leads to poor quality control in additive manufacturing processes [85].

2.2. The Inception of Additive Manufacturing

2.2.1. First Steps

The inception of additive manufacturing goes back to 1980 when Hideo Kodama [86], of the Nagoya Municipal Industrial Research Institute of Japan, invented the vat photopolymerization process and filed a patent for a “stereoscopic figure drawing device”. Kodama [87] developed a rapid, low-cost, and automated process for selectively curing liquid photo-hardening polymer using ultraviolet (UV) energy. Selective curing was accomplished by either a mask pattern or point-by-point using a laser, and repeated layer-by-layer to build

a three-dimensional part. Although this work marks the first published record of a successful additive manufacturing process, it did not generate any commercial traction and Kodama's patent expired without proceeding past the examination stage.

In 1984, Charles Hull [88] patented and commercialized the first AM technology. He developed an "apparatus for production of three-dimensional parts by stereolithography," which was named SLA-1 [89]. In addition to inventing the machine and method, he created the STL (an abbreviation of stereolithography) file format to store geometric data for parts. This machine falls into the vat photopolymerization family of AM technologies. Hull [88] developed the SLA-1 with the intent of more efficiently producing prototypes. Closely following Hull's patent, the selective laser sintering (SLS) process, a type of powder bed fusion, was patented in 1986 by Deckard et al. [90]. They formed the company DMT based on their SLS technology, which was later acquired by 3D Systems. In 1987, Masters [91] patented a process for ejecting particles or droplets or using a laser to attract material to a specific point to automatically create three-dimensional objects. Masters' patent covers both material jetting and direct energy deposition processes. The following year, the sheet lamination process was patented by Feygin [92] with the company Helisys. Woven fiber composites impregnated with a bonding agent were initially used as feedstock material to build 3D parts with the sheet lamination method [93]. In 1989, two additional patents were filed that covered fused deposition modeling (FDM) [94],

a type of material extrusion, and 3D Printing [95], the copyrighted name for binder jetting. Crump [94] started the company Stratasys based on FDM, while Sachs et al. [95] invented the binder jetting process at the Massachusetts Institute of Technology (MIT) and then licensed their technology to several companies. A timeline of the patents and first published accounts with a ceramic material is shown in Figure 2.2.

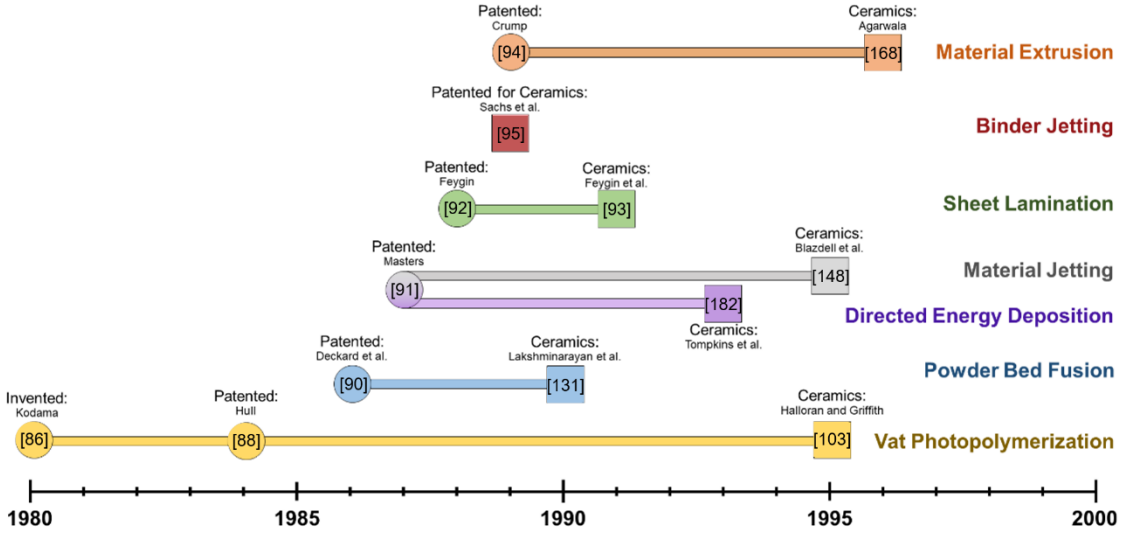

Figure 2.2. The invention of additive manufacturing processes occurred in the 1980s, but the adaptation of these techniques for ceramic materials extended into the 1990s. The time between invention and ceramic material use varied greatly, with binder jetting being invented using ceramic materials versus vat photopolymerization which was invented 15 years before ceramic materials were successfully demonstrated.

2.2.2. Rapid Prototyping to Additive Manufacturing

These processes, then termed rapid prototyping techniques, were first surveyed in 1991 by Kruth [96]. In their infancy, additive manufacturing techniques were believed to be solely useful for prototyping. However, during the 1990s few new processes were developed and instead an effort was made to move towards higher process efficiency and production of end-use parts [97].

Indeed, the term ‘additive manufacturing’ had already begun to replace ‘rapid prototyping’. Six-fold and eight-fold decreases in process time for vat photopolymerization and material extrusion, respectively, were realized during the 1990s [97]. This decrease in processing time enabled a new wave of rapid throughput manufacturing, where one-off parts could be ordered, manufactured, and shipped in under 24 hours [98].

Even more importantly, however, was the rapid expansion of materials amenable for additive manufacturing processes: high performance polymers, metals, and ceramics enabled the development of functional, end-use parts. AM has great potential for creating composite parts with graded compositions, where virtually any powder material can be combined and printed into heterogeneous components with spatially tailored properties [99]. This trend continues currently, where the major goals of AM research include the development of quality control mechanisms and expanding the AM material library to facilitate the production of end-use parts [100]. Today, major players in the ceramic AM commercial sector produce end-use components for medical, aerospace, defense, automotive, and energy applications [101].

2.3. Vat Photopolymerization for Advanced Ceramics

2.3.1. Foundations

Vat photopolymerization, originally called stereolithography, was the first family of additive manufacturing processes adopted for commercial use. 3D Systems dominated the market with their SLA-250 machines [89], an industrial

iteration on their SLA-1 prototype machine. Three-dimensional parts are produced layer-by-layer, by the selective application of UV energy to photocurable resin, as illustrated in Figure 2.3A. In order to print ceramic parts, ceramic powder is loaded into the resin [102]. Resin can be cured point-by-point using a laser or layer-by-layer using a light projector or masked liquid-crystal display (LCD) screen. Processes where the entire layer is cured simultaneously can reduce build times by a factor of 100 [97]. This AM technique excels at producing highly complex geometries with fine resolution and good surface finish. Vat photopolymerization can be carried out in either a bottom-up or a top-down approach [96]. The bottom-up approach has the advantage that uncured resin will drain back into the vat, reducing the volume of resin necessary to build a part [100]. Vat photopolymerization is an indirect process for ceramic materials because the photocurable resin, which is essential to the polymerization process, must be removed through post-processing steps to obtain a dense ceramic component.

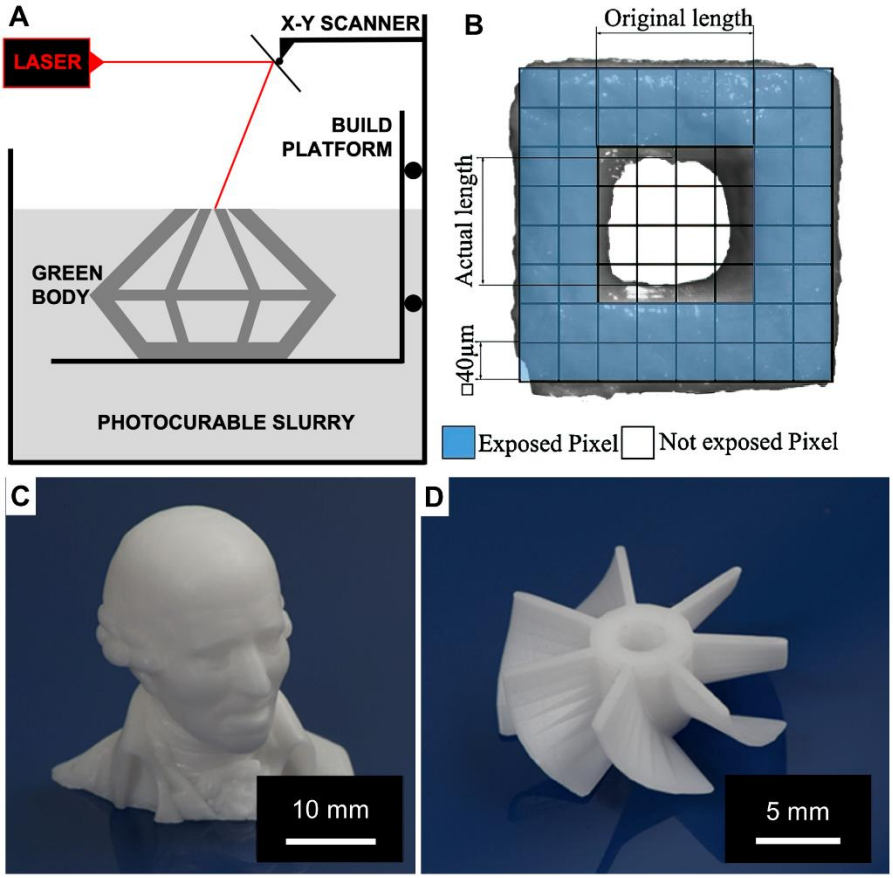

Figure 2.3. (A) Diagram illustrating the vat photopolymerization technique, where three-dimensional parts are created by selectively curing a photocurable resin layer-by-layer. (B) Overexposure occurs due to light scattering in highly loaded particulate suspensions [5]. (C,D) Dense zirconia specimens with complex geometry were produced with no visible layer interfaces after post-processing [5].

2.3.2. Evolution

In 1995, Griffith and Halloran [103] first demonstrated the use of vat photopolymerization for fabrication of ceramic parts, with the goal of more rapidly producing metal casting molds. Vat photopolymerization was studied for silica, alumina, and silicon nitride particulate loaded resins. Major challenges were the cure depth and rheology of the ceramic loaded resins. Viscosity increases exponentially with volume fraction ceramic material, which competes with the

requirement that the resin must be able to flow across the build surface. The three main factors found to determine cure depth were particle size, interparticle spacing, and refractive index difference between the resin and ceramic particles, with refractive index difference as the dominant factor [104]. Alumina and silica were both cured at depths of hundreds of micrometers, but silicon nitride could only be cured to tens of micrometers due to its large refractive index difference from the diacrylate resin. Silicon nitride parts could not be produced due to the low cure depth. Alumina parts were produced from 40 vol.% alumina powder (average particle size of 0.34 μm) in diacrylate resin with dimensional stability in both thick and thin sections. Due to light scattering, parts showed 5-15% dimensional errors. Sintering at 1550°C resulted in 100% relative density and fracture surfaces free of printing artifacts such as layer lines [105].

Two years later, Griffith and Halloran [106] conducted a thorough follow-up study on the effects of laser parameters with the goal of predicting and improving the cure depth for many advanced ceramics, including TiO_2, SiC, Si_3N_4, and Al_2O_3. Cure depths were modeled for 40-50 vol.% ceramic particulate loaded resin. Cure depth can be modeled using a Beer's law equation combined with an extinction coefficient,

$$D_c = \frac{2\langle d \rangle}{3\tilde{Q}} \frac{n_0^2}{\Delta n^2} \ln\left(\frac{E_0}{E_{crit}}\right), \tag{2.1}$$

where $\langle d \rangle$ is average particle size, Q is the scattering efficiency term, Δn^2 is the squared refractive index difference between the ceramic and photocurable monomer, and E_0 is the energy density [106]. The refractive index difference

between the ceramic and resin was, again, found to have the greatest effect on cure depth, followed by interparticle spacing, and lastly (less important than previously thought) ceramic particle size. Although particle size has a minor effect for cure depth, it significantly impacts slurry rheology and post-processing characteristics, and must be carefully controlled. For highly-loaded colloidal alumina and silica suspensions, Garg et al. [107] studied light adsorption differences between short-pulse and constant light sources. Relationships were experimentally verified and, in agreement with previous work, interparticle spacing has an important effect.

In 1998, Hinczewski et al. [108] determined that heating the vat of photocurable suspension will significantly reduce viscosity, which enables higher ceramic content. For an alumina-diacrylate photocurable suspension, viscosity was reduced by a factor of six as temperature was increased from 25 to 70°C. This novel method enabled an unusually high ceramic content of 53 vol.%, while maintaining acceptable rheological (less than 5 Pa*s) and cure-depth (greater than 200 µm) properties for printing.

2.3.3. Recent Developments

Challenges faced in early vat photopolymerization studies of ceramic materials, including suspension rheology, particulate-induced light scattering, and low cure depth, remain a major focus in recent studies [102]. The requirement for feedstock material with high ceramic content leads to rheological challenges, scattering, and low cure depth. With the goal of eliminating rheological

challenges, Chartier et al. [5] used a novel processing approach in 2002 that enabled the use of photocurable suspensions with ceramic content up to 60 vol.%. Instead of relying on fluid flow to recoat the build surface, the photocurable alumina suspension was dispensed using a piston and spread in even layers using a doctor-blade. This method enabled the printing of uniform layers down to 25 µm. An added benefit of tape-casting feedstock material for the vat photopolymerization method is that over-hang structures are supported, and shrinkage, warping, and cracking are reduced. Alumina (average particle size of 1.5 µm) parts sintered at 1700°C achieved relative densities of 97% and had flexural strengths of 275 MPa, comparable to those of traditionally processed specimens (250-350 MPa). Zhang et al. [109] added fine grains and sintering additives to improve the densification of parts printed from large particle-size alumina powder. For a ceramic content of 50 vol.%, alumina (average particle size of 10.34 µm) parts sintered at 1600 °C showed minimal densification. By using a bimodal mixture of alumina powder with average particle sizes of 10.34 (85%) and 1.05 µm (15%), in addition to 1 wt.% MgO and 3 wt.% TiO_2, a relative density of 92.97% was achieved. While a relative density of 93% is insufficient for structural ceramic components, this study demonstrates the potential of low-cost feedstock powders combined with fine grains and sintering additives. For printed zirconia parts, adding 7.5 vol.% 3Y-TZP increased the relative density from 91.84% to 96.40% [110].

In the mid-2010s Schwentenwein et al. [111] and Scheithauer et al. [112] used a masked, bottom-up approach, termed digital light processing (DLP), to improve the resolution and processing speed for alumina parts. During the build process, a part is submerged into the vat of photocurable suspension with the build surface just 25 μm from the bottom of the vat. The entire layer is then cured at the same time using a digital micromirror device (DMD) based on light-emitting diodes (LED). Build-up speeds less than 30 s per layer, irrespective of layer complexity or selected area, were achieved through the dynamic masked curing process. Mitteramskogler et al. [113] utilized different light curing strategies to reduce printing flaws and improve densification. Overexposure, where material outside of selected pixels is cured, is caused by light scattering and is shown in Figure 2.3B. Constant, exponential, and softstart light curing strategies, which change light intensity with respect to time during curing, were tested by pulsing the DMD at a specified duty-cycle. The softstart strategy starts curing at a low intensity (duty-cycle near 10%) and then steps up to full intensity (duty-cycle of 100%). No significant change was observed for exponential curing as compared to constant curing. Conversely, softstart curing reduced cracks and increased green density. A second strategy, using a cure depth greater than the layer height, was shown to improve interlayer bonding. For a layer height of 25 μm, cure depth of 150 μm, and softstart curing strategy, dense zirconia specimens were produced with no visible layer interfaces after post-processing (Figure 2.3C,D).

Ding et al. [114] fabricated SiC green bodies using vat photopolymerization in 2019, a major accomplishment because the high absorbance of SiC and high refractive index difference between SiC and photocurable resin. The refractive indices for diacrylate monomer, Al_2O_3, Si_3N_4, and SiC are 1.46, 1.70, 2.10, and 2.65, respectively. A large refractive index difference and absorbance results in a low cure depth, which impedes vat photopolymerization processing. This phenomenon was initially reported on by Griffith and Halloran [106], and fabrication of parts using Si_3N_4 and SiC suspensions was not achieved. Ding et al. [114] achieved a cure depth of 60 μm by using large SiC particulates of diameter 15 μm and a ceramic content of 40 vol.%. Cure depth was increased to 66.8 μm by adding 1 wt.% nanometer-sized SiC powder [115]. The nanometer-sized SiC powder also improved suspension stability, which enabled fabrication of complex SiC green bodies. However, neither the post-processing characteristics, sintered density, nor mechanical performance of these parts was reported on; low ceramic content and large particle size will hinder densification during sintering. In a subsequent study, Ding et al. [116] printed small-scale (<5 cm) SiC mirrors for potential aerospace applications. Photocurable suspensions contained 45 vol.% ceramic content, consisting of 1 wt.% alumina (sintering additive), 1 wt.% nanometer-sized SiC powder, and remainder micrometer-sized SiC powder. Sintering at 1800°C resulted in a relative density of 85.2% and flexural strength of 78.6 MPa. To increase structural performance, polycarbosilane was infiltrated into the sintered

parts and then pyrolyzed at 1200°C. After eight cycles, a relative density of 93.5% and flexural strength of 165.2 MPa was achieved.

A notable alternative to loading ceramic particles into photocurable resins is the polymer derived ceramic (PDC) method. In this approach, photocurable preceramic resins are formed through vat photopolymerization and then pyrolyzed at temperatures 1000-1300°C to derive ceramic parts with final properties [117]. Significant energy savings are realized by using these relatively low post-processing temperatures, as compared to traditional ceramic sintering temperatures. In addition, this method enables the production of ceramic parts with excellent surface finish. One major advantage is that carbides, borides, and nitrides can all be derived from preceramic resins [118]; these materials are challenging to cure using traditional ceramic particle loaded resins due to their large refractive index differences and high absorbance values. A variety of ceramic materials can be produced by varying the preceramic feedstock, including SiOC using siloxane-based polymers, SiOCN by combining siloxanes with silazanes, and SiC by adding silane-based polymers [119]. An initial study by Eckel et al. [120] from HRL Laboratories demonstrated the feasibility to produce dense SiOC microlattices that outperform ceramic foams with respect to shear and compressive strength. In 2020, O'Masta et al. [121] used the PDC method in combination with reinforcement particles (mullite, alumina, and silicon nitride) and whiskers (SiC) to produce ceramic matrix composites with improved toughness. The addition of SiC whiskers to the SiOC matrix increased toughness

by a factor of three. Guo et al. [122] demonstrated an additional benefit of the PDC method, wherein elastomeric material can be printed, stretched/deformed, and then pyrolyzed into ceramic lattices with unique geometries that may be difficult to print in a single orientation. The main drawback of the PDC approach is shrinkage-induced cracking and pore formation during pyrolysis, which imposes limits to the maximum thickness of structures. Thus, this method shows significant promise for lattice structures with strut diameters below approximately one millimeter but will face challenges for structural applications that require dense, bulk ceramic components.

The PDC method is not limited to vat photopolymerization processes, and has been demonstrated for powder bed fusion [source], binder jetting [source], material jetting [source], material extrusion [123].

2.4. Powder Bed Fusion for Advanced Ceramics

2.4.1. Foundations

The powder bed fusion (PBF) process, originally called selective laser sintering (SLS) or selective laser melting (SLM), produces three-dimensional parts by fusing powder via selective application of laser energy in a layer-by-layer process, as shown in Figure 2.4A. This process is unique in that it can be a direct or indirect ceramic AM process. If a high-power laser is used that can melt or fully-sinter the ceramic powder, a dense part with final properties is directly created and no further processing necessary. Conversely, if the laser only partially melts or joins powder, post-processing steps are required to attain final

properties. PBF, like other powder bed processes, has the advantage that overhangs are supported by unbound powder, which is removed in post-processing steps. The application of PBF for structural ceramics has seen limited success because green bodies have low relative densities. One potential method for improving final sintered density is isostatic pressing of printed green bodies prior to pyrolysis and sintering [124]. Other challenges include poor surface finish and thermal-gradient induced cracking, which restricts geometry and overall dimensions.

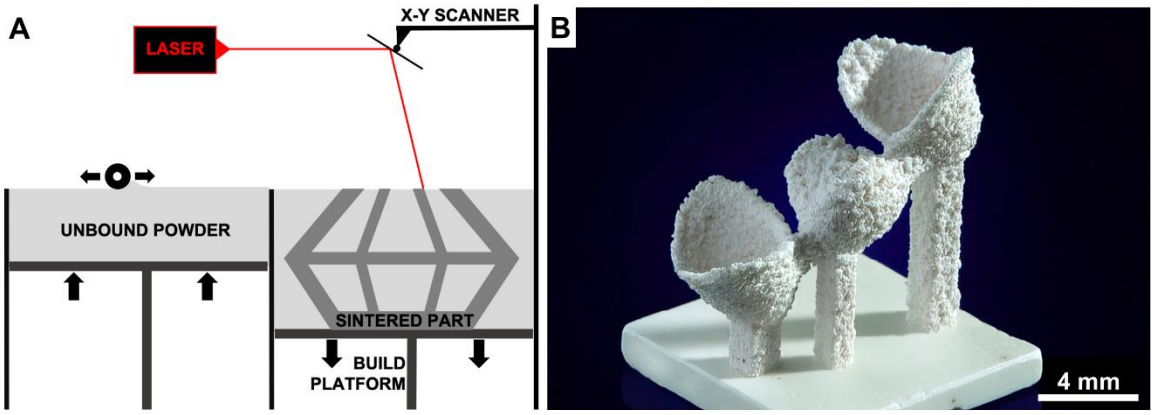

Figure 2.4. (A) Diagram illustrating the powder bed fusion technique. (B) A fully dense zirconia toughened alumina dental restoration with acceptable mechanical properties [6]. The dental restoration highlights a major challenge of PBF, poor surface finish.

2.4.2. Evolution

Original powder bed fusion methods used for advanced ceramics required the ceramic powder to be coated in a thin polymer layer, which is melted by the laser beam to selectively bond powder together into a green body [125]. Post-processing, namely binder removal and sintering, was therefore required to produce the final part. Relatively few publications [126–128] cite successful fabrication of dense ceramic parts using a single step PBF process, because

thermal shock causes part failure and is intrinsic to the rapid heating and cooling cycle of creating a melt pool. Thus, many approaches create porous scaffolds, which are subsequently infiltrated with molten polymeric or metallic material. This process produces composite parts with improved toughness. In order to reduce thermal-shock-induced cracking, each powder layer can be pre-heated, which decreases the temperature differential between unbound powder and the melt-pool [129]. An additional complication of PBF of ceramic materials is their low density relative to metallic powders, which further hinders the flowability of fine ceramic powders. To address this issue, Mapar et al. [130] used spray-drying to increase the flowability of fine powders (1-5 μm) by creating larger agglomerates with 30 μm diameter.

Lakshminarayan et al. [131] performed the first powder bed fusion study for ceramic materials in 1990. Alumina parts were produced through an indirect process, where an alumina-ammonium phosphate powder mixture was used. During laser irradiation, the ammonium phosphate powder melts and forms a glassy phase around the alumina particles. Ammonium phosphate has a melting point of just 190°C, which significantly reduces the laser power required. Complex shaped parts were produced but showed poor dimensional tolerance, surface finish, and mechanical properties due to high porosity.

A different indirect approach used by Vail et al. [132] in the following year employed polymer coatings as intermediate binders for printing soda-lime glass parts. Glass powder was mixed with polymer and spray dried through the

centrifugal atomization method. Parts fabricated using coated powders had improved edge definition and stability compared to those created from a powder-polymer mixture. A similar trend was observed by Subramanian et al. [125], where green parts built from binder-coated powder showed flexural strengths twice that of mixed systems. The flexural strength of green parts increases with energy density up to a point, followed by a reduction in strength as polymer degradation occurs. Therefore, short scan vectors are optimal for increasing green strength, while avoiding polymer degradation. Further, green strength significantly decreased as particle size was reduced from five to two μm, resulting in unstable parts. For particle sizes below five μm, powder should be agglomerated prior to coating with polymer.

Nelson et al. [6,133] modeled thermal diffusion within the powder bed for polymer coated ceramic materials. Polymer coating thickness showed the most significant effect on thermal properties; thermal calculations provide data to optimize scan speed, laser power, and raster width. The model was used to predict the flexural strength for green test bars produced using different processing parameters and showed good agreement with experimental 4-point bend testing results. The flexural strength of green test bars was found to increase linearly with energy density up to an elbow point at 1.2 cal/cm^2, after which the rate of increase in strength reduces by 80%. This phenomenon is due to polymer degradation from excessive heating. This finding is important for any AM process that uses a laser for selective energy application to both liquid and

powder beds. In order to address excessive heating, a thermal efficiency term, input energy density (IED), is introduced

$$IED = energy\ density * f\left(\frac{2\omega}{L}\right). \quad (2.2)$$

This term takes into account the energy density that material receives and the frequency of laser spot passes, where overlap will heat each location several times at different energy densities. This is important because heat is rapidly lost during a scanning cycle as the laser moves away from a specific point and then returns to pass over an adjacent area. Therefore, large parts will have a heating process with a lower thermal efficiency because each location has more time to cool during longer scan vectors.

In 1999, Gureev et al. [134] fabricated piezoelectric elements in the first reported direct PBF study. A stoichiometric mixture of TiO_2, ZrO_2, and PbO powders was sintered using a Nd:YAG laser with a spot size of 50 μm. Laser powers between 11-14.5 W and scan speeds from 15-30 mm/s produced cohesive parts containing approximately 80 vol% porosity. Fabricated parts were annealed at 1240°C for 3 hours to enable PZT phase formation and reduce residual stresses. Annealing reduced porosity to approximately 75 vol%. Annealed parts showed piezoelectric properties but could only withstand a maximum electric field of 0.95 kV/mm; above this threshold breakdown occurred due to porosity.

2.4.3. Recent Developments

Thermoset binders were studied for used in ceramic PBF by Evans et al. [135] in 2004. Thermoset polymers cannot be remelted like thermoplastics, but instead leave a high volume-fraction of carbon when subjected to temperatures above their volatilization point. Phenolic resin was used to bond SiC powders due to its high carbon yield of 40-70 wt.%. Unlike the thermoplastic binders used in previous studies, phenolic resin maintains green body strength after pyrolysis; phenolic resin transforms into carbon ash with yields of 40-70 wt.% during pyrolysis. During sintering, the phenolic ash functions as a sintering aid and can even be used as a preceramic polymer when paired with metal infiltration.

In order to achieve high density and mechanical properties, Shahzad et al. [136] processed green alumina parts fabricated by PBF with pressure infiltration (PI) and warm isostatic pressing (WIP) before sintering at 1600°C. Alumina parts that were not processed with PI or WIP reached relative densities of 39% when sintered. Relative density was increased to 64% using PI (alumina-ethanol solution at 13MPa) and 89% using WIP (64MPa and 135°C). Interestingly, using PI and WIP together resulted in a lower relative sintered density of 88%. However, by infiltrating porosity before WIP, shrinkage is significantly reduced, which limits the potential for warping or cracking of complex geometries. An average flexural strength of 148±22 MPa was achieved for these crack-free complex alumina parts. Similar work by Liu et al. [137] achieved complex alumina

parts with relative densities of 92% by cold isostatic pressing printed green bodies and sintering at 1600°C.

In 2006, Gahler and Heinrich [126] demonstrated direct fabrication of alumina-silica ceramics with relative densities up to 92%. To achieve this density, a doctor blade was used to spread 100 µm layers of ceramic slurry, consisting of 50 wt.% silica, 16 wt.% alumina, and 34% water, which were selectively melted using a continuous-wave CO_2 laser. The alumina-silica system enabled crack-free specimens withing narrow composition and laser parameter ranges. In a different direct PBF study, a low relative density of 56% was achieved for yttria stabilized zirconia parts due to the use of a lower power laser that caused partial melting, which resulted in net shaped parts of the same density as the powder bed [138]. An advantage of partial melting is the significantly lower thermal stresses, which enables the fabrication of larger parts, and the large volume-fraction of open porosity could be infiltrated to improve relative density.

Two decades after the first ceramic PBF studies, Hagedorn et al. [127] successfully demonstrated direct fabrication of fully dense oxide ceramic components with mechanical properties comparable to oxide ceramics produced through traditional routes. In order to reduce thermal stresses that cause cracking and part failure, a CO_2 laser was used to heat the entire 30 x 40 mm^2 build area to above 1700°C. Complete melting of the ceramic powder was accomplished using a continuous-wave Nd:YAG laser. The rapid melting and cooling produced a fine-grained microstructure, resulting in a flexural strength of

more than 500 MPa for ZrO_2-Al_2O_3 parts of 2.5 mm in height [128]. However, parts of height 10 mm had severe cracking due to thermal gradients between top and bottom layers. A three-unit dental restoration was fabricated using this technique and loaded to 1000 N without failure [7]. The dental restoration, Figure 2.4B, highlights a major challenge of PBF, poor surface finish. Furthermore, heating the whole powder bed above the feedstock material's sintering temperature is expensive and difficult to scale.

2.5. Binder Jetting for Advanced Ceramics

2.5.1. Foundations

Binder jetting, known under the trademarked name 3D Printing (3DP), was the very first AM process used for producing ceramic parts. In fact, this was the only process created specifically for processing ceramic powders and then later adapted to metallic and polymeric materials [95]. To create a three-dimensional part, liquid binder is applied to selectively bind powder in a thin layer, loose powder is spread over the top, and the binding process is repeated. The binder jetting process is illustrated in Figure 2.5A. Complex geometries with overhangs, which are supported by unbound powder, can be fabricated from any powdered ceramic material of appropriate particle size; powder smaller than 50 μm will agglomerate and inhibit flow [139]. Resolution is limited by powder size or binder droplet size, depending on which is larger. The excellent dimensional accuracy of the binder jetting technique is enabled by using nozzle orifices less than 50 μm. Binder rheology and nozzle geometry play important roles in controlling the size

of droplets [140]. Binder can be applied through either drop-on-demand or continuous-jet techniques. Continuous-jet printers use a pressurized ink reservoir and a piezoelectric element to break the ink jet into droplets. Droplets are charged as they exit the nozzle and pass between electrodes, which allows them to be steered either back into the reservoir or onto the build platform by a strong electric field. For this reason, inks must be conductive for the continuous-jet process. Drop-on-demand printers use a piezoelectric actuator to produce a pressure pulse in the nozzle that ejects droplets of ink and does not require conductive inks. The continuous-jet process produces droplets at a much faster rate (64 kHz), which enables a higher build rate compared with drop-on-demand systems.

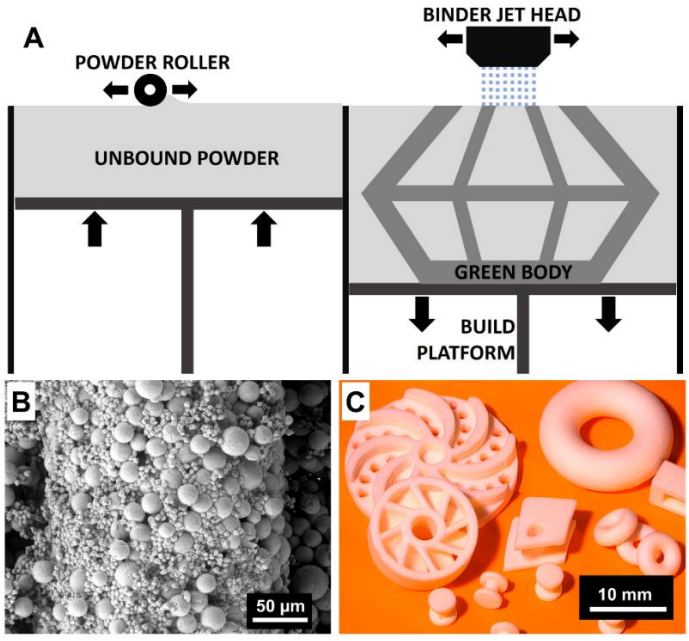

Figure 2.5. (A) Diagram illustrating the binder jetting technique, where a three-dimensional object is produced by selectively depositing binder droplets into a powder bed layer-by-layer as the build platform lowers and fresh powder is spread to create a loosely bound green body. (B) A bimodal particle size distribution enables better surface finish, and small particles tend to migrate to the surface [7]. (C) Several complex alumina parts with good surface finish and edge definition [7].

2.5.2. Evolution

In 1990, Sachs et al. [82] performed the first additive manufacturing study using a non-polymeric material. Binder jetting was initially developed to print ceramic molds for casting metal parts with the goal to reduce the cost and lead-time of producing complex metal parts. In a traditional metal casting process, molds cost between $5k-50k and can take several months to manufacture. While traditional molds enable high-volume production, binder jetting could provide significant benefit for unique, one-off parts. Build rate is determined by three main steps. First, powder spreading will take 0.1-1 s for dry powder and 1-10 s for wet powder. Second, printing a 0.5x0.5m layer would take approximately 0.025 s for a continuous jet process and 5 seconds for a drop-on-demand process, if the head is designed with a line of jets so as to print in a single pass. Third, the binder must set, which is estimated between 0.1-1 s for solvent-based binders.

The physics of the ballistic impact of binder droplets into the powder bed has implications in x-y resolution, surface finish, mechanical properties, and even resolution in the build direction due to powder compaction. Droplet overlap and interaction provide the green strength necessary to maintain form after removing loose powder. Vertical dimensional error is caused predominantly by displacement from compaction of the powder bed due to the weight of subsequent layers. Increasing the packing density of the powder bed reduces this error. For a powder bed of packing density 54 vol% comprised of 30 μm

alumina powder, vertical accuracy errors of approximately 50 μm were measured for middle layers [141]. Middle layers in a powder bed will always show the highest compaction displacement as sufficient weight from upper layers and sufficient room for displacement both exist. Powder scattering occurs due to the kinetic energy of the binder droplets, which reduces dimensional accuracy and surface finish. Powder scattering is significantly reduced for powder beds that are misted with water to loosely fix powder in place [142]. These alumina cores bound with silica are used to cast metal parts, such as turbine blades.

Yoo et al. [143] used binder jetting to produce ZTA parts with functionally graded yttria doping, with the goal of tailoring transformation toughening mechanisms. The binder jetting system utilized a multiple nozzle print head where either binder, binder-yttria ink, or a ratio of the two were jetted into the powder bed. By carefully controlling the yttria dopant composition, the ZTA phase was tailored locally between monoclinic and tetragonal. Multilayer composites with tailored internal stresses and transformation toughening were formed and pressureless sintered to 99% theoretical density. Post-processed parts showed an increase in flexural strength of 441 MPa, which indicates that compressive stresses were successfully developed at specimen surfaces.

2.5.3. Recent Developments

Sachs et al. [144] demonstrated the use of ceramic powder with a bimodal size distribution to reduce surface roughness in 2003. Fine powders of particle size less than two μm improve surface finish and sinterability but cannot be

spread dry due to Van der Waals forces. Fine powder must be spread wet in slurry form, which significantly slows the process and increases its complexity. On the other hand, coarse powders can be spread dry, but cause rough surface finish and poor densification during sintering. In this study, a bimodal size distribution of spherical alumina powder was spread dry and compared with results from a unimodal alumina powder. Coarse powder used measured 20 and 30 μm and fine powder used measured 2.5 and 5 μm. Coarse powders were mixed with 10-25 vol% fine powder and spread across the bed. Surface roughness is significantly reduced using the bimodal distribution as seen in Figure 2.5B. Interestingly, fine particles tend to migrate to the surface as the binder droplet selectively binds material, which explains the reduction in surface roughness. In addition to improving surface finish, a wider particle size distribution can increase green body density. Several complex alumina parts (Figure 2.5C) were fabricated with good quality and edge definition. Gonzalez et al. [145] produced alumina parts with relative density of 96.51% and compressive strength of 146.6 MPa, by using a bimodal particle size distribution. Kunchala et al. [8] added nanoparticle densifiers to the liquid binder to improve green body density. Alumina green bodies with nanometer-sized alumina particles were produced with a relative density of 65.7%, compared to green bodies without nanoparticle additions that had a relative density of 35.7%. Although these parts were not sintered, the significant increase in green body density indicates

sintered density and mechanical properties would greatly improve via nanoparticle additions.

Recently, II-VI MCubed demonstrated binder jetting of SiC preforms that were subsequently reaction bonded (RB) with Si [146]. SiC preforms with dimensions of 4 x 4 x 0.25 inches were fabricated using binder jetting. Preforms were printed using SiC feedstock powder with monomodal and bimodal particle size distributions. The printed preforms were then infiltrated with molten Si at a temperature above 1410°C in an inert atmosphere to form SiC-Si composites. The density, elastic modulus, flexural strength, and fracture toughness of all printed and RB specimens increased with volume fraction SiC. Specimens fabricated using bimodal feedstock powders had higher density, elastic modulus, flexural strength, and fracture toughness at all tested volume fraction SiC. Compared to traditionally formed and RB SiC, specimens formed via binder jetting and then RB had comparable density, elastic modulus, and flexural strength, but lower fracture toughness.

2.6. Material Jetting for Advanced Ceramics

2.6.1. Foundations

Material jetting, originally named ballistic particle manufacturing, uses ink-jet printers with nozzle diameters in the range of 20-75 μm to print low viscosity ceramic particle suspensions, termed ‘inks’ [147]. Material jetting is depicted in Figure 2.6A. There are two main methods of material jetting, drop-on-demand and continuous-ink-jet. If a multi-nozzle printing head has separate reservoirs

with different inks, composition can be varied to create functionally graded parts. Material jetting of ceramic materials is difficult because ink formulation must follow conflicting requirements, such as the ink needing to be low enough viscosity to avoid nozzle clogging while also containing enough ceramic content that the green body can be sintered to full density. Material jetting enables the use of ceramic materials of particle size less than 100 nm that are well dispersed as inks. Using these ultra-fine powders promotes sintering to enable full-density parts after post-processing.

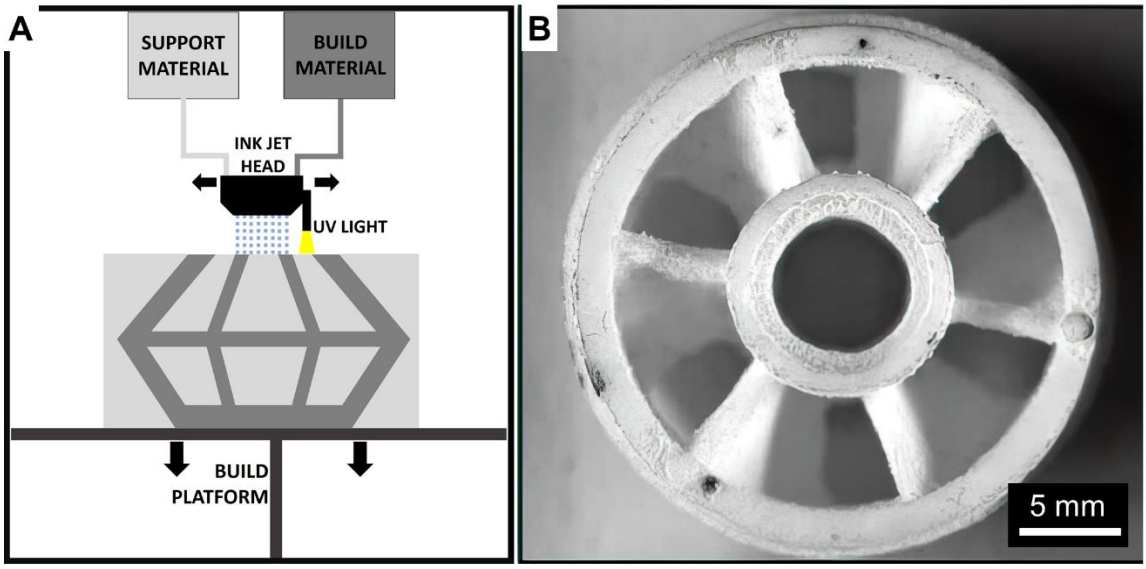

Figure 2.6. (A) Diagram illustrating the material jetting technique. (B) Alumina impeller produced by material jetting of a highly-loaded ink [8].

2.6.2. Evolution

In 1995, Blazdell et al. [148] produced three-dimensional yttria stabilized zirconia parts using the material jetting process. A 70 µm nozzle array was used with the capability to dispense 50,000 droplets per second. Printed traces and thin wafers were pyrolyzed and sintered, and were free from printing defects,

cracks, and shape distortion effects. In 1997, Teng et al. [149] used continuous-ink-jet printing to create ceramic green bodies. Ceramic inks used for jet printing ceramic components must be well dispersed and dilute to have an acceptably low viscosity. However, it is important to load the maximum possible volume fraction of ceramic material into inks to produce high density green bodies that can be sintered into dense ceramic parts. In addition, inks must be conductive to enable the steering and detection of droplets during the jetting process. For these reasons, the development of optimal ceramic inks for jet printing is vital to the success of the material jetting technique.

Inks should have a conductivity of greater than 0.1 S/m, viscosity between 1-10 mPas, surface tension between 25-70 mN/m, and particle size less than 1 μm. Teng [149] found that an ideal ink composition contained 2.4 vol.% grade HSY3 submicron ZrO_2 powder, 1.43 wt.% ATSURF dispersant, and remainder ethanol as the solvent. To increase the conductivity of the ink, ethanol was modified with 2 wt.% ammonium nitrate. The optimal ink formulation had a conductivity of 0.298 S/m and viscosity of 1.64 mPas. The jetting nozzle had a diameter of 65 μm. Ceramic green bodies with acceptable dimensional resolution were successfully fabricated using this ink.

Two years later, Song et al. [147] developed ZrO_2 components of height 2.5 mm (1700 layers) using a continuous-ink-jet printer with nozzle diameter 60 μm. The development of an optimal ink formulation was focused on and resulted in an optimally functioning ink with 4.4 vol.% ZrO_2. The ZrO_2 powder (grade

HSY3) was stabilized with 5.4 wt.% yttria of particle size 100 nm. Printed parts were pyrolyzed and sintered at 400 and 1450°C, respectively. Viscosity must be below 100 mPas to avoid satellite formation during droplet ejection; satellites are small drops that break off the main droplet. Ink formulations dispersed solely using ultrasonic agitation were found to clog nozzles and cause irregular droplet ejection; powder agglomerates were not eliminated. In order to fully breakdown agglomerates, a twin-roll mill was used for high-shear mixing of subsequent formulations and resulted in consistent droplet formation and avoided nozzle clogging. Compared with passive drying, surface quality and dimensional accuracy was found to be improved by active drying via hot air flow after each layer is deposited. Although bulk shapes were achieved, walls were not vertical and surfaces are dimpled and curved.

2.6.3. Recent Developments

In order to solve issues related to printing low ceramic content inks, such as poor surface finish and dimensional accuracy, in 2001 Seerden et al. [150] formulated wax-based ceramic inks with up to 40 vol.% ceramic powder that were successfully ejected from an ink-jet head. Optimal formulations contained 20-40 vol.% Al_2O_3 powder (400 nm diameter), 0.65-1.2 wt.% surfactant Hypermer LP1, 0.33-1.2 wt.% stearylamine, and remainder paraffin wax. Optimal printing conditions were 100-110°C and 10-13 kHz droplet frequency. In order to successfully print the 40 vol.% formulation, pressure was applied to the ink reservoir to aid the piezoelectric actuator driven pressure pulses. Ceramic green

bodies were developed using the drop-on-demand method with feature sizes of less than 100 μm using an ink with 30 vol.% ceramic content. Fabricated green bodies showed good shape retention and dimensional accuracy, with vertical walls and sharp corners well defined.

Reis et al. [151] tested ZrO_2 and PZT using paraffin wax based inks with the drop-on-demand method. Sintered bodies retain features such as corners and vertical walls, and no warping, cracking or delamination is observed as illustrated in Figure 2.6B. The use of thermal energy to lower the viscosity of wax-based ceramic inks shows great promise for increasing the maximum ceramic content of material jetting processes, which enables to development of dense, structural ceramic components. Driving pressure must be carefully controlled to eject uniform droplets of the high viscosity wax-based ceramic inks; relevant parameters include electric signal voltage amplitude, frequency, pulse duration, and waveform. Acoustic pressure wave superposition of two or more consecutive waves are necessary to provide the necessary energy to eject droplets of high viscosity ink [152]. A relationship is outlined between ejected drop volume and velocity and a dimensionless quantity Z,

$$Z = \frac{(d\rho\gamma)^{0.5}}{\eta} = Oh^{-1}, \tag{2.3}$$

where d is nozzle diameter, ρ is ink density, γ is ink surface tension, η is ink viscosity, and Oh^{-1} is the inverse of the Ohnesorge number. Fromm [140] used this relationship to predicted that droplet formation in DOD systems is only possible for Z > 2 and that droplet volume increases with increasing Z.

Dense PZT components with good shape retention were fabricated using a wax-based ceramic ink with a PZT content of 35 vol.% [10]. The optimal ink formulation contained 35 vol.% PZT (particle sizes less than 500 nm), 1% polyester, 0.5% stearylamine, and remainder paraffin wax. To further reduce the viscosity, solid paraffin wax was replaced with a 60/40 paraffin oil/wax mixture. A porosity of less than 1% was achieved for sintered components.

2.7. Sheet Lamination for Advanced Ceramics

2.7.1. Foundations

Sheet lamination, commonly called layered object manufacturing (LOM), involves the cutting and layering of prefabricated ceramic tapes, often made via tape casting, into three-dimensional parts. A rectangular block is produced containing the desired object surrounded by ‘tiled’ support material. The ‘tiled’ regions are produced by cutting the negative space around the desired shape into a grid. Blocks of green material are then sintered and de-cubed, wherein support cube grids are mechanically removed to extract the final geometry. Sheet lamination is depicted in Figure 2.7A. The process of tape casting thin ceramic sheets was patented in the 1940s to enable the mass production of capacitor dielectrics [153,154]. The idea of layering ceramic tapes, cut to specific geometries, was patented in the 1960s [155]. Interestingly, the commercial application of layering ceramic tapes for the production of three-dimensional parts lagged for nearly 30 years, when sheet lamination was patented in 1988 [92]. The reason for this lag in application is primarily due to the limited control of

laser scanning equipment and software that could convert a 3D model into slices and motion planner to raster the laser in an efficient automated process to build parts. Sheet lamination processes face challenges related to the quality of interfaces, where defects such as delamination, porosity, and thermal-stress induced cracking cause failure of components.

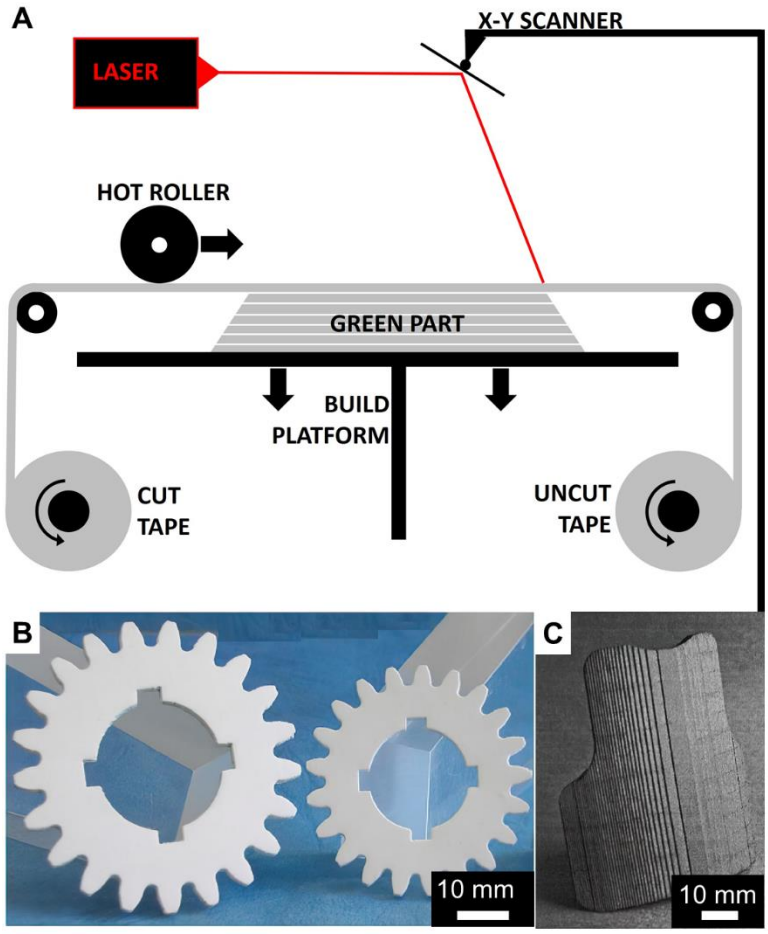

Figure 2.7. (A) Diagram illustrating the sheet lamination technique. (B) Glass-ceramic gears in green (left) and sintered (right) state demonstrating successful densification without warping or cracking [9]. (C) Complex curved SiC component produced by sheet lamination of bimodal SiC tapes [10].

2.7.2. Evolution

In 1991, Feygin et al. [93] and Helisys, Inc. first demonstrated the use of sheet lamination for producing three-dimensional parts; many materials were successfully demonstrated including ceramics, paper, plastics, composites, and even metals. In 1994, Griffin et al. [156] fabricated advanced structural ceramic components with complex geometries using LOM. In order to verify the mechanical performance of printed parts, rectangular bars of alumina were prepared by LOM and traditional dry-pressing. Alumina sheets for LOM were produced by casting a slurry with a doctor blade into 15 μm thick green tapes. Green tape is loaded onto the supply roll and fed over the build platform. A laser is used to cut a grid outlining the desired shape, which can be easily removed in post-processing steps. Heat and pressure are applied to each layer to aid layer lamination. Both pressed and LOM'ed parts were pyrolyzed at 600°C to remove organic material and then sintered at 1550°C for 2 h. Specimens from both processes sintered to full density with less than 1% porosity. Flexural strength, hardness, and fracture toughness values for the LOM'ed bars were all within one-standard deviation of those for the traditionally processed bars. Expanding on their previous work, Griffin et al. [9] fabricated complex ceramic ZrO_2-Al_2O_3 composites. Two different thicknesses, 58 and 116 μm, of tapes were produced with compositions of Ce-ZrO_2 and Ce-ZrO_2/Al_2O_3. Composite parts were developed by alternating layers of the two compositions. Green bodies were post-processed by pyrolysis and then sintering at 1600°C for 6 h. Final parts

contained less than 1% porosity and no delamination of macroscopic defects were observed. Final layer thicknesses in densified parts were approximately 85 and 44 μm for starting tapes of thicknesses 116 and 58 μm. Comparing monolithic parts to composite parts, the flexural strength increased 20% by alternating composition layer-by-layer. Complex geometries with curved and vertical surfaces were successfully produced with composite structures. Hardness varied locally with composition.

Three ceramic systems were studied by Klosterman et al. [157] in 1996: (1) Coarse SiC powder of size 30 μm that enables post-process infiltration; (2) Bimodal SiC with particle sizes 2 and 30 μm; and (3) AlN powder with particle size 2 μm. Ceramic feedstock material was prepared using a standard tape casting process. A slurry consisting of 60 vol.% ceramic powder, binder, plasticizer, and solvent was cast into tapes of thicknesses 150-175 and 300-325 μm. Ceramic tapes were manually loaded into the sheet lamination system. In order to prevent the oxidation of these carbide materials during the sheet lamination process, a blower supplies an inert gas at the focal point of the laser to shield the cutting process. In order to increase the green strength of LOM'ed parts, a particle binder burnout cycle was run that volatilized the plasticizer but left the binder. Subsequent silicon infiltration and reaction bonding resulted in near net-shape parts with little dimensional change, shown in Figure 2.7C. However, poor layer bonding led to delamination and a relatively low flexural

strength of 160 MPa. In comparison, SiC components produced via binder jetting and reaction bonding have flexural strengths of approximately 280 MPa [146].

Himmer et al. [158] demonstrated an automated tape casting process connected to a sheet lamination system in 1997, eliminating the need to manually place feedstock material. Plastic was rolled over the top of ceramic slurry into 0.25 mm thickness sheets, which avoided the need to let the slurry dry into a solid tape. In this fashion, a continuous layer of slurry and plastic was fed into the sheet lamination system, where the plastic was then separated from the layer of slurry. Complete separation is important, because any slurry that sticks to the plastic will leave voids in the laminated part. Parts with complex geometries were built to up to 20 layers successfully. After pyrolysis and sintering parts contained 10-15% porosity, which led to low strength and delamination. Macroscopic voids were observed due to incomplete plastic-slurry separation prior to sheet lamination.

Klosterman et al. [159] published a follow-up study in 1998 focused on improving the interfacial bonding of laminated sheets. SiC tapes were produced using a doctor-blade and slurry containing biomodal SiC powder (2-3 and 60 μm particle sizes), graphite powder, and binder system. The lamination roller was set to 180°C, above the binder melting point, to achieve sufficient interlayer bonding. Pyrolysis at 600°C and reaction bonding with silicon at 1600°C produced near-net-shaped parts. A low flexural strength of 80 MPa (compared to the expected 300-400 MPa) was measured. Large voids were observed at layer interfaces.

Strength was increased to 155 MPa by increasing the graphite powder content from 5 vol.% to 20 vol.%. In order to further improve strength, the layer bonding needs to be improved. To improve bonding, a solvent was misted on the tape prior to lamination and the temperature and pressure of the lamination roller were increased. Using these methods, interlayer bonding was improved to the point that parts could not be de-cubed. It was found that a secondary cutting operation around the profile of each layer, after creating the support grid, enabled successful de-cubing even at higher lamination pressures and temperatures. This operation left a thin layer of power at the interface between cubed support regions and the desired part, which facilitated the removal of the cubed material. Through the use of the secondary cutting operation and better lamination parameters, defect free layer interfaces were demonstrated.

2.7.3. Recent Developments

Rodrigues et al. [160] fabricated silicon nitride parts using the sheet lamination process in 2000. They found a direct correlation between the feedstock quality, i.e. homogenous ceramic tapes with uniform thickness, and the mechanical properties of final parts. In addition, lamination roller pressure and temperature were carefully optimized to yield sufficient interlayer bonding. LOM'ed parts were pyrolyzed at 500°C and sintered at 1750°C, resulting in less than 3% residual porosity. The flexural strength and fracture toughness of silicon nitride parts produced with sheet lamination matched that of silicon nitride parts made using traditional methods. Fracture surfaces reveal complete layer bonding

and no interlayer defects are observed. Travitzky et al. [161] tape casted preceramic polymers filled with SiC of varying particle sizes, and fabricated functionally graded ceramics using the sheet lamination technique. SiC structures with graded particle size showed 25% higher flexural strength over those produced with uniform particle size. Gomes et al. [162] increased the strength of glassy ceramic components by rotating feedstock tape by 90 degrees for each layer of the sheet lamination process. Complex Li2O–ZrO2–SiO2–Al2O3 green parts were sintered at just 700°C and achieved near full density, shown in Figure 2.7B.

That same year, Park et al. [163] characterized the LOM process to determine important sources of dimensional error. Error was found to be largest in the build direction due to moisture absorption and subsequent tape swelling. Low relative humidity during the forming process was found to be important. Two years later, Karunakaran et al. [164] proposed an efficient method for separating the desired object from the surrounding block of material. A major drawback of the sheet lamination process is the significant time of cutting the support grid and then de-cubing the fabricated part. Their method is analogous to extracting a casting from a mold, where the mold primarily consists of two halves and can contain plugs to create internal cavities. Instead of making many cuts to form a grid, the negative space of each layer is cut into two halves. The cuts are coordinated across layers to create a consistent seam that enables the

separation of the support material in two pieces, compared with many cubes in the traditional sheet lamination process.

Weisensel et al. [165] demonstrated the fabrication of biomorphic ceramic composites via the sheet lamination technique, with the goal of mimicking natural cellular materials. A cellulose based paper was used with a phenolic resin adhesive. After laminating several layers and creating a three-dimensional part, the paper and phenolic resin were pyrolyzed to leave a layered carbon structure with porosity templated from the natural cellulose structure. Through reaction melt infiltration with silicon, the carbon structure was converted to a Si-SiC composite with 16 vol.% residual carbon and negligible porosity. A flexural strength of 130 MPa was measured by four-point bend testing. To further increase the mechanical properties of these biomorphic composite structures, the melt infiltration process should be optimized to fully react with the carbon template.

2.8. Material Extrusion for Advanced Ceramics

2.8.1. Foundations

The material extrusion process, commonly known as Robocasting, involves the extrusion of a high ceramic content slurry through a nozzle in a specific pattern layer-by-layer to produce a three-dimensional part [47]. This line of deposited material is known as a trace. Material extrusion is demonstrated in Figure 2.8A. The material can be extruded continuously or in droplets, and self-supports via gelation, cooling, UV-curing, or other rheological effects [166]. Yield-

pseudoplastic rheology enables the ink to retain structural integrity up to its yield stress, followed by shear-thinning behavior [48,49]. This behavior is critical for ink to both flow through a small nozzle (high-shear environment) and retain its shape post-extrusion (low-shear environment). Advantages of the material extrusion technique include low-cost machinery, versatile feedstock, and high green density. Challenges include achieving small feature size, low precision, and poor surface finish.

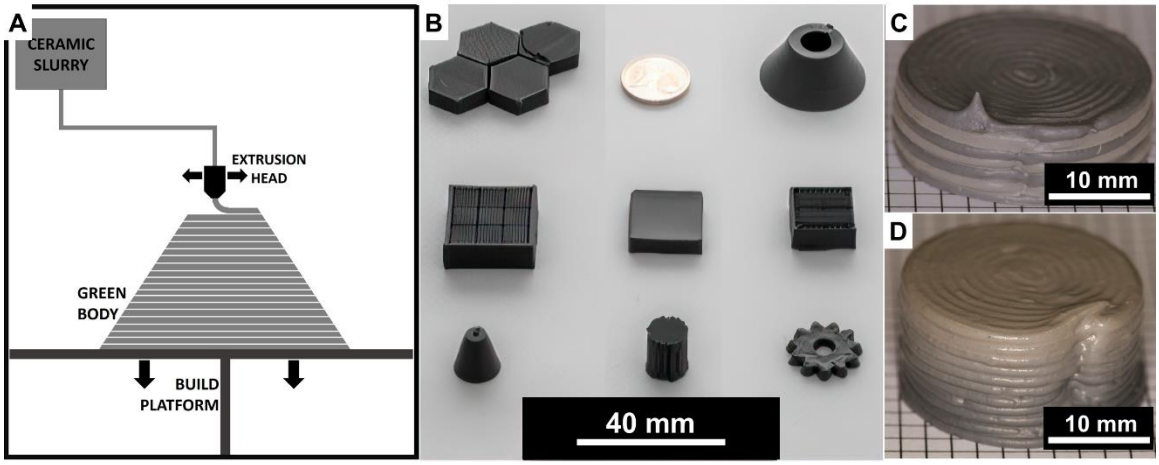

Figure 2.8. (A) Diagram illustrating the material extrusion technique. (B) Complex boron carbide components were processed using spark plasma sintering and cold isostatic pressing to achieve less than 5% residual porosity [167]. (C,D) Discrete and continuous SiC-B4C parts printed using a material extrusion system with in-line mixing capabilities [11].

2.8.2. Evolution

In 1995, Danforth's group [168] developed the fused deposition of ceramics (FDC) method in the Center for Ceramic Research at Rutgers University. The feedstock material used in this process is thermopolymer filament loaded with ceramic powder. FDC is analogous to fused deposition modeling, developed by Stratasys, where thermopolymer filament is melted and extruded to

build plastic parts. Thermoplastic filament loaded with 55 vol.% Si_3N_4 was printed and sintered to greater than 98% relative density and average flexural strength of 824 MPa [169]. Printing defects are a major concern for material extrusion processes, because inconsistent toolpath generation can cause large voids between traces of printed material [170]. During the creation of simple testing geometries, toolpath files can be manually optimized to reduce defects. However, manual modification is not possible for more complicated geometries.

Kupp et al. [171] used a different approach termed multiphase jet solidification (MJS), where a thermoplastic-ceramic mixture is directly fed through a heated nozzle using a piston. Time-consuming filament production is avoided in this technique. The feedstock material contains 50-70 vol.% ceramic material. Fabrication of SiC parts with complex geometry was successfully demonstrated.

A year later, Cesarano and Grieco [172] conducted a high-impact material extrusion study using ceramic materials at the Sandia National Laboratory. This study termed the common name of Robocasting for the material extrusion of ceramic slurries. His motivation was to increase the green density of ceramic AM parts to improve post-processing behavior, namely debinding and sintering processes. Slurries of 50-65vol.% ceramic and less than 1vol.% organic were developed and successfully printed. In contrast with ceramic parts made in binder jetting and vat photopolymerization processes, these parts could be post-processed in less than 24 hours versus several days due to the much lower organic content. In addition, the high ceramic content enabled sintering to higher

relative density and less shrinkage, resulting in improved final properties. Producing ceramic slurries of such high ceramic content faced several technical challenges including difficult rheological control and drying kinetics. Previous work by Cesarano and Aksay [173] discussed the development of aqueous alumina suspensions and provided a basis for the slurries printed at Sandia National Laboratory. Well-mixed suspensions of alumina, Darvan-821A, and water showed yield-pseudoplastic behavior for ceramic content below 60 vol.%, followed by dilatant behavior. Low viscosity and slow drying results in slumping, whereas high viscosity and fast drying enables good shape retention. Robocasting suspensions exhibit significant yield-pseudoplastic behavior during printing, but quickly change to dilatant behavior after extrusion and minimal drying to retain their specified geometry. Alumina geometries were made by Robocasting of yield-pseudoplastic ceramic slurries. Finite element analysis (FEA) simulations indicate fast drying results in good shape retention, voids form for medium drying rates, and low drying rates lead to significant slumping [167].

In 2000, Lewis et al. [53] conducted an in-depth rheological study of colloidal ceramic suspensions, with the goal of enabling Robocasting with smaller nozzles, improving shape retention, and producing defect-free parts. Technical challenges faced included isolating printing and rheological parameters. To perform this study, a mixing system was designed that allowed for on-the-fly binder content adjustment in the printed slurry. This methodology enables high-throughput discovery of the optimal ceramic content in extruded slurries for

different powdered materials. The viscosity of several notable slurry compositions was measured across a range of shear rates, with an emphasis on isolating the shear rate for each step in the printing process. Four printing process steps were identified as pumping, mixing, extrusion, and deposition. In addition, FEA simulations were used to verify shear-rate regime calculations. Through this work, alumina slurries were successfully printed from nozzle sizes 0.254-1.370mm and showed good shape retention with no observable defects.

2.8.3. Recent Developments

Jafari et al. [174] developed a multi-head FDC system, capable of printing up to four unique ceramic loaded thermoplastic filaments. Two filaments, one loaded with PZT-5H and one loaded with PZT-8, were used to produce multilayer parts with alternating layers of the two piezoelectric materials. The dielectric constant of the parts was tunable based on the ratio of PZT-5H to PZT-8, with applications for improving the performance of transmitting devices. Smay et al. [43] conducted a comprehensive multi-material study using two types of machine set-ups, a multi-head arrangement where each tool head deposits a different material and a single head arrangement where active mixing inside of the tool head enables the tailoring of composition to any ratio of the feedstock materials. The motivation was to create cermet materials and ternary composition gradients. Technical challenges faced include difficulty in controlling the rheology of multiple input materials where differences in viscosity or compressibility will cause poor printability and variation in surface chemistry between metallic and

ceramic powders. Printing ternary mixtures of barium titanate, strontium titanate, and barium zirconate, requires the rheology of each material to be matched across a range of shear rates that the slurries experience during processing. Both ternary mixtures and cermets were demonstrated and showed good final properties after post-processing. Pelz et al. [80] fabricated functionally-graded carbide parts using a print head with an extrusion screw to mix two feedstock materials in-line. Discrete and continuous composition variation were demonstrated as shown in Figure 2.8C,D. Full density was achieved, and hardness values match traditionally processed carbide materials. A part with alternating SiC and B_4C layers was printed but cracked due to residual stress arising from coefficient of thermal expansion mismatch.

Iyer at al. [175] produced strong, dense Si_3N_4 components using the FDC technique. Filament contained 55 vol.% Si_3N_4 (average particle size of 0.5 µm). Printing parameters include a nozzle width of 250 µm, layer height of 254 µm, and x-y or z testing bar orientations. After sintering, the full density Si_3N_4 bars printed in the x-y and z orientations had flexural strengths of 908 and 888 MPa, respectively. The near-isotropic strength of these parts is very promising and indicates printing defects are nonexistent and layer lines are fully eliminated during sintering. Rueschhoff et al. [54] used a low-cost ($2k) commercially available material extrusion printer to produce strong, dense alumina parts. Slurry compositions from 51-58 vol.% ceramic content were formulated with 5 vol.% binder content. The rheology of each suspension was characterized and it

was found that a composition of 55 vol.% alumina, 4.2 vol.% Darvan 821A, and 4.9 vol.% PVP produced the best print results. Post-processing included debinding at 700°C and sintering at 1600°C with no sintering additives or applied current or pressure resulted in parts with greater than 98% relative density. These parts showed flexural strengths comparable to those of traditionally processed alumina parts. In a second study, boron carbide suspensions were formulated using the same low-cost extrusion system [58]. A major motivation for this research is the fact that dense B_4C parts cannot be made using other AM techniques, such as vat photopolymerization (very high refractive index difference) or binder jetting (low density green bodies). The rheology of each suspension was characterized and it was found that a composition of 54 vol.% B_4C, 5 vol.% PEI (25k g/mol), and 5 vol.% HCL enabled optimal printability. The binder PEI was tested at two different molecular weights, 25k and 750k g/mol, and it was found that the lower molecular weight results in a lower apparent viscosity. Good layer adhesion and shape retention were achieved, with limited shrinkage and warpage during post-processing. Parts were debound at 500°C and sintered at 2000°C with no sintering additives or applied pressure, resulting in parts of 82% relative density. This low relative density is due to the strong covalent bonding in carbide ceramics, which leads to very high melting temperatures. Eqtesadi et al. [59] demonstrated improved results for material extrusion of B_4C materials, producing complex geometries such as gears, cones, and hexagons (Figure 2.8B). In order to create fully dense sintered specimens,

green prints were first cold-isostatic pressed. This increased green density from 53% to 58% of theoretical. Green bodies were then densified via spark plasma sintered at 2100°C to produce specimens with less than 5% porosity.

A unique characteristic of material extrusion processes is the pressure gradient in the nozzle, which enables the alignment of fibers and high aspect-ratio particles [176–180]. Bismuth titanate structures with oriented microstructures were fabricated by Allahverdi et al. [176] using the FDC technique to align BiT platelets. Using this technique, ceramic matrix composites were developed by Franchin et al. [177], which involved a SiC suspension loaded with 30 vol.% chopped carbon fiber. Fibers inside the SiC matrix reduce cracking that occurs due to post-processing. Fiber direction can be varied within a layer based on trace pathing. A maximum fiber loading of 30 vol.% was achieved due to rheological effects. Feilden et al. [178] used the nozzle pressure gradients, unique to material extrusion techniques, to align alumina platelets in epoxy-ceramic composites to create bioinspired structures. Bouligand structures, analogous to those in fish scales, with high ceramic content were produced. Upon loading and cracking, the structure guides crack propagation in a three-dimensional twisting motion that improves the toughness. Fabricated structures outperform the strength of nacre by a factor of two while maintaining a similar R-curve behavior (representative of toughening mechanisms that inhibit crack propagation). Kemp et al. [180] printed SiC fiber reinforced ZrB_2 components, which can function as structural ultra-high temperature ceramics. However, at 10

vol.% SiC fiber content, significant porosity developed, and mechanical performance was limited.

2.9. Directed Energy Deposition for Advanced Ceramics

2.9.1. Foundations

Directed energy deposition (DED), commonly known as laser cladding [12] or laser engineered net shaping (LENS) [12,181], uses a laser to melt powder or wire feedstock in layer-by-layer traces to build a three-dimensional part. This process is similar to welding, where a melt pool is formed by melting feed wire and is depicted in Figure 2.9A. DED is the only ceramic AM process that is solely a single step process, which means parts formed do not require post-process densification. However, the use of DED for fabrication of bulk ceramic parts is limited due to thermal cracking, which results from the rapid heating and cooling in the melt-pool induced by the laser. This effect is similar to that previously described for single-step powder bed fusion. Further, poor surface finish and dimensional stability are occur due to freeform fabrication with complete melting. Interestingly, the authors did not find a ceramic DED study that reported flexural strength, while fracture toughness was often reported.

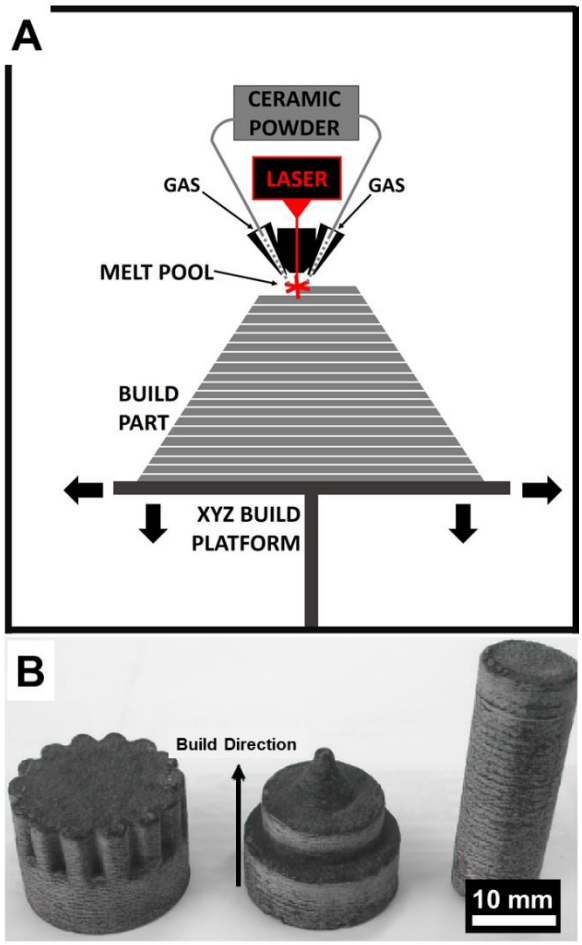

Figure 2.9. (A) Diagram illustrating the directed energy deposition technique. (B) Complex alumina components fabricated by DED, a maximum dimension of 25 mm was achieved for a cylinder [12].

2.9.2. Evolution

The first published account of a ceramic DED process studied the selective area laser deposition (SALD) method in 1993, which uses a laser to selectively heat a substrate and cause material deposition based on precursor gas, the feedstock material. Using tetramethylsilane as the precursor gas, Tompkins et al. [182] demonstrated small SiC deposits could be made selectively onto an alumina substrate. A second study of the SALD process by Jakubenas et

al. [183] used $TiCl_4$ gas to selectively deposit titanium oxide. Deposit morphology is highly dependent on oxygen concentration in the precursor gas; low oxygen content leads to smooth deposits and high oxygen content results in dendritic depositions. However, in both studies the build heights were limited to a single layer because large thermal gradients caused cracking and irregular growth when printing a second layer. Fessler et al. [184] created a gradual, graded composition change using the directed energy deposition process and utilized a powder mixing system. Through gradual composition change, thermal gradients were reduced, and cohesive parts were successfully fabricated.

A similar method is the selective area laser deposition vapor infiltration (SALDVI) approach, where powder is fused together using a selective chemical vapor deposition process. Crocker et al. [185] demonstrated this technique using tetramethylsilane as the precursor gas to selectively infiltrate SiC into Mo, SiC, ZrO2, and WC powder beds. A laser is used to selectively deposit SiC into the powder bed, layer by layer, to create multi-layer parts. A rectangular part with four 250 μm thick layers was produced from tungsten carbide powder fused with the infiltrated silicon carbide. To obtain a sufficient infiltration depth, slow laser scan speeds must be used. However, at low scan speeds, SiC was not deposited evenly. Due to these competing factors, fabricated parts had poor surface finish and large voids.

2.9.3. Recent Developments

In 2008, Balla et al. [12] first demonstrated the successful production of bulk alumina ceramics by the LENS technique. Figure 2.9B shows several complex parts fabricated by DED, a maximum dimension of 25 mm was achieved. Fabricated alumina parts had relative densities near 96%, and through a short heat-treatment at 1600°C relative density was increased to 98%. Heat-treated parts had average compressive strengths of 276 MPa. To create bulk parts that did not fail due to the large temperature gradients intrinsic to direct energy deposition processes, precise thermal management of the melt pool was performed. Niu et al. [181] again studied directed energy deposition of alumina, but with the addition of zirconia and yttria dopants to reduce processing defects and improve the microstructure. Fully dense parts of 50 mm in height were successfully fabricated. Fully dense parts with nanometer-sized eutectic microstructures were developed by the combined doping of alumina with zirconia and yttria [186]. A eutectic grain structure of spacing 100 nm was achieved, resulting in high hardness (17.15 GPa) and fracture toughness (4.79 $MPa*m^{1/2}$). Hu et al. [187] used the directed energy deposition process to create functionally graded ZTA parts. Zirconia contents were varied from 5-40 wt.%, which enabled the local tailoring of both different microstructures and phases locally. Through phase control of the heterogeneous structure, both toughness and hardness were improved. Adding 20 wt.% zirconia improved the hardness by 6.1%, but additional zirconia additions lowered hardness in comparison with monolithic

alumina specimens. Fracture toughness increased consistently with increasing zirconia content with a maximum improvement of 38.2%, equal to 3.7 MPa*$m^{1/2}$, at a dopant level of 41.5 wt.% zirconia. Hu et al. [188] used an ultrasonic vibration assisted directed energy technique to produce bulk ZTA parts. Cracks that developed in parts fabricated without vibration were not present in parts made using identical processing parameters but assisted by ultrasonic vibration. Cracking is reduced because ultrasonic vibration reduces thermal gradients and refines grain size. Grain size was refined from 16 to 8 µm by the application of vibration, which increases nucleation rate in the melt pool during DED processing. Hardness and compressive strength were both improved for parts fabricated by vibration assisted DED. In addition, ultrasonic vibration improves optical absorptivity, resulting in 9% energy savings compared to non-assisted DED techniques [189]. Yan et al. [190] produced nanometer-sized eutectic ZTA microstructures with spacing 60-70 nm. The fully dense parts had residual compressive stress at their surface due to DED processing, which resulted in a high fracture toughness of 7.67 MPa*$m^{1/2}$.

2.10. Conclusions and Future Directions

2.10.1. Conclusions

Whereas metal and polymeric AM has experienced great success for both prototyping and industrial production, ceramic AM remains in the research and development phase due to the difficult processing conditions intrinsic to ceramic materials. Nevertheless, great progress has been accomplished for several

ceramic AM techniques. Seminal papers for initial research efforts for each family of additive manufacturing processes were examined and their major findings, breakthroughs, and challenges were discussed. Progress in the 1990^{s} centered around basic technique advancements, processing parameter optimization, and process modeling. This led to the production of dense, mechanically sound parts and expansion of the material selection. Recent efforts focus on novel structuring, multi-material capabilities, and further achievement of structural and functional parts. In the realm of ceramics, the following are the most promising methods:

- Vat photopolymerization produces parts with superior surface finish and resolution, but faces major, and yet unsolved, challenges for dark-colored ceramic materials with high absorbance and index of refraction difference from photocurable resins. For this reason, many advanced ceramics including carbides, borides, and nitrides have experienced limited success in this technique. Industrial ceramic additive manufacturing is heavily focused on this technique, with oxide ceramics as the main feedstock material.
- Powder bed processes, binder jetting and powder bed fusion, have the benefit of supported overhang structures and wide material selections, but demonstrate poor surface finish and low green body density. Powder feedstocks for these processes are generally coarse in size to maintain free-flowing behavior. Conversely, the final properties of ceramic components rely heavily on fine microstructures and full density, which require the use of fine,

often sub-micrometer, feedstock powders and high green body density [48]. This technique excels at producing scaffolds with high porosity for applications such as medical implants.

- Sheet lamination has the longest history to draw upon for insights and process optimization due to its beginnings from tape-casting in the 1940s. The tape-casting process is well understood and is currently automated and scaled for industrial use. If interfacial defects and delamination issues can be minimized, this is one of the most promising processes for manufacturing structural ceramic components and composites.
- Material extrusion processes enable a wide material selection and utilize low-cost equipment. Using two or more nozzles or a mixing head, composite parts can be produced with discrete and continuous composition variation. Feedstock material can be loaded to the highest ceramic content out of all AM families, enabling dense, structural components. The main drawbacks are poor resolution and surface finish.

The commercial ceramic AM sectors are focused on the above processes: vat photopolymerization, binder jetting, powder bed fusion, sheet lamination, and material extrusion. Most of the major commercial suppliers of ceramic AM equipment and parts utilize vat photopolymerization, including 3DCeram, Admatec, EnvisionTEC, Lithoz, and Tethon3D [191]. Admatec printers use a hybrid process between vat photopolymerization and sheet lamination, wherein a doctor blade is used to produce a uniform thickness layer of high ceramic-content

photocurable slurry that is selectively cured using UV light. ExOne uses binder jetting to form green ceramic parts that are subsequently sintered, while II-VI MCubed uses binder jetting to print ceramic preforms followed by reaction bonding. Wuhan Binhu manufactures printers for PBF of ceramic materials. Helisys printers use the sheet lamination process and focus on creating composites. 3D Systems, Solidscape, Stratasys, and nScrypt produce material extrusion equipment focused on dental and bioprinting applications. Commercial suppliers support relatively few ceramic materials including alumina, zirconia, and silicon nitride, but are beginning to gain ground proving the industrial viability for these few optimized material systems.

2.10.2. Future Directions

Although substantial progress has been made, challenges identified in initial research and during the inception of additive manufacturing processes still exist today. Challenges include feedstock design, printing and post-processing related defects, process control and monitoring, and anisotropic mechanical properties [101]. To mature ceramic AM, each of these areas must be addressed.

Feedstock design challenges continue to hold back ceramic AM. Databases should be developed that contain the physical and chemical properties, optimal printing and post-processing parameters, resultant microstructural evolution, and application-based recommendations for ceramic feedstock materials. For example, a database could outline reactive processing relationships between

various ceramic materials [192]. Reactive processing techniques such a reaction bonding [146] and melt infiltration [165] were discussed in this review, but were achieve during post-processing. A database of compatible feedstock materials would accelerate research into in-situ reactive processing for direct AM processes such as PBF [193], which show significant promise but need further development for industrial use. Similarly, a database of precursor materials for polymer-derived ceramics and their processing parameters could advance progress in that area. Schmidt et al. [194] demonstrated multi-scale ceramic lattice structures using a hybrid AM process combining DLP and two-photo lithography (2PL). In this work, the PDC method enabled sub-micron features on centimeter-sized parts by removing the challenge of using sub-micron ceramic feedstock materials that can also be sintered to full density. Successful research into sub-micron ceramic feedstock materials that can be processed could enable a similar hybrid approach for bulk, structural ceramics.

In-situ monitoring of the printing process needs to be explored to improve quality control and control defects. Several monitoring techniques have been explored for polymer and metal AM processes, including nozzle pressure and temperature sensing[195] and melt-pool thermal analysis for metal PBF [196], but little work on in-situ monitoring and feedback control for ceramic AM processes exists. A process monitoring technique based on image signature analysis was developed to detect defects for FDC [197], but a feedback loop was not implemented and the system required manual calibration and image pre-

processing. Implementing nozzle pressure sensors with feedback control for ceramic suspension extrusion processes would enable consistent trace width and improve part quality. Monitoring by X-ray computed tomography has the potential to detect voids in real-time, which could provide valuable feedback to optimize processing parameters and reduce printing derived defects.

Few direct processes have been explored due to the high processing temperature and brittle nature of ceramic materials. Future research should look in-depth at direct processes because much of the time and energy costs for ceramic AM stem from post-processing. Novel sintering methods such as flash and microwave sintering may offer opportunities to improve single-step ceramic AM processes. Recent work by the Kovar group at UT Austin [198] studied the use flash sintering for ceramic PBF with limited success due to thermal cracking and uneven initiation of flash. Improved process control will be necessary to push these novel methods forward.

Compared with the direct AM processes used for metals and polymers, indirect processing of ceramic materials is an advantage when it comes to avoiding anisotropic mechanical properties. If printing defects can be eliminated, post-processing and densification should eliminate layer interfaces. Microstructure texturing that occurs in direct metal AM processes should not affect ceramic components, which are sintered in secondary steps. Through the use of composition gradients, sharp transitions in multi-material parts that lead to internal stress concentrations, cracking, and delamination at interfaces may be

eliminated [97]. Material deposition processes, including material jetting, material extrusion, and directed energy deposition, are especially suited to multi-material fabrication as they are essentially one-dimensional processes where the feed can be adjusted at any voxel. Fabrication of functionally graded composites has the potential to greatly improve damage tolerance of ceramic materials, which are typically brittle with defect-dominated mechanical properties. Further, hierarchical design, following that of natural structures, should be explored through several levels of structuring: macro and meso-scale features can be produced by nozzle pathing; fiber and particle alignment at the microscale could be controlled with shear gradients from doctor blades used for tape casting and spreader blades for vat photopolymerization or pressure gradients in extrusion nozzles; nanoscale structures could be achieved by grain boundary additives.

2.10.3. Acknowledgement

Chapter 2, in full, is a reprint of material that has been published: J. Pelz, N. Ku, L. R. Vargas-Gonzalez, M. A. Meyers, “Additive Manufacturing of Structural Ceramics: A Historical Perspective,” Journal of Materials Research and Technology, 2021. The dissertation author was the primary investigator and author of this paper.

CHAPTER 3. DIW SYSTEM DESIGN

3.1. Design Overview

The custom DIW system has two main modules, the print head and feed system. These modules were designed and optimized, using Autodesk's computer-aided design (CAD) software Fusion 360, to allow simultaneous extrusion of multiple ceramic inks through a single nozzle. The feed system has two units that are controlled independently, allowing output of material A, B, or any combination of the two. The ink is fed, using leadscrew driven plungers, through tubes to the print head. The print head contains an auger that achieves in-line mixing and volumetric extrusion, enabling simultaneous extrusion of inks with different rheological properties. The print head is designed to integrate with a LulzBot Taz 6 3-D printer, which removes the need for development of a 3-axis CNC and G-code communication protocols. The Taz 6 was chosen due to suitable precision, print volume, and open-source design. In order to integrate the print head, the Taz 6 firmware was modified to account for temperature-related errors, print head spatial variations, and custom tool path modifications. The print head is made from plastic parts, which were printed using the Taz 6 with its provided FDM print head. Communication between the Taz 6, which controls the print head, and the feed system is accomplished with the I2C communication protocol. The I2C protocol allows single character transmission from the Taz 6 to the feed system microcontroller. As each G-code line is processed by the Taz 6, it is echoed character by character to the feed system. The feed system

microcontroller then parses each G-code line and extracts values for extrusion lengths, feed rates, and ratios. This line-by-line communication is a robust method to precisely sync the material output from the feed system with the movements of the print head. Additionally, G-code files can be easily modified in any text editor to include additional information that could benefit the DIW process.

3.2. Print Head

The print head uses its auger to actively mix and extrude ceramic ink received from the feed system. The auger has three sections, which each perform a distinct function to successfully mix and convey material from the feed inlets through the nozzle. The first section has deep channels at a large pitch, which enables a large flow rate and small residence time. The second section has kneading blocks offset by 60° and works to provide additional shearing action. A 60° offset between adjacent kneading blocks provides a small amount of conveying action in combination with good mixing action. The third section has shallow channels at a small pitch, which provides a large conveying force and high residence time. The last section develops the necessary pressure to extrude material through a small nozzle orifice. The print head interfaces with the Taz 6 via the T-adapter with communication handled through the Taz 6 wiring harness. The Taz 6 controls the print head's 3-D positioning and auger speed. Figure 3.1 shows CAD renderings and cross-section analyses developed in Fusion 360.

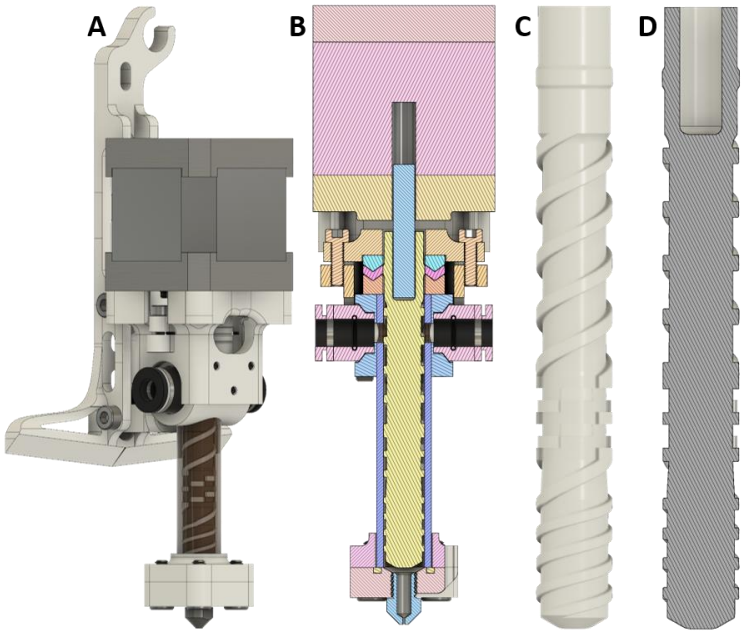

Figure 3.1. The print head was designed and rendered in Fusion 360. a) Rendering and b) cross section of the full print head assembly, and c) rendering and d) cross section of the auger.

The majority of the print head's components are printed using the Taz 6's provided FDM tool head. The auger is printed out of a polycarbonate-acrylonitrile butadiene styrene (ABS) alloy, which has improved strength and wear resistance over conventional ABS filament. Other printed components, which do not come in contact with the ceramic ink, are made out of ABS. The print head can be easily disassembled to clean or replace components. Figure 3.2 shows an exploded view of the print head with each component labeled.

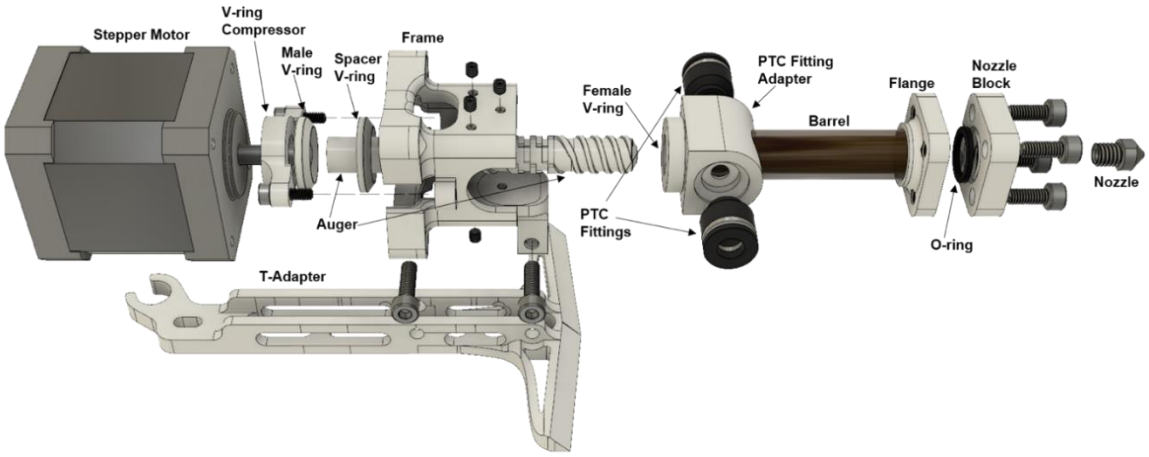

Figure 3.2. Exploded view of the print head to demonstrate component positioning.

The V-ring assembly provides a rotary seal between the top of the barrel and auger. The spacer V-ring is press fit around the extruded section of the auger. Proper sealing force is maintained with the V-ring compressor, which is adjusted using two M3 bolts. Two push-to-connect (PTC) fittings are used to attach the feed tubes. The barrel, a 3/8-inch inner diameter (ID) polycarbonate tube, has two holes aligned with the PTC fittings. The PTC fitting adapter and flange are press fit around the barrel. The PTC fitting adapter slides into the bottom of the frame and is secured in place with six cone-point M3 setscrews. The stepper motor is bolted to the frame with its D-cut shaft aligned in the female end of the auger. A square-profile O-ring seals the flange to the nozzle block, which is tapped with an M6 thread for compatibility with any standard FDM 3D printer nozzle. This allows the user to tune nozzle orifice size to their specific application. A variety of abrasion-resistant 3D printer nozzles exist, which are necessary for the highly abrasive ceramic inks.

3.3. Feed System

The feed system includes two identical units, which are independently controlled to allow input of material A, B, or any ratio of the two to the print head. The use of feed system units provides a scalable design, which could be modified to support additional materials by simply adding more units. Each unit has a syringe (ink reservoir) with a capacity of 100 ml. Figure 3.3 displays a feed system unit, designed and rendered in Fusion 360. The syringe can be removed, loaded with ceramic ink, and slid back into position. A short length of 16 AWG wire can be used to break the plunger gasket seal to allow it to slide into contact with the loaded ink. If the plunger does not contact the ink, the compressible air gap will significantly reduce feed rate control. Figure 3.4 shows an exploded view of the feed system unit with labeled components.

Figure 3.3. The feed system was designed and rendered in Fusion 360. This feed system unit has a capacity of 100 cc, provides excellent positional precision using a geared down leadscrew, and can generate pressures over 100 psi.

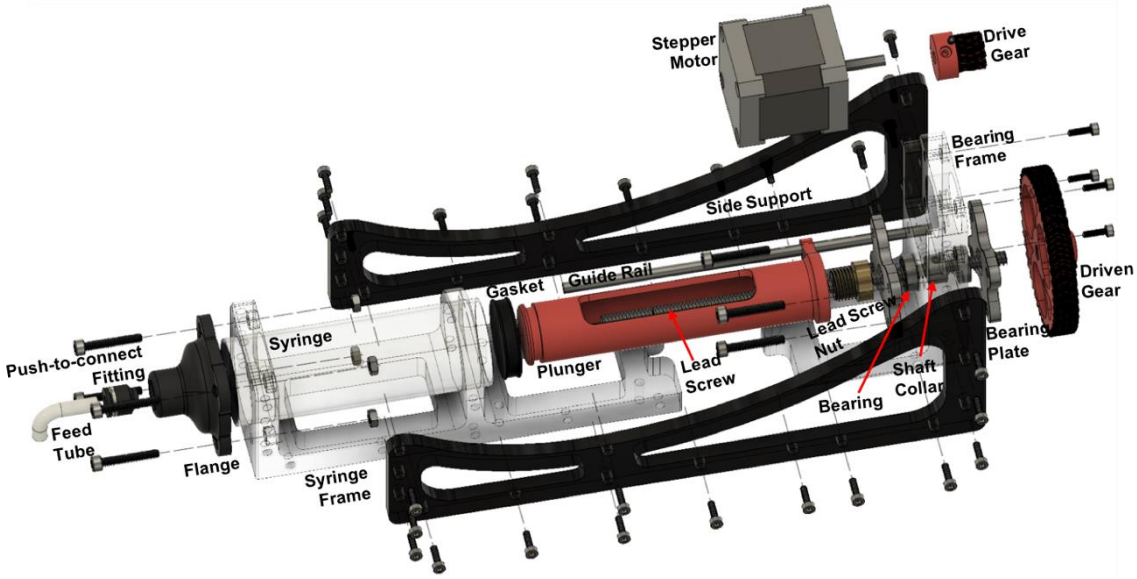

Figure 3.4. Exploded view of the feed system showing component positioning.

Each feed system unit consists of a stepper motor, bearing assembly, drive and driven gear, leadscrew, leadscrew nut, guide rail, plunger and gasket, modified syringe, flange, push-to-connect fitting, two side supports, bearing frame, and syringe frame. The bearing assembly includes two bearings, two bearing plates, and a shaft collar. The bearing assembly reduces rotational resistance while locking the leadscrew's linear position. The collar is fastened onto the leadscrew, leaving 30 mm exposed on the shorter side. The bearings are slid on either side of the collar and then inserted into appropriate hole in the bearing frame. The bearing plates are then fastened on either side using 25-mm-long 4M bolts. The driven gear is attached to the end of the leadscrew and secured with two 3M cup-point setscrews. The drive gear is attached to the stepper motor using a 3M cup-point setscrew and the stepper motor is bolted onto the bearing frame with the drive gear teeth correctly aligned to the driven

gear. The leadscrew nut is glued into place in the plunger and threaded onto the leadscrew. The guide rail, a 5-mm-diameter steel rod, is slid through the plunger arm and glued in place to the bearing frame and syringe frame. The plunger gasket was taken off the original plunger and fitted over the printed plunger head. The side supports can then be secured to the bearing and syringe frames using 4M bolts. The modified syringe is glued in place inside the flange, which bolts to the syringe frame. A PTC fitting, glued into the flange, provides a robust connection with the feed tube and prevents material leakage. Figure 3.5 shows a cross-section analysis of a feed system unit, which highlights the mechanics of the drivetrain and positioning of components. The drivetrain, which includes a drive gear, driven gear, and leadscrew, converts the rotational motion of the stepper motor into the plunger's linear motion. The gearing ratio is 9:47, which gives a torque multiplication factor of 5.22. The leadscrew has a lead of 1/16 inch per revolution, which, in combination with the gearing ratio, results in very precise linear movements of less than 0.01 mm per stepper motor step. Figure 3.6 highlights various subassemblies including the gears, guide rail, and bearing assembly. Custom feed system parts were printed in ABS.

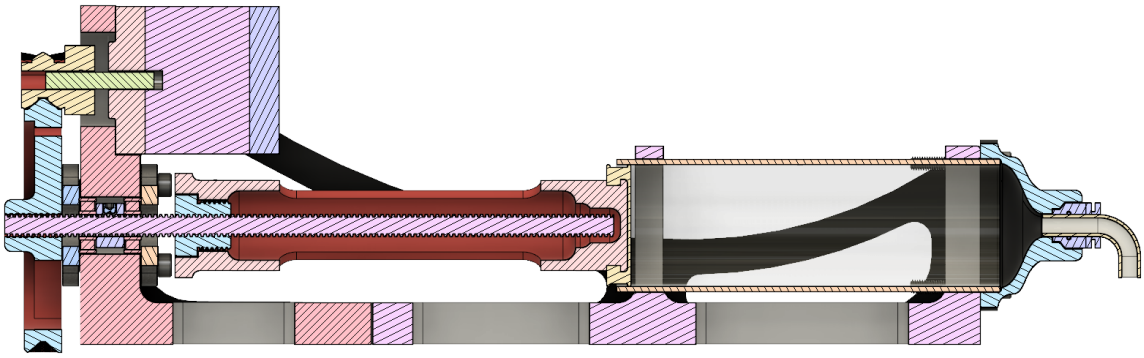

Figure 3.5. Feed system unit cross section highlighting the mechanics of its drivetrain, which includes a drive gear, driven gear, and precision leadscrew. The gearing creates a large mechanical advantage, as well as allowing for very small linear movements, below 0.01 mm stepper motor step.

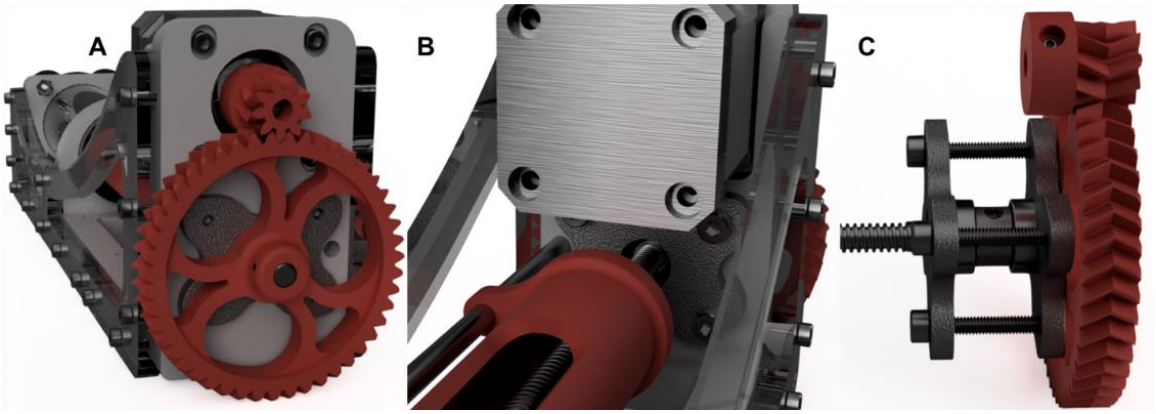

Figure 3.6. Renderings of a feed system unit highlighting various subassemblies. a) A 9:47 gearing ratio is used to couple the stepper motor with the leadscrew. b) The plunger uses a guide-rail to prevent rotation. c) The bearing assembly includes a shaft collar, two bearings, and two bearing plates. This robust setup locks the linear position of the leadscrew and reduces rotational resistance.

Several feed system parts were validated using finite element analysis simulations. Simulation studies were performed in Fusion 360 with an applied pressure of 100 psi at the plunger gasket, to simulate maximum operating conditions. ABS plastic was used as the simulation material. Compared with cast or extruded parts, 3-D printed parts have reduced strength and anisotropic mechanical properties due to weaker interfaces between layers. Therefore, a minimum factor of safety of 2.5 was chosen to validate these parts. In order to

reduce print time and material use, topology optimization studies were paired with finite element analysis static stress studies for the side supports and plunger arm. Simulation criteria included a target mass reduction of 40% and the objective of maximizing stiffness. Boundaries were placed at each end to preserve necessary geometries. Topology optimization results were used to inform the removal of non-essential material from initial designs. Modified designs were then run through secondary finite element analysis simulations at 100 psi to verify their structural integrity. Figure 3.7 showcases results for the plunger, where mass reduction through shape optimization reduced printing time and material use by nearly 30%.

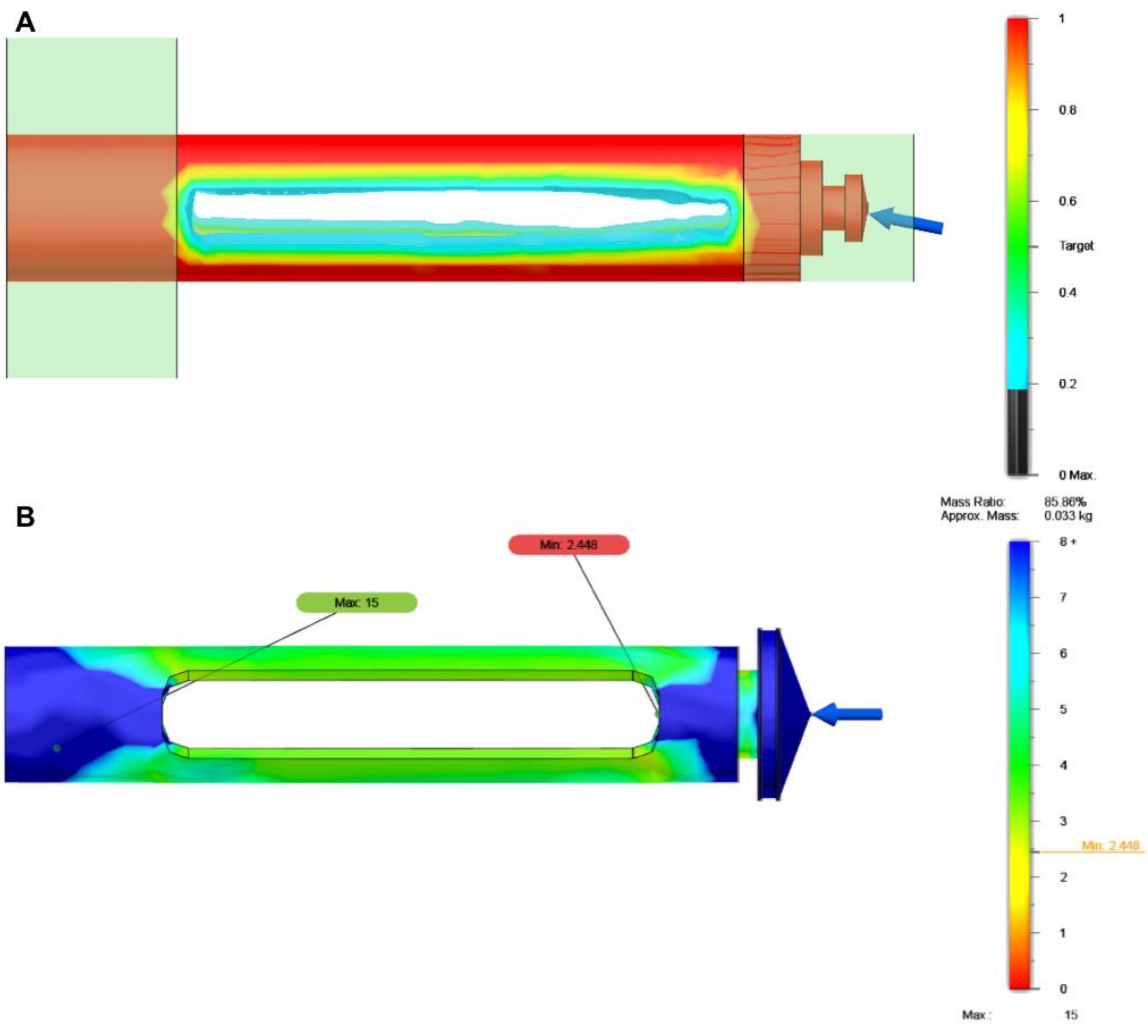

Figure 3.7. CAD simulation studies were performed in Fusion 360 with an applied pressure of 100 psi. a) Topology optimization was used to remove non-essential material. b) The shape optimized plunger, designed out of ABS plastic, was studied using a static-stress simulation to validate the topology optimization solution.

DXF vector data files for the feed system side supports and bearing plates, which were exported from Fusion 360 and edited in Autodesk's CAD software AutoCAD, are shown in Figure 3.8. First-generation bearing plates were made from 1/4-inch-thick aluminum plate, but during feed system operation significant bending caused plastic deformation and loss of feed precision. Therefore, the bearing plates were water-jet cut out of 3/16-inch-thick steel plate.

Side supports were laser cut out of 1/4-inch acrylic. Each feed system unit has a front and rear bearing plate. The rear bearing plate has smaller holes, which are tapped with 4M threads. Threading directly into the rear plate allows the driven gear to sit flush against it, instead of needing space for a nut.

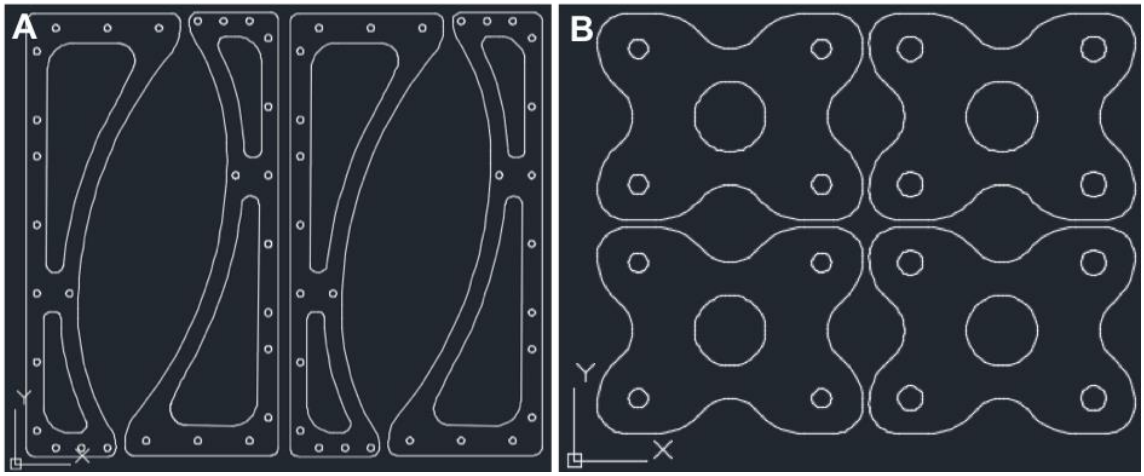

Figure 3.8. Vector data files for two feed system units: a) Side supports machined with a laser cutter and b) bearing plates machined with a water-jet cutter.

3.4. Control Structure

While DIW a ceramic part, the Taz 6 and feed system must communicate so the material feed matches the print head motion and extrusion. The Taz 6 follows a G-code file to control the print head auger's rotation direction and speed as well as the print head's x, y, and z position. The feed system, controlled by a separate Arduino Mega microcontroller, relies on echoed G-code lines to determine feed rate, volume, and ratio. The diagram in Figure 3.9 shows the structure of the feed system control hardware. The feed system controller consists of an Arduino Mega, two Big Easy Drivers (BEDs), an Arduino power supply, and two BED power supplies.

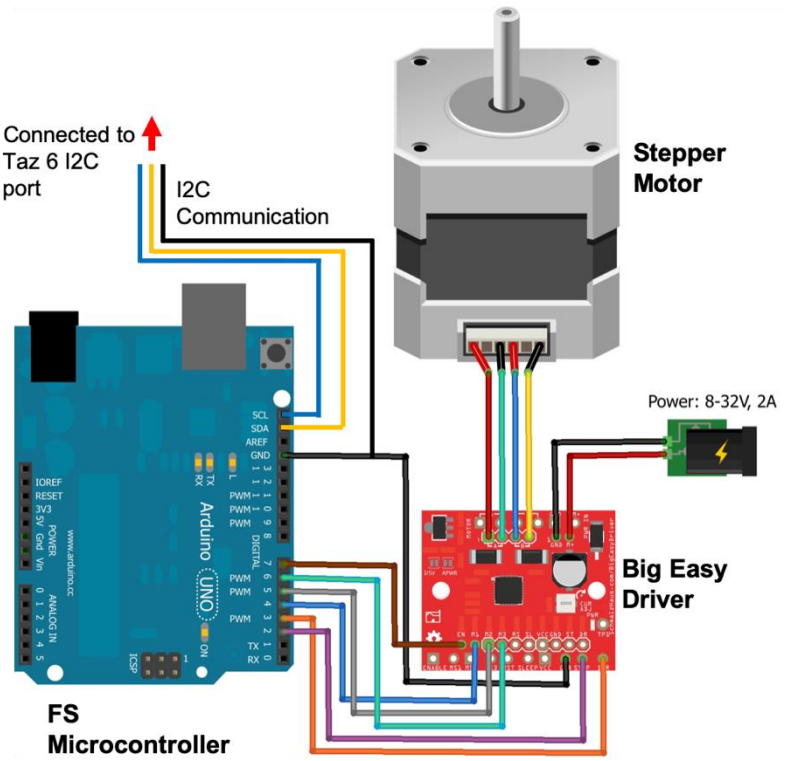

Figure 3.9. Wiring schematic showing connections between the feed system controller components.

An Arduino program was written to parse the echoed G-code lines and control the stepper motors to keep the print head and feed system synchronized. When the Taz 6 reads a G-code command off its secure digital (SD) card, the G-code line is sent character by character to the feed system microcontroller using the I2C protocol. The G-code line is then stored in an array and searched for “F”, “E”, and “R” qualifiers. An F designates feed rate in millimeters per minute, an E designates extrusion length in millimeters, and an R designates the ratio between 0 to 1, where 0 is 100% material A and 1 is 100% material B. If any of these qualifiers are found, the values are stored, and flags are set for each respective

qualifier. This function is blocking and will interrupt the main loop each time a new line of G-code is received.

The main loop has three sections, the serial monitor check, the flag check, and the step timing. The first section checks the serial monitor for user input, either an “e” or “r”, and if present executes the respective functions. If the user inputs an e, both stepper motors will turn forward one revolution. If the user inputs an r, both stepper motors will turn backward one revolution. These functions allow the user to increase or decrease pressure to the print head. The second section checks for flags signifying a new extrusion length or ratio has been received. If a new extrusion length is flagged available, the extrusion sign is checked to set step direction and the feed function is called. The feed function updates the steps stepper motor A and B must take based on new extrusion length and current ratio. The function also checks for the new rate flag, and, if available, updates the stepping period. If a new ratio is flagged available, the ratio is checked and depending on the value several actions will proceed. Case 1 (ratio equals 0): stepper motor A is primed, stepper motor B is reversed, and then stepper motor B is disabled to reduce idle time. Case 2 (ratio equals 1): stepper motor B is primed, stepper motor A is reversed, and then stepper motor A is disabled to reduce idle time. Case 3 (ratio is between 0 and 1): both stepper motors are enabled, the motor that was previously stepping will be half-reversed, and the stepper motor that was previously disabled will be half-primed. Case 4 (ratio equals –1): both stepper motors are disabled. The third section checks to

see if either stepper motor needs to step. If a step needs to be taken, the time since it last stepped is compared to the stepping period and, if greater, a single step is executed. The feed system uses 1/16 microstepping to reduce vibration and increase feed precision.

The extrusion length calculated by the Taz 6 must be converted into an extrusion volume and then into linear distances each feed system unit plunger must move. The gearing ratio and leadscrew threads-per-inch values relate the rotation of the drive gear to the linear motion of the plunger. The travel per revolution is calculated using Equation 3.1.

$$x_{travel\frac{mm}{rev}} = \frac{9}{47} * \frac{1}{16} * \frac{25.4\ mm}{1\ in} \tag{3.1}$$

The gearing ratio is 9:47 and the leadscrew's threads-per-inch is 1/16. Breaking the drive gear's revolution into steps allows x_{travel} to be converted from per revolution to per step, shown in Equation 3.2.

$$x_{travel\frac{mm}{microstep}} = \frac{9}{47} * \frac{1}{16} * \frac{25.4\ mm}{1\ in} * \frac{1}{3200} \tag{3.2}$$

The feed system stepper motors are operated at 1/16 microstepping, resulting in 3200 microsteps per revolution. The feed system feed volume per microstep rate is calculated using the known feed system syringe diameter and is related to the G-code extrusion length with Equation 3.3. The resulting stepping factor is the number of microsteps needed to equal a G-code extrusion length of 1 mm.

$$stepping\ factor = \frac{x_{travel\frac{mm}{microstep}*\pi*\left(\frac{D_S}{2}\right)^2}}{1mm * \pi * \left(\frac{D_F}{2}\right)^2} \quad (3.3)$$

If the syringe diameter (D_S) is 35 mm and the filament diameter (D_F) is 3 mm, the stepping factor is calculated as 92.52. Next, using the ratio, the number of steps each stepper motor must take can be updated.

$$Steps_A = E * 92.52 * (1 - R) \quad (3.4)$$

$$Steps_B = E * 92.52 * (R) \quad (3.5)$$

The G-code extrusion length, E, is converted into a number of microsteps for stepper motors A and B using Equations 3.4. and 3.5.

3.5. LulzBot Taz 6 Integration

The LulzBot Taz 6 3-D printer is the latest version of Aleph Objects successful line of desktop FDM printers. Key features include a large print volume, robust and precise performance, and an open-source, modular design. When developing this custom DIW system, the open-source, modular design was extremely important because it supported modification of the firmware and hardware. In fact, many of the Taz 6's parts are printed using Aleph Object's arsenal of 3-D printers, which makes modifications and repairs more accessible.

To swap the provided FDM tool head out with the DIW print head, the wiring harness connector is detached and a single M3 bolt is unscrewed. The DIW print head wiring connector can then be plugged into the Taz 6 wiring harness and M3 bolt screwed back in once the print head T-adapter is aligned in the Taz 6 tool head adapter's V-channel. Shorter feed tubes reduce the pressure

gradients that develop in the ink during operation, so the feed system units are mounted onto the top of the Taz 6 frame with their outlets positioned above the middle of the print bed. To reduce wire length, the control structure hardware is also mounted on top of the LulzBot Taz 6 frame. The print bed is borosilicate glass covered with a thin PEI sheet and can be heated.

Following hardware integration, the firmware must be modified to account for several differences between the provided FDM head and custom DIW print head. To modify the firmware, the */Software/Marlin version 1.x.x.x* zip file was downloaded from www.lulzbot.com. The firmware was modified using the Arduino IDE. Two sections of the firmware file were modified starting with the *Conditionals_LulzBot.h* tab:

1. Change '#define LULZBOT_EXTRUDE_MINTEMP' from 120 to 5.
2. Change '#define LULZBOT_INVERT_E0_DIR' from true to false.
3. Change '#define LULZBOT_INVERT_E1_DIR' from true to false.
4. Change '#define LULZBOT_Z_SAFE_HOMING_Y_POINT' from 258 to 254.
5. Change '#define LULZBOT_MANUAL_FEEDRATE_E from 1.0 to 2.0.
6. For '#elif defined(LULZBOT_USE_AUTOLEVELING) && defined(LULZBOT_TAZ_BED)'
7. Change 'LULZBOT_RIGHT_PROBE_BED_POSITION' from 288 to 286.
8. Change 'LULZBOT_BACK_PROBE_BED_POSITION' from 289 to 285.

9. Change LULZBOT_NOZZLE_PARK_POINT {x, y, z} to { 206, 236, 3 }.

10. For the #define LULZBOT_ACTION_ON_PAUSE_AND_RESUME find the #elif for LULZBOT_IS_TAZ. Change the code to: “G91\nG0 Z15 F600\nG90\nG0 X206 Y236 F3000\nG0 Z3 F600\nM117 Print aborted.”

Next, Configuration.h was edited:

1. Change ‘#define TEMP_SENSOR_0’ from LULZBOT_TEMP_SENSOR_0 to 998.

2. Add ‘//’ in front of ‘#define USE_XMAX_PLUG LULZBOT_USE_XMAX_PLUG’ to comment it out.

Next, Configuration_LulzBot.h was edited:

1. Delete // in front of ‘#define LULZBOT_Oliveoil_TAZ6’.

2. Delete // in front of ‘#define TOOLHEAD_Tilapia_SingleExtruder’.

Next, Marlin_main.cpp was edited:

1. Search for 'void process_next_command()’. Inside this function on the line before the comment “// Parse the next command in the queue” paste the following code:

```
Wire.beginTransmission(125);
Wire.write(current_command);
Wire.endTransmission();
```

This code will make the Taz 6 echo each line of G-code to the feed system Arduino Mega right as it processes that line of G-code.

3.6. G-code Generation

In order to simplify the printing process, Slic3r, free slicing software commonly used for FDM printers, is used to generate G-code. Several Slic3r profile modifications must be made in order for the print head to be compatible with the G-code, which is usually generated for an FDM toolhead.

1. Due to the fluid dynamics of the ink and attainable pressure of the DIW system, a lower print speed of 4 mm/s was used for testing.

2. Print head heating is not supported, so extruder temperature must be set to Heated-bed capabilities are unchanged, so bed temperature can be set.

3. Relative extrusion distances must be used because of the feed system program logic, which adds each extrusion length.

4. Filament diameter must be set to the value used in the stepping factor calculation from Equation 3.3. A diameter of 3 mm works well according to the auger geometry. Slic3r uses this diameter setting in combination with the E_steps value (found in the configuration tab of the Taz 6's liquid crystal display [LCD] screen) to calculate the volume of plastic filament fed into the heating chamber per stepper motor revolution. The E_steps value stores the number of stepper motor steps to move the plastic filament 1 mm. Taz 6 firmware executes 1/16th microstepping, which results in a total of 3200 steps per revolution for the 1.8° NEMA 17 stepper motor. To calculate the filament diameter setting for Slic3r, the volume of material extruded per revolution for the specific auger must be known. The calculation is done with Equation 3.6.:

$$D_F = \sqrt{\frac{V_A * E\_steps}{800 * \pi}} \quad (3.6.)$$

where DF is filament diameter, VA is auger extrusion volume per revolution, and E_steps is the configuration value set through the Taz 6's LCD screen.

5. Lulzbot Taz 6 printers use a 'safe homing position' for z-homing, which enables the z-stop limit switch to home the nozzle-tip position instead of an arbitrary end-stop switch position.

6. The custom start, stop, and toolhead change G-code must be pasted into the Printer Settings > Custom G-code Slic3r profile section. The toolhead change G-code moves the print head to the dumping location, far right of bed, purges an extrusion length of 400 mm, pauses to let the user wipe off the nozzle, and then resumes printing.

3.6.1. Custom Start G-code:

```
;This G-Code has been generated specifically for the LulzBot TAZ 6 with
Custom DIW print head
M73 P0 ; clear GLCD progress bar
M75 ; start GLCD timer
G26 ; clear potential 'probe fail' condition
M107 ; disable fans
M420 S0 ; disable previous leveling matrix
G90 ; absolute positioning
M82 ; set extruder to absolute mode
G92 E0 ; set extruder position to 0
G28 ; Home all axis
G1 E-10 F100 ; retract filament
G1 X-9 Y-9 F3000 ; move above first probe point
M204 S100 ; set probing acceleration
G29 ; start auto-leveling sequence
M420 S1 ; activate bed level matrix
```

M425 Z ; use measured Z backlash for compensation
M425 Z F0 ; turn off measured Z backlash compensation.
G1 X0 Y0 Z15 F5000 ; move up off last probe point
G4 S1 ; pause
M400 ; wait for moves to finish
G1 Z2 E10 F75 ; prime tiny bit of filament into the nozzle
M117 DIW System Printing… ; progress indicator message on LCD

3.6.2. Custom Stop G-code:

M400 ; wait for moves to finish
M107 ; disable fans
G91 ; relative positioning
G1 E-1 F300 R-1.00 ; filament retraction to release pressure
G1 Z2 E-5 X-20 Y-20 F3000 ; lift up and retract even more filament
G90 ; absolute positioning
G1 X206 Y236 F3000
G1 Z3 F600
M77 ; stop GLCD timer
M84 ; disable steppers
M117 Print Complete. ; print complete message

3.6.3. Custom Tool-head Switch G-code:

; Change T0,T1 to R0,R1 and move it directly above this line at the end of the most recent G1 line.
G1 F1500 X295 Y115 ; Purge Gcode
G4 S5
G1 F100 E50
G1 F100 E50
G1 F100 E50
G1 F100 E50
G1 F100 E50
G1 F100 E50
G1 F100 E50
G1 F100 E50
G4 S15

Once a part has been sliced and the G-code has been generated, ratio commands must be manually entered into the G-code file using a text editor. Add

a ratio command to the end of the first G1 line after the custom start G-code. Then, add ratio commands at other desired locations to change the ratio during the print. For example, if the user wants to start with 100% material A, R0.00 would be entered. Then, if the user wants to change to a ratio of 50% material A and 50% material B, R0.50 would be entered. And finally, to switch to 100% material B, R1.00 would be entered. Alternatively, if binary material switches are desired, multimaterial settings in Slic3r can be used to automatically add the toolhead change G-code followed by “T0” or “T1” for toolhead 1 or 2. The T can be changed to R using a text editor and moved to the G1 line directly above the custom toolhead switch G-code. The ratio command must be placed at the end of a G1 line, because if it is placed on a separate line it will be ignored and will not be echoed to the feed system microcontroller.

3.7. Results and Discussion

Damage tolerance is highly dependent on sintered density because even small imperfections will induce stress concentrations that lead to failure. A prerequisite of high sintered density is high green density, which requires an optimized printing process. An optimized printing process should reduce air bubbles, defects, warping, and slumping. Several areas of the printing process must be optimized including ink rheology, auger geometry, and G-code generation. Rheology will be optimized to increase ink printability. The auger geometry will be optimized with a focus on the mixing–dead space relationship

and reduction of air bubbles. The G-code design workflow will be optimized using a print complexity timeline.

The highly loaded, colloidal ceramic inks used for DIW contain around 50 vol.% ceramic powder, 5 vol.% binder, 5 vol.% dispersant, and water. To produce inks with yield-pseudoplastic behavior, each ceramic powder type must be characterized for surface chemistry, particle size, and shape. This information can then be used to choose a specific binder/dispersant system that will effectively disperse the colloids, while providing adequate green body strength. Correct rheology is critical for printed parts to retain their shape, while still allowing extrusion through a fine tip. In-line mixing and dead space, which is the volume of material in the nozzle between the ink inlets and tip, must be optimized to enable development of complex, heterogeneous structures. Mixing facilitates the development of gradient structures with smooth, controllable compositional changes, while reducing dead space allows for quick compositional changes. Figure 3.10 illustrates a feasible mechanism for in-line mixing. The difference in interaction between the ceramic ink and barrel wall versus auger surface drives mixing convection cells. If particles show a stronger interaction with the barrel wall than the auger surface, the convection cells will be driven in the directions shown in Figure 3.10. Adequate mixing can be achieved using a long auger screw, but a long screw will result in a large dead space. These competing factors must be balanced to allow both rapid changes in composition and sufficient mixing.

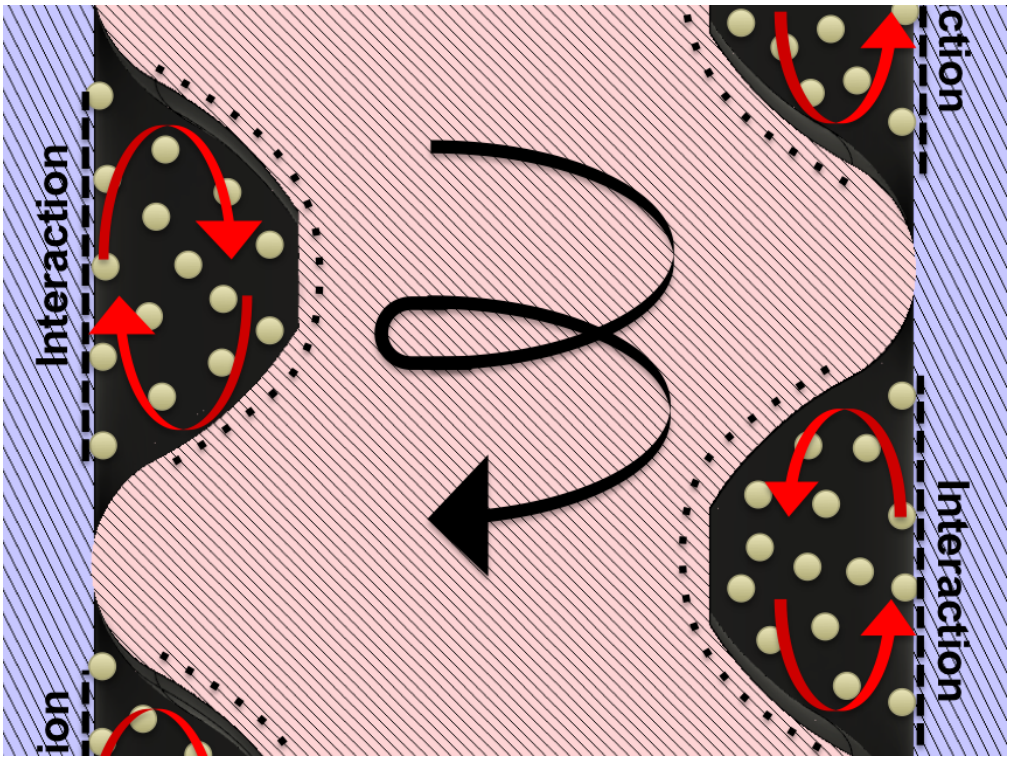

Figure 3.10. In-line mixing diagram showing mixing convection cells driven by particle interaction with the barrel (purple) and auger (pink) during auger rotation.

Following the development of optimized inks and auger geometry, printing parameters are fine-tuned for each print. The capability to print with multiple materials and mix in-line enables both discrete layers and gradients of composition. Relevant parameters include raster speed, trace width and height, layer change settings, and feature sequence (walls versus infill first). Radial gradients can be formed by priming material A, starting the infill in the center, and switching to 100% material B immediately. Due to the dead space, the composition change will occur over a number of traces. Figure 3.11 shows a radial gradient printed using two colors of Play-Doh. The switch from blue to white takes the majority of the shown layer, with only the last four perimeters at 100% white Play-Doh. Figure 3.12 shows a layer-wise gradient of boron carbide

to silicon carbide, where the composition was changed by 10% each layer. Figure 3.13 shows a layered boron carbide and silicon carbide print, with an ABAB pattern. A G-code error resulted in the second layer remaining material A. Prime and purge steps are used to create layered parts. As an A layer finishes, material B is primed, material A is reversed, the dead space is purged into a dumping container, and then the next layer is started. DIW process optimization will drive the advancement and capability of this system; successful optimization will result in the printing of heterogeneously graded parts with structural organization at multiple length-scales.

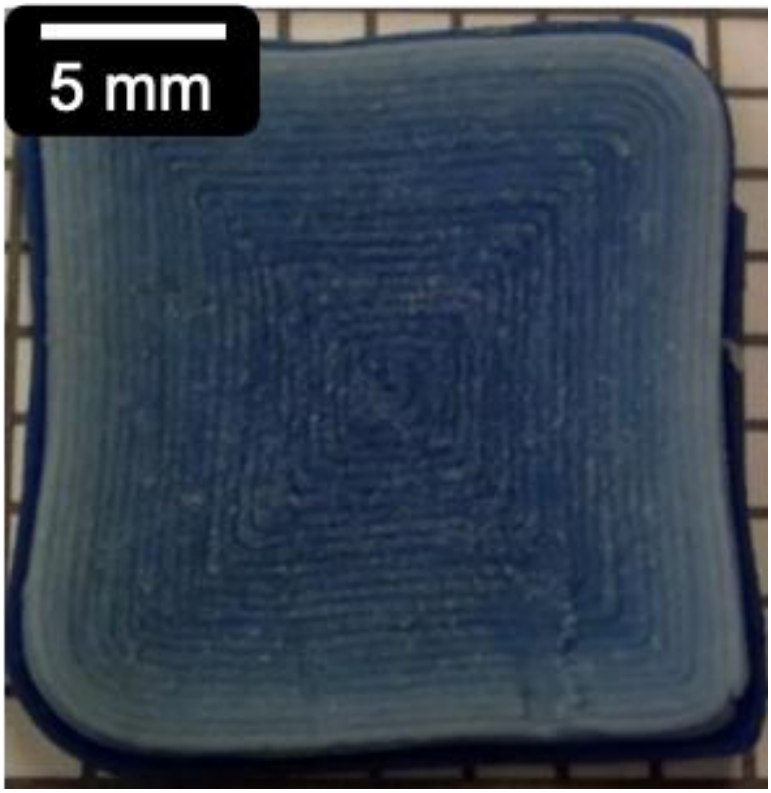

Figure 3.11. Radial gradient printed using blue and white Play-Doh. Print parameters are: 0.6-mm layer height, 0.8-mm nozzle width, 10-mm/s print head speed, and center-to-perimeter concentric fill pattern.

Figure 3.12. Gradient boron carbide (bottom) to silicon carbide (top) 1-inch diameter cylinder produced by DIW. Print parameters are: 1.2-mm layer height, 1.2-mm nozzle width, 4-mm/s print head speed, and center-to-perimeter concentric fill pattern.

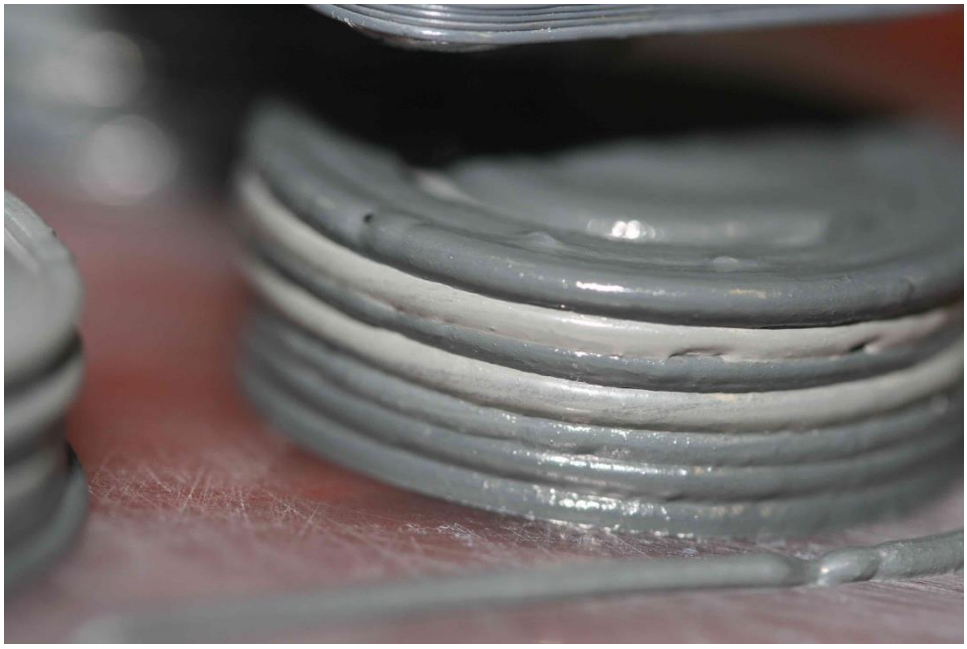

Figure 3.13. Layered boron carbide (dark-gray) and silicon carbide (light-gray) 1-inch diameter cylinder produced by DIW. Print parameters are: 1.2-mm layer height, 1.2-mm nozzle width, 4-mm/s print head speed, and center-to-perimeter concentric fill pattern.

This custom DIW system, shown in Figure 3.14, addresses several deficiencies many other ceramic AM platforms have, including those of other DIW systems. AM systems that can print with multiple materials throughout a single print are limited to extrusion-based systems, due to the difficulty of switching material types when using a powder or liquid bed. Commercially available DIW systems tend to use a plunger to extrude material from a syringe. Plunger-driven extrusion systems require a tool head switch to change composition and cannot print composition gradients. These deficiencies reduce their ability to print functional structures and take advantage of extrinsic toughening mechanisms.

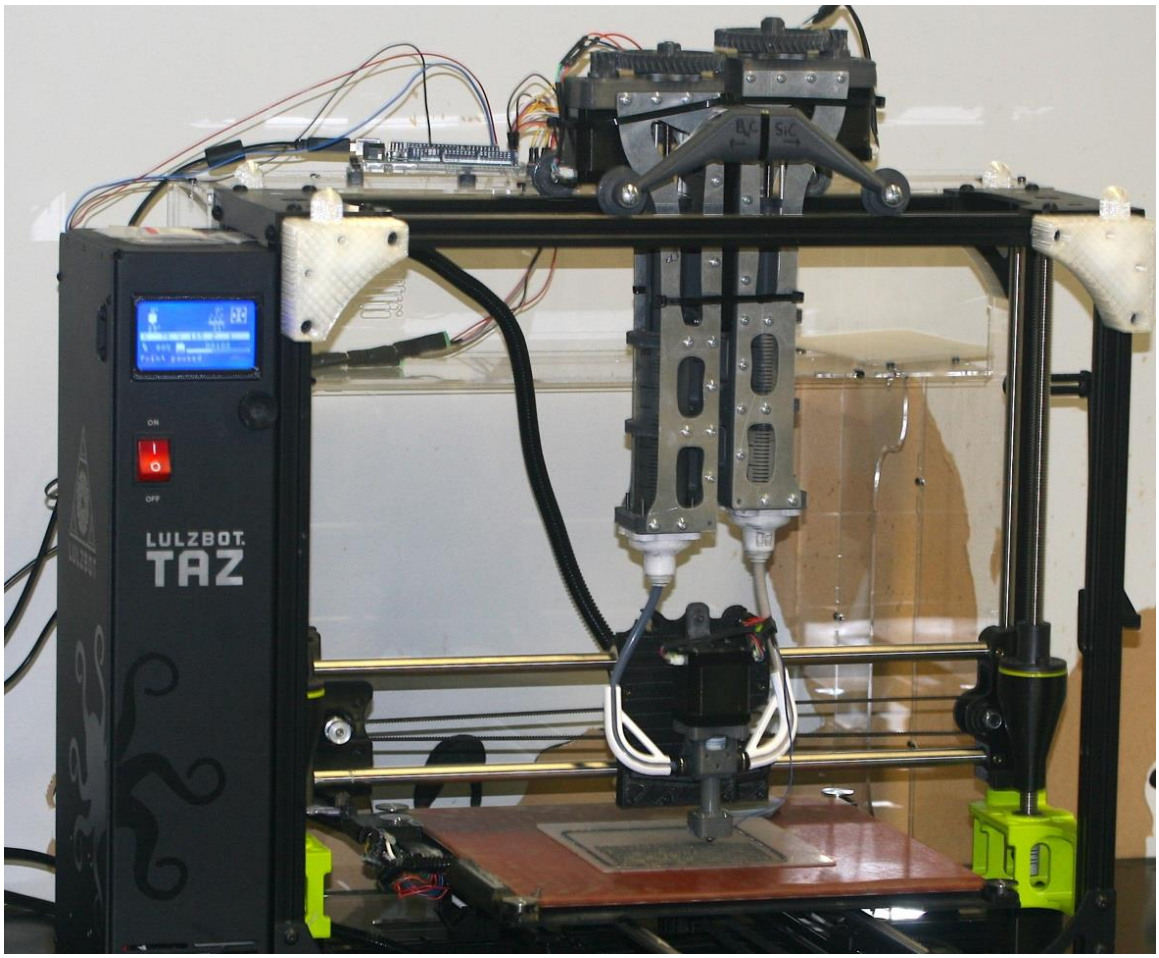

Figure 3.14. Custom DIW system mounted on a Lulzbot Taz 6 printer. A rolling truss allows the feed system to follow the x-axis motion of the print head. This system has multimaterial and in-line mixing capabilities, which enable printing of functionally graded ceramic composites.

3.8. Summary

3.8.1. Conclusion

Chapter 3 summarizes the development of a custom DIW system with multi-material and in-line mixing capabilities for use with yield-pseudoplastic ceramic inks. The DIW system gives researchers the means to study the effects of functional design on ballistic performance in composite ceramic armor. Additionally, models of the structure-property relationship can be developed and

verified for dynamic responses in composite ceramics. Finally, armor designs inspired from notably tough biological structures including fish scales and abalone nacre can be tested. Future work includes additional optimization of the auger, modification of the print head barrel to allow heating to adjust ink viscosity, modification of the print head nozzle to allow polarization of magnetically susceptible inks, and the addition of a UV light to allow printing of UV curable inks.

3.8.2. Acknowledgement

Chapter 3, in part, is a reprint of material that has been published: J. Pelz, N. Ku, M. A. Meyers, L. R. Vargas-Gonzalez, “Additive Manufacturing Utilizing a Novel In-Line Mixing System for Design of Functionally Graded Ceramic Composites,” ARL-TR-8851, CCDC Army Research Laboratory, 2019. The dissertation author was the primary investigator and author of this paper.

CHAPTER 4. HETEROGENEOUS STRUCTURING OF ADVANCED CERAMICS

4.1. Overview

A custom DIW system, described in Chapter 3, was developed to enable the printing of carbide components with heterogeneous structuring. Boron carbide and silicon carbide powders were suspended as aqueous inks and used as the feedstock for printing heterogeneous carbide specimens. The custom DIW system was assessed for its ability to print and mix multiple materials at specified ratios. Printed specimens were tested for shape retention, density, microstructure, and mechanical properties to elucidate the advantages and limitations of our ceramic AM method.

4.2. Experimental Procedures

4.2.1. Feedstock Preparation

B_4C (mean particle size ~ 0.8 µm, ESK Tetrabor 3000F B_4C, Kempten, Germany) and SiC (mean particle size ~ 0.7 µm, Superior Graphite 490N SiC, Chicago, IL) powders were processed into high ceramic content aqueous ink formulations, with rheological behavior controlled using mixtures of organic binders and dispersants. Brunauer–Emmett–Teller (BET) particle surface area was measured using a Micromeritics Tristar II Plus (Norcross, GA). The B_4C ink contained polyethyleneimine (25kDa PEI, Sigma-Aldrich, Louis, MO), hydrochloric acid (96.99% HCl, Sigma-Aldrich, Louis, MO), methylcellulose (4000cP MC, Sigma-Aldrich, Louis, MO), and deionized water. The SiC ink

contained of polyethyleneimine (25kDa PEI, Sigma-Aldrich, Louis, MO), methylcellulose (4000cP MC, Sigma-Aldrich, Louis, MO), and deionized water.

A stock solution of 5 vol.% methylcellulose (MC) and deionized water was made to simplify processing at the time of mixing. Four grams of MC powder were slowly added to 80 mL of deionized water at 95ºC on a mixing hot-plate. Once all MC powder was dissolved, the solution was placed into an ice-bath until it became clear, signifying gel-network formation [199].

Ink formulations were mixed in 120 g batches using a DAC 400 VAC SpeedMixer (Flacktek, Landrum, SC). PEI and one-half of the ceramic powder were added to a 150 g Flacktek container and mixed at 800, 1200, and 1600 RPM steps for times of 30, 30, and 15 s, respectively. Next, using the same mixing procedure twice, the deionized water and HCl were incorporated into the Flacktek container along with small amounts of ceramic powder. The MC solution and remaining ceramic powder were then added into the Flacktek container and mixed with 800, 1200, 1600, and 2000 RPM steps for times of 60, 60, 30, and 15 s, respectively, to be homogenized. The three rough mixing stages and final homogenizing mixing stage resulted in a total mixing time of 7 minutes and 45 seconds. SiC ink formulation follows the same procedure as the B_4C ink, with the exclusion of the HCl addition, as no further modification of particle surface charge is necessary to attain dispersion. In a preliminary sintering study, a B_4C ink was formulated as described, but without the addition

of MC. Inks were formulated directly prior to printing to reduce potential gravity separation effects.

4.2.2. Rheology

Rheological characterization of inks was performed using an MCR 302 (Anton Paar, Graz, Austria). A concentric cylinder fixture with a nominal diameter of 27 mm and a gap of 1 mm was used for testing of the ceramic inks. A damp paper towel was placed at the top of the concentric cylinder apparatus to reduce water loss during testing. Rheological testing was conducted at a controlled temperature of 25 °C. Samples were pre-sheared after loading at 30 s^{-1} for 60 s and allowed to equilibrate for 5 min before testing to remove shear history from the sample. The viscosity was measured with a continuous flow test from 0.1 to 100 s^{-1}.

4.2.3. Direct Ink Writing

Carbide parts were formed via DIW using a custom-built system, described in Chapter 3 and re-depicted in Figure 4.1, with multi-material and in-line mixing capabilities [13]. This system has two primary modules, the print head and the feed system, and interfaces with a low-cost fused filament fabrication (FFF) 3D printer (LulzBot Taz 6, Aleph Objects, Loveland, CO). The feed system consists of two units, which are independently controlled to output two different ceramic inks to the print head. Each unit utilizes a leadscrew driven plunger for precise, volumetric feed rate control. Ceramic ink is fed through 4 mm inner-diameter Teflon tubes to the print head, which contains an auger to

enable in-line mixing and precise extrusion. The auger, depicted in Figure 4.1C, provides shear mixing to blend highly viscous inks, which tend to resist turbulent flow and are therefore difficult to mix with impellers or other turbulent dispersion methods. The mixed ink is extruded through the 1.2 mm orifice of the nozzle. The Taz 6 3D printer serves as the 3-axis motion system, allowing for either FFF of plastic parts using the provided tool head or DIW of ceramic specimens using the custom-made print head and feed system. In fact, several components of the print head and feed system were printed from ABS filament (Chroma Strand Labs, Loveland, CO) and PC-ABS filament (Proto-pasta, Vancouver, WA) using the Taz 6 with its FFF tool head. The Taz 6 was selected due to its suitable precision, print volume, and open-source design, and its firmware was modified to remove temperature related errors, print head spatial variations, and custom tool path modifications.

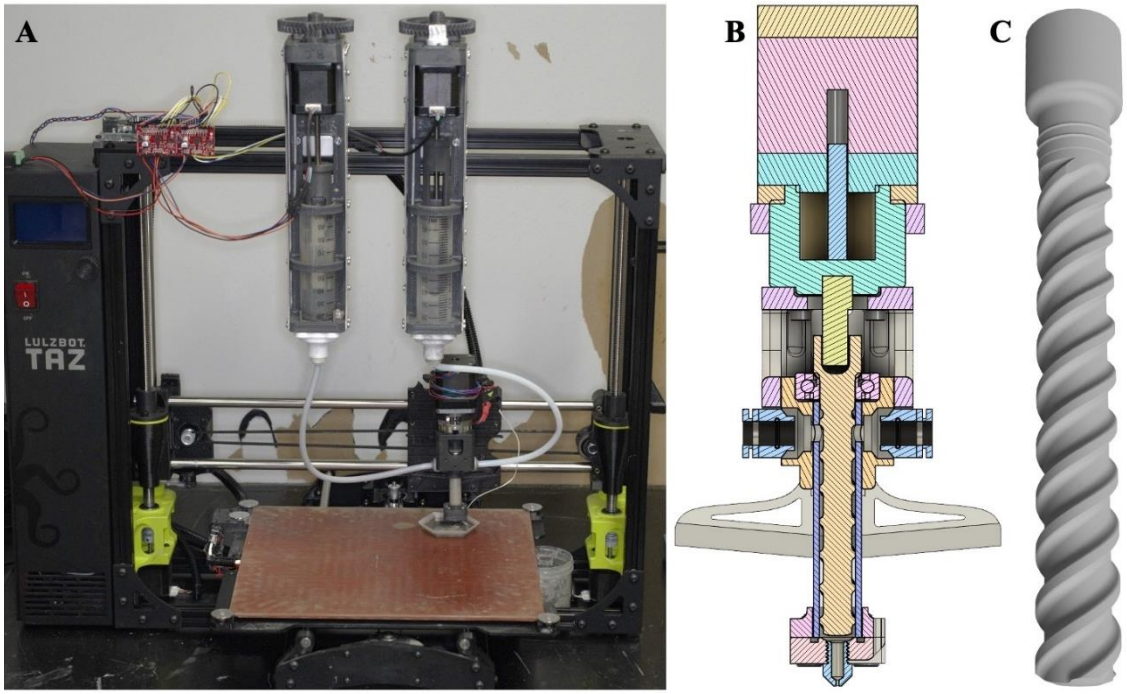

Figure 4.1. (A) The DIW system consists of two feed system units, the feed system controller, and the print head mounted on a LulzBot Taz 6 printer. (B) Cross-section view of the print head illustrating the mechanisms involved in mixing and extrusion. (C) The auger uses a series of channels to provide high-shear mixing and consistent material extrusion.

Slic3r (https://slic3r.org/), a 3D slicing engine, was used to prepare the G-code sent to the Taz 6. Relevant slicing parameters include a 1.2 mm layer height, 1.2 mm trace width, and print speed of 5 mm/s. The 1.2 mm trace width is determined by the nozzle width of 1.2 mm. The 1.2 mm layer height was chosen to reduce nozzle dragging effects (observed for lower layer heights), while maintaining acceptable print quality. At layer heights greater than 1.2 mm, print quality was visually reduced as extruded material tended to deflect sideways before contacting the previous layer. A conservative print speed of 5 mm/s was selected to reduce under-extrusion, visually observed as thinner traces with gaps in between, which tended to occur at higher speeds.

Composition was controlled automatically using G-code, whereby commands were sent to the feed system to adjust feed rate and ratio. Feed system unit 0 was loaded with B_4C ink and feed system unit 1 was loaded with SiC ink. The G-code composition command uses an 'R' identifier followed by a 0.00 to 1.00 value to denote composition changes of any ratio as a function of vol.% SiC. For example, R0.25 would adjust the feed ratio to 75 vol.% B_4C and 25 vol.% SiC. A purge operation was used during compositional changes. The purge operation moves the print-head over a waste container, located beside the build platform, and extrudes a specified volume of material to clear any remaining ink of the prior composition from the print head. Prior to printing, 'R' identifier commands were manually added to the G-code files used for printing heterogeneous parts, with the purpose of commanding composition changes at the correct locations. Carbide specimens with composition variation in the build direction were printed onto acrylic squares, which were mounted on the Taz 6 build platform. Directly after each print completed, the acrylic squares were moved to a chamber, which allowed the specimens to dry in a controlled environment. The chamber was set to 77% relative humidity and ambient temperature. Printed carbide specimens were dried for 48 h.

In order to calculate the purge volume, different colors of Play-Doh were printed in zig-zag formations using the same printing parameters. The trace length required to fully change Play-Doh color following a composition change was measured from a photograph of the zig-zag print. Trace length was

converted to volume by assuming a cylindrical geometry with a diameter of 1.2 millimeters. Play-Doh was used as a surrogate for the ceramic ink due to its superior optical contrast, ease of acquisition, and similar yield-pseudoplastic behavior.

4.2.4. Printability

The printability of the carbide inks was determined by three tests. First, ink formulations were continuously extruded through nozzle orifice diameters of 0.6, 0.8, 1.0, and 1.2 mm in a purge operation to verify no clogging would occur during a print. Second, a single wall of stacked traces was printed, allowed to dry, and total height loss was measured. Total height loss is the difference of the measured height of the stacked traces from the nominal height, which is equal to the programmed layer height multiplied by the number of layers. Third, after drying, the total height loss was calculated for the heterogeneous carbide specimens.

4.2.5. Green Body Characterization

Following drying, blended B_4C-SiC parts were fractured to reveal layered cross sections, mounted on scanning electron microscope (SEM) stubs, and sputter-coated with carbon. Microstructure and chemical composition were characterized using a SEM and energy-dispersive spectroscopy (EDS) (FEI Apreo SEM, Hillsboro, OR). The composition of in-line mixed and extruded test filaments was analyzed using a Bruker D2 PHASER (Billerica, MA) x-ray diffractometer (XRD). The XRD utilized a Cu K-α source generated at 30 kV and

10 mA. Test conditions for the analysis consisted of a 2Θ range of 15-80° with an increment of 0.015° and step time of 1.5 s. Printed test filaments were prepared with ethanol using a mortar and pestle. For reference, 10g powder batches with the same nominal compositions as in-line mixing trials were weighed and then mixed in ethanol using a vibratory mixer (Resodyn LabRAM, Butte, MT). Powder dispersions were pipetted on to Si XRD sample holders and allowed to dry, forming thin layers of powder for XRD analysis.

4.2.6. Pressureless Sintering

Monolithic B_4C, monolithic SiC, and blended B_4C-SiC parts were densified with (1) pyrolysis by ramping at 1ºC/min up to 650ºC and holding for 24 h and (2) pressureless sintering by ramping 25ºC/min up to 1350ºC and holding for 1 h and then ramping at 25ºC/min up to either 2150ºC or 2250ºC and holding for 1 h. The sintering process was performed in a flowing argon atmosphere in a graphite furnace.

4.2.7. Pressure-Assisted Sintering

Two heterogenous B_4C-SiC specimens, one with discrete composition variations and one with a continuous composition variation along the build direction, were both (1) pyrolyzed by ramping at 1ºC/min up to 650ºC and holding for 24 hours and (2) densified through hot pressing. The specimens were hot pressed at 35 MPa and 1950ºC for 2 hours, using a 25ºC/min ramp rate and including an intermediate hold at 1350ºC for 1 hour to volatilize oxide species.

4.2.8. Dense Body Characterization

Two methods were used to obtain density values, the Archimedes method using the Mettler Toledo Model AX205 (Columbus, OH) and an envelope density method using the Micromeritics GeoPyc Model 1360 (Norcross, GA). Archimedes densities measurements for blended parts sintered at 2150ºC failed to establish equilibrium during the immersion step, possibly due to entrapped air from open porosity within the sample. Therefore, an envelope density measurement was used for the two blended samples. The GeoPyc determines density through displacement of a highly flowable, uniform-packing powder bed. This allows for a true envelope density of the sample to be measured, which includes both open and closed porosity in the sample volume. Densities were reported as a percentage of theoretical density, which was calculated using a rule of mixtures with values of 2.52 g/cc for boron carbide and 3.21 g/cc for silicon carbide [17]. Density calculations for blended parts used composition ratio values extracted from XRD results.

Specimens with sufficient density were cross-sectioned, mounted in epoxy, and polished using diamond media. Rough polishing was accomplished using a 125 µm diamond embedded disk until specimen surfaces were exposed and planar. Next, colloidal diamond suspensions of sizes 30, 9, and 3 µm were used to polish both specimens for times of 30, 30, and 90 minutes, respectively. A final polish was done using 1 and 0.25 µm colloidal diamond suspensions for times of 45 and 60 minutes, respectively. All polishing steps were performed at a

20N load and with plate and head speeds of 300 and 150 RPM, respectively, in a co-rotating configuration. SEM micrographs were taken of the resulting polished cross-sections (FEI Apreo SEM, Hillsboro, OR). ImageJ was used for all measurements on SEM micrographs [200]. Layer height, crack length, crack spacing, and crack opening displacement are reported from at least 25 measurements.

4.2.9. Scale of Segregation

A central theme of this dissertation is the process-structure-property relationships of heterogeneous multi-phase carbide ceramics. In order to determine these relationships, a quantitative measure of heterogeneity is necessary. Danckwerts [201] developed a quantitative method of expressing "goodness of mixing" using two independent metrics, the scale of segregation (S) and intensity of segregation (I). Scale of segregation gives a quantitative measure of clump (in our case inclusion) size, location, and distribution. This is shown in the form of a correlogram, with S equal to the integral of the curve. A larger S value corresponds to larger clumps. Intensity of segregation gives a quantitative measure of 'discreteness of inclusion/clump boundaries'. If clumps are discrete with little to no interface diffusion, I = 1. If boundaries are perfectly diffuse (i.e. mixing is homogenous and no concentration gradients exist) I = 0. Effectively, I is a measure of the variance in concentration of clumps from the mean. Our sample size (a pixel) is smaller than the powder size, as opposed to

gases and liquids, where individual atoms/compounds would be much smaller than the sample size. Thus, intensity of segregation doesn't apply well.

The statistical method of determining scale of segregation is based on two-point correlation analysis, which produces a spatial correlation function that can be used to quantify porosity, specific surface area, grain sizes, and other microstructural features [202]. In our case of multiphase carbide ceramics, the two-point correlation function can be defined as the likelihood that two points a distance r apart in a specimen both lie in a region within a single phase. Figure 4.2 demonstrates the physical meaning of S, where larger values of S correspond to larger clumps, irrespective of the volume fraction of the dark phase.

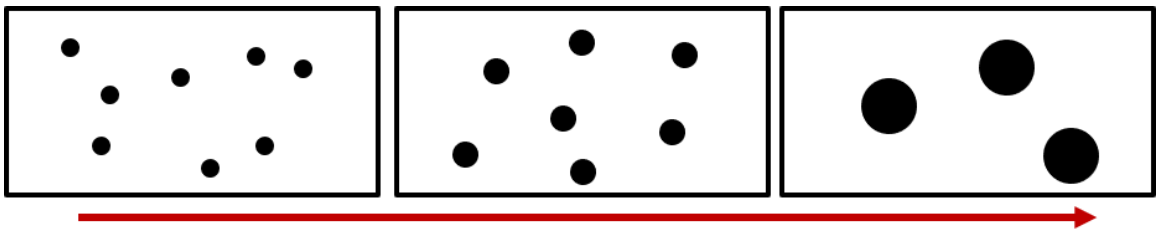

Figure 4.2. In a unimodal inclusion distribution, the effect of inclusion size on the scale of segregation, where increasing size, irrespective of inclusion volume fraction, increases the scale of segregation.

Based on this previous literature, we developed a MATLAB script that takes an image file, processes it, and then calculates S. First, for a mixture of two phases, A and B, that are immiscible, the volume fraction at any point of A will be a and of B will be b. Also, for the entire mixture, $\bar{a}$ and $\bar{b}$ are the average concentrations for A and B, respectively. Thus,

$$a + b = 1 \text{ and } \bar{a} + \bar{b} = 1. \tag{4.1}$$

If the concentration of phase A or B is measured at two points a distance r apart, the difference in concentration at each point from mean can be multiplied together,

$$(a_1 - \bar{a})(a_2 - \bar{a}) \text{ or } \left(b_1 - \bar{b}\right)\left(b_2 - \bar{b}\right) , \tag{4.2}$$

and for a large number, N, of pairs the average deviation from mean phase concentration at any distance r is

$$\overline{(a_1 - \bar{a})(a_2 - \bar{a})} \text{ or } \overline{\left(b_1 - \bar{b}\right)\left(b_2 - \bar{b}\right)}. \tag{4.3}$$

The coefficient of correlation can then be found by dividing the average deviation from mean at any point r by the average square deviation of the entire mixture. Thus, the coefficient of correlation

$$R(r) = \frac{\overline{(a_1 - \bar{a})(a_2 - \bar{a})}}{\overline{(a - \bar{a})^2}} = \frac{\overline{\left(b_1 - \bar{b}\right)\left(b_2 - \bar{b}\right)}}{\overline{\left(b - \bar{b}\right)}^2} \tag{4.4}$$

is the statistical likelihood that any two points a distance r apart are both in the same phase. $R(r)$ will equal any value between 0 to 1 for infinitely small sample volume, perfectly random mixing, and no long range order (values greater than 1 or less than 0 indicate one or more of these assumptions are incorrect). Because B_4C and SiC have a finite particle size, which is sufficiently larger than our sample volume (pixel size), our mixture will act like an immiscible liquid with discrete boundaries between phases and with concentrations at any point equal to 0 or 1, fully B_4C or SiC.

An interesting feature of correlograms is their ability to quickly determine the size and distribution of clumps (even for irregular shapes) as demonstrated in

Figure 4.3. For a unimodal distribution, Figure 4.3A, the x-intercept of the correlogram will equal 1 due to the r/d relationship. In a bimodal distribution, Figure 4.3B, the elbow point occurs at an x value equal to the diameter ratio of the two inclusion sizes (eg. for this case x_{elbow} is 0.125 for inclusions with a diameter of 1/8 that of the larger inclusions) and the x-intercept relates to the larger inclusions.

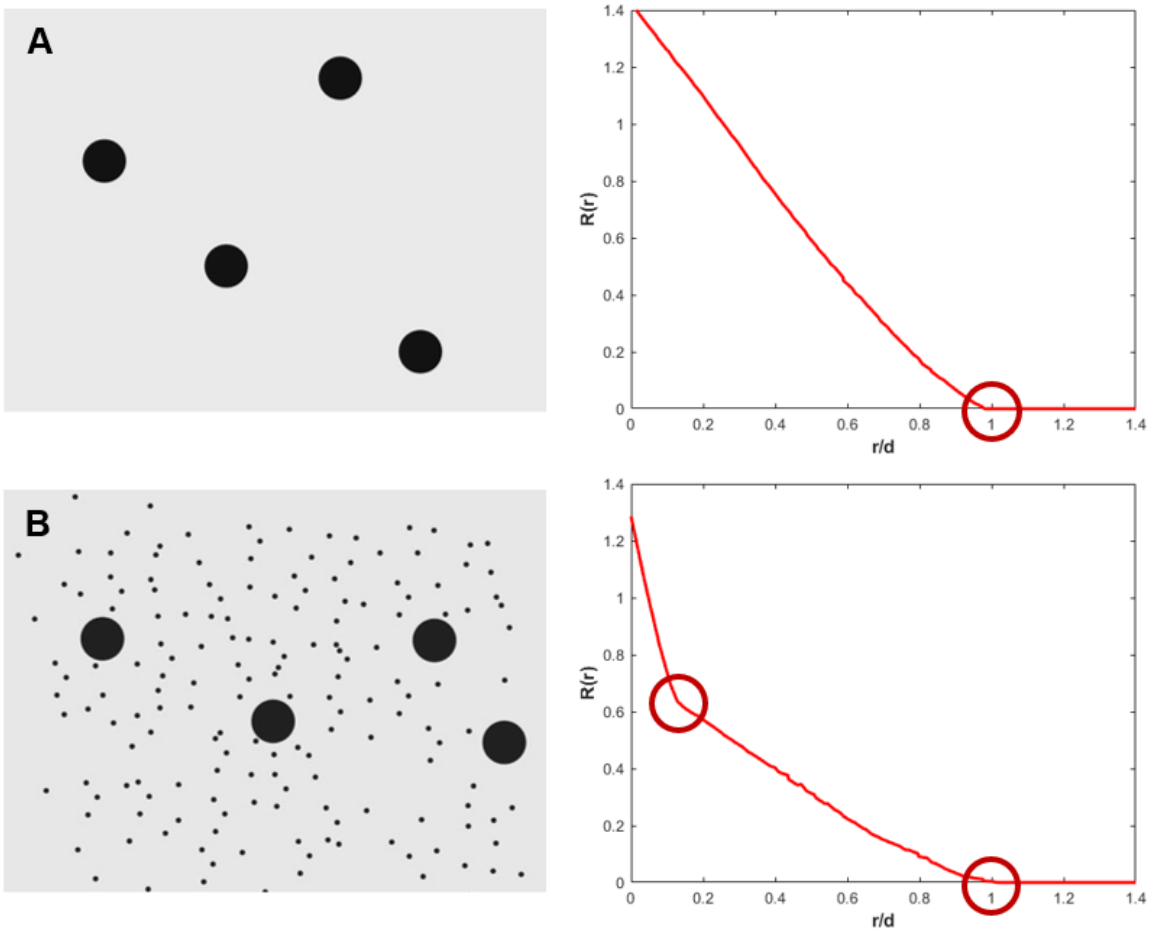

Figure 4.3. The x-intercept and elbow features of the correlogram relate to inclusion size and distribution. A) In a unimodal distribution, the x-intercept of the correlogram will equal 1 due to the r/d relationship. B) In a bimodal distribution, the slope of the first section intersects at an r/d ratio equal to the diameter ratio of the two inclusion sizes and the x-intercept relates to the larger inclusions.

The scale of segregation, S, can then be found by integrating over all values r

$$S = \int_0^{\infty} R(r)dr \ , \tag{4.5}$$

where ∞ can be approximated as equal to the largest clump or inclusion.

4.2.10. Hardness Testing

Knoop indentation was performed using a Wilson VH3100 automatic hardness tester (Buehler, Lake Bluff, IL). Indents were made at 2 kgf with a 10 s dwell and at sufficient spacing according to the ASTM C1326-13 standard [203]. An automatic grid pattern was used to create indents on the polished cross-sections of the discrete and continuous specimens. A 3×10 grid was used for the discrete specimen, with 10 indents each in the B_4C, SiC, and B_4C-SiC interface regions. A 5×36 grid was used for the continuous specimen, which allowed for 36 sampling locations of 5 measurements each along the build direction. Hardness data for the continuous specimen is reported as a function of distance along the build direction, starting from the B_4C-rich portion of the specimen.

4.3. Results and Discussion

4.3.1. DIW System Calibration

Communication between the Taz 6, which controls the print head, and the feed system is achieved using the I2C serial communication protocol. This provides a simple, yet effective, method for synchronizing the feed system and print head behavior via G-code, including the custom 'R' identifier to command feed ratio changes. Thus, for any point in 3-D space, the Taz 6 and feed system

can communicate to adjust print speed, feed rate, and material composition. Mixing of the two ceramic inks requires a finite volume of material between the ends of the feed tubes and the nozzle tip, which results in a lag time between composition changes. Figure 4.4 demonstrates the lag time between when a composition change is commanded and the actual change in composition of extruded material. A lag volume of 3.2 cm^3 was calculated by measuring the trace length required to fully change material color following a commanded change. During composition changes, the calculated lag volume is purged.

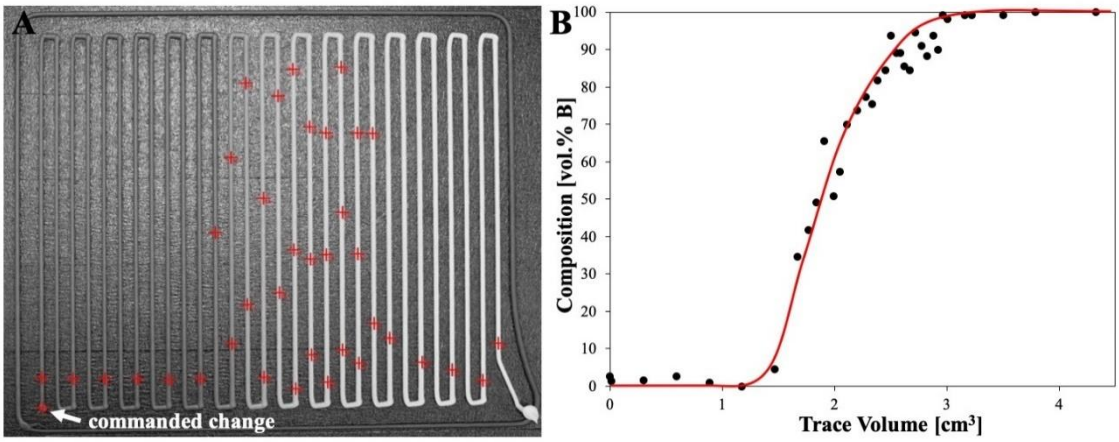

Figure 4.4. (A) A single zig-zag trace was extruded to demonstrate composition adjustment in real-time. The composition was changed from 100% A (dark Play-Doh) to 100% B (light Play-Doh) at 'commanded change' point. (B) Gray-scale values were used to calculate composition values along the zig-zag, which were converted to volume by assuming a cylindrical geometry of diameter 1.2 mm. Play-Doh was used for this experiment because it provides higher optical contrast than carbide ink.

4.3.2. Ink Rheology and Printability

Ink formulations were developed with the goal of matching ceramic content and flow behavior across relevant shear rate regimes in order to maintain an optimal balance between printability and sinterability. High printability is defined by minimal slumping, which improves shape retention, and consistent

extrusion. Increasing ceramic content and decreasing binder content improves the green density of printed parts, resulting in higher sinterability. Similarly, high surface area ceramic powder promotes densification during sintering but reduces printability.

Ink formulations used for printing the monolithic B_4C, monolithic SiC, and blended B_4C-SiC parts are reported in Table 4.1., with optimal solids-loadings of 56 and 50 vol.%, respectively. Differences in powder morphology and surface chemistry between B_4C and SiC led to the difference in optimal solids-loading; the smaller SiC particle size of approximately 0.7 µm (compared to approximately 0.8 µm for the B_4C powder) leads to a higher influence of Van Der Waals forces, resulting in a greater tendency of soft agglomerate formation. Soft agglomerates increase viscosity and cause clogging.

Table 4.1. Ink formulations used for DIW of monolithic B4C, monolithic SiC, and blended B4C-SiC parts.

Ink Type	Ceramic Powder (vol.%)	PEI (vol.%)	HCl (vol.%)	Water (vol.%)	Methylcellulose (vol.%)
SiC	50.00	3.00	-	46.51	0.49
B_4C	56.00	3.79	5.00	34.86	0.35

Monolithic B_4C, monolithic SiC, and blended parts were produced using the custom DIW system. Studied compositions were B_4C, $0.75B_4C$-0.25SiC, $0.5B_4C$-0.5SiC, and SiC. Figure 4.5 highlights two competing factors, feature definition versus void filling. Traces of SiC ink slump due to lower ceramic content, and therefore viscosity. Slumping leads to the filling in of voids and other defects resulting from the printing process. Traces of B_4C ink retain their

shape better due to higher ceramic content and viscosity. However, better definition results in defects (voids and line-gaps) that persist due to minimal slumping. Additional printing defects (skin drag and over-extrusion) can be seen in the SiC and blended parts due to less precise processing control, a function of the lower ink viscosity, which leads to nozzle leakage. Leakage results in successive build-up of layer height, which produces skin drag defects due to the nozzle tip interacting with the semi-solid part surface. Ink development towards an optimal compromise between slumping and shape-retainment will enable production of complex parts.

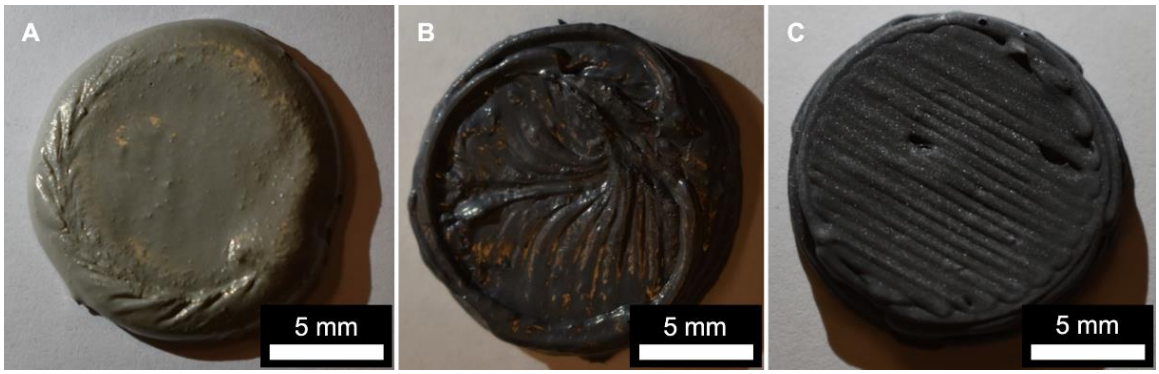

Figure 4.5. Green bodies with three notable compositions, (A) SiC, (B) 0.5B_4C-0.5SiC, and (C) B_4C, were formed via DIW. Solids-loading increases from left to right, with B_4C and SiC inks containing 56 and 50 vol.% ceramic powder, respectively.

A SEM micrograph of the cross-section of a green extruded filament is presented in Figure 4.6, with EDS performed at three spots of interest, (1) a light inclusion, (2) a dark inclusion, and (3) the gray matrix. The nominal composition, as input into the print head, is 0.5B_4C-0.5SiC. High-shear mixing occurs in-line via the auger, located inside the print head. From EDS data, the light inclusion can be determined as a SiC agglomerate, the dark inclusion can be determined

as B_4C, and the gray matrix as a fine-scale mixture of B_4C and SiC. Several pores can be observed and are due to air-entrapment during the process of loading ink into the feed system. These findings indicate that mixing is not complete and higher shear is needed to disperse B_4C and SiC particles homogenously.

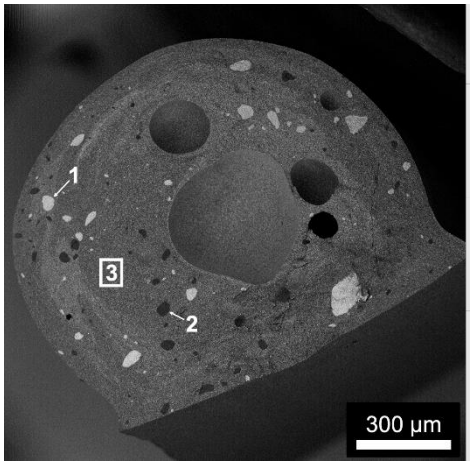

	Element
Spot 1	Si
	C
	O
Spot 2	B
	C
	O
Spot 3	B
	Si
	C
	O

Figure 4.6. SEM micrograph showing a cross-section of green extruded filament with a nominal composition of $0.5B_4C$-0.5SiC. Elements detected through EDS analysis are presented for three spots of interest.

To determine bulk composition of the $0.75B_4C$-0.25SiC and $0.5B_4C$-0.5SiC samples, diffraction patterns were analyzed by Rietveld refinement with GSAS-II [204]. Starting values for the lattice constants and atomic positions for the 6-H [205], 15-R [206], and 4H [206] polytypes of silicon carbide along with boron carbide [207] were taken from respective references. The relative amounts of each phase, lattice constants, and sample displacement were refined to achieve weighted R values near 15% in both cases. Figure 4.7 presents the diffraction patterns of inline-mixed filaments along with the standard powder mixtures prepared at the same nominal compositions. Major phases are identified with

colored symbols. Boron carbide contents were measured to be 61 and 68 ± 2 vol.% for the 50 and 75 vol.% nominal compositions, respectively. The observed variation from nominal compositions is likely a consequence of having used inks with different viscosity and compressibility, which will affect feed rates to the print head and mixing characteristics inside the print head. These effects are the motivation for changing to the final ink formulations used, shown in Table 4.2.

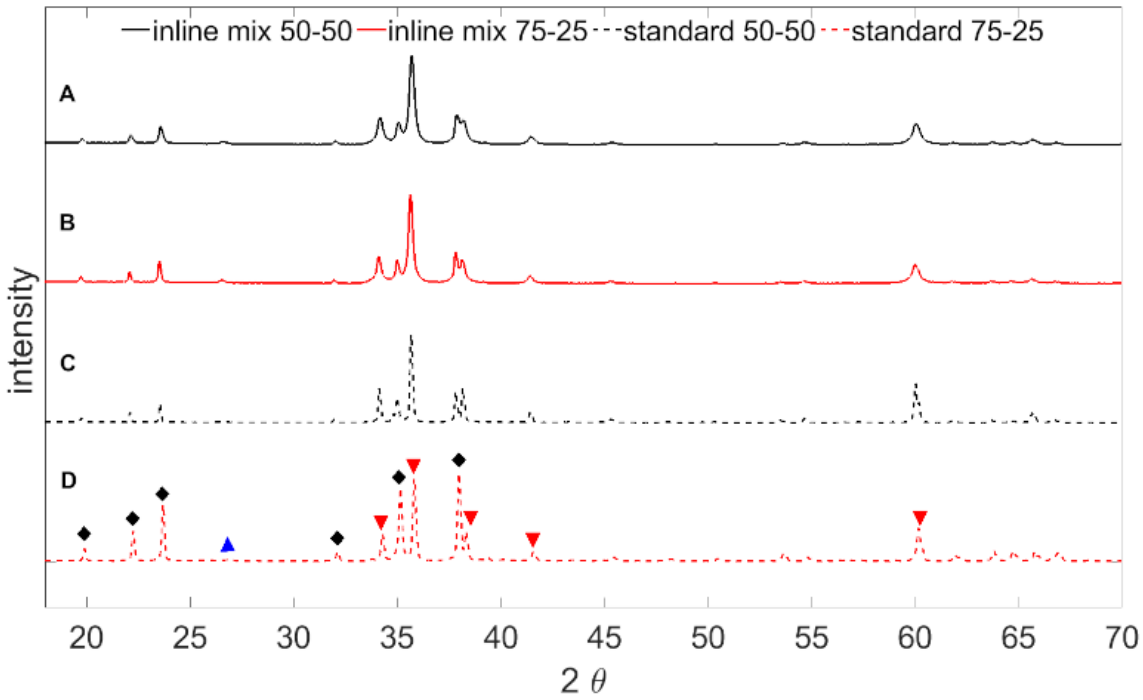

Figure 4.7. Collected diffraction patterns for in-line mixed and extruded green filaments with nominal compositions of (A) 0.50B_4C-0.5SiC and (B) 0.75B_4C-0.25SiC are compared with known standards for B_4C-SiC powder mixtures at (C) 0.5B_4C-0.5SiC and (D) 0.75B_4C-0.5SiC. Symbols correspond to (♦) boron carbide, (▲) graphitic carbon, and (▼) silicon carbide.

Ceramic powder and aqueous binder/dispersant systems were characterized to determine which combination would provide the highest stability colloidal dispersion. BET measured surface areas for B_4C and SiC powders were 11.23 and 12.55 m^2/g, respectively. The surface area values and ceramic

content were used to tailor various binder-dispersant systems. An exact binder-dispersant addition is necessary because colloid dispersion is improved until all particle surfaces are covered, with excess leading to pockets of agglomerated polymer that leave pores in sintered specimens. Polyethyleneimine (PEI) provided the most stable dispersion across a wide range of pH values for B_4C and SiC powders. Figure 4.8A shows a plot of Zeta potential versus pH for the B_4C-PEI and SiC-PEI systems. Through the addition of PEI, carbide powders show optimal dispersion effects, defined as a Zeta potential value above 30 mv (absolute), in a wide pH range of 2 – 8. Ink formulations with lower sensitivity to pH variation have greater flexibility during the simultaneous extrusion of multiple inks.

Optimal formulations for B_4C and SiC were developed by varying ceramic and MC content to enable desired printability and maintain high ceramic content. The viscosities of notable formulations are plotted against shear rate in Figure 4.8B to illustrate the effects of ceramic powder type and content and secondary binder content. All formulations show a significant decrease in viscosity with increasing shear rate, which is indicative of shear-thinning behavior. An increase from 47.5 to 50.0 vol.% ceramic content while holding methylcellulose content at 1.0 vol.% led to an increase in viscosity at all shear rates. Similarly, increasing the volume fraction of MC increased the viscosity at all shear rates. These relationships held true for all tested B_4C and SiC inks. SiC ink formulations at

equivalent ceramic and MC content showed higher viscosities at all shear rates as compared with B_4C inks.

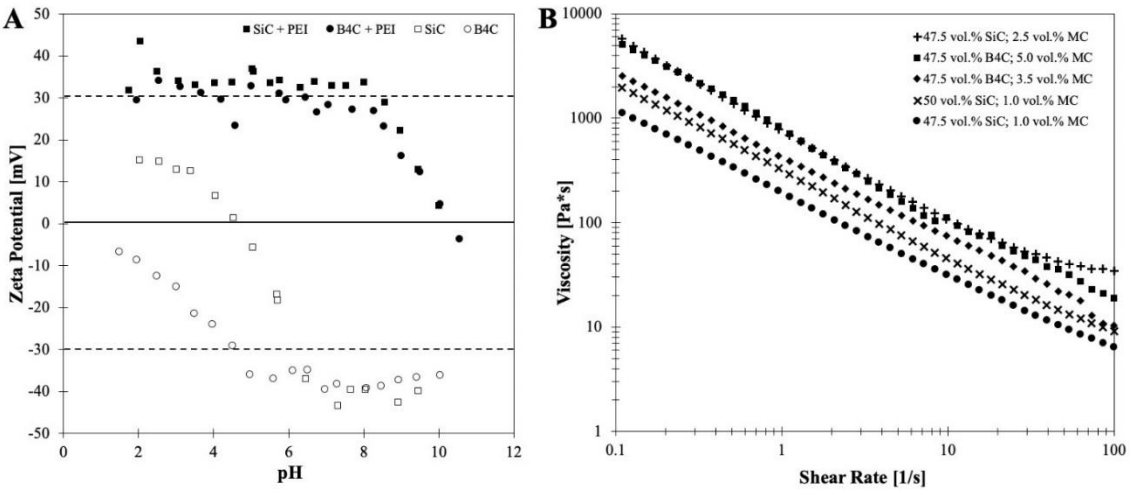

Figure 4.8. (A) A zeta potential plot demonstrating the stabilizing effect of PEI additions to B_4C and SiC powders. (B) Rheological curves of SiC and B_4C inks illustrate their yield-pseudoplastic behavior. Viscosity is matched for + and ■ formulations across a wide range of shear rates through the use of high viscosity methylcellulose.

Final ink formulations for B_4C and SiC are reported in Table 4.2., with ceramic content constant at 47.5 vol.% and MC contents of 5.0 and 2.5 vol.%, respectively. Differences in powder morphology and surface chemistry between B_4C and SiC led to the difference in optimal methylcellulose content; the smaller SiC particle size of approximately 0.7 µm (compared to approximately 0.8 µm for the B_4C powder) leads to a higher influence of Van Der Waals forces, resulting in a greater tendency of soft agglomerate formation. Soft agglomerates increase viscosity and cause clogging. Carbide ink formulations reported in Table 4.2. were tested for consistent extrusion, and all tested nozzle sizes (0.6-1.2 mm) passed without clogging.

Table 4.2. Final, optimized ink formulations used for direct ink writing of ceramic parts.

Ink Type	Ceramic Powder (vol.%)	PEI (vol.%)	HCl (vol.%)	Water (vol.%)	Methylcellulose (vol.%)
SiC	47.50	3.00	-	47.00	2.5
B_4C	47.50	3.79	5.00	38.71	5

Multi-phase carbide parts were fabricated with the custom DIW system using the final, optimal ink formulations. To verify the printability of formulated inks, single stacked traces were printed and their shape retention was studied by comparing the expected and measured height of the traces. Figure 4.9A highlights the shape retention capability of the B_4C ink, with less than 7% height loss from slumping for six stacked layers. As expected, because the flow behavior was matched, stacked traces printed with SiC ink show similar results with less than 9% height loss from slumping for six stacked layers. Stacked traces of a single wall thickness set the upper-bound for height loss due to their large aspect ratio. To verify the printability of two inks simultaneously, cylindrical parts were printed while changing composition along the build direction in real-time. Figure 4.9B shows the printing process for a discrete specimen, where composition is changed from pure B_4C to pure SiC and vise-versa, layer-by-layer. All specimens were printed at 100% infill using inside-out concentric patterns. Concentric infill was found to produce fewer defects than rectilinear patterns, where abrupt direction changes resulted in void formation between perimeter and infill traces. Cylinders of 25.4 mm diameter incorporating discrete and continuous composition variation were printed to nominal heights of 8.4 and 13.2

mm, respectively. After drying, the continuous specimen measured 12.87 mm in height, corresponding to a total height loss of 2.5%, and its external walls retained their vertical form. A similar height loss was measured for the discrete specimen.

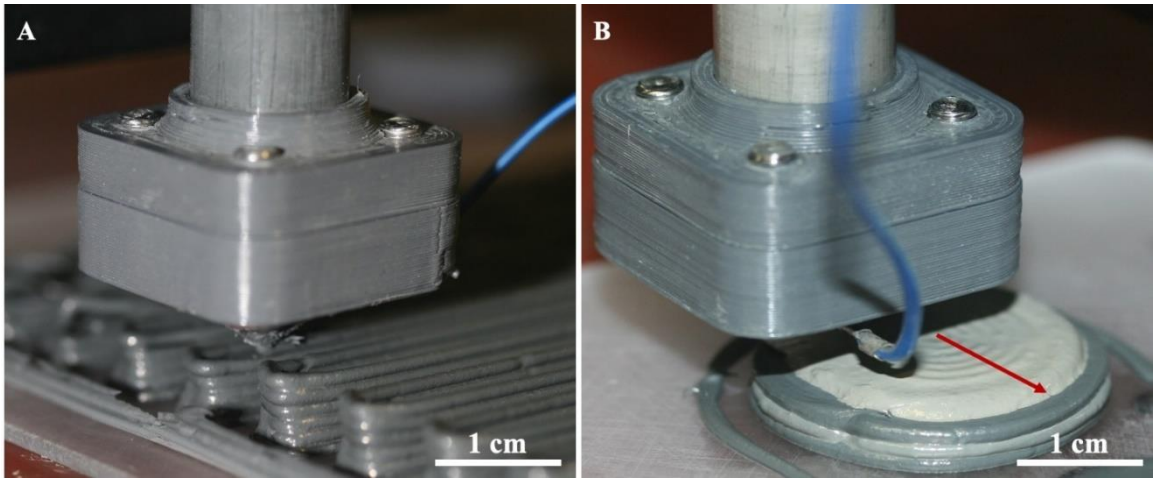

Figure 4.9. (A) Stacked traces printed from the optimized B_4C ink demonstrate good shape retention post-extrusion and indicate a sufficient yield stress. (B) Inside-out concentric infill patterns were found to reduce printing related defects over rectilinear infill patterns.

4.3.3. Green Body Characterization

SEM micrographs in Figure 4.10 highlight the mixedness of B_4C and SiC at the micro- and mesoscales in green blended parts formed via DIW. The swirling microstructure, an artifact of the in-line mixing process, results in layered B_4C-rich and SiC-rich matrix regions. A significant range in size of B_4C and SiC inclusions can be observed, likely due to variations in shear throughout the in-line mixing process. Dragging effects, indicated by swirl directionality, occur at layer interfaces (denoted by dotted lines). The printing direction, indicated by arrows, leads to the directionality of these dragging effects. Pores, seen as black circular regions, are the product of entrapped air in the ink. These micrographs show the

viability of AM for tailoring local structuring and composition. For example, inclusions in the hundreds of micrometer range can be positioned via extrusion of a drop of material, while smaller scale features can be controlled with composition gradients by in-line mixing.

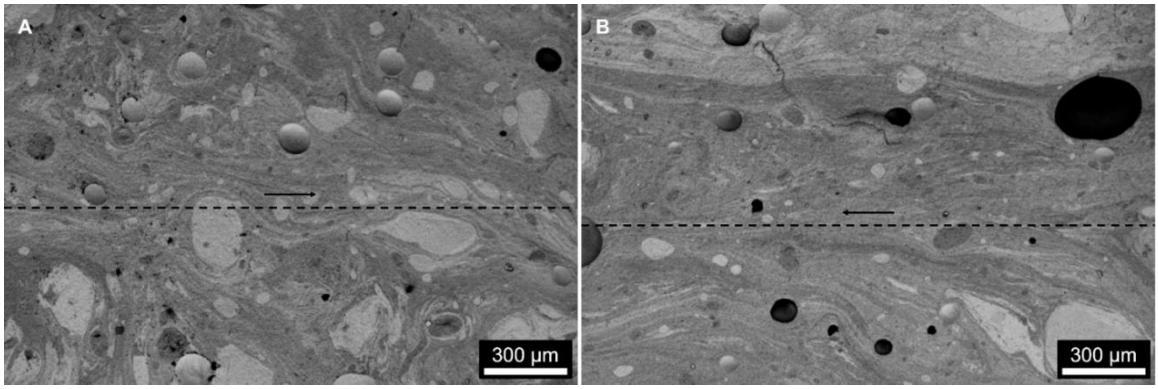

Figure 4.10. SEM micrographs showing representative microstructures of green ceramic bodies formed via direct ink writing. Printed layers are oriented horizontally. Lighter regions are SiC-rich and darker regions are B_4C-rich. The nominal compositions are (A) $0.5B_4C$-0.5SiC and (B) $0.75B_4C$-0.25SiC. Arrows represent printing direction and dotted-lines represent layer interfaces.

To analyze the range in feature size in-line mixing produces, SEM micrographs of blended B_4C-SiC green bodies formed via DIW and in-line mixing were obtained with EDS overlays and are presented in Figure 4.11. Boron and silicon are indicated by purple and red colorations, respectively, and can be interpreted as B_4C and SiC. At the hundreds of micrometer scale, swirling B_4C-rich and SiC-rich features and B_4C and SiC inclusions are observed in Figure 4.11A-D. B_4C and SiC inclusions in the tens of micrometer range are seen in Figure 4.11E. Micrometer-scale particle-particle mixing is indicated by a homogenous distribution of dark and light particles in Figure 4.11F.

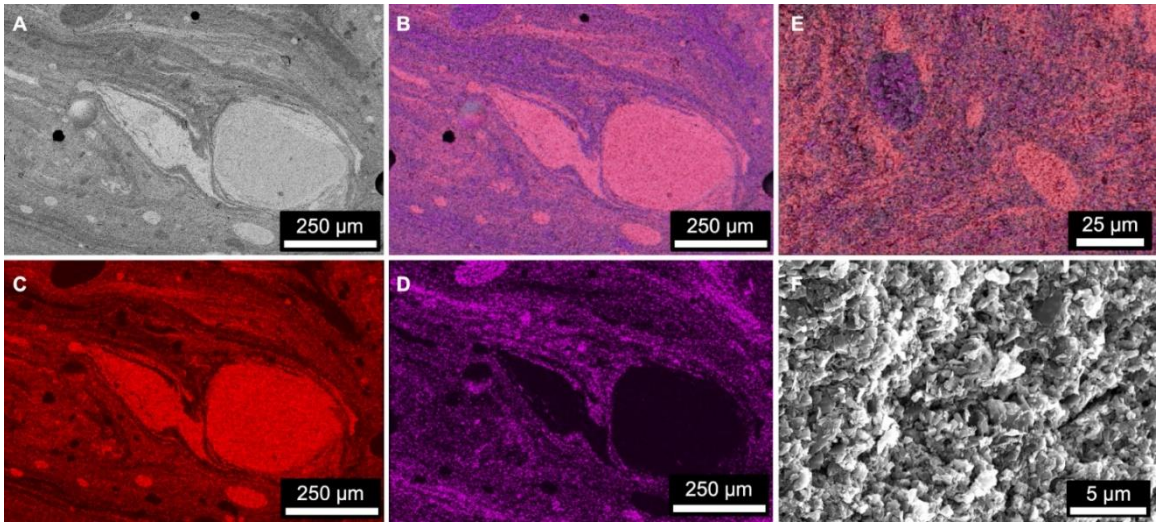

Figure 4.11. SEM micrographs of blended B_4C-SiC green bodies formed via direct ink writing and in-line mixing with EDS overlays. (A-D) Micrographs highlighting the B_4C-rich and SiC-rich swirling regions and 100^s of micrometer sized inclusions in a $0.75B_4C$-0.25SiC part. (C) Red coloration indicates silicon and (D) purple coloration indicates boron. (E) Micrograph of a $0.75B_4C$-0.25SiC part with spectral overlay highlighting 10^s of micrometer sized B_4C and SiC inclusions. (F) Micrograph of a $0.5B_4C$-0.5SiC part showing particle-particle mixing achieved in matrix regions.

4.3.4. Pressureless Sintering Trials and Densities

Past studies have concluded that sintering-aids and/or field-assisted sintering techniques are needed to produce fully dense B_4C and SiC specimens [17,37,208]. With this in mind, our goal is to explore the viability of sintering printed specimens without applied pressure to allow complex geometries. Furthermore, if specimens can be sintered to achieve closed porosity, a secondary step utilizing hot isostatic pressing (HIP) should result in fully dense specimens [17]. A preliminary sintering study was conducted on a monolithic part formed via DIW using a B_4C ink without methyl cellulose, with the goal of maximizing ceramic content and minimizing binder content. Microstructural characterization of this specimen, shown in Figure 4.12, demonstrates the feasibility of sintering parts formed via direct ink writing ceramic inks. Sintering

performed at 2250ºC in a flowing argon atmosphere with no sintering additives, applied pressure, or field-assisted techniques, resulted in a theoretical density of 92.6% and closed porosity. There appears to be intimate bonding of printed traces and no observable artifacts of the DIW process, which suggests these printed parts will show similar properties as parts made from other powder-processing techniques.

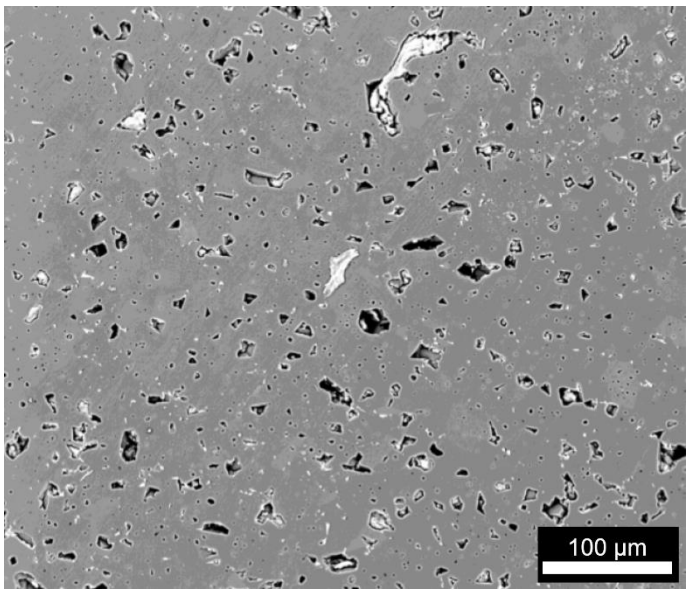

Figure 4.12. SEM micrograph of a post-processed monolithic B_4C part formulated without methyl cellulose and produced via direct ink writing. Sintering was performed without applied pressure or sintering additives at 2250ºC and resulted in a theoretical density of 92.63%.

Subsequent pressureless sintering results are reported for specimens produced from inks formulated with methylcellulose for increased printability. As hypothesized, lower densities are achieved due to higher binder content. A sintering temperature of 2250ºC led to theoretical densities of 87.0% and 74.2% for B_4C and SiC parts, respectively. A major contributor to this difference in density is the lower solids-loading in the SiC ink, 50 vol.% compared to 56 vol.%

in the B_4C ink. The variation in density, again, highlights the importance of a high volume fraction of ceramic powder and low binder content. It was not possible to determine the densities of blended specimens sintered at 2250ºC, because they were extremely porous and fragile. A SEM micrograph of a 0.5B_4C-0.5SiC part with EDS point analysis is shown in Figure 4.13. Elements identified at points 1, 2, 3, and 4 indicate the presence of large, faceted graphite grains as well as a second carbon-rich phase in addition to the expected silicon carbide and boron carbide. In their study of the eutectic, Shaffer et al. [30] also reported the presence of well-formed graphite crystals for a composition of 0.7B_4C-0.3SiC sintered above 2245ºC. Thus, it is likely a significant volume of eutectic liquid formed during sintering, which resulted in these fragile, high-porosity specimens.

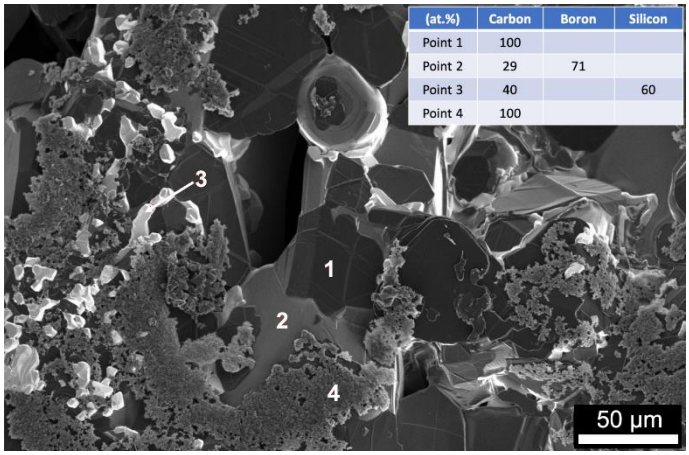

Figure 4.13. SEM micrograph of a 0.5B_4C-0.5SiC part formed via direct ink writing. Sintering performed without applied pressure or sintering additives at 2250ºC resulted in highly porous specimens. EDS analysis at points 1, 2, 3, and 4 indicates the presence of graphite, boron carbide, silicon carbide, and amorphous carbon, respectively.

A lower temperature of 2150ºC was used in the following sintering trial to avoid the formation of a eutectic liquid phase. This lower sintering temperature resulted in theoretical densities of 89.6%, 83.8%, 89.0%, and 73.8% for B_4C,

0.75B_4C-0.25SiC, 0.5B_4C-0.5SiC, and SiC, respectively. While the lower temperature successfully avoided liquid phase formation, overall closed porosity was not achieved. The 2245ºC eutectic in the B_4C-SiC system effectively caps the range of suitable sintering temperatures for development of dense microstructures; sintering at successively higher temperatures is not a viable route for attainment of full density specimens. Instead, further ink optimization, sintering additives, and/or field-assisted sintering techniques must be used to realize fully dense B_4C, SiC, and blended parts formed through DIW.

4.3.5. Characterization of Hot-Pressed Specimens

The discrete and continuous specimens were fabricated using the ink formulations in Table 4.2. Macro specimen images in Figure 4.14 demonstrate the novel multi-material capabilities of the custom DIW system, which uses active in-line mixing to tailor composition in real-time to any ratio of the two feed inks. Continuous and discrete specimens are shown in Figure 4.14 in (A, C) green and (B, D) sintered states. In the green state, visually, B_4C shows up as dark gray and SiC shows up as tan. Figure 4.14A shows the gradual transition in composition from B_4C (bottom layer) to SiC (top layer), whereas Figure 4.14C shows discrete compositional changes layer to layer. Through the use of a humidity chamber, no drying-induced warpage or cracking was observed in the green specimens. No macroscopic pores were observed in the cross-sections of the dense parts. Based on the rule of mixtures of expected material feed during printing, densities of 99.2% and 98.6% of the theoretical value were calculated

for the continuous and discrete B_4C-SiC specimens, respectively. The absence of macroscopic pores and ~50% linear shrinkage resulting from hot pressing indicate near full density and validate theoretical density calculations.

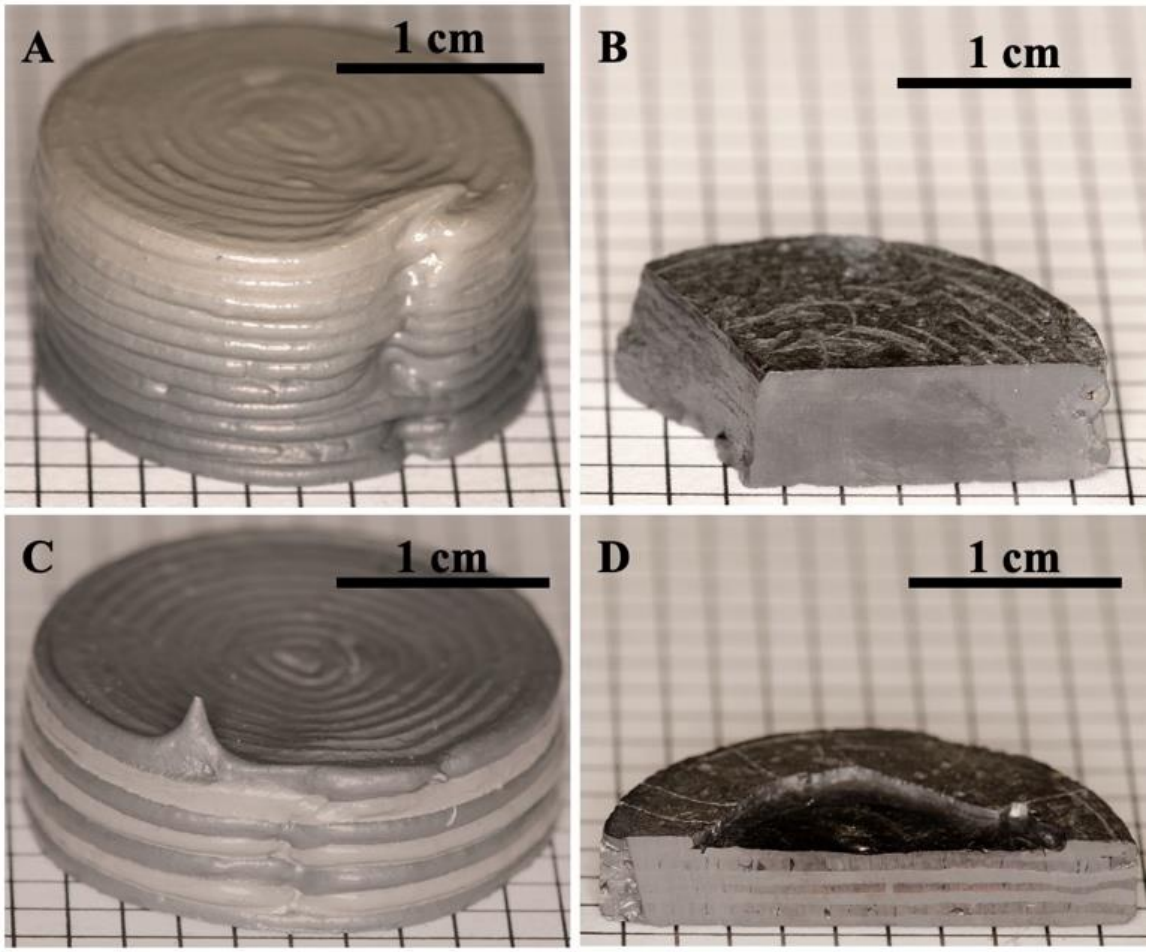

Figure 4.14. A continuous carbide ceramic specimen produced via DIW in its (A) green and (B) sintered states. A discrete carbide ceramic specimen produced via DIW in its (C) green and (D) sintered states. Unidirectional shrinkages of approximately 50% in the build direction (bottom to top) resulted from the hot pressing process. Light and dark materials are SiC and B_4C, respectively.

SEM micrographs of the cross-section of the discrete B_4C-SiC specimen in the sintered state are shown in Figure 4.15. Micrographs were taken using the backscatter detector to highlight elemental contrast. B_4C and SiC phases show

up as dark and light regions, respectively. B_4C and SiC layers were measured to be 549±102 and 526±95 micrometers, respectively. B_4C and SiC inclusions, dark and light spots, range in size from tens to hundreds of micrometers. These inclusions are the product of soft agglomerates that were not completely dispersed during in-line mixing of the ceramic inks. Printing pure SiC or B_4C is not possible as there will always be residual material inside the barrel and nozzle following a ratio change. Therefore, SiC layers are actually SiC-rich matrix regions with many pure SiC inclusions and a few pure B_4C inclusions. Similarly, B_4C layers are B_4C-rich matrix regions with many pure B_4C inclusions and a few pure SiC inclusions.

Significant cracking seen in B_4C layers is likely due to the thermal expansion mismatch between B_4C ($5.5*10^{-6}$ K^{-1}) and SiC ($3.0*10^{-6}$ K^{-1}) [15]. These cracks occur preferentially within B_4C layers and are perpendicular to the interface. Cracks bifurcate and close as they traverse across layer interfaces into SiC layers. Interestingly, layer interfaces show good cohesiveness and no delamination is observed. The absence of cracking along layer interfaces may be the product of a limited amount of mixing that occurs between layers during the printing process. The small mixed zone, wherein the composition grades over a few micrometers, is shown in Figure 4.15B.

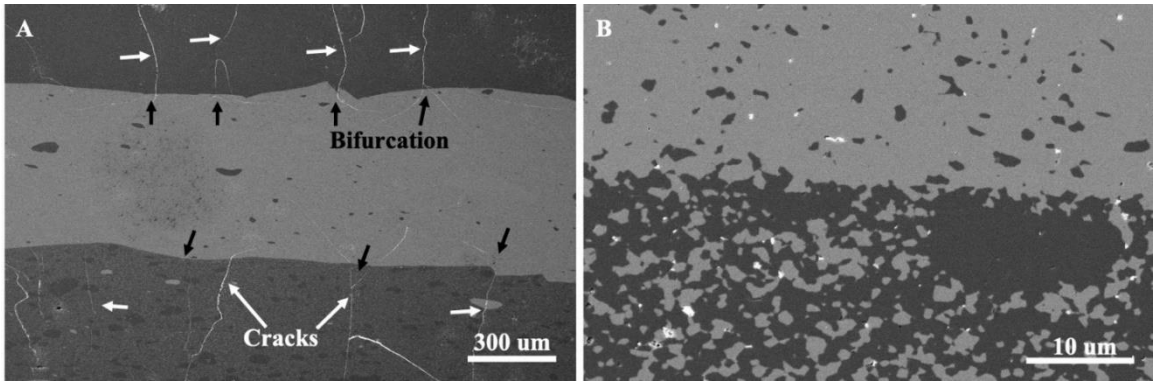

Figure 4.15. SEM micrographs of the discrete B_4C-SiC specimen produced via direct ink writing. Dark material is B_4C and light material is SiC. B_4C and SiC inclusions appear as dark and light spots, respectively. Significant cracking is observed in B_4C layers.

SEM micrographs of the continuous specimen are shown in Figure 4.16. In addition to the overall composition gradient, a gradient of inclusion distribution can be observed that follows the overall grading of composition. The number of B_4C and SiC inclusions decrease and increase, respectively, as the composition is graded from B_4C to SiC. White speckles seen in Figures 4.15B and 4.16B are intergranular porosity. Minimal cracking can be seen originating from the SiC-rich surface of the continuous specimen in Figure 4.16C. In contrast with the discrete specimen, the gradual composition change in the continuous specimen significantly reduced cracking. This finding is important in understanding how to tailor crack behavior and, ultimately, tune the fracture toughness of carbide materials through functional grading.

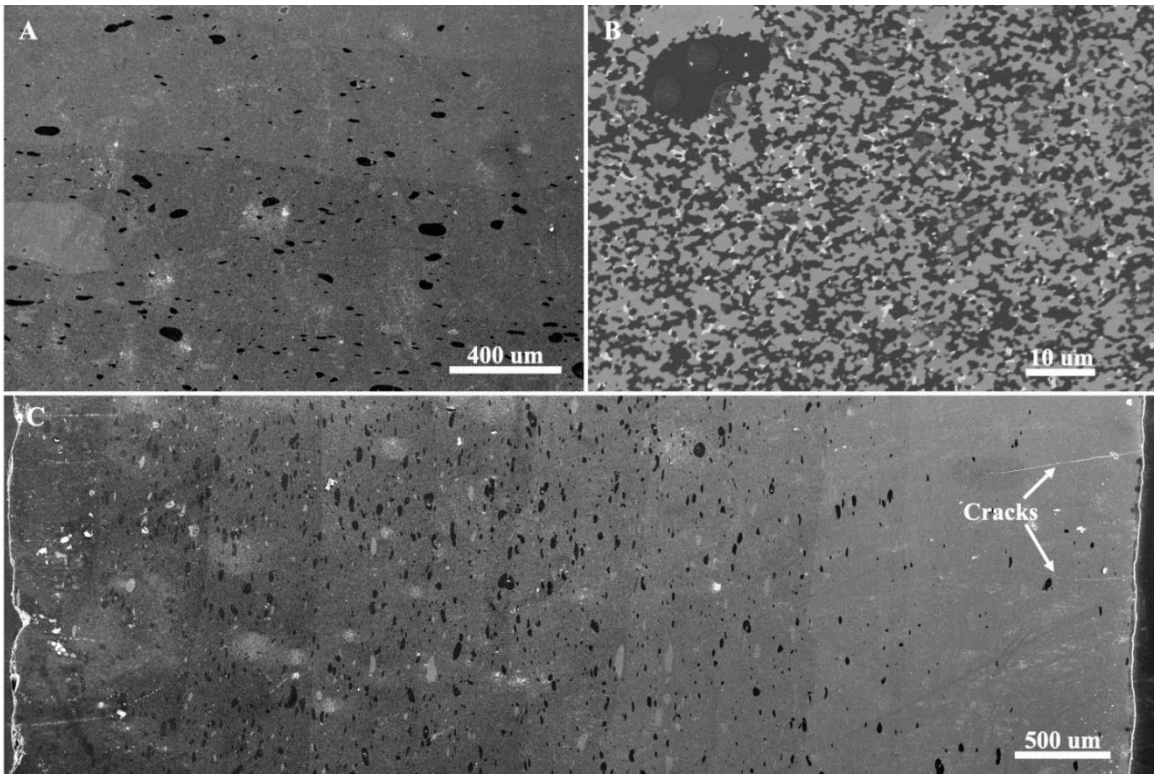

Figure 4.16. SEM micrographs of the continuous B_4C-SiC specimen produced via direct ink writing. Dark material is B_4C and light material is SiC. B_4C and SiC inclusions appear as dark and light spots, respectively. It should be noted that micrograph (C) has been rotated clockwise 90° with respect to all other micrographs, which orients its build direction from left to right.

4.3.6. Scale of Segregation Analysis

Scale of segregation analysis was performed on blended 50/50 specimens prepared using augers with parameters pitch and channel depth varied. The ink formulation history of each specimen was also tracked. The specimens in this study contained a mixture of B_4C and SiC and are characterized through scanning electron micrographs. To determine the scale of segregation, five SEM images were captured at high-resolution, a magnification of 150X, 10V, and 3.2 nA to produce images with sufficient phase contrast and pixel size greater than ten times the grain size. During image processing, a thresholding algorithm

developed by Otsu [209] was used to binarize micrographs into white (pixel value = 1) for SiC and black (pixel value = 0) for B_4C. The scale was set knowing the magnification and image resolution and the SEM parameter bar was removed. Figure 4.17 shows (a) raw and (b) post-processed binary images.

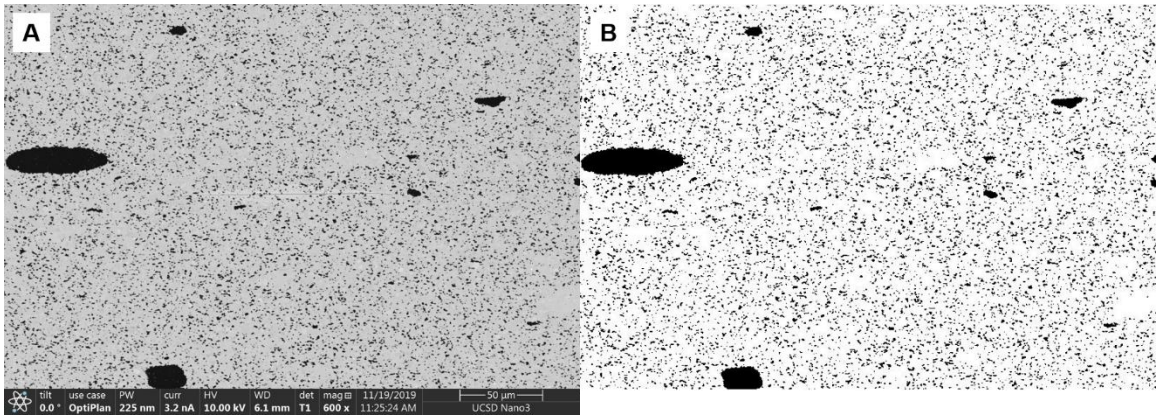

Figure 4.17. A) Raw SEM image captured at high-resolution, a magnification of 150X, a voltage of 10V, and current of 3.2 nA. B) Post-processed image where all pixels are binarized into white (pixel value = 1) for SiC and black (pixel value = 0) for B4C.

Post-processed images were analyzed using a custom MATLAB script developed for this study. The script uses an algorithm to randomly select N 'center pixels' and store their compositions. Then, branching out in directions of 0, 45, 90, 135, 180, 225, 270, and 315 degrees, store the compositions of each pixel along the eight paths to correlate their composition to the center pixels. Thus, for each image, eight correlograms are created based on each direction and then averaged to determine a final correlogram. The scale of segregation is then calculated by integrating over the averaged correlogram. The number of center pixels, N, used was 300,000 to determine a statistically significant S. The maximum distance r each center pixel was correlated to was determined experimentally to be 80 micrometers to sufficiently capture the largest inclusion

sizes for the specimens characterized in this study. Figure 4.18 demonstrates the two-point correlation algorithm developed for this study. A center pixel is randomly chosen, Figure 4.18A, and the compositions of pixels along eight directions are correlated to the composition of the center pixel. This process is repeated 300,000 times, Figure 4.18B, to create a statistically significant correlogram that can be used to determine the scale of segregation.

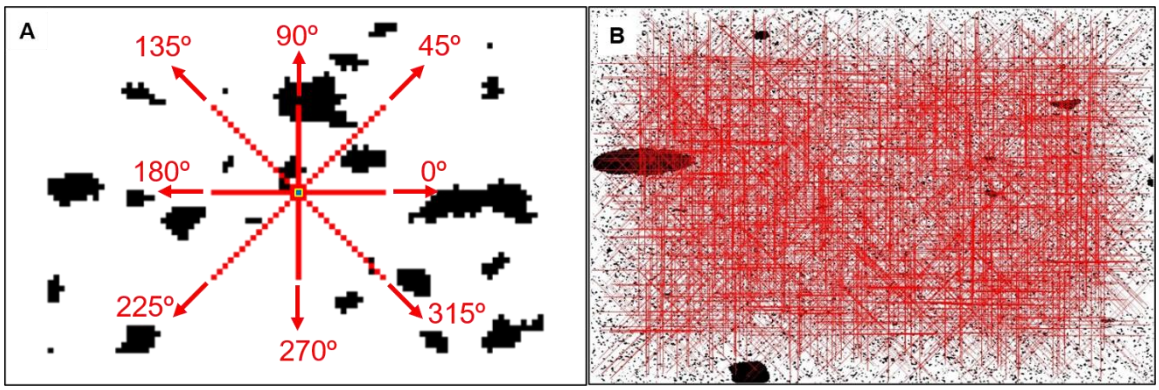

Figure 4.18. A) The center pixel location (blue with yellow border) is chosen randomly and then the composition of pixels around it are correlated in eight branching directions. B) A large number of center pixels are used to create a statistically significant correlogram.

The correlogram for this example is shown in Figure 4.19. The scale of segregation is equal to 1.3820. Interestingly, if the plot is cropped to show values of r only up to 3 um, the elbow is near 1 um, which is approximately equal to the particle size. The x-intercept of the tail represents the largest inclusions.

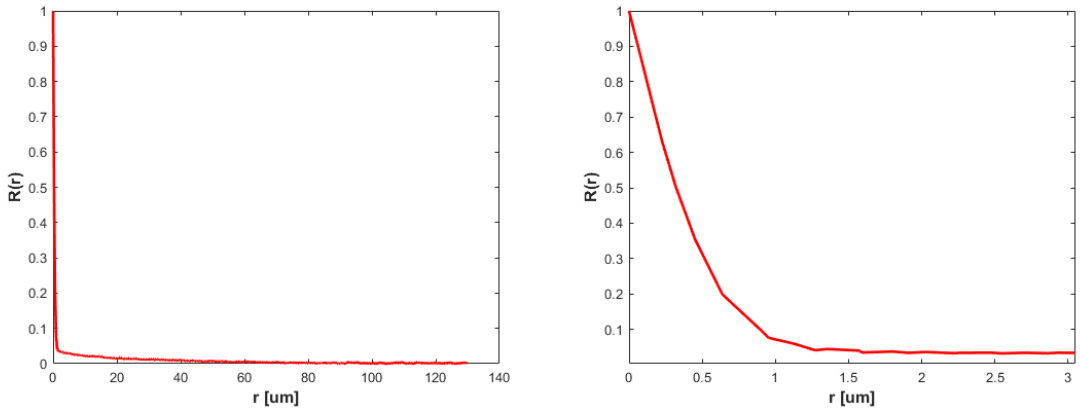

Figure 4.19. A correlogram (left) and cropped view (right) for the example micrograph in Figures 4.17 and 4.18. The elbow region represents the particle size, while the x-intercept of the tail represents the largest inclusions

Using scale of segregation analysis, we determined relationships between auger parameters, ink formulation, and processing parameters with the 'goodness of mixing', which is inversely proportional to inclusion size and content. This analysis enables a rapid throughput method of process-structure characterization based on electron micrographs of sintered specimens. Further, microstructural features such as grain size and phase volume fraction were elucidated by this analysis.

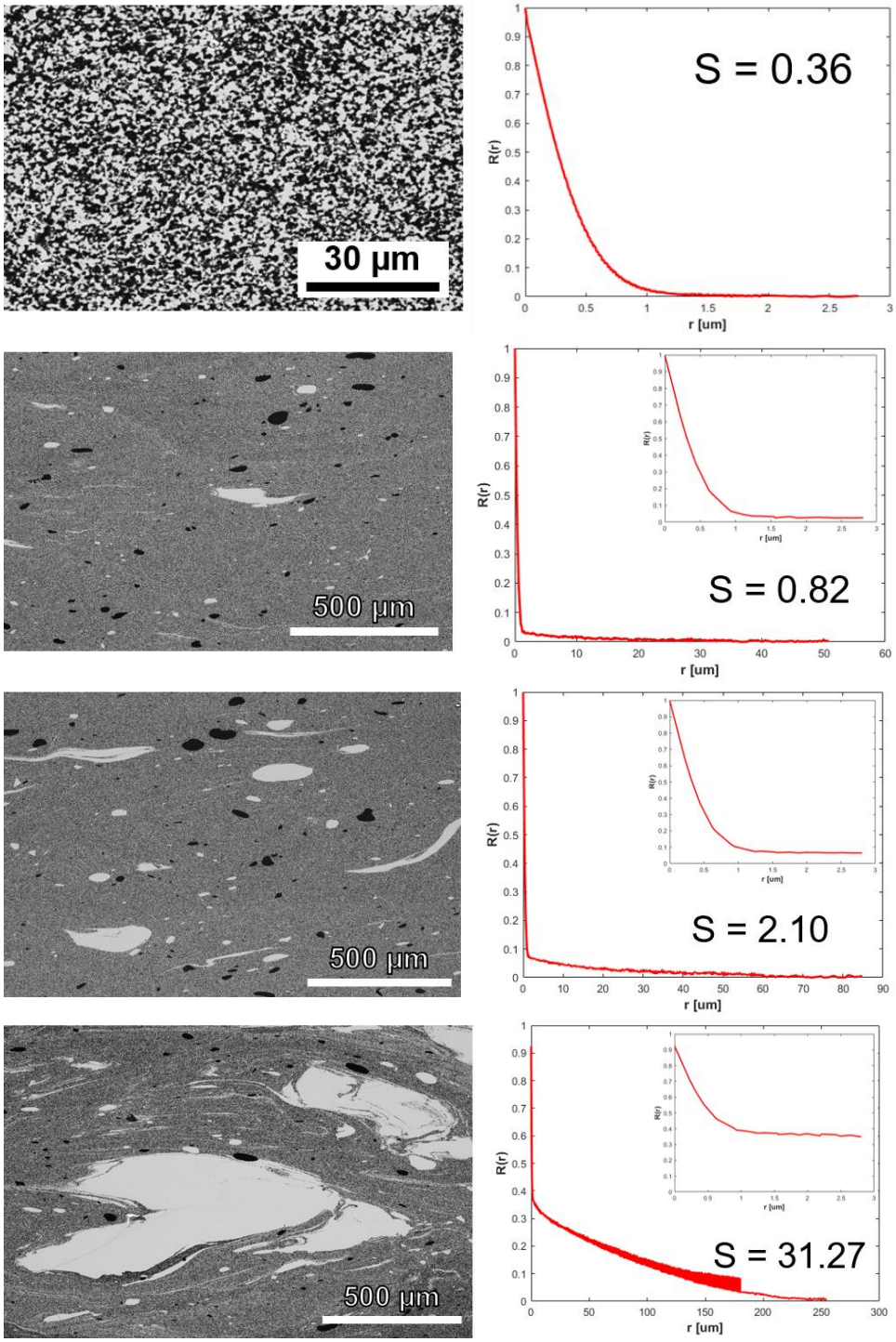

Figure 4.20. Four multi-phase carbide microstructures developed using the auger mixing print head at different printing parameters and ink formulation history.

Auger parameters pitch and channel depth were not found to have a significant effect on S, while ink formulation history had a major effect. Augers with parameters channel pitch and depth were used to print blended 50/50 specimens.

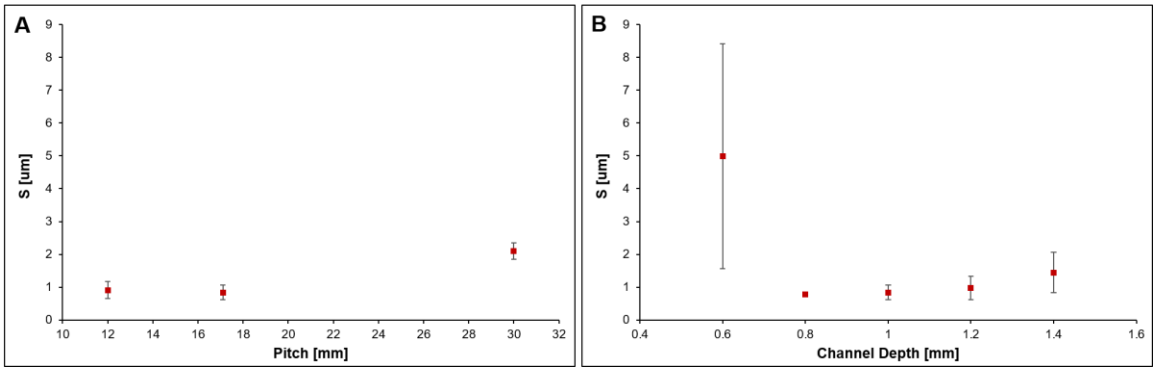

Figure 4.21. The effect of a) auger pitch and b) auger channel depth on the scale of segregation in blended 50/50 specimens.

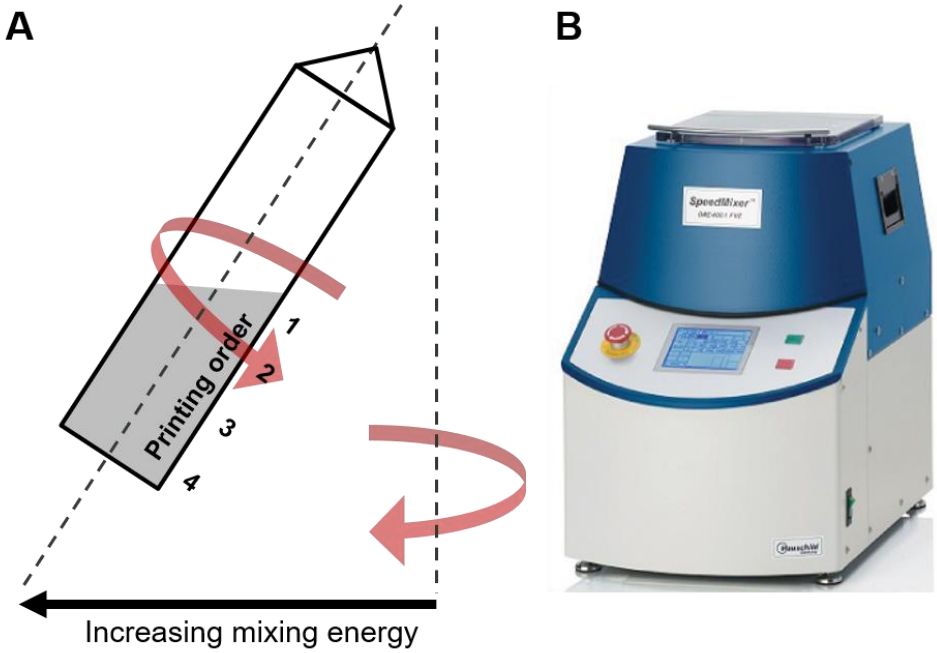

Figure 4.22. A) Printed components will include ink from different regions with in the syringe, where the ink at the bottom of the syringe will experience greater shear forces during the mixing process. B) The Flack Tek SpeedMixer is a dual-asymmetric centrifuge mixer that imparts high shear forces on mixtures without the need for contact, through mixing blades or otherwise, with the mixture.

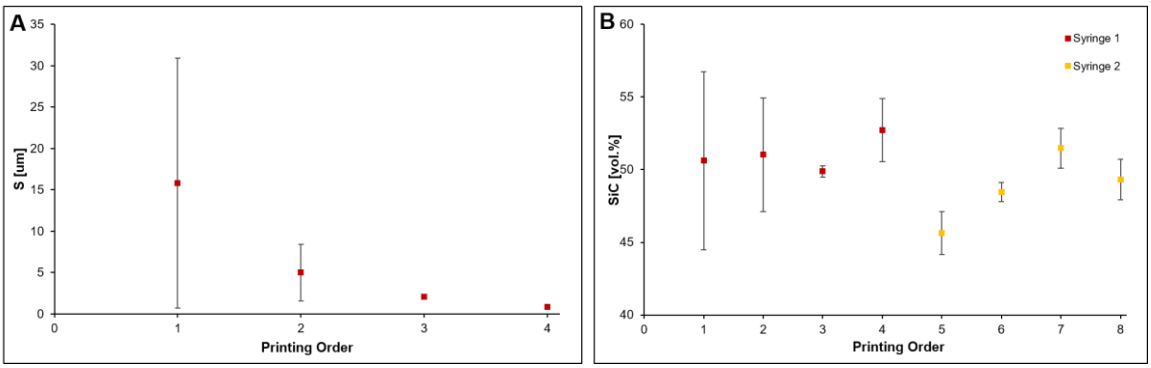

Figure 4.23. A) The ink formulation history, including the location of the material within the mixing vessel and length of time between formulation and printing, has a significant effect on the scale of segregation within the printed components. B) The overall composition of all specimens falls within ± 5 vol.% of the commanded composition of 50 vol.% SiC.

4.3.7. Analysis of Stress and Crack Formation due to Coefficient of Thermal Expansion Mismatch

An analytical discussion of the mechanisms underlying the cracking seen in the discrete specimen is performed to provide a framework to inform future design of heterogenous parts with controlled residual stresses (σ_r) and fracture behavior. The approach used here follows one discussed by Meyers et al. [210], who evaluated two stress release mechanisms for Ti6Al4V-Al_3Ti laminate composites. First, creep can relieve residual stresses at temperatures above approximately half a material's melting temperature (T_m). Second, crack propagation relieves stresses below ~0.5T_m as materials, generally, have higher fracture toughness at elevated temperatures above. Thus, creep is the dominant mechanism above ~0.5T_m and crack propagation is the dominant mechanism below ~0.5T_m.

For ceramic materials, such as B_4C and SiC, creep occurs above the 'joining' temperature (T_j) and is assumed to release all σ_r generated above this

temperature [211]. Creep becomes inactive as temperature drops below T_j. With this in mind, when calculating the residual stresses from coefficient of thermal expansion (CTE) mismatch, a zero-stress state is assumed for temperatures above T_j and that cracking is the dominant mechanism at temperatures less than T_j. The residual stresses of a layered composite with finite thickness and alternating brittle layers (of potentially different thickness) are:

$$\sigma_{r1} = \frac{E_1' E_2' f_2 (\alpha_2 - \alpha_1) \Delta T}{E_1' f_1 + E_2' f_2} \text{ and} \tag{4.6}$$

$$\sigma_{r2} = \frac{E_1' E_2' f_1 (\alpha_1 - \alpha_2) \Delta T}{E_1' f_1 + E_2' f_2}, \tag{4.7}$$

where $E_i' = E_i/(1-\upsilon_i)$, $f_1 = \frac{l_1(N+1)}{2h}$, $f_2 = \frac{l_2(N-1)}{2h}$, E_i and υ_i are the elastic modulus and Poisson's ratio of component i, l_i is the layer thickness of component i, α_i is the CTE of component i, ΔT is the difference between T_j and ambient temperature, N is the total number of layers, and h is the total specimen height. B_4C and SiC are defined as component 1 and 2, respectively, T_j is equal to the sintering temperature of 1950ºC, ambient temperature is 25ºC, and N is 7. Figure 4.24A defines relevant parameters used in this analysis and is simplified to only show one full B_4C layer and two partial SiC layers. The material properties used for the residual stress calculations of B_4C and SiC layers are shown in Table 4.3. The above equations and material properties are adapted from work by Orlovskaya et al. [15,26,211]. Layers are assumed to be pure B_4C and SiC in all calculations. The calculated residual stresses are -1.11 and +1.42 GPa for the B_4C and SiC layers, respectively, where tension and compression

are denoted by '-' and '+'. Based on these calculated residual stresses and the fact that the flexural strength of B_4C ranges from approximately 350-500 MPa [17,212,213], the B_4C layers should fracture. Indeed, these calculations are supported by microstructural observations, where cracks occur in tensile B_4C layers and then bifurcate and close as they traverse into compressive SiC layers.

Using Equations 4.6. and 4.7., residual stresses can be calculated as a function of the ratio l_1/l_2 to determine layer height configurations with lower residual tensile stresses. Tensile residual stresses in B_4C layers are inversely related to compressive residual stresses in SiC layers. Layer configurations that reduce tensile residual stress should maximize the l_1/l_2 ratio, which yields thick B_4C layers and thin SiC layers. Diminishing returns suggest an optimal layer thickness ratio at or slightly above 4.

Table 4.3. Material properties of carbides used to calculate residual stresses [15].

Component	E (GPa)	Poisson's ratio	CTE (10^{-6} K^{-1})
B_4C	483	0.17	5.5
SiC	411	0.16	3.0

Crack spacing (s) and crack opening displacement (w_c) for the discrete B_4C-SiC specimen were measured from SEM micrographs and found to have values of 283 ± 44 and 0.7 ± 0.3 μm, respectively. The equilibrium crack spacing can be estimated analytically by using an energy balance approach and making simplifying assumptions: strain energy is released by crack opening displacement and provides the energy for the creation of new surface area during crack formation. The surface energy per unit area of cracks is γ. Cracks are

assumed to have a constant opening displacement, to be perpendicular to the layer interface, and to be arranged in a 2-dimensional network with equal spacing. Thus, the total strain energy (U_t) equals:

$$U_t = U_s + U_e \ , \tag{4.8}$$

where U_s is the increase in surface energy due to the creation of two new crack surfaces and U_e is the elastic strain energy due to tensile residual stress. The increase in surface energy is equal to:

$$U_s = t * l_1 * 2\gamma * n_c = l_1 * 2\gamma * t * \frac{2L}{s} = \frac{4\gamma}{s} * V \ , \tag{4.9}$$

where t is layer width, l_1 is layer thickness, and the number of cracks is n_c. The number of cracks equals $2L/s$, where L is layer length and the term $2/s$ represents the 2-dimensional network of cracks of spacing s. The total increase in surface energy per unit volume is then $4\gamma/s$ from Equation 4.9. The elastic strain energy is:

$$U_e = \frac{\sigma_r^2}{2E^*} * l_1 * t * L = \frac{E^* \varepsilon^2}{2} * V \ , \tag{4.10}$$

where E^* is the effective elastic modulus of the layered structure and ε is the strain. Equation 4.5. is adapted into elastic strain energy per unit volume in the following equation:

$$U_e = \frac{E^* \varepsilon^2}{2} = \frac{\frac{E_1' E_2' f_2}{E_1' f_1 + E_2' f_2} \left((\alpha_2 - \alpha_1) \Delta T + \frac{w_c}{s} \right)^2}{2} \ , \tag{4.11}$$

which accounts for elastic strain energy from both the CTE mismatch and the crack opening displacement by including w_c/s. The rationale for adding w_c/s to relax CTE mismatch strain is adapted from a methodology developed by

Matthews and Blakeslee (1974), where misfit strain ε_m is relaxed by the displacement *b* (Burgers vector) and spacing *s* of misfit dislocations in the form $\varepsilon = \varepsilon_m + b/s$ [214,215]. By definition, ε_m and *b/s* must have different signs to cause stress relaxation, which holds true for our case where w_c/s and CTE mismatch strain are of different sign. According to the equilibrium theory of Van der Merwe (1972), the stable configuration can then be calculated by setting the derivative of U_t with respect to $1/s$ equal to zero [216]. Thus,

$$\frac{\partial U_t}{\partial {}^{1}/_{s}} = 4\gamma + \frac{E^*\left(2w_c\left((\alpha_2-\alpha_1)\Delta T+\frac{w_c}{s}\right)\right)}{2} = 0 \ , \qquad (4.12)$$

which can be modified to solve for equilibrium crack spacing

$$s = \frac{-E^* w_c^2}{4\gamma+E^* w_c(\alpha_2-\alpha_1)\Delta T} \ . \qquad (4.13)$$

The free surface energy for B_4C is approximately 3 J/m^2 [217,218]. Solving Equation 4.12. using $\gamma = 3\frac{J}{m^2}$, $w_c = 0.7\ \mu m$, $\Delta T = 1925\ K$, and material properties in Table 4.3., the equilibrium crack spacing is calculated as 148 μm; equilibrium being defined as all residual stress relieved by cracking. Thus, the difference between our calculated value and the measured value of 283 μm indicates residual stresses have not been fully relieved by cracking. Another likely factor in this difference is error in our crack opening displacement measurements. For example, if w_c is set to 1.5 μm, the equilibrium crack spacing is calculated as 314 μm. The sensitivity of equilibrium crack spacing to changes in crack opening displacement is demonstrated in Figure 4.24B. The measured

experimental value, represented as a diamond, is presented beside calculated curves for comparison. Surface energy seems to have a minimal effect on the equilibrium crack spacing, indicating the majority of the strain energy is released through crack opening displacement. Equilibrium crack spacing increases with increasing crack opening displacement and specific surface energy, resulting in fewer cracks.

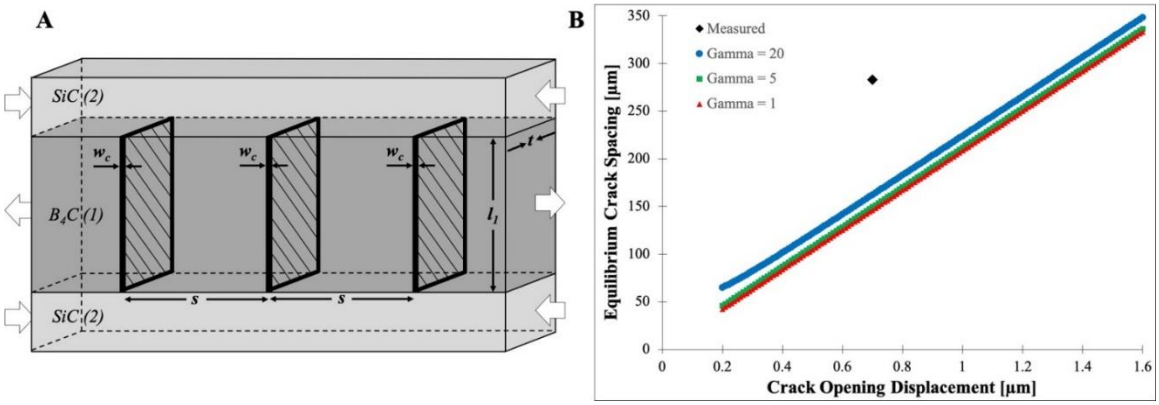

Figure 4.24. (A) Diagram highlighting relevant parameters for the analysis of thermally-induced residual stresses, which shows one full B_4C layer and two partial SiC layers. (B) Plot of equilibrium crack spacing versus crack opening displacement for specific surface energies of γ =1, γ =5, and γ =20.

4.3.7. Hardness Testing

Reported hardness values in the literature for monolithic B_4C and SiC vary significantly due to differences in specimen preparation, testing methods, and testing conditions, with one major influence being the indentation size effect (ISE). The ISE results in a trend of decreasing measured hardness with increasing indentation load up to a plateau. Swab [213] found the Knoop hardness to be load-independent at 1 kgf Knoop or higher for many common armor ceramics. Vargas-Gonzalez et al. [17] studied the ISE for B_4C and SiC

and found both Knoop and Vickers measured hardness to vary with load up to 2 kgf.

Figure 4.25 summarizes Knoop indentation hardness results for the (A) discrete and (B) continuous specimens, which were collected consistent to the 2 kgf standard prescribed in ASTM C1327 to avoid the ISE. No significant change in hardness was detected between B_4C, SiC, and interface regions in the discrete specimen, which had HK2 and standard deviation values of 21.44±0.74, 21.29±0.42, and 21.26±0.34 GPa, respectively. The larger standard deviation in hardness values measured for the B_4C layers is likely due to the presence of cracks; while residual stress is zero at crack surfaces, tensile stresses are likely still present in uncracked material. For the continuous specimen, indents made in regions with nominal composition ratios of 10-90 vol.% B_4C had hardness values of 21.53±0.33 GPa, while indents in regions with nominal compositions closer to pure SiC or B_4C had HK2 values of 20.85±0.31 GPa. Knowing the hardness of B_4C exceeds that of SiC, one could expect the hardness to decrease with increasing SiC content. However, looking at Figure 4.25, hardness gradually increases with SiC content until about 4mm, where it then decreases towards pure SiC. The trend observed is hypothesized to be due to two factors: (1) softening in regions of pure B_4C and SiC due to edge-effects and (2) thermally-induced residual stresses due to composition variation. Based on CTE calculations, B_4C-rich regions will tend towards tensile residual stress, which would decrease hardness, and SiC-rich regions will be under compressive

stress, which would increase hardness. However, past 4mm, the hardness of the nominally pure SiC decreases as residual stresses are partially relieved due to cracking.

A challenge in measuring the hardness of these printed specimens was the presence of large inclusions (hundreds of micrometers), which were of similar size as the indenter tip. Thus, indents made in a B_4C layer may be over the matrix region, a B_4C inclusion, or even a SiC inclusion. Knoop hardness values for the printed B_4C-SiC specimens were within one standard deviation of HK2 values for fully-dense, monolithic B_4C (21.7±0.9 GPa) and SiC (20.6±0.2 GPa) materials reported by Vargas-Gonzalez et al. [17].

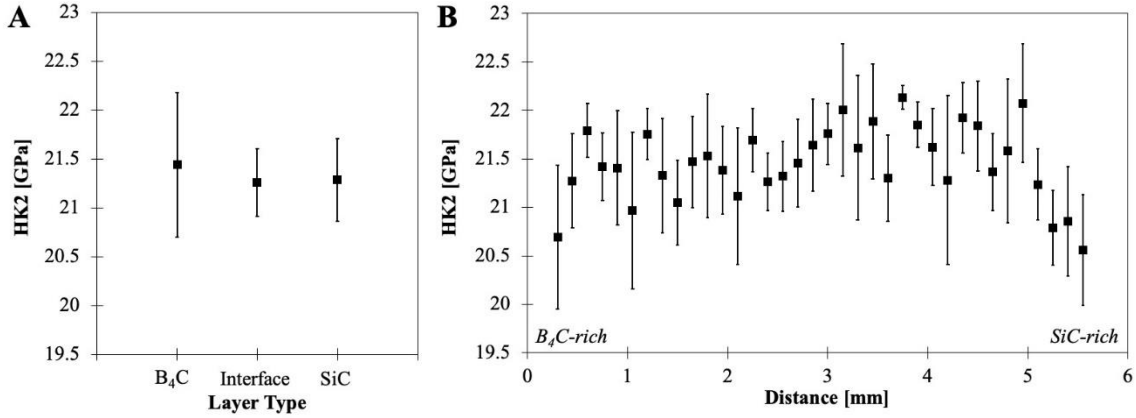

Figure 4.25. Knoop indentation hardness data collected for the (A) discrete and (B) continuous B_4C-SiC specimens. All indentations were collected consistent to the 2 kgf standard prescribed in ASTM C1327 to avoid the ISE. Error bars indicate ± one standard deviation.

4.4. Summary

4.4.1. Conclusion

Multi-phase carbide parts were formed via DIW using a custom-built system with multi-material and active in-line mixing capabilities. B_4C and SiC

were printed as aqueous ink formulations with high ceramic content and yield-pseudoplastic rheology. The flow behavior of B_4C and SiC inks, having identical ceramic content, was matched across relevant shear rates through the addition of high viscosity methylcellulose. Active, in-line mixing enabled the successful fabrication of discrete and continuous specimens; demonstrating the capability to create both gradual and discrete composition variations in real-time. High-shear mixing achieved by the auger produced micrometer scale mixtures, observed as matrix regions, as well as B_4C and SiC inclusions of sizes tens to hundreds of micrometers. Near full density was achieved for heterogeneous carbide specimens via hot pressing. Cross-sections of densified parts show intimate layer bonding and no printing artifacts. Minimal cracking observed in the continuous specimen reveals that a gradual composition variation reduces residual stress from CTE mismatch, as compared with discrete variations. Residual stress calculations support microstructural observations, where cracking occurs in the B_4C layers due to tensile stress. The hardness of printed B_4C-SiC specimens approximately matched or exceeded that of traditionally processed carbide ceramics. These results indicate the feasibility of tailoring the structure of advanced ceramics through multi-material additive manufacturing.

4.4.2. Acknowledgement

Chapter 4, in part, is a reprint of material that has been published: J. Pelz, N. Ku, W. T. Shoulders, M. A. Meyers, L. R. Vargas-Gonzalez, “Multi-Material Additive Manufacturing of Functionally Graded Carbide Ceramics via Active, In-

Line Mixing," Additive Manufacturing, 2021. The dissertation author was the primary investigator and author of this paper.

CHAPTER 5. DAMAGE TOLERANCE IN CERAMICS VIA HETEROGENEITY

5.1. Overview

While advanced ceramics are the hardest and strongest known materials, their low damage tolerance remains a major challenge for real-world use in dynamic environments. Similarly, the commercial application of ceramic additive manufacturing is impeded by the defect-sensitivity and poor toughness characteristics intrinsic to ceramic materials. To enable widespread use of printed ceramic components, mechanisms to improve damage tolerance must explored. We propose that heterogeneous structuring will unlock extrinsic toughening mechanisms, which will enable the use of printed ceramic components for structural applications in the aerospace, defense, and energy sectors. A central question of this chapter is how heterogeneous structuring affects crack propagation at high strain-rates.

Carbide specimens with continuous (gradient) and hybrid (layered-gradient) composition variation along the build direction were fabricated using the custom DIW system described in Chapter 3. Blended B_4C/SiC specimens were printed as control specimens to determine baseline properties. Post-processing, namely sintering, of multi-phase ceramics generates residual stress due to coefficient of thermal expansion mismatch between the two phases. Printed specimens were characterized and mechanically tested in quasi-static and

dynamic strain-rate regimes. Relationships between process, structure, and properties are discussed, with a focus on dynamic mechanical response.

5.2. Introduction

5.2.1. Applications of Advanced Ceramics

Advanced ceramics are necessary in applications with extreme temperature, wear, and corrosive environments. Environments such as the turbine blades in airplane engines, protective systems such as body and vehicle armor, and high-wear components of medical implants. Due to the lower density and higher use temperature of ceramic materials compared to metals, ceramic, CMC, and ceramic thermal barrier coating turbine blades enable higher thrust to weight ratios. Ultra-high temperature ceramics (UHTCs) have been studied for applications such as leading edges of wings and include zirconium diboride, hafnium diboride, and silicon carbide [219]. Previous research characterized common advanced ceramics, aluminum oxide and silicon and boron carbide, for armor applications and found trends in mechanical properties followed density and microstructure [17]. Alumina, silicon carbide, and boron carbide are used in dynamic applications where strain rates of 10^4 s^{-1} to 10^6 s^{-1} exist [220] and inertial effects begin to dominate [221].

5.2.2. Damage Tolerance in Advanced Ceramics

The pursuit of damage tolerant ceramics has been extensively explored in the literature with mixed success. In dynamic applications, amorphization has been widely reported on in B4C and can dramatically reduce damage tolerance

at high strain rates [23,222] and ballistic impacts where the existence of a critical impact regime causes a drop in dynamic mechanical performance [1]. Research by Orlovskaya [15] into the use of multilayered advanced ceramics to tailor residual stress, related to coefficient of thermal expansion mismatch, to inhibit crack propagation and improve toughness. Ravichandran [223] developed a residual stress model for material gradients and found that a linear gradient reduced residual stress the most. Feilden [178] used nature to inspire damage tolerant structures based alumina platelet alignment, inspired by Bouligand structures, to tune crack propagation and improve toughness. Previous research has shown the ability to produce dense advanced ceramic components, such as alumina ceramics [54], boron carbide by pressureless with density of 82 %TD [58] and SPS of B4C ceramics (RC + CIP) has, despite its ~5% residual porosity, a hardness of ~27 GPa and a compressive strength of ~1800 MPa [59]. Multi-material additive manufacturing enables local tailoring of material properties, such as stiffness, wear resistance, and corrosion resistance [224].

To understand the damage tolerance of advanced ceramics, we need to understand damage evolution processes for different loading conditions. In tension, brittle materials fail due to the single largest defect, while in compression brittle materials fail axially due to the coalescence of many microcracks that grow ‘wing-tip’ tension cracks axially [225–227]. Interestingly, based on the method of processing, namely sintering, these wing-tip cracks may grow in a stable or unstable manner. For techniques such as hot pressing, the smaller grain size

and lower defect concentration tends toward stable growth [cite from split Hopkinson dynamic papers], while pressureless sintering may lead to unstable growth conditions due to larger grains and defects. As loading rate changes from quasi-static electromechanical testing to dynamic, explosive charge driven split-Hopkinson pressure bar testing, inertial effects in crack propagation result in mode-I fracture toughness increases by 10-30% for Al_2O_3 and SiC and 40% for Si_3N_4 [228]. Crack growth can be inhibited in microcracking materials, resulting in improved toughness, because microcracking ahead of the crack tip reduces elastic modulus and induces dilatation [229].

5.2.3. Dynamic Performance in Advanced Ceramics

The split-Hopkinson pressure bar can be used to reach strain rates of 10^3 s^{-1} to 10^5 s^{-1}, but for ceramic materials a maximum strain rate of roughly 3000 s^{-1} is possible due to the need to reach equilibrium [230,231]. Prior to failure, the specimen must reach stress equilibrium and be experience a constant strain rate simultaneously [232], and based on experimental data for a glass-epoxy composite and for PMMA the constant strain rate criteria may be more restrictive and be the limiting factor for maximum achievable strain rate in SHPB testing. Brittle specimens, which are sensitive to stress concentrations, can fail due to 1) poor flatness or parallelism of the specimen, 2) poorly aligned bars, and 3) specimen indentation into the bar ends [232].

5.3 Experimental Procedures

Additively manufactured carbide ceramics of two heterogeneous designs, continuous and hybrid, were tested against a blended control specimen. These specimen types, illustrated in Figure 5.1, were characterized and tested for their dynamic and quasi-static mechanical properties, with the goal of elucidating process-structure-property relationships in dynamic and quasi-static regimes.

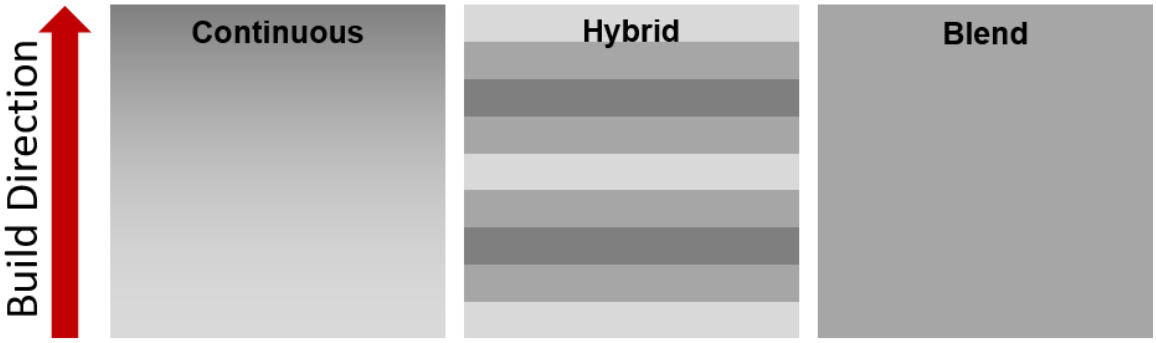

Figure 5.1. Heterogeneous carbide ceramic design types. The light, medium, and dark shades of gray represent B_4C-SiC mixtures of 60, 50, and 40 vol.% SiC, respectively.

5.3.1 Feedstock Preparation

Two aqueous carbide inks, one boron carbide and one silicon carbide, were formulated with yield-psuedoplastic behavior for use as the DIW feedstock material. The boron carbide ink consists of 47.5 vol.% B_4C powder (mean particle size ~ 0.8 µm, HC Stark, Germany), 3.79 vol.% polyethyleneimine (25kDa PEI, Sigma-Aldrich, Louis, MO), 5 vol.% hydrochloric acid (96.99% HCl, Sigma-Aldrich, Louis, MO), 5 vol.% methylcellulose (4000cP MC, Sigma-Aldrich, Louis, MO), and remainder deionized water. The silicon carbide ink contains 47.5 vol.% SiC powder (mean particle size ~ 0.7 µm, Superior Graphite 490N SiC, Chicago, IL), 3.00 vol.% polyethyleneimine (25kDa PEI, Sigma-Aldrich, Louis, MO), 2.5

vol.% methylcellulose (4000cP MC, Sigma-Aldrich, Louis, MO), and remainder deionized water. Ink formulations are described in Table 4.2.

The inks were homogenized using a DAC 400 VAC SpeedMixer (Flacktek, Landrum, SC). Powder, binders, dispersants, and water were added in steps and mixed thoroughly. In total, three rough mixing stages (up to 1600 rpm) and one final mixing stage (up to 1800 rpm) were used to formulate the carbide inks. The rheological properties of both inks were characterized using an MCR 302 (Anton Paar, Graz, Austria) with a concentric cylinder fixture. The viscosity was measured with a continuous flow test from 0.1 to 100 s^{-1} and confirmed to be pseudoplastic (shear thinning) with an appropriate yield stress for DIW processing. The formulation and characterization of the carbide inks used in this study are based on and described in detail in previous work by the authors [80].

5.3.2 Multi-Material Direct Ink Writing

This work builds on previous work by the authors wherein the development of the original system is detailed [13,80]. The system includes two feed system units, print head, controller, and three-axis motion platform. One unit was loaded with boron carbide ink and the other was loaded with silicon carbide ink. The controller coordinates movement and feed rate, so that the correct feeding ratio is provided to the print head to tailor the geometry and composition. For example, a continuous design type is printed by incrementally changing the feed ratio (the relative amounts of boron carbide and silicon carbide inks from each feed unit) between two set-points. The print head utilizes an auger to in-line

mix and extrude the ceramic ink at any specified ratio as the motion platform traces out the desired layer.

To improve the performance of the system, shown in Figure 5.2, a custom three-axis motion platform was developed based on delta-kinematics. The feed system units remain relatively similar, but now include much shorter feed tubes that have a larger inner-diameter to reduce flow resistance. The printhead uses an ‘open-system’ design wherein the top of the barrel is not sealed against the shaft of the auger and material is driven towards the nozzle and overcomes the pressure drop based on a metered auger design. This design enables the de-aeration of material as it is compressed through the metering section and reduces printing defects. Further, the elongated auger 80mm vs 50mm provides a greater driving force and thus reduces printing performance variation based on feedstock rheological properties. The auger is both longer and has shallower channels with the goal of breaking down soft-agglomerates within the ink.

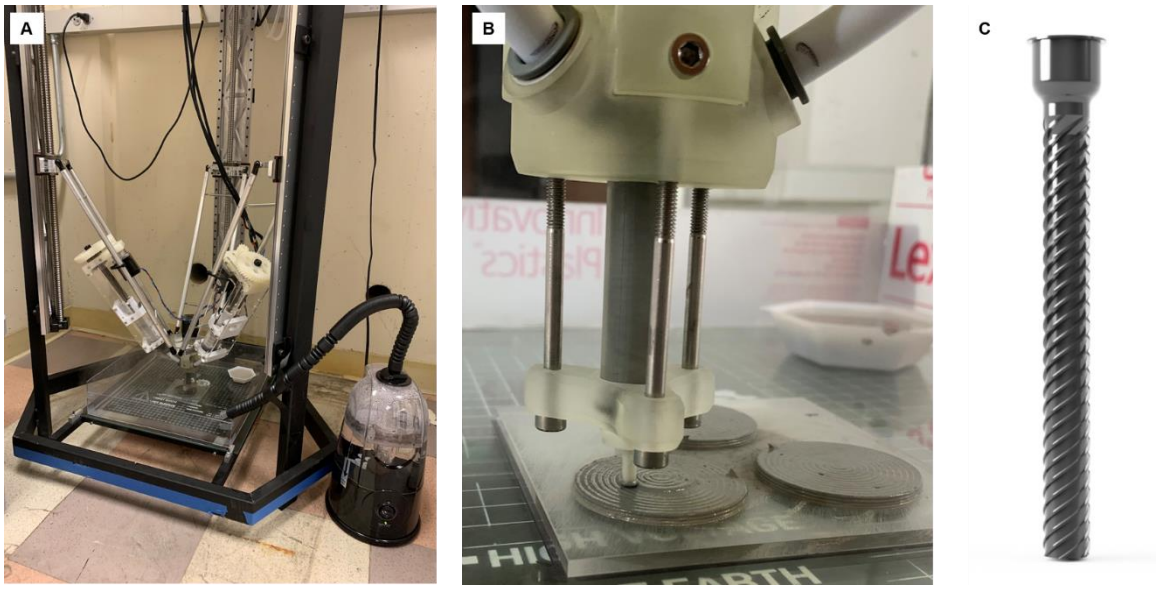

Figure 5.2. Updated custom DIW system based on the original design previously reported on by the authors [13]. A) DIW system including 3-axis delta motion system, two feed system units, controller, and print head. B) Close-up on the print head processing 38.1 mm cylinders with composition varied in the build-direction. C) The metered auger design includes conveyance, transition, and shear sections in the top, middle, and bottom thirds of the auger, respectively, to provide conveyance and high-shear mixing.

The print head uses a 15 mm long alumina tube with an inner diameter of 1.6 mm as the nozzle, printing speed of 12 mm/s, and varying layer height between 0.5-0.75 mm. Due to the two-stage material change process, total residence time and residence time, where a certain volume of material must be extruded before any composition change occurs and a second stage where the material grades from the initial composition to the commanded composition. To save material, the commanded change occurs on a previous layer at a point equal to the first stage volume before the end of the layer. Then, a sacrificial puck is used to purge during the second stage where composition grades between the initial and commanded compositions. This process is demonstrated in Figure 5.3.

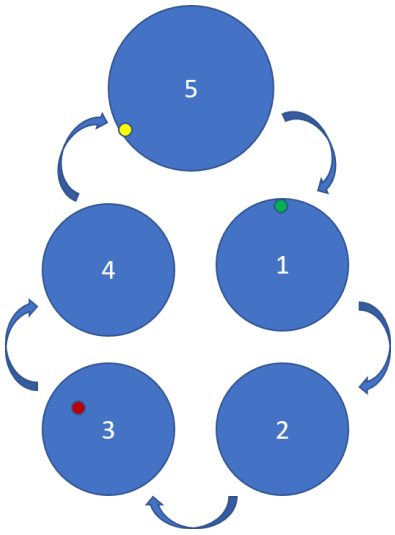

Figure 5.3. Printing process using a sacrificial ‘purge’ puck and composition changes at specified points based on residence time and total residence time. The red, yellow, and green dots illustrate the command, completion of stage one, and completion of stage two, respectively. Printing goes from puck 1 to puck 5 and layer-by-layer until the entire parts are created. In order to create a composition change, the change must be commanded at the red dot during the previous layer.

Green bodies of the desired composition variation (continuous, hybrid, and blend) were printed as 38.1 mm diameter by 10.55 mm height pucks. Pucks were printed on removable acrylic plates that were placed into a sealed container immediately after printing to avoid cracking. Drying was carried out over a one-week period. Figure 5.4 demonstrates a symmetric hybrid green body that was dried and broken in half. The puck was printed in 9 layers that varied from 100% SiC (light gray) on the top and bottom to 100% B_4C (dark gray) in the middle in steps of 25% each layer.

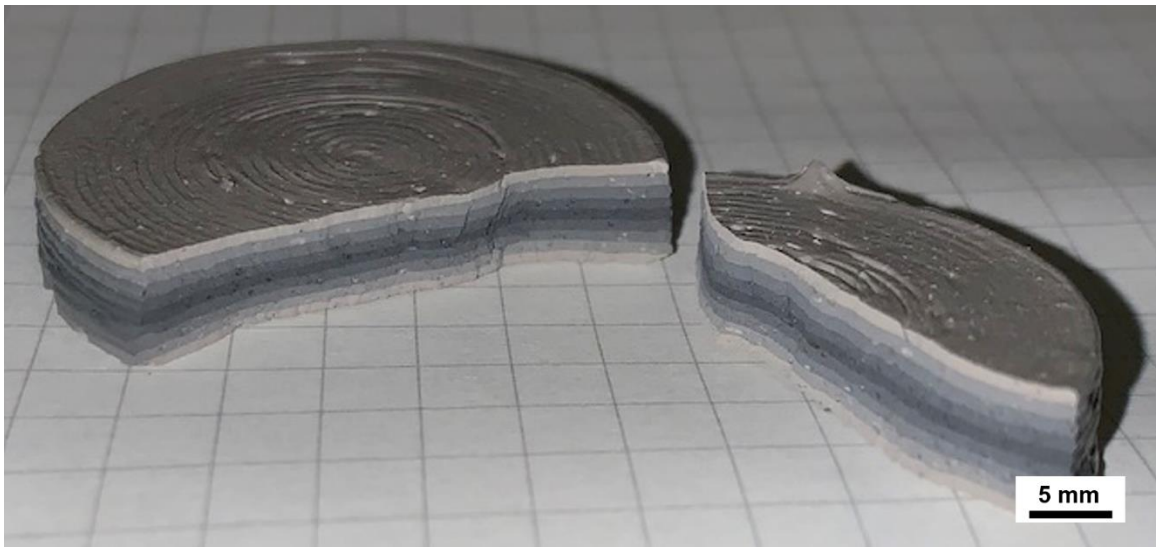

Figure 5.4. Example green part that has been dried and broken in half to reveal the heterogeneous layering. Composition was varied from 100% SiC (light gray) on the top and bottom to 100% B_4C (dark gray) in the middle in steps of 25% each layer.

5.3.3 Post-processing

Dried specimens were (1) pyrolyzed by ramping at 1 °C/min up to 650 °C and holding for 6 h and (2) densified through hot pressing. The specimens were hot pressed at 35 MPa and 1950 °C for 3 h, using a 20 °C/min ramp rate and including an intermediate hold at 1300 °C for 1 h to volatilize oxide species such as B_2O_3, and then 10 °C/min up to sintering temp. Final, dense specimens were grit blasted to remove graphfoil adhered to the surface from the hot-pressing process. Specimens were ground to a height of 3 mm and sectioned into bars using an automatic surface grinder. The bars were further sectioned using a slow-speed saw (Model 650, South Bay Technology, San Clemente, CA) and hot-pressed diamond blade (MTI Corporation, Richmond, CA) with a 63 µm grit size. Figure 5.5 demonstrates the four-millimeter wide bars and three-millimeter

cubes excised from each 38.1 mm puck. Two pucks each were sectioned for the continuous and hybrid type specimens and one blend type puck was sectioned. All sides of every section were polished to a 15 μm grit size to meet mechanical test sample surface finish requirements. A lapping fixture (South Bay Technologies) was used to polish the cubes to ensure parallel testing surfaces. The sections used for hardness testing and microstructural characterization were mounted in epoxy and polished following rough, intermediate, and final steps. Rough polishing was accomplished using a 125 μm diamond embedded disk until specimen surfaces were exposed and planar. Next, colloidal diamond suspensions of sizes 30, 9, and 3 μm were used to polish both specimens for times of 30, 30, and 90 min, respectively. A final polish was done using 1 and 0.25 μm colloidal diamond suspensions for times of 45 and 60 min, respectively. All polishing steps were performed at a 20 N load and with plate and head speeds of 300 and 150 RPM, respectively, in a co-rotating configuration.

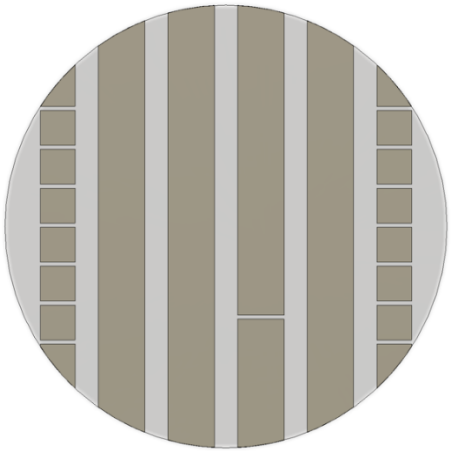

Figure 5.5. Bars and cubes were excised from printed and post-processed cylinders of diameter 38.1 mm. The top and bottom surfaces and vertical cuts were made using an automatic surface grinder. Horizontal cuts were made using a slow-speed saw.

5.3.4 Characterization

SEM micrographs were taken of the resulting polished cross-sections (FEI Apreo SEM, Hillsboro, OR). ImageJ was used for all measurements, including grain and inclusion size determination, on SEM micrographs [200]. Phase determination was accomplished via XRD. A small piece of each specimen was excised and milled into powder using a ball mill (8000M Mill, SPEX SamplePrep, Metuchen, NJ). Milling was performed for two minutes in a polycarbonate capsule with two tungsten carbide milling media. Powder was dispersed into a small amount of ethanol, pipetted on to Si XRD sample holders, and allowed to dry, forming thin layers of powder for XRD analysis. Analysis was performed using a Bruker D2 PHASER 2nd-Gen (Billerica, MA) x-ray diffractometer (XRD). The XRD utilized a Cu K-α source generated at 30 kV and 10 mA. Test conditions for the analysis consisted of a 2Θ range of 10-100° with an increment of 0.02° and step time of 1.0 s. Density was determined using the Archimedes method. Densities are reported as a percentage of theoretical density, which was calculated using a rule of mixtures with values of 2.52 g/cc for boron carbide and 3.21 g/cc for silicon carbide [17]. The relative amounts of each phase, used in the rule of mixtures calculation, were determined by quantitative phase analysis from XRD patterns using the Rietveld method.

The residual stress state within each heterogeneous design was calculated through an analytical treatment and tested with Raman spectroscopy and the Sin^{2}Psi XRD method. The residual stresses of a layered composite with

finite thickness and alternating brittle layers (of potentially different thickness) are:

$$\sigma_{r1} = \frac{E_1' E_2' f_2(\alpha_2 - \alpha_1)\Delta T}{E_1' f_1 + E_2' f_2} \text{ and} \tag{5.1}$$

$$\sigma_{r2} = \frac{E_1' E_2' f_1(\alpha_1 - \alpha_2)\Delta T}{E_1' f_1 + E_2' f_2}, \tag{5.2}$$

where $E_i' = E_i/(1 - v_i)$, $f_1 = \frac{l_1(N+1)}{2h}$, $f_2 = \frac{l_2(N-1)}{2h}$, E_i and v_i are the elastic modulus and Poisson's ratio of component *i*, l_i is the layer thickness of component *i*, α_i is the CTE of component *i*, ΔT is the difference between T_j and ambient temperature, *N* is the total number of layers, and *h* is the total specimen height. B_4C and SiC are defined as component 1 and 2, respectively, T_j is equal to the sintering temperature of 1950ºC, ambient temperature is 25ºC, and N is 7. Material properties are listed in Table 4.3. The above equations and material properties are adapted from work by Orlovskaya et al. [15,26,211].

5.3.5 Mechanical Testing

Quasi-static (hardness, compression, and three-point bending) and dynamic (split-Hopkinson pressure bar compression) mechanical testing was performed on the excised samples for the continuous, hybrid, and blend type specimens. Dumbbell type specimens were used, in addition to cubes, for quasi-static and dynamic compression testing to reduce invalid tests due to edge effects problematic in cylinder and cube geometries [233]. For a cylindrical aluminum nitride specimen compressed using a steel SHPB, stress concentrations at the edges were calculated to be 2.7 times the stress at the

center of the specimen exist due to the difference in stiffness between steel and aluminum nitride [234].

Knoop indentation hardness testing was performed in two test variations to determine the Knoop hardness (HK) values and the indentation size effect (ISE). Knoop indentation was performed using a Wilson VH3100 automatic hardness tester (Buehler, Lake Bluff, IL). HK values were determined following the ASTM C1326-13 standard [203] at a 19.61 N load, 10 s dwell, and spacing greater than 1.5 times the long-diagonal of the indent. HK2/10 values were determined on the polished cross-section of each specimen type. Ten valid indents were measured for the homogenous blend (B) specimen. For the hybrid (H) specimen, 10 valid indents each were measured in the B_4C, 50/50, and SiC layers. For the continuous (C) specimen, a 5 x 11 grid of indents was made to measure five points each at the centers of all layers that range from 40 to 60 vol.% SiC in increments of 2 vol.%. The ISE was determined for the B, C, D, and H specimens using a 10 s dwell and sufficient spacing with loads varying from 0.98 to 19.61 N. ISE indents were made on the top and bottom polished surfaces of the specimens to drive cracking perpendicular to layer interfaces. Five valid indents were made for each load.

Three-point flexural strength* measurements were performed on the excised bars from the heterogeneous carbide pucks. Four 3 mm x 4 mm x 25 mm bars each were evaluated for blend, continuous-B_4C, and continuous-SiC type specimens, while eight 3 mm x 4 mm x 25 mm hybrid bars were tested. The

flexural strength ASTM standard for advanced ceramic materials specifies at least 10 bars must be tested and if a 3 mm x 4 mm cross-section is used the outer-span must be 40 mm [235]. In this study, we determined that a puck height of 3 mm was necessary to achieve the desired composition variations, but only had access to a 38.1 mm hot pressing die. For these reasons, flexural strength* values we report will not adhere to ASTM requirements and should only be used for qualitative comparison between heterogeneous designs within this study. A load frame (Universal Testing System 3367, Instron, Norwood, MA) with a 30 kN load cell and displacement control was used for flexural testing. Three-point bend testing was performed at a displacement rate of 0.5 mm/min (strain rate equal to 10^{-4} s^{-1}) with a 20 mm outer-span and 4.5 mm diameter rollers. The failure load, P, was used to determine flexural strength* (S) using the equation,

$$S = \frac{3PL}{3bd^2}\,, \tag{5.3}$$

where L is the outer-span, b is the bar width, and d is the bar height, provided by the ASTM C1161 flexural strength of advanced ceramics standard [235].

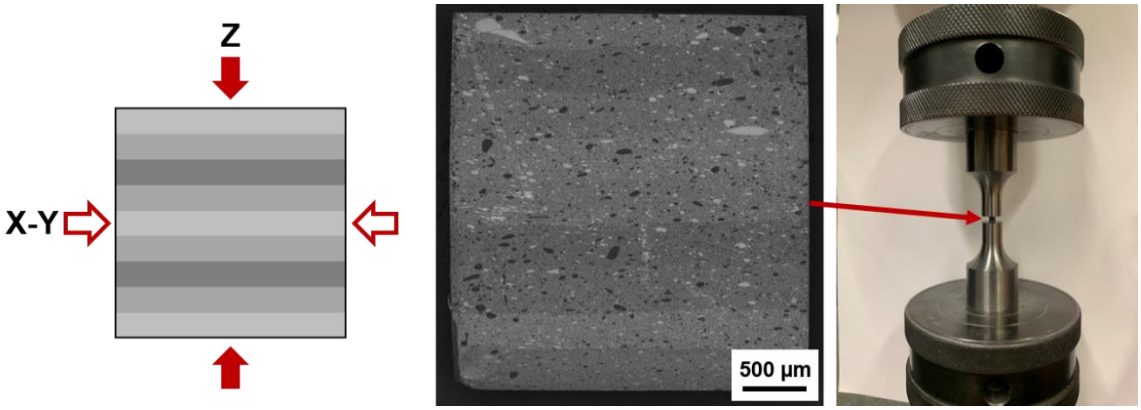

Figure 5.6. Carbide cubes were tested in compression at quasi-static (10^{-3} s^{-1}) and dynamic (10^{2} s^{-1}) strain rate regimes in two orientations. The Z orientation aligns with the DIW build direction and is normal to layer interfaces, while the X-Y orientation is parallel to layer interfaces. In addition, the Z orientation is parallel to the hot pressing direction. Tapered tungsten carbide platens were placed between the carbide cube and steel compression platens.

The compressive strength of the heterogeneous carbide specimens was determined by crushing the 3 mm x 3 mm x 3 mm cubes excised from the 38.1 mm pucks. Six cubes were tested for each orientation for all specimen types to determine a mean compressive strength. Quasi-static compression testing was done on a load frame (Universal Testing System 5982, Instron, Norwood, MA) with a 100 kN load cell. As shown in Figure 5.6, tungsten carbide platens that taper from 25.4 mm to 6.35 mm were used to eliminate interfacial stresses that would arise due to interactions between the carbide cubes and more compliant steel compression platens. An extension rate of 0.5 mm/min was used for compression testing, which correlates to a strain rate of 10^{-3} s^{-1}. After failure, fragments were collected to analyze fracture mechanisms. Dynamic compression testing, strain rates between 100 s^{-1} to 250 s^{-1}, was achieved using a split-Hopkinson pressure bar (SHPB), also known as a Kolsky bar. The system uses Maraging steel incident, transmission, and striker bars of diameter 18.95 mm and

length 2 m, 2 m, 250 mm, respectively. Compressed Ar gas is used to repeatably launch the striker bar into the incident bar. The system was aligned using laser-sights and good alignment was confirmed by symmetric incident, reflected, and transmitted wave signals for a 'blank' tests without any specimen. Strain gauges were mounted at the center of the incident and transmission bars in an active two-leg half-bridge configuration, where both strain gauges are used to actively measure strain, while cancelling out bending stresses. Wheatstone bridge adapters were connected to the strain gauges and connected to signal conditioners (CDV-900A, KYOWA, China) to amplify and condition wave signals. An oscilloscope (GDS-1102A-U, GWINSTEK, Taiwan) was used to record the wave forms. The signal conditioners were used to apply a 100 kHz low-pass filter during measurement to reduce noise. Tungsten carbide platens of diameter 12.7 mm and 6.35 mm thick, which were impedance matched to the Maraging steel bars, were placed between the incident and transmission bars and the carbide cube specimen. The platens eliminate unwanted stress concentrations at the specimen edges and corners, in addition to reducing damage to the steel bar ends. A 5.1 mm diameter by 2 mm thick annealed copper disk was placed between the striker and incident bar to ramp the pulse and produce a longer loading time to enable stress equilibrium prior to specimen failure. Post-test, wave forms were analyzed to confirm that both stress equilibrium and constant strain rate conditions were met by the time failure occurred. The compressive strength (σ_c), strain rate ($\dot{\varepsilon}$), and failure strain (ε) were determined by:

$$\sigma_c = E_b \frac{A_b}{A_s} \varepsilon_T, \tag{5.4}$$

$$\dot{\varepsilon} = -2 \frac{C_b}{L_s} \varepsilon_R, \tag{5.5}$$

$$\text{and } \varepsilon = -2 \frac{C_b}{L_s} \int_0^t \varepsilon_R dt, \tag{5.6}$$

where E_b is the elastic modulus of the Maraging steel bars, C_b is the wave speed in the bars, A_b is the area of the bars, A_s is the area of the specimens, L_s is the length of the specimen, ε_T is the transmitted wave strain, and ε_R is the reflected wave strain. These equations and test validity criteria are referenced from Chen and Song [232].

5.4 Results & Discussion

5.4.1 Microstructural Characterization

A typical microstructure is shown in Figure 5.7 for the 3D printed heterogeneous carbide specimens. Light gray and dark gray materials are SiC and B_4C, respectively, with bright speckles being intergranular porosity. The particle scale mixing in the matrix creates a fine mixture of single grains of B_4C and SiC, which surrounds larger inclusions composed of many grains of a single material. The average grain size of 0.93 µm and 1.63 µm was determined for the B_4C and SiC grains, respectively. Inclusions in the tens to hundreds of micrometers were quantified and an average inclusion size of 19.44 µm and 18.92 µm was determined for B_4C and SiC, respectively. For SiC, only three inclusions over one-hundred micrometers were observed with the largest being 161.81 µm, whereas for B_4C forty-three inclusions over one-hundred

micrometers were observed with the largest being 285.47 μm. Likely due to the hot pressing process, inclusions tend to be elliptical with their long axis parallel to layer interfaces or normal to the hot pressing direction.

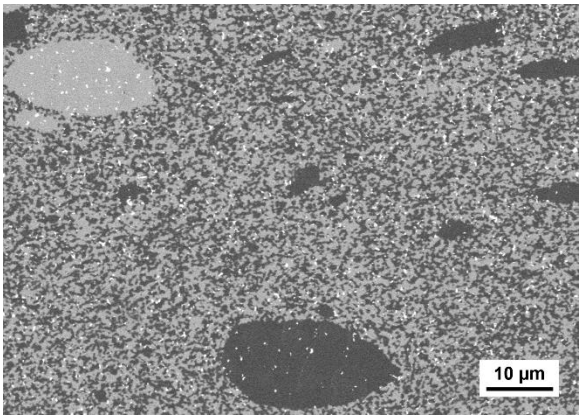

Figure 5.7. SEM micrograph showing the 'salt and pepper' matrix, composed of particle-scale mixing of the carbide inks, surrounding B_4C and SiC inclusions. Light gray and dark gray materials are SiC and B_4C, respectively, with bright speckles being intergranular porosity.

To determine bulk composition of the $0.75B_4C$-0.25SiC and $0.5B_4C$-0.5SiC samples, diffraction patterns were analyzed by Rietveld refinement with GSAS-II [204]. Starting values for the lattice constants and atomic positions for the 6-H [205], 15-R [206], and 4H [206] polytypes of silicon carbide along with boron carbide [207] were taken from respective references. The relative amounts of each phase, lattice constants, and sample displacement were refined to achieve weighted R values near 15% in both cases. Figure 5.8 illustrates the Rietveld analysis results for one of the heterogeneous carbide specimens that were ground into powder. Rietveld quantitative phase analysis results are reported in Table 5.1. The continuous and blend specimens were expected to have 50 vol.% SiC, while the hybrid specimen was expected to have 51.1 vol.% SiC. The observed variation from nominal compositions is likely a consequence of having

used inks with different viscosity and compressibility, which will affect feed rates to the print head and mixing characteristics inside the print head. These effects will need to be quantified in future studies to enable more precise control over printed composition.

Table 5.1. Rietveld quantitative phase analysis results for each heterogeneous specimen.

Type #	6H (wt%)	15R (wt%)	4H (wt%)	B4C (wt%)	WC (wt%)	SiC (vol%)	B4C (vol%)
Continuous	44.3	1.9	4.8	44.5	4.6	47.5	52.5
Hybrid	54.4	1.1	4.0	37.7	2.8	55.3	44.7
Blend	44.7	2.7	5.3	41.0	6.3	50.2	49.8

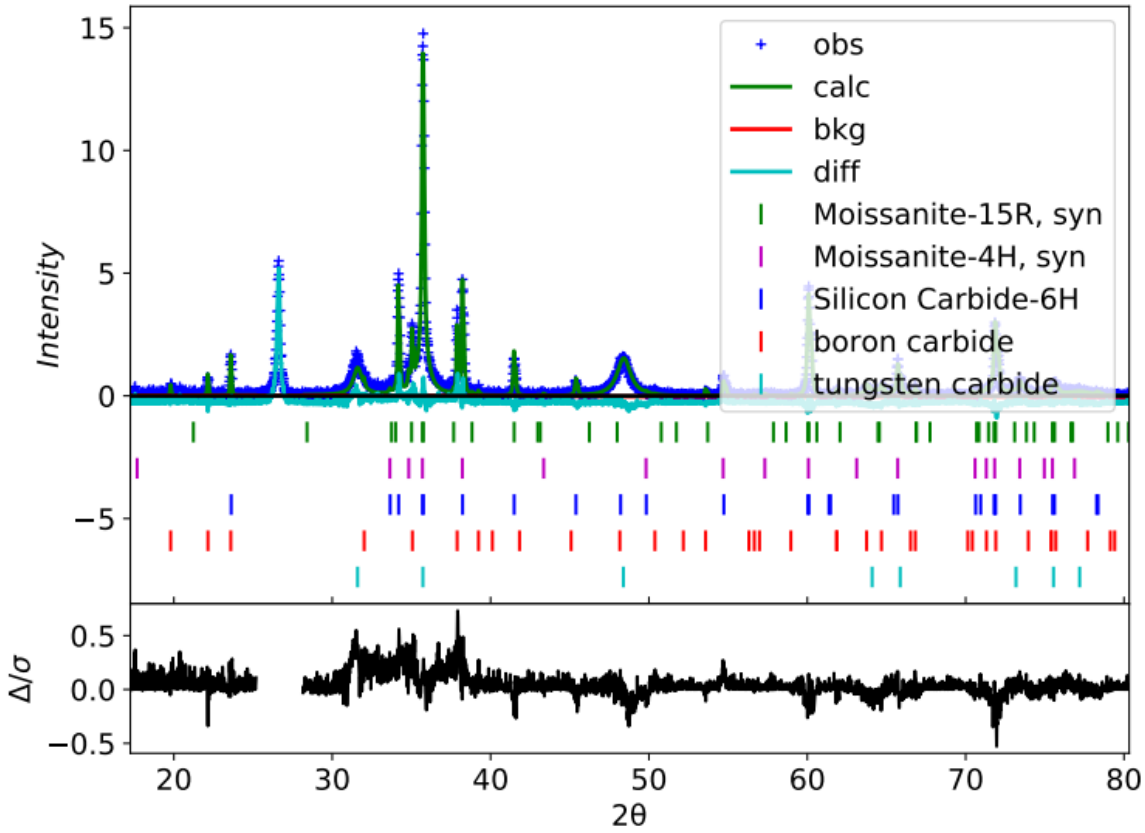

Figure 5.8. A typical result of quantitative phase analysis using the Rietveld method on XRD patterns for the 3D printed heterogeneous carbide specimens that were ground into powder. A small amount of tungsten carbide is present due to the ball milling process.

5.4.2 Residual Stress from Heterogeneity

We developed an analytical residual stress model based on previous work by the authors [80]. This model enables the fine-tuning of residual stress based on layer height, composition variation, and puck diameter. In-plane, shear, and peeling stress can all be quickly calculated to determine the feasibility of sintering specific heterogeneous designs as well as to understand non-uniform stress distribution throughout each layer. One interested result is the significant difference between symmetric and asymmetric structures, where asymmetric structures bend along a central axis parallel to layer interfaces and experience residual stress of several times less than that of similar symmetric structures. Also, as hypothesized, continuous composition variations reduce residual stress as compared to discrete composition variation. These trends are demonstrated in Figure 5.9. Further, bending in asymmetric specimens results in non-uniform stress distributions across a single layer.

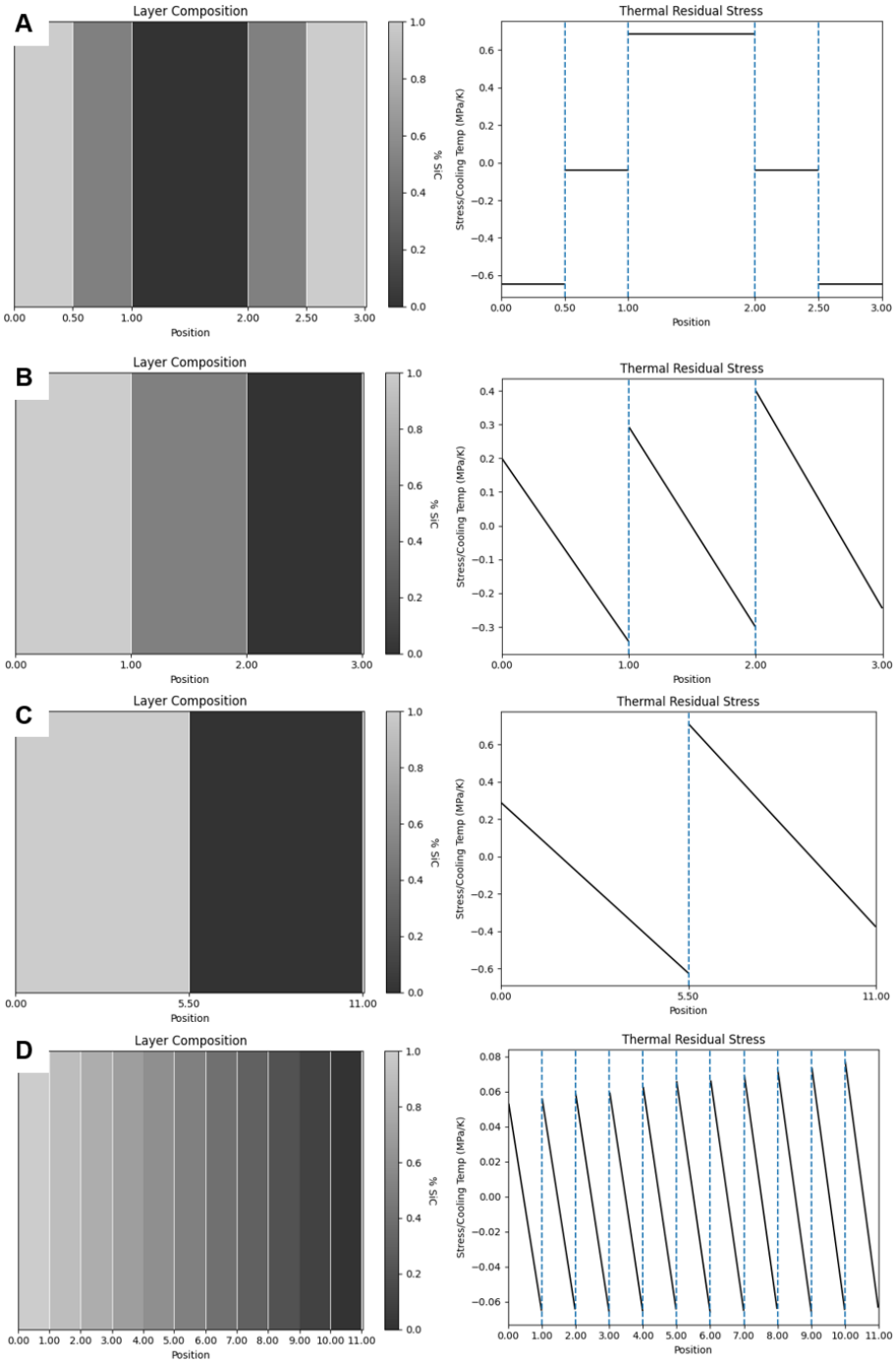

Figure 5.9. Heterogeneous design enables the tailoring of residual stress based on symmetry and variation magnitude. Comparing a) symmetric and b) asymmetric hybrid structures, bending in the asymmetric structure reduces stress by a factor of two. Comparing c) discrete and d) continuous structures, composition gradients reduce stress by a factor of 10. Bending in asymmetric specimens also creates non-uniform stress through each layer. Residual stress values are reported as MPa/K, which results in a multiplier of 1925 (sintering temperature minus room temperature).

5.4.3 Mechanical Testing

The hardness, compressive strength, and flexural strength were tested for each heterogeneous design with the goal of elucidating the effects of microstructure on mechanical performance. Knoop hardness measurements were made across layers to test compositional effects and at different loads to determine the effects of residual stress of damage evolution. Compressive strength was tested in quasi-static and dynamic regimes and at orientations perpendicular (Z) and parallel (X-Y) to layer interfaces. Results for quasi-static and dynamic mechanical testing are summarized in Table 5.2.

Table 5.2. Mechanical properties of additively manufactured heterogeneous carbide ceramics.

Specimen	Density [g/cm^3]	Relative Density	Flexural Strength [MPa]	Compressive Strength [GPa]		Knoop Hardness (HK2) [GPa]
				Quasistatic (10^{-3} s^{-1})	Dynamic (10^{2} s^{-1})	
Blend (control)	2.70	94.0%	281.6 ± 81.3	2.53 ± 0.45	3.68 ± 0.56	17.0 ± 0.7
Continuous - SiC	2.74	94.4%	249.6 ± 101.1	2.36 ± 0.56	2.75 ± 0.64	19.4 ± 0.2
Continuous - B4C			360.4 ± 18.2			17.5 ± 0.9
Hybrid	2.70	94.2%	365.9 ± 72.9	1.77 ± 0.54	2.37 ± 0.77	18.4 ± 0.5

The flexural strength and Knoop hardness values are reported twice for the continuous specimen because it is asymmetrical, meaning the top is B_4C-rich while the bottom is SiC-rich. Continuous-SiC and continuous-B_4C flexural strength values represent the flexural strength when the SiC-rich or B_4C-rich side is in tension, respectively. Similarly, Knoop hardness values for continuous-SiC and continuous-B_4C represent indents made on the SiC-rich or B_4C-rich surface, respectively. The hardness value reported for the hybrid specimen in Table 5.2 was determined with indents on top surface, which is 60 vol.% SiC. Knoop

hardness values for the blend, continuous, and hybrid specimens are plotted against composition in Figure 5.10, and were calculated based of indents made along specimen cross-sections. Hardness increases with volume-fraction silicon carbide in all cases.

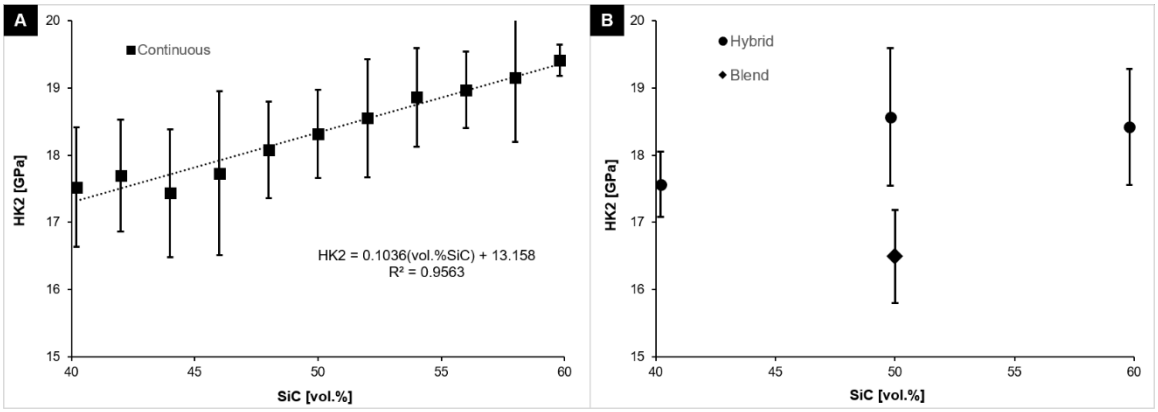

Figure 5.10. Knoop hardness values at a 2 kgf indenter load and 10 s dwell. A) HK2 values plotted against volume-fraction SiC for the continuous specimen. B) HK2 values plotted against volume-fraction SiC for the hybrid and blend specimens.

The ISE for the blend, continuous-SiC, continuous-B4C, and hybrid specimens are plotted in Figure 5.11. Performing indentation size effect testing was studied to elucidate interactions between the heterogeneous microstructure and crack propagation. Patel et al. [236] studied the indentation size effect in transparent ceramics (AlON and $MgAl_2O_4$) and observed a critical indenter load, above which fracture around the indentation became dominant over plastic deformation that tends to dominate at lower loads. However, no such mechanism was observed in the heterogenous carbide specimens tested. Instead, Knoop hardness values decrease with increasing load up to 5 kgf and then become load independent. This demonstrates the necessity of using standard indenter loads

for hardness testing of advanced ceramic materials if values in the literature are to be compared.

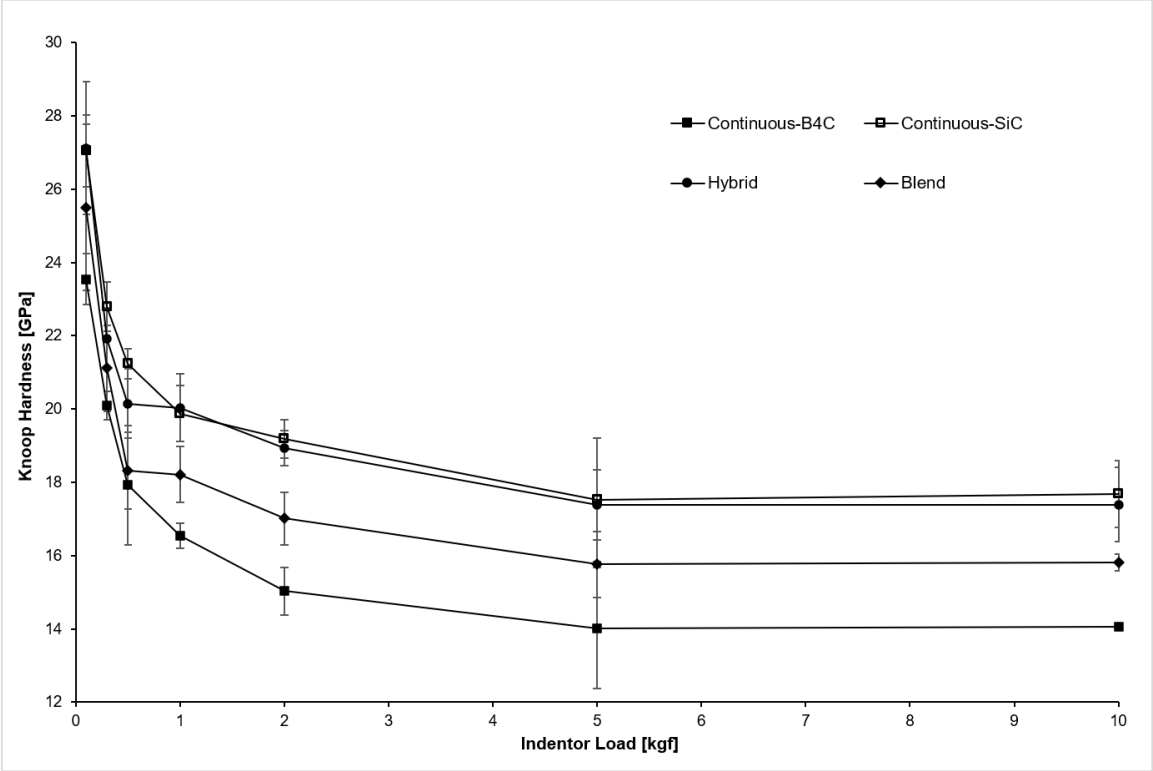

Figure 5.11. Knoop hardness values with respect to indenter load, which varies from 0.1 to 10 kgf.

*Flexural strength values are reported in Figure 5.12, with respective heterogeneous designs illustrated. The continuous specimens vary from SiC-rich (60 vol.% SiC) to B4C-rich (40 vol.% SiC) in 11 layers with 2 vol.% composition change per layer. The hybrid specimen has 9 layers that vary from SiC-rich (60 vol.% SiC) on the bottom, middle, and top with B4C-rich (40 vol.% SiC) regions in between separated by 50 vol.% SiC layers. The blend specimen is a homogeneous mixture with a composition of 50 vol.% SiC. The continuous specimens tested with the SiC-rich surface in tension had the lowest *flexural

strengths and greatest standard deviation. The hybrid and continuous-B_4C specimens showed the highest bending strengths and the blend specimen fell in the middle. These trends can be explained by the residual stress states present at the tensile surface. For the specimens that showed high bending strength, our analytical model predicts that coefficient of thermal expansion mismatch between silicon carbide and boron carbide will result in compressive stresses on the tensile surfaces of the three-point bend test. In order for a crack to propagate, the bend test would first need to overcome the compressive residual stress, which would artificially increase the flexural strength of the hybrid and continuous-B_4C specimens. On the other hand, our analytical model predicts thermal residual tensile stresses with be present on the tensile surface of the continuous-SiC specimen during bend testing, which would reduce flexural strength. As expected, the blend specimen falls in the middle due to the absences of compressive or tensile thermal stress.

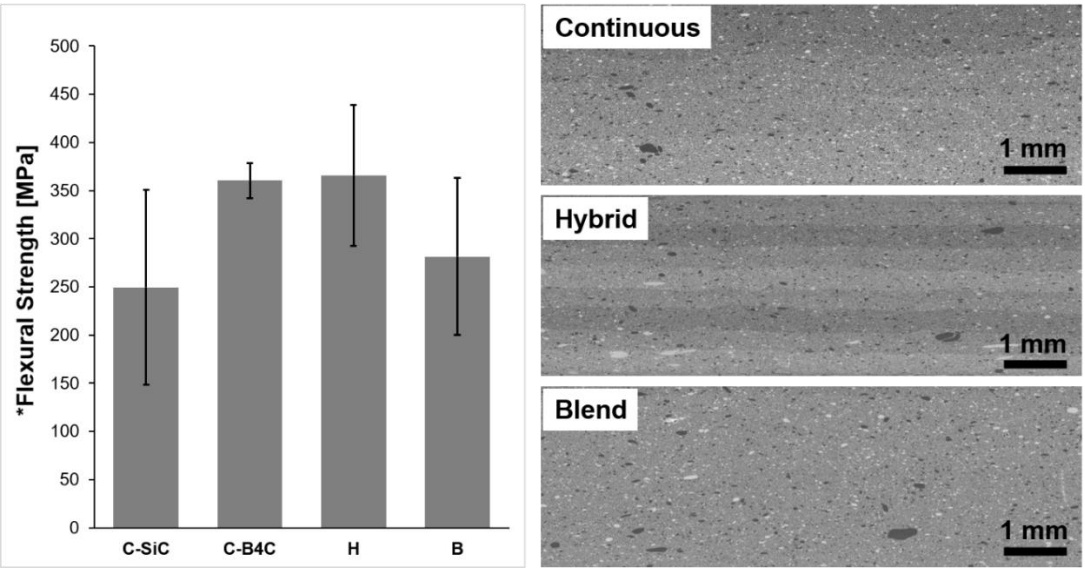

Figure 5.12. *Flexural strength values for continuous, hybrid, and blend specimen types.

Fracture surface analysis of the bend bars is presented in Figures 5.14 and 5.15. A fracture mirror can be readily identified on the fracture surface of the continuous-SiC bend bar, Figure 5.14. The fracture mirror is surrounded by Wallner lines, commonly called hackle lines, which radiate out from and point to the fracture origin. At a higher magnification, such as in Figure 5.13, cleavage step hackle lines can be identified running through single grains and are indicative of fracture interacting with preferred crystallographic orientations in silicon carbide and boron carbide. The fracture origin in Figure 5.14 can be identified as a void connected to a porous region near the tensile surface. Similarly, the fracture origin in Figure 5.15 can be identified as a large B4C inclusion with a large amount of intergranular porosity. The fracture surfaces in Figure 5.16 show an interesting phenomenon where the origin, a group of large pores, doesn't link up with the tensile surface of the hybrid bend bar. This bend bar showed the highest *flexural strength of 457 MPa, but due to the fracture origin being away from the tensile surface, the actual tensile stress that caused failure is less than 457 MPa as it is closer to the neutral axis. In addition, the fracture mirror has a sharp transition that is parallel to the tensile surface of the bend bar. The reason this fracture mirror isn't the typical elliptical shape is due to the interaction with the residual stresses, where the stress state changes after two layers and the mirror transitions into hackle lines. This change in behavior from the continuous specimens can be explained by the much sharper composition variation (10 vol.% SiC) in the hybrid specimen compared to the

continuous specimen (2 vol.% SiC). The fracture surface in Figure 5.17 shows the fracture origin as an unidentified phase, likely an impurity in the bulk powder, within a B_4C inclusion. Electron micrographs of the fracture surface of a hybrid bend bar are shown in Figure 5.18. Images collected by the backscatter detector (Figure 5.18A) and secondary electron detector (Figure 5.18B) are composited to illustrate the significant effect that the structure, a thus residual stress state, has on the fracture propagation. Large fracture steps can be seen aligned with compositional variation, which indicates residual stress can tailor crack propagation. On this larger scale, the inclusions seem to have a slight effect of crack propagation, because large inclusions (greater than 50 μm diameter) show up as dimples on the fracture surface. However, this only occurs outside of the fracture mirror, and it is our hypothesis that the interaction of crack propagation with meso- and microscale features in heterogeneous ceramics is rate dependent. This is supported by Figure 5.18, where the fracture steps appear past the neutral axis once enough energy has been released and the crack propagation slows down (again, indicated by a transition from the fracture mirror to hackle lines). On the other hand, at the initiation of failure (near the tensile surface and within the fracture mirror) the fracture surface and crack propagation are entirely transgranular. These findings are reinforced by failure analysis done on fragments from compressive test specimens.

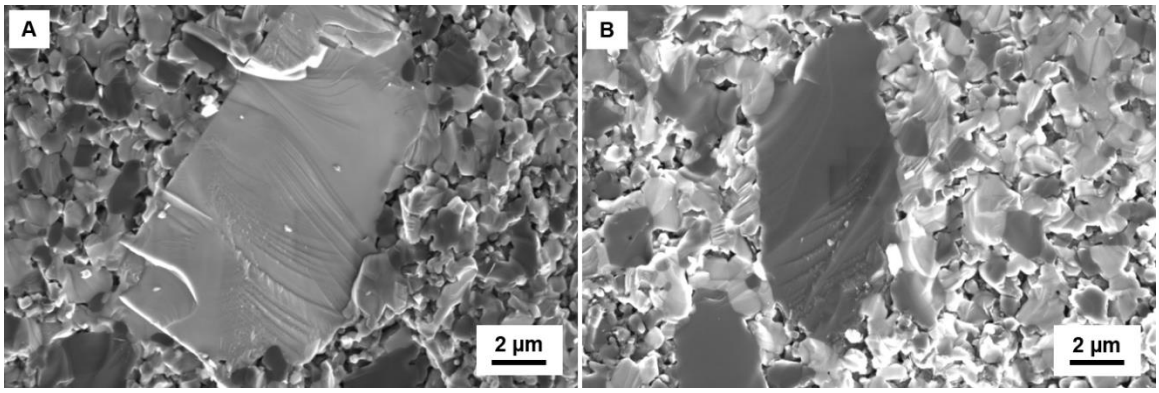

Figure 5.13. Cleavage step hackle lines show an interaction between fracture propagation and the preferred crystallographic orientations in large grains of A) SiC and B) B_4C.

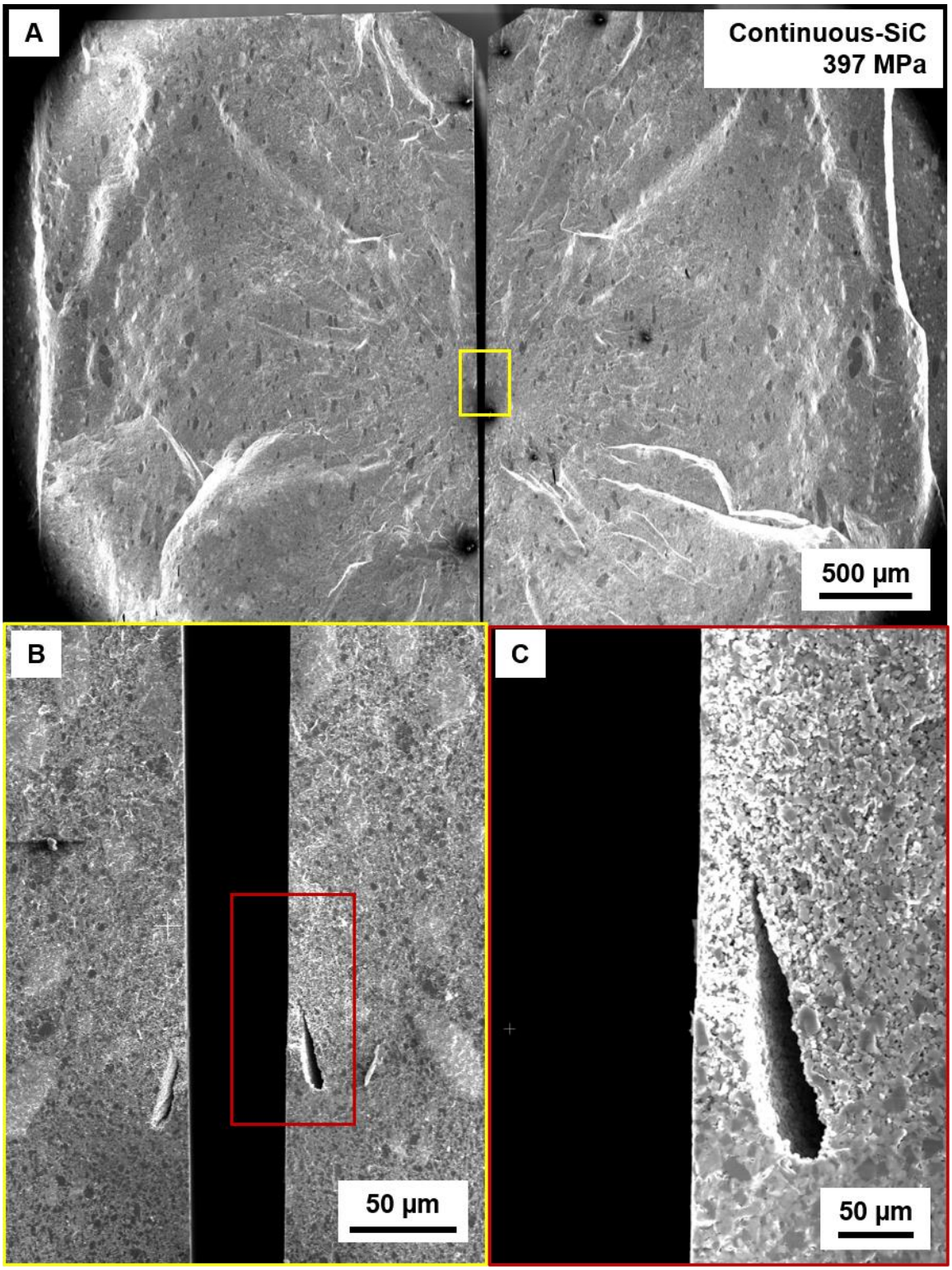

Figure 5.14. Fracture surface of a continuous bend bar. The tensile surface was on the SiC-rich side. A-C) SEM images show a porous region caused failure at a stress of 397 MPa.

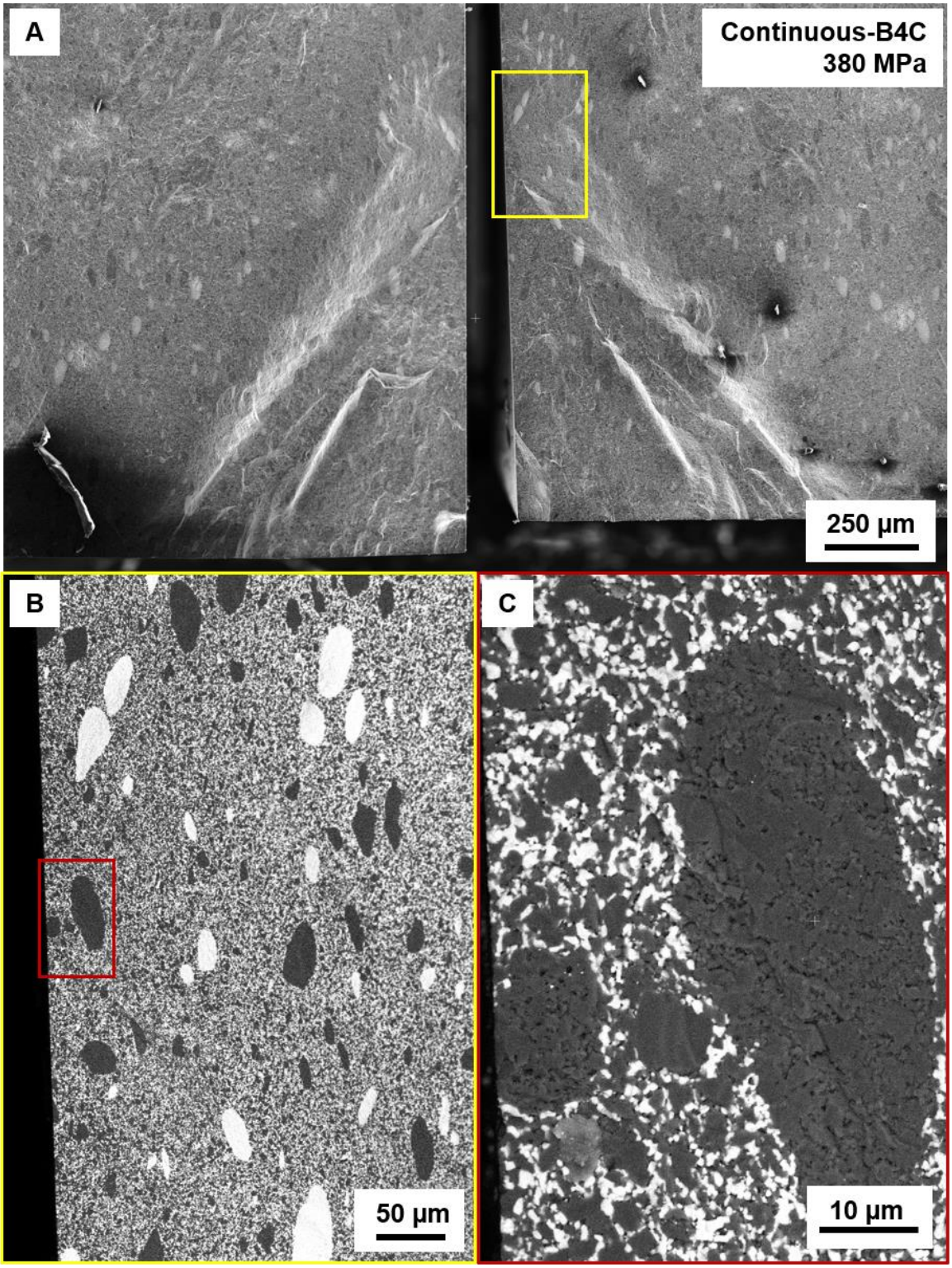

Figure 5.15. Fracture surface of a continuous bend bar. The tensile surface was on the B_4C-rich side. A-C) SEM images show a porous B_4C inclusion caused failure at a stress of 380 MPa.

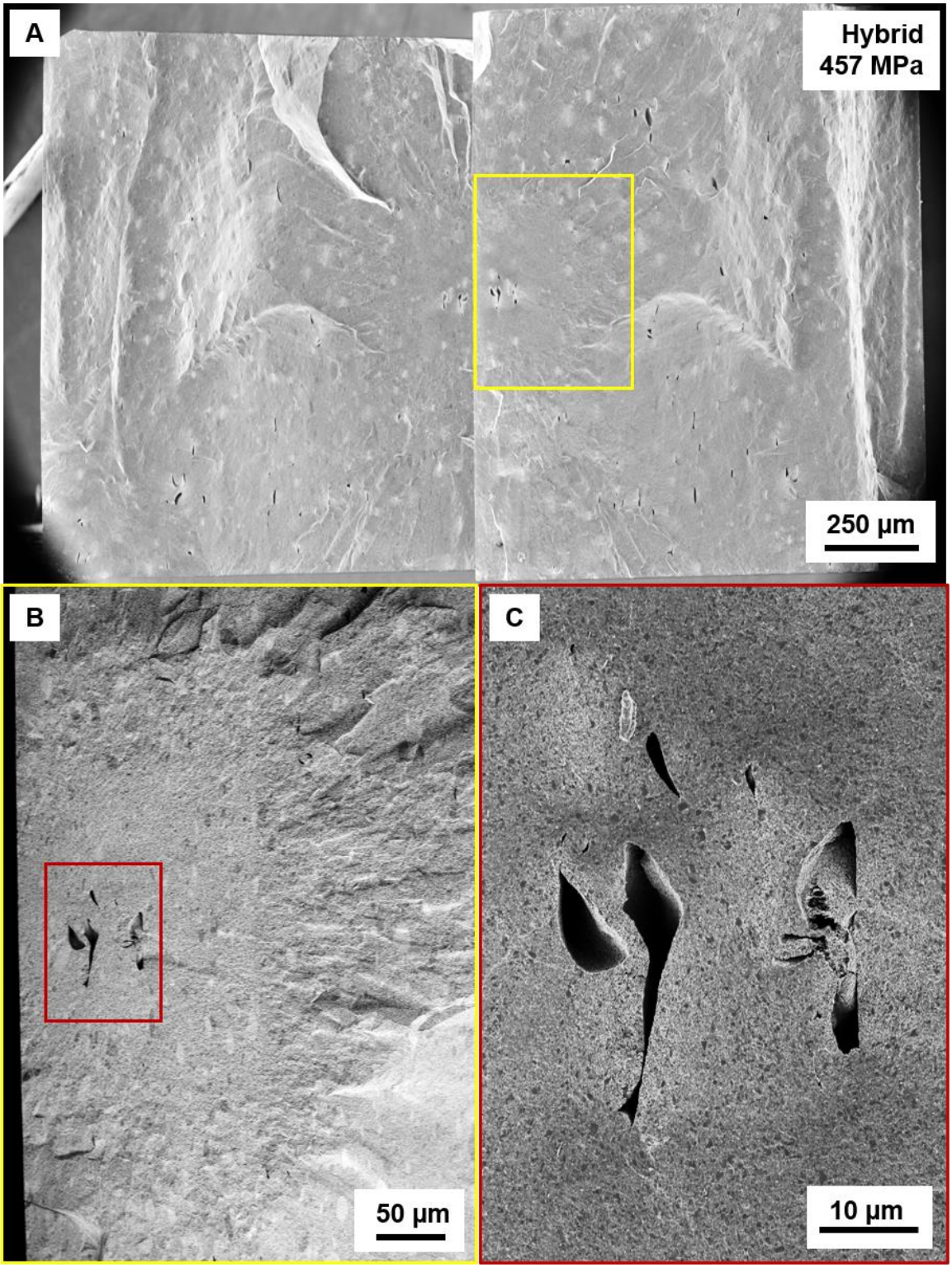

Figure 5.16. Fracture surface of a hybrid bend bar. A-C) SEM images show a pronounced fracture mirror that extends through the first two layers and then transitions into hackle lines.

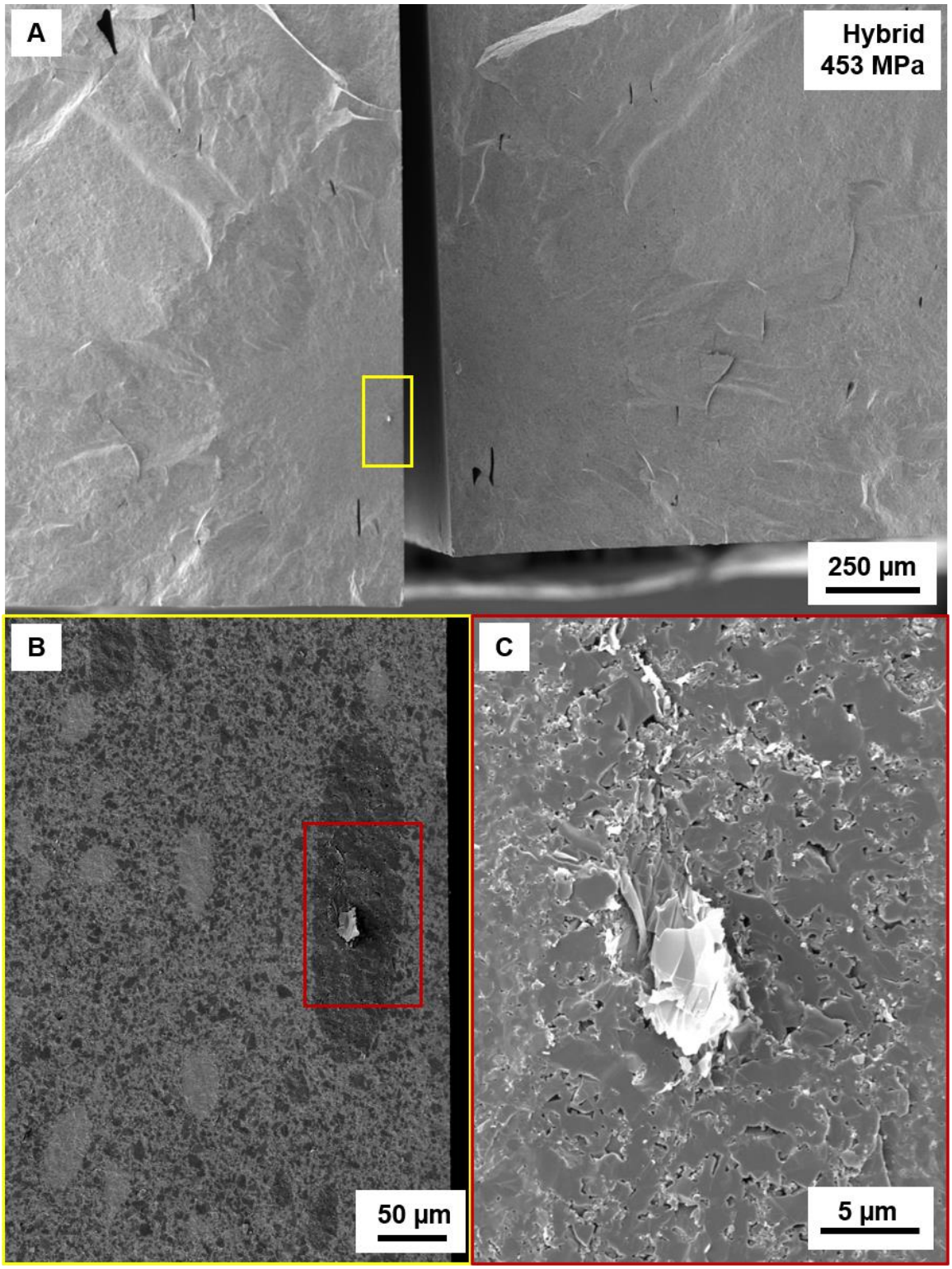

Figure 5.17. Fracture surface of a hybrid bend bar. An unidentified particulate within a porous B_4C inclusion caused failure at a stress of 453 MPa.

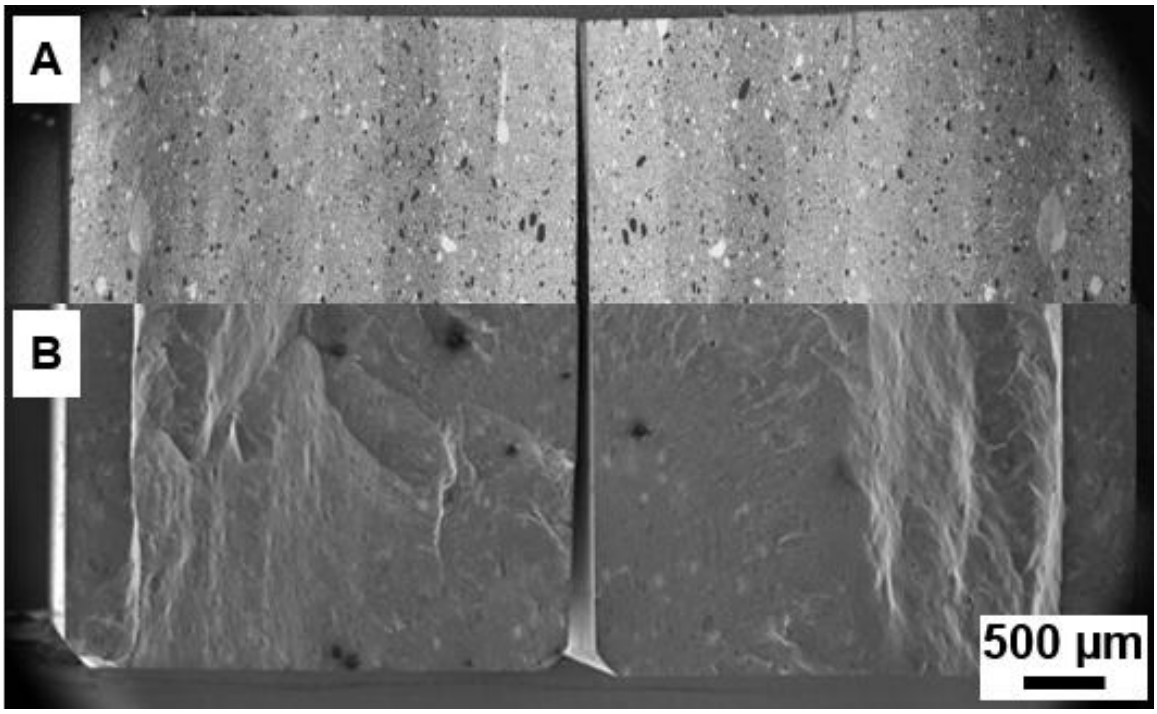

Figure 5.18. Fracture surface of a hybrid bend bar as a composite between A) backscatter and B) secondary electron microscopy showing the fracture steps perfectly align with layer interfaces.

The compressive strength of the 3 mm x 3 mm x 3 mm heterogeneous carbide cubes is presented in Figure 5.19. Cubes were tested in dynamic and quasi-static compression with strain rates of 10^{2} s^{-1} and 10^{-3} s^{-1}, respectively. A clear trend of increasing compressive strength with increasing strain rate is demonstrated, even across different sub-groupings including by orientation or heterogeneous design type. Farbaniec et al. [237] observed a significant orientation effect on the compressive strength of hot-pressed boron carbide cubes. It was determined that hot pressing driven texturing of free-carbon rich inclusions (long axis normal to hot pressing direction) lead to low compressive strength in the hot pressing direction due to wing cracks favoring the flake-like carbon inclusions. The compressive stress of cubes tested in the study did not

have any orientation effect. This finding is likely due to the B_4C and SiC inclusions in the heterogeneous carbide cubes being more intimately bonded to the matrix than the free-carbon rich inclusions. A different study on the orientation effect of hot pressed boron carbide-silicon carbide materials (that did not have large flake-like second-phase inclusions) on compressive stress also did not find any significant difference [238]. However, it is still interesting that the residual stress state doesn't interact with micro-crack growth differently based on orientation. In fact, contrary to our hypothesis that compressive stresses within the heterogeneous cubes would improve compressive strength, the compressive strength trends from this study seem to indicate that stress free (at least in terms of CTE mismatch stress) specimens have a higher compressive stress. The authors now believe that the tensile stresses within the B_4C-rich layers of the hybrid speed up the overall coalescence of microcracks that eventually lead to failure. It is still unclear why this effect doesn't appear to be related to testing orientation. Through the SEM analysis of fragments, it is found that compressive failure under both quasi-static and dynamic strain rates results in transgranular fracture as shown in Figure 5.20.

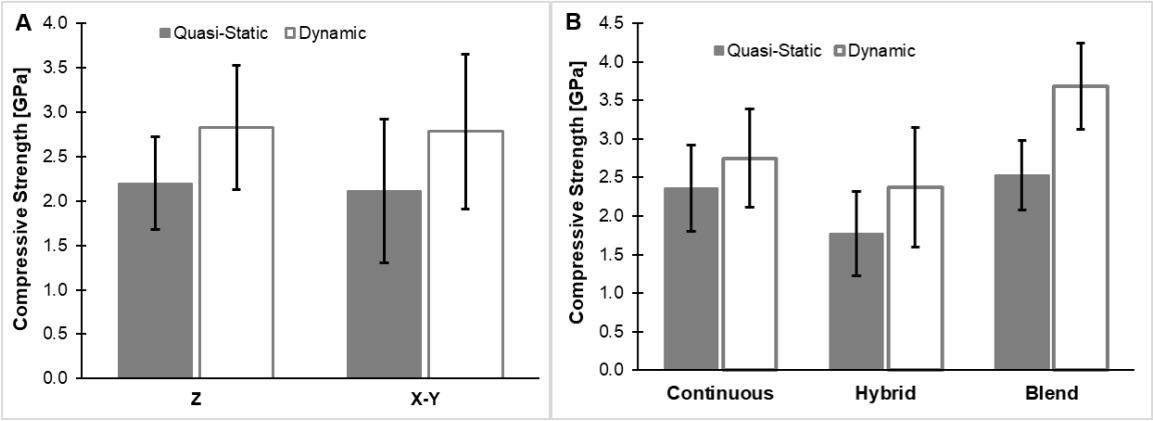

Figure 5.19. Compressive strength with respect to strain rate graphed as a function of A) testing orientation and B) heterogeneity.

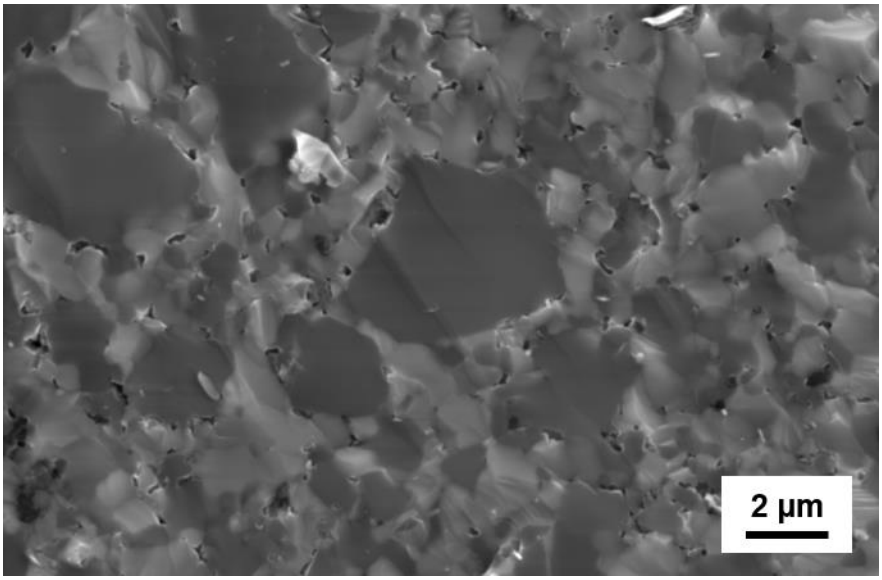

Figure 5.20. Fracture surface of a dynamic compression test specimen illustrating the transgranular fracture behavior.

5.5 Summary

5.5.1 Conclusion

DIW processing of advanced ceramic materials using an auger to provide high-shear mixing provides a path for tailoring meso- and microstructure features. Two types of heterogeneous designs, continuous (gradient) and hybrid

(layered-gradient), were compared against a homogeneous blended design of a single composition. The composition variation (heterogeneity) led to thermal residual stresses. The hardness, *flexural strength, and compressive strength were tested and discussed with respect to heterogeneity. Hardness values, using a Knoop indenter, showed an increasing trend with increasing SiC volume-fraction. The carbide materials fabricated in this study all showed an indentation size effect up to indenter load of 5 kgf, after which hardness became load-independent. The *flexural strength of the materials was dependent of the residual stress state of the tensile surface. For a compressive state, *flexural strength increased, and for a tensile state the *flexural strength decreased and the standard deviation increased. The compressive strength of cuboidal specimens excised from printed and post-processed carbide materials showed a strain rate dependance (increasing strength with rate), was not affected by testing orientation, and decreased when residual stresses (even compressive) were present.

5.5.2 Acknowledgement

Chapter 5, in part, is currently being prepared for submission for publication of the material. J. Pelz, N. Ku, W. T. Shoulders, L. R. Vargas Gonzalez, M. A. Meyers. The dissertation author was the primary investigator and author of this paper.

CHAPTER 6. DESIGN AND TESTING OF AN AFFORDABLE 3D PRINTED PROSTHESIS

6.1. Abstract

Recent advances in 3D scanning and computer-aided design enable the creation of ultra-personalized medical devices based on a patient's 'digital twin' or computer-generated model from 3D scan data. Medical devices, such as prosthetic limbs and orthotic braces, can be designed around the patient's digital twin to optimize fit and function, leading to improved comfort and medical outcomes. However, the leap in scanning and modeling technologies has left behind traditional subtractive manufacturing processes, such as milling, where the complex, organic geometries necessary to support or replace human limbs aren't feasible. For this reason, several research groups have turned to additive manufacturing because of its ability to fabricate parts with complex geometry. A significant challenge for additive manufacturing techniques is certification, especially for medical devices where each part is unique. All common additive manufacturing techniques are layer-by-layer processes, and thus suffer from anisotropic mechanical properties, where in-plane mechanical strength is significantly higher than interlayer bonding strength.

This chapter explores the fused-filament fabrication technique, from the material extrusion family of additive manufacturing processes, for the creation of a transtibial prosthetic limb. The process-structure-property relationships to tie mechanical properties to FFF printing parameters are explored for several

engineering-grade thermoplastic materials, with and without chopped fiber. Unfilled nylon was found to have an optimal balance of interlayer bonding strength and flexibility for prosthetic devices. Following the international standard for the certification of lower-limb prosthetic devices, the 3D printed single-piece transtibial prosthesis was tested and passed all require loading.

6.2. Introduction

6.2.1. The LIMBER Project

LIMBER combines the latest in scanning, digital design, and additive manufacturing technologies to develop affordable and personalized ‘unibody’ prosthetic devices. We leverage LiDAR and structured light scanning embedded in smartphones to create a digital twin of the patient. Using digital design, scan data is transformed into a personalized device that can be 3D printed. This unique approach enables us to print the entire prosthesis in a single piece while retaining multi-axial dynamic gait performance through our patent-pending design (PCT/US22/11939). Our ‘unibody’ design is the key to unlocking the benefits of digital design and 3D printing, because alignment and functionality are translated from scan data to printed product.

6.2.2. The Prosthetic Accessibility Crisis

In 2017, the World Health Organization (WHO) estimated that globally there were 35-40 million people in need of prosthetics or other assistive devices, with this number expected to double by 2050 [239]. Only 5-15% of people in need have access to prosthetics or other assistive devices, in both underserved

and developed countries. As a result, a staggering 34-38 million people, 2.1 million of whom are in the United States, live restricted and often painful lives. Among the contributing medical conditions that are causing more than 185,000 Americans to lose limbs every year are vascular disease (54%), trauma (44%), and cancer (2%) [240]. People with diabetes are especially prone to vascular problems necessitating lower limb amputation and this situation has been exacerbated by the COVID-19 pandemic. The elderly, particularly in aging populations with an increased incidence of diabetes, are especially at risk. Mobility and health-related issues resulting from amputation adversely affect patients' quality of life and, particularly in children and adolescents, may result in psychological and psychosocial issues as well [241]. Recovery and rehabilitation are adversely affected by the cost and manufacturing time of prosthetics. This situation is particularly serious in developing countries where amputees often have limited access to medical facilities and experienced practitioners.

6.2.3. Background on Transtibial Prosthetic Devices

Transtibial, or below-knee, prosthetic devices are necessary when an amputation is made in the calf section, wherein the tibia is shortened, but the amputee still has function of their knee. Conventional transtibial prosthetic devices are formed from multiple expensive components. Patient specific designs are typically achieved by manual molding, sculpting and composite lay-up to fabricate the socket, and then assembling an appropriate prosthetic from expensive 3rd-party components.

Figure 6.1. Traditional transtibial prosthetic limb with composite socket, metal pylon, composite foot-blade, and pyramid connectors for alignment.

The three basic components of a conventional transtibial prosthetic limb, Figure 6.1, include the socket, pylon, and ankle-foot complex. The socket attaches the prosthesis to the wearer, such as via corsets, straps, lock-pins, or vacuums. Sockets are typically made from composite materials such as carbon fiber reinforced polymer (CFRP). The pylon is commonly made of aluminum or CFRP and is used to adjust height and transfer load between the socket and foot. Connections between socket, pylon, and ankle-foot complex can be made with pyramid connectors, which allow for proper trochanter(hip)-knee-ankle (TKA) line adjustment. Adjustable prosthetic devices are called endoskeletal systems and are very popular for a number of reasons, including greater flexibility, lower weight, improved gait performance and better comfort, among other things [242].

If components are rigidly fixed together and cannot be aligned post-fabrication, the device is an exoskeletal system. The ankle-foot complex serves to interface with the ground and can be active or passive to provide proper gait mobility. Simpler passive systems are stiff and don't enable energy capture and release, which results in high metabolic cost for walking and an asymmetrical gait. High-performance passive systems use special materials and designs to store and release energy during the gait cycle to reduce metabolic cost of walking and increase comfort and functionality. Active systems use powered motors, servos, and sensors to control the gait cycle and can significantly enhance performance. However, active systems are prohibitively expensive, less reliable, require a power-source, and very difficult to access for the majority of the world's amputee population.

The fitting process for a conventional prosthetic device is complex and expensive, requiring multiple steps. Even more problematic is the complexity of making a comfortable and functional prosthesis. Prosthetists require many years, if not decades, of experience to be able to provide effective prosthetic care using traditional molding and sculpting processes. One of the main reasons amputees choose not to wear their device is an uncomfortable socket, and the socket will only be as good as the prosthetic who shapes it. Further, to solve the prosthetic accessibility crisis, it is estimated upwards of 75,000 more prosthetists are needed worldwide [243]; training new prosthetists is an expensive time-consuming endeavor.

Designs of the ankle-foot complex have benefited from advancements in materials science and manufacturing technology. In general, whether the foot-ankle complex is active or passive, the top of the complex includes a horizontal edge to offer a connection with the pylon. The Solid Ankle Cushioned Heel (SACH) model is a simple passive prosthetic foot having a resilient foot inset. The static design of the SACH foot, results in asymmetric gait characteristics, high metabolic costs, and low energy return benefit [244]. While basic prosthetic foot models similar to the SACH model are commonly used, new materials and designs are emerging. Passive energy storing and return (ESAR) prosthetic feet utilize spring-like materials, such as carbon fiber composites, to store and release energy during the gait cycle [245]. Passive ESAR type prosthetic feet include running-blades, the Niagara foot, and the Seattle foot. The negative and positive work output from these feet (during the gait cycle) are directly related to their geometry and material properties [246]. Running-blades are carbon fiber blade-type feet that are designed for running and use large displacements to store and release energy. The Niagara foot, a futuristic-looking solid ankle foot, is made from Hytel. Hytel is a thermoplastic polyester elastomer that provides superior durability and energy return. The Niagara foot has been tested to more than 3,000,000 loading-cycles and shows increased durability over carbon fiber feet [247]. Seattle feet incorporate molded and manufactured components of various materials including carbon fiber, nylon, and metal. Seattle feet can either

be bolted directly to the pylon or attached with special adapters that simulate ankle articulation [248].

More recent efforts focus on digital fabrication and additive manufacturing. Summit [249] describes a method to create an exoskeletal prosthetic limb that can be simultaneously printed in one piece from a single material. Although the designs disclosed in this patent are novel, exoskeletal systems have lost favor over endoskeletal systems due to many limiting factors. One such important factor is the inability to adjust the design post-fabrication, which is a common problem for all amputees and even more important for new amputees whose amputated limb will change shape significantly during the first several months to 1 year. If exoskeletal devices are used for these newer amputees, the patient will either endure a painful, poorly functioning socket or must go back to the prosthetist to be remeasured and a new device constructed. One disclosed design includes elongated members that span the length of the lower leg having front and rear members that resemble the outer shape of the contralateral limb. Weight is distributed between the front and rear members. These members are coupled with a basic solid foot and are printed in a single photopolymer material. The use of a single material has significant disadvantages in functionality, because regions that would benefit from being stiff have to compromise with regions that should be flexible and compliant. Further, while the Vat Photopolymerization method, specified by Summit as the preferred printer type, can produce detailed parts with fine features, photopolymers generally have

lower strength, flexibility, and durability compared to thermopolymers. Other disclosed designs include ball and socket connections between an elongated front member to the foot. Other designs include multiple mechanical linkages in the knee area and ball and sockets in the ankle area. The mechanical linkage and ball and socket connections are likely to wear and become loose after many cycles of movement, which will negatively affect the gait of a user. The simple foot and solid elongate supports that extend from knee to foot will be relatively thick and heavy to meet requirement for applied forces. The use of photopolymer material will lead to catastrophic failure if loads exceed material capability, and could result in a severely injured patient. Layman et al. [250] describes imaging and digital processes to make a 3D printed socket. A check socket is first fabricated and matched with traditional alignment connectors, pylon, and foot/ankle componentry. Alignment and socket fit adjustment is achieved through manual methods requiring an experienced prosthetist and patient visits. A digital copy of the aligned device is then produced using a scanner. The digital copy is used to design a patient-fit socket with attachment points aligned for the specific patient. The printed socket may improve fit, but the time-consuming and manual fitting and alignment process will reduce the efficacy of this method. Further, the use of traditional hardware, connectors, pylon, and ankle-foot complex will increase cost and weight, while reducing time savings and customization afforded by a digital process. Valenti [251] describes monolithic socket and rod-shaped solid pylon that can be fitted to a prosthetic foot. The creation and fitting

of prosthetic devices remains expensive. Most patients are fitted with prosthetic devices that are formed from separate and expensive components. Separate components add weight, complexity, and expense. Recently, a Japanese company Instalimb [252] has used 3D-CAD, 3D printing and machine learning (AI) technology to create a 3D printed transtibial prosthetic. The printed prosthesis is a printed socket parts that is then joined with a standard solid pylon and foot. The printed socket offers a cost and fitting advantage compared prior devices. Fitting of a pylon and foot still requires skill and can be expensive.

In the prosthetic and orthotic sector digital transformation has been seen over the past decade with the introduction of new digital workflows in the dental and orthopedic implant fields. The introduction of digital workflows and additive manufacturing in the prosthetic sector has remained fairly uninvestigated. Some early attempts focused on the replacement of components from traditional prosthetic assemblies. Some of these works have demonstrated the feasibility of using AM to produce certifiable custom prosthetic sockets. Some of the most advanced work in this topic has studied the use of multi-material 3D printing to optimize and generate region compliant sockets that demonstrated improved comfort and functionality [253,254]. Osteointegrated prosthetic sockets use attachment points embedded in the residual bone, a method recently approved by the United States Food and Drug Administration [255]. Yet there is still a lot of room for innovation in this field. Our previous work on the design of a monocoque transtibial prosthetic leg [14], shown in Figure 6.2, lays the groundwork for the

research presented in the Chapter. The aim of this work is to validate the use of AM, more specifically Fused Filament Fabrication (FFF), to produce a safe and certifiable unibody below the knee prosthetic leg.

Figure 6.2. The LIMBER UniLeg, a patent-pending 3D printed single-piece transtibial prosthetic limb [14].

6.2.4. Thermoplastic Additive Manufacturing

Recently, a greater focus on the use of AM to produce functional, end-use parts from polymeric materials. One of the most common techniques is fused-filament fabrication (FFF) due to low complexity and high versatility. Fused-filament fabrication falls into the material extrusion family of additive manufacturing techniques [4]. FFF is among the most widely used, researched, and flexible AM techniques due to the simple process, cheap feedstock material, and low-cost equipment. The functional and structural requirements of each application determine the process parameters and materials selected. Typical

polymers used for 3D printing are ABS, PLA, PC, PETG, PA, PEI and PEEK. The thermoplastic filaments used in FFF processes enable the production of components with a wide range of mechanical properties, and thus afford a greater design space than power and resin feedstock materials. Further, the FFF process is one-dimensional, meaning material is extruded at a single point from the nozzle orifice that can be represented by a voxel, or volumetric (three-dimensional) pixel. This leads to an affinity for multi-material capability, which is contrasted by liquid vat and powder bed processes, where changing material during a print is difficult to impossible.

One significant downside to additive manufacturing is the development of anisotropic mechanical properties. Processing factors responsible for the differences between inter-trace and interlayer bonding strength include infill orientation, print speed, layer height, and bonding temperature differential. Cantrell [256] studied the effects of build orientation and infill direction on the mechanical properties of ABS and PC tensile and shear specimens. Build direction was found to have a major effect on failure mechanism, where specimens printed in the Z-direction failed in a brittle manner. A volumetric flow rate that is too high will cause die-swelling (bulging material out of the nozzle tip), which can adversely affect interlayer bonding due to a reduction in contact pressure between traces.

Designed porosity coming from infill type and volume fraction, commonly called infill density, has a significant effect on mechanical properties, although in

the author's opinion cross-sectional area has been changed and thus reported values of strength, toughness, etc. are incorrectly calculated (not even mentioning the fact that most mechanical testing standards followed in these articles don't have provisions for material with major porosity, designed or otherwise). Many materials including PLA, ABS, and Nylon [257] have all been tested in tension at various infill levels with a clear trend of decreasing mechanical properties, including strength, modulus, and elongation, with decreasing infill density.

The exact effects of printing parameters on the material properties of printed specimens tend to be ambiguous due to the near impossibility of truly isolating variables. For example, many studies cite a reduced bonding strength with increasing layer height [257], especially past 50% of the nozzle diameter. However, the actual dynamics of the relationship between layer height and inter-trace and inter-layer bonding are complicated by the fact that increasing layer height means, holding other parameters constant, a higher volumetric flow rate, which can in-turn lead to under-extrusion and incomplete heating of extruded material, both of which have been identified as major inhibitors of strength. Conflicting reports on the effect of printing speed on mechanical properties have been published with claims of insignificant, increasing, and decreasing strength with increasing print speed [257]. This is likely due to poor control of other variables including temperature differential and contact pressure.

One major branch of FFF research is the development of composite parts through the use of chopped or continuous fiber, often glass or carbon fiber, and has been reviewed in-depth by [258–262]. The addition of fiber can dramatically improve strength, stiffness, durability, and temperature resistance, while also reducing printing issues such as warping, delamination, and bed adhesion. Chopped or short fiber processes show a limited improvement in strength up to around 20% tensile strength, but significantly improve stiffness and temperature resistance. Short fiber content significantly decreases thermal expansion in thermoplastic materials [263]. Continuous fiber processes have gained significant industrial traction as research has demonstrated the significant gains in strength, stiffness, etc. MarkForged produces several patented printers that enable continuous fiber FFF. Using the MarkForged Mark2, Caminero [264] studied continuous carbon, glass, and Kevlar fiber reinforced FFF and found that for a matrix of nylon, carbon fibers provided the highest interlayer bonding strength and stiffness due to their preferred interaction with nylon as compared with glass and Kevlar fibers that tended to delaminate due to poor matrix-fiber wettability. Tian [261] developed a novel continuous fiber FFF technique where fiber-matrix bonding occurs in-line during the printing process. Based on this technique, PLA parts reinforced with 27% continuous carbon fiber bundles achieved flexural strength of 335 MPa and modulus of 30 GP.

6.2.5. Certification of Lower-Limb Prosthetic Devices

In regard to prosthetic devices, the LIMBER monocoque work [14] demonstrates that AM can increase build rates by a factor of four, lower production costs by half, and require little to no post processing and alignment. The main question that remains is to prove the mechanical properties of LIMBER 3D printed devices via FFF.

To certify a prosthetic device a series of tests and best practices have been established by the International Organization for Standardization, set in ISO 10328 (Prosthetics - Structural testing of lower-limb prostheses - Requirements and test methods) [16]. Specific to lower limb prostheses, the standard ISO 10328 was created to facilitate the assessment of the conformity of lower limb prosthetic devices/structures with the strength requirements. The standard is broken down into three main components:

1) the principal structural test validates the ultimate strength and fatigue resistance of the limb;
2) the torsion test validates the ability of the limb to withstand torque in both directions; and
3) the proof strength, ultimate strength, and fatigue resistance of the ankle-foot complex.

This testing series provides a comprehensive set of loading and boundary conditions that verify the safety of a lower-limb prosthesis. The test loading level P5 is based on data from all amputees including a few whose body mass

exceeded 100 kg. The test loading levels P4 and P3 are based on locomotion data from amputees whose body mass is less than 80 kg or 60 kg, respectively.

6.3. Experimental Procedures

6.3.1. Patient Specific Workflow

The LIMBER workflow, Figure 6.3, starts with a scan of amputee via the Comb scanner app (Comb O&P, Chardon, OH), which uses the facial-recognition camera in smartphones to generate 3D models of the of physical objects. Scan data is supplemented by a patient measurement form and used to design a personalized prosthetic limb that follows the external shape of their mirrored contralateral limb. The digital design process for every device is done under the supervision of a certified prosthetist (CPO). The socket is created using scan data and patient measurements with prosthetic design software Neo (Rodin4D, Italy). The pylon with its bioinspired truss structure is created using topology optimization software nTopology (nTopology, New York, NY) controlled to implement a pylon of the invention having a unitary bioinspired truss structure of interconnected elongated supports. The multi-axial dynamic foot-ankle complex is created in Fusion360 (Autodesk, San Rafael, CA) controlled to implement a foot-ankle complex of the invention that provides multi-axial dynamic flex. Finally, alignment and blending of the socket, pylon, and foot-ankle complex into the single-piece UniLeg is done in Meshmixer (Autodesk, San Rafael, CA). The finished model is sliced into G-code the 3D printer can interpret using Simplify3D (Simplify3D, Cincinnati, OH). The FFF manufacturing process uses engineering

grade thermoplastics to produce a strong and durable endoskeletal prosthetic device. The UniLeg is shipped to a prosthetist or physician who helps the amputee put on their personalized limb and confirms a smooth, symmetric gait. If any modifications are desired, thermoforming can be used to adjust fit and alignment.

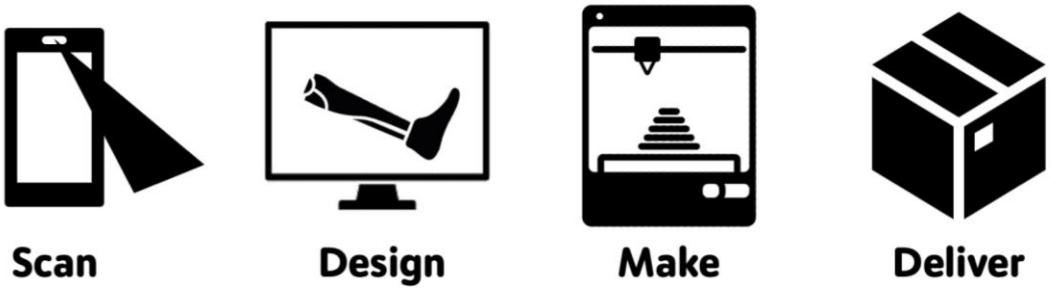

Figure 6.3. The LIMBER process starts with a scan of the amputee's limbs. Next, using digital design, the scans are transformed into a personalized prosthesis that is manufactured using a 3D printer.

6.3.2. Imaging and Modelling

Pervasively available smartphone imaging technology is useful to create 3D models of the patient. The Comb scanner app (Comb O&P, Chardon, OH) uses the front-facing facial-recognition camera available on many smartphones, e.g. the TrueDepth camera on iPhones (Apple, Cupertino, CA). Imaging, Figure 6.4, can be performed on-site anywhere in the world and the scan data and measurement form are then sent to a fabricator (or a cloud operated by the fabricator). At a minimum, scans are taken of the amputee's residual limb and contralateral side.

Figure 6.4. A smartphone is used to 3D scan an amputee's limbs using the front-facing TrueDepth camera on the iPhone.

6.3.3. Socket Design

Scan data from the amputee's residual limb is used as the starting shape for the socket, in a process illustrated in Figure 6.5. Modifications are made with Neo (Rodin4D, Italy) to properly distribute load and prevent pressure spots. The process is as follows: (1) the mesh is cleaned, smoothed, and the volume is reduced by 3% (Figure 6.5A1,2); (2) a 2 cm wide by 1 cm deep slot is carved for the patellar tendon bar, which is a primary load-bearing feature, and the medial-lateral area is compressed by 2% (Figure 6.5B1,2); (3) socket trim lines are

delineated to allow proper knee mobility and the socket walls are thickened to 4 mm (Figure 6.5C); and (4) an extruded section at the distal end is created to house the shuttle-lock (Figure 6.5D). Modification values can change from patient to patient, and this process can benefit from guidance by a CPO.

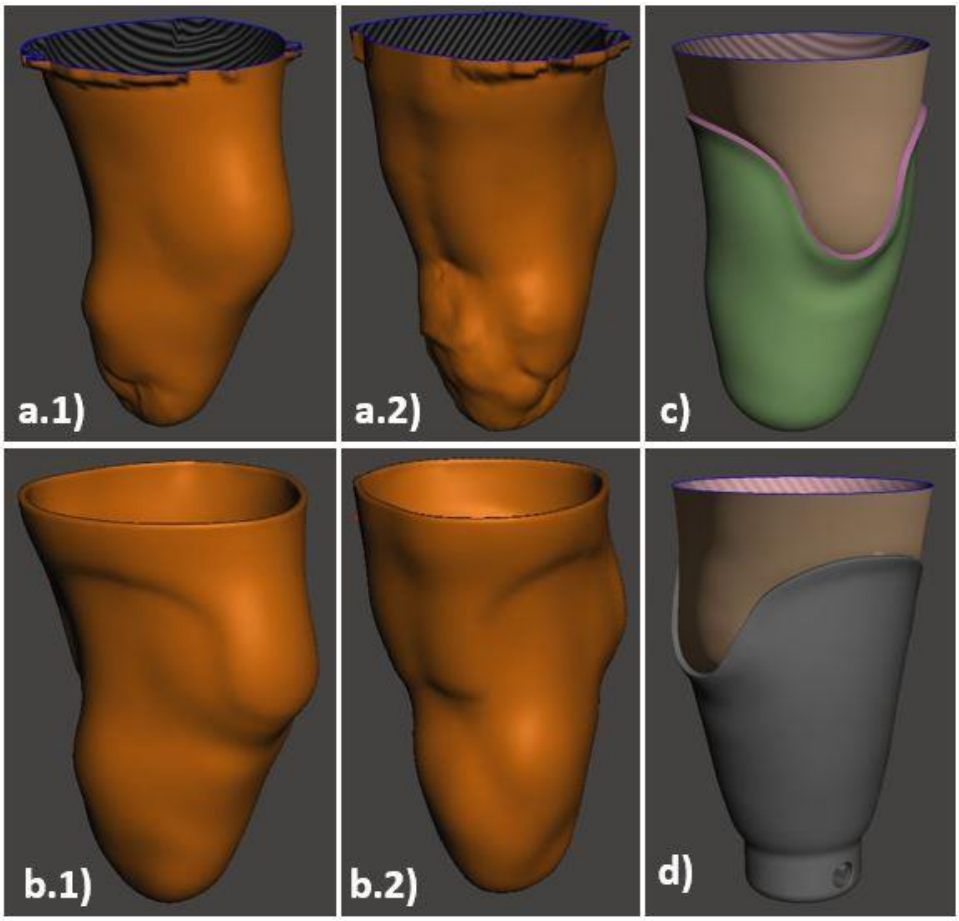

Figure 6.5. Socket modification process includes A) scan data, B) mesh processing, C) socket wall delineations, and D) addition of pinlock mechanism.

6.3.4. Pylon Design

A pylon of the invention is designed to be strong and 3D printable, while reducing material use to reduced cost and manufacturing time. The pylon is expected to withstand a series of compressive and torque loads based on patient

weight and activity level and following ISO standard 10328. Topology optimization (TO) software nTopology (nTopology, New York, NY) is used to generate an optimal truss structure consistent to provide the unitary bioinspired truss structure of interconnected elongated supports having open spaces therebetween. The mirrored model of the transtibial section of the amputee's contralateral limb is used to generate the pylon. In cases where a bilateral amputee doesn't have a sound limb, a generic transtibial limb can be selected from a database and then reoriented and scaled to fit the patient. Model preparation for TO requires the definition of design space (Figure 6.6A), where topology is optimized, and boundary condition regions (top and bottom disks in Figure 6.6A), where loads and constraints are placed. Topology optimization is performed with the objective of maximizing stiffness.

The resultant mesh, Figure 6.6B, was exported as an STL file and then imported into mesh modeling software Meshmixer (Autodesk, San Rafael, CA) to be smoothed and scaled to the correct dimensions. The final personalized bio-truss structure of the invention, Figure 6.6C, has an outer contour that follows that of the mirrored contralateral limb of the specific amputee. A significant advantage of the endoskeletal truss structure is that it can deform without buckling, which enables adjustment of alignment by thermoforming.

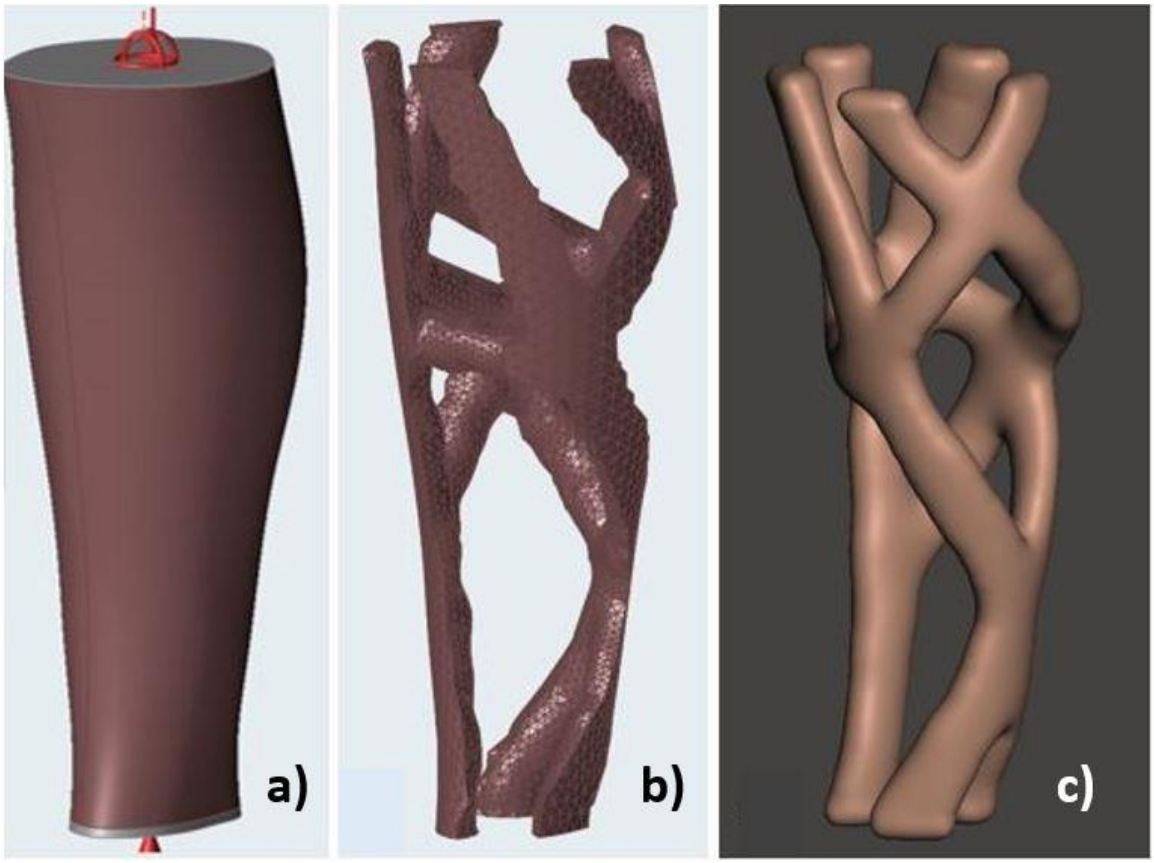

Figure 6.6. A) 3d Scan of tibial region of healthy leg. B) Topology Optimization of Pylon Region. C) Smooth version of the optimized pylon.

6.3.5. Ankle-Foot Complex

The foot-ankle complex is designed to provide a multi-axial dynamic response to enable dorsiflexion, plantar flexion, inversion and eversion motion for smooth symmetric gait performance and energy capture and return, which is illustrated in Figure 6.7A-C. As discussed above, the foot-ankle complex includes s-shaped posterior and s-shaped anterior sections that are separated from each other by a gap. This defines a split ankle that enables plantar flexion during heel-strike, demonstrated in Figure 6.7C. As the person transitions to mid-stance, Figure 6.7B, the split ankle gap closes, providing stability. Transitioning to

terminal stance, the entire foot-ankle complex coils to capture energy, Figure 6.7A, which will be released to drive forward into the next gait cycle. The top of the ankle-foot complex is blended into the base of the pylon, which provides a smooth transfer of load from the ground through the dynamic pylon up to the socket. The sole portion may include a split toe and split heel. The split toe and heel are useful for uneven terrain, where exaggerated inversion and eversion is beneficial.

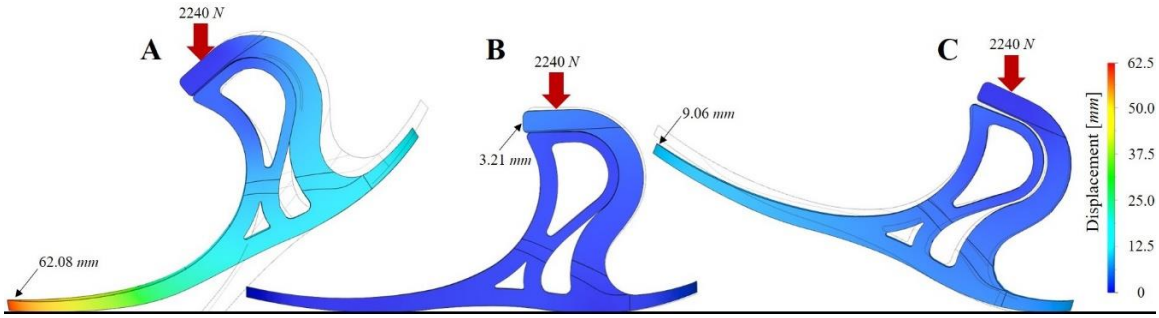

Figure 6.7. Foot unit FEA results showing deformation in A) forefoot, B) mid-stance, and C) heel loading conditions.

6.3.6. Digital Alignment and Integration

The socket, pylon, and foot-ankle complex are aligned and blended into the single-piece UniLeg in Meshmixer (Autodesk, San Rafael, CA), as illustrated Figure 6.8. Alignment is guided using the mirrored model of the contralateral limb. A cylinder is drawn that runs through the middle of the mirrored leg to align the knee and ankle positions, Figure 6.8A. The resulting unibody design, Figure 6.8B, can be fully printed in one piece. The only commercial component used is a shuttle lock and pin system to secure the residual limb in the socket. If necessary, an on-site prosthetist or physician can make minor adjustments to

alignment and socket fit through thermoforming. A heat gun is used to raise the temperature of the pylon until it is pliable, which allows manual rotation and translation in the sagittal, frontal, and transverse planes. Adjustments to fit within the socket are achieved by heating the region of interest to pliability and then using a sturdy wooden bar with a rounded end that is pressed into the region of interest to increase or relieve pressure on the patient's residual limb.

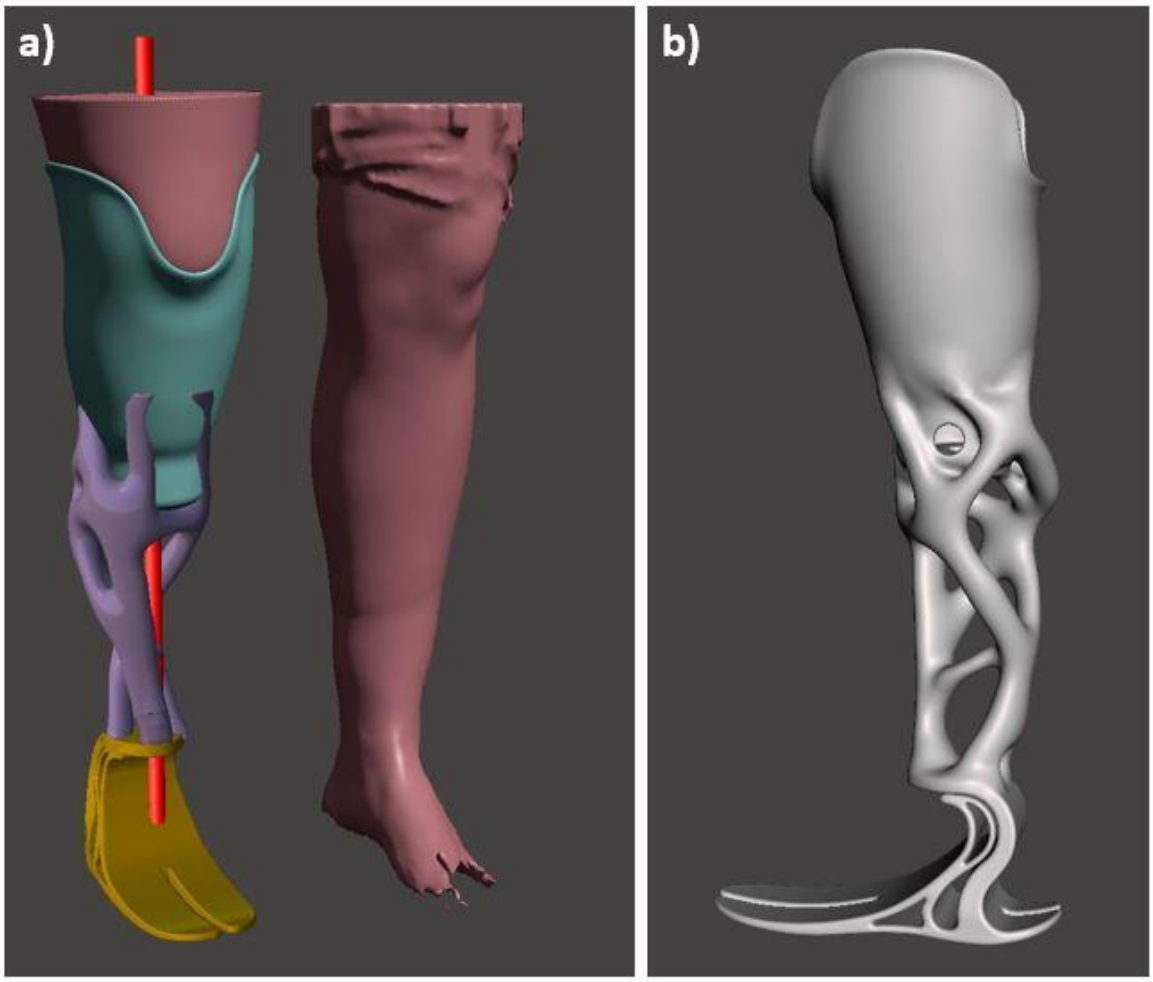

Figure 6.8. A) Using the healthy leg scan and its mirrored model we were able to properly scale and align all components so a ready to use monocoque version could be printed. B) Side view of final monocoque design.

Thermoforming is a common practice in traditional prosthetic clinics as many check sockets are thermoplastics. However, traditional prosthetic sockets often employ composite materials so fit cannot be adjusted. The LIMBER UniLeg provides a great advantage as it can be easily modified via thermoforming if a patient experiences discomfort either during initial fitting or during a follow up appointment during the device lifetime.

6.3.7. Material Selection

To achieve high-strength, engineering-grade unfilled and fiber-reinforced thermoplastics were utilized. Three materials, Nylon (PA645), chopped carbon fiber filled nylon (PACF), and polycarbonate (PC), were selected for printing the prosthetic limbs. PA645 filament was sourced from Taulman3D (Missouri, USA) and PACF and PC filament were sourced from Matterhackers (California, USA). Polyamides, commonly called nylon, are among the best mid-temperature thermoplastic materials used in additive manufacturing [18]. PA has excellent layer adhesion, toughness, and elongation. For medical device applications, the high toughness and elongation of nylon prevent catastrophic failures that can lead to serious injury [19,20]. PA also has excellent fatigue resistance, which is important for our prosthetic limb application where cyclic loading (walking) exists. Nylon reinforced with carbon fiber have strength-to-weight ratios approaching that of aluminum, high durability, and good thermal and chemical resistance [21]. Fibers also significantly improve the printability of polyamides because they stabilize shrinkage resulting from the liquid-solid phase transformation.

Polycarbonates have the highest toughness of mid-temperature thermoplastics, an important property for the dynamic environments that prosthetic components experience.

6.3.8. Manufacturing

To print the single-piece prosthesis developed in this study, a large-format fused-filament fabrication (FFF) 3D printer was developed that can regulate chamber temperature (up to 80 ºC) and has a hardened nozzle that can achieve temperatures up to 500 ºC. A super-volcano hotend (E3D, Oxfordshire, UK) with a 1.4 mm nozzle was used to achieve high flow rates (up to 12 times that of common desktop FFF printers). Prusaslicer, open-source slicing software, was used to prepare G-code for the printer based on the digital model of the prosthesis. Printing parameters such as layer height (0.7 mm), speed (40 mm/s), and trace width (1.4 mm) were kept constant for all tested components, while other parameters such as nozzle temperature (235-275 ºC), bed temperature (90-155 ºC), and fan speed (0-100%) were set within recommended ranges from the filament manufacturers. For all components, a chamber temperature of 70 ºC was used to reduce thermal stresses during the printing process and improve layer adhesion. In fact, PA645 (unfilled nylon filament) components were not able to be printed without the actively heated chamber. Printing platforms with similar specifications are commercially available, such as the Delta WASP Industrial 4070 X (3Dwasp, It), which costs roughly $20,000 USD. The majority of FFF

printers are significantly less expensive than the multi jet fusion 3D printers (HP, USA) that are often used to print orthotics and prosthetic sockets.

6.3.9. Mechanical Testing

Figure 6.9 demonstrates the testing orientations for the ankle-foot complex. The heel side wedge was prescribed with an angle of 15 degrees from the horizontal plane and the forefoot wedge with an angle of 20 degrees. The longitudinal axis of the foot shall also be turned by 7 degrees to give a toe out position of the ankle-foot device or foot unit. For the highest loading level of P5, the proof, ultimate, and cyclic loads are specified as 2240 N, 4480 N, and 1330 N, respectively, as shown in Table 6.1. The cyclic test oscillates between a minimum (50 N) and maximum (1330 N) test force to simulate one gait cycle. Loading rate for each test is specified at 100-250 N/s. The standard requires a total of 2 million cycles to certify the durability of components.

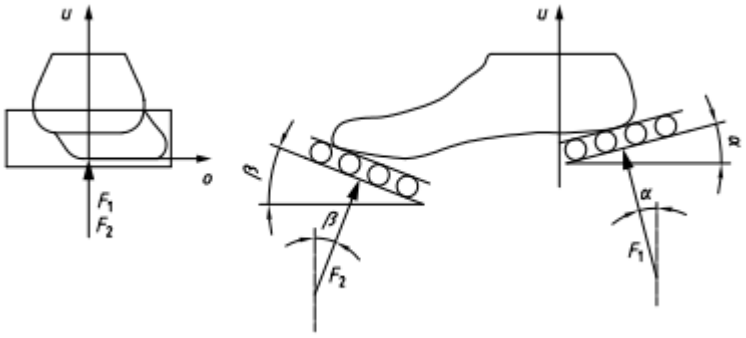

Figure 6.9. The ankle-foot complex should be loaded at an outset angle of 7 degrees. For heel and toe loading, angles of 15 and 20 degrees should be used, respectively.

Table 6.1. Test forces and loading conditions for ankle-foot devices [16].

Test procedure and test load			Unit	Test loading level (P_x) and test loading condition (F_{1x}; F_{2x})					
				P5		P4		P3	
				Heel loading, F_{1x}	Forefoot loading, F_{2x}	Heel loading, F_{1x}	Forefoot loading, F_{2x}	Heel loading, F_{1x}	Forefoot loading, F_{2x}
Static test procedure	Proof test force	F_{1sp}, F_{2sp}	N	2 240	2 240	2 065	2 065	1 610	1 610
	Ultimate static test force	$F_{1su,\ lower\ level}$, $F_{2su,\ lower\ level}$	N	3 360	3 360	3 098	3 098	2 415	2 415
		$F_{1su,\ upper\ level}$, $F_{2su,\ upper\ level}$	N	4 480	4 480	4 130	4 130	3 220	3 220
Cyclic test procedure	Minimum test force	F_{1cmin}, F_{2cmin}	N	50					
	Cyclic range	F_{1cr}, F_{2cr}	N	1 280	1 280	1 180	1 180	920	920
	Maximum test force	F_{1cmax}, F_{2cmax} $F_{xcmax} = F_{xcmin} + F_{xcr}$	N	1 330	1 330	1 230	1 230	970	970
	Mean test force	F_{1cmean}, F_{2cmean} $F_{xcmean} = 0{,}5\ (F_{xcmin} + F_{xcmax})$	N	690	690	640	640	510	510
	Cyclic amplitude	F_{1ca}, F_{2ca} $F_{xca} = 0{,}5\ F_{xcr}$	N	640	640	590	590	460	460
	Final static force	F_{1fin}, F_{2fin} $F_{xfin} = F_{xsp}$	N	2 240	2 240	2 065	2 065	1 610	1 610
	Prescribed number of cycles		1	2×10^6					

6.4. Results and Discussion

The structural integrity of the LIMBER UniLeg ankle-foot complex was studied through simulation and mechanical testing. The simulations and experimental results for the pylon and ankle-foot complex were compared to draw insights about the validity of finite element modeling for complex geometries 3D printed from engineering-grade thermoplastics. Additionally, the fit and

function of the single-piece 3D printed prosthesis was tested through patient trials with oversight from a certified prosthetist.

6.4.1. Simulation Results

In this study, the proof force, as defined by the ISO 10328:2006, was analyzed using nonlinear static stress FEA simulations at heel, forefoot, and ankle locations to verify plastic yielding and elastic deformation values stay within set boundaries. The proof force is defined as the set of loading conditions where success is dependent on minimal permanent deformation occurs. The proof force for activity level P5 at heel and forefoot loading conditions for ankle-foot devices and foot units in the static test procedure is 2240N. Material used for these simulations was isotropic Nylon Polyamide 12. In the forefoot loading condition, Figure 6.7A, a maximum deflection of 62.08 mm occurs at the toes and the maximum Von Mises stress is 95.61 MPa. In the heel loading condition, Figure 6.7C, a maximum deflection of 9.06 mm occurs at the toes and the maximum Von Mises stress is 43.06 MPa. A maximum deflection of 3.21 mm in the negative u-direction occurred at the ankle joint and maximum Von Mises stress of 31.75 was calculated for Figure 6.7B. transition and is enabled due to the disconnected-surface foot design. Normal loading along the u-axis resulted in a small deflection that was within acceptable limits for acute hip height misalignment, as validated by CPO Herb Barrack. The mid-stance to forefoot-liftoff transition is aided by the stored spring energy from the 62.08 mm deflection, resulting lower metabolic costs during the gait cycle.

Finite Element Analysis (FEA) was used to validate the structural integrity of the topology optimized pylon section. We applied the ISO 10328:2006 loads of maximum compression (3220 N) and maximum torque (50 Nm) on the top of the model and fixed the bottom surface for translation and rotation. We defined boundary conditions as fixed on the bottom face and loads applied on the top face, the material used was isotropic Nylon Polyamide 12, and the mesh was created and refined by the solver in SolidWorks. The results, Figure 6.10, show the Von Mises stress (N/m2) regions under ISO standard loads. Maximum stress can be found on the frontal-bottom section as well as the back bottom section, both regions can be seen in red color in Figure 6.10. A maximum stress of 16 MPa is derived from the pylon simulation, which, when compared to its yield strength of 60 MPa for PA-12, results in a satisfactory factor of safety of 3.75.

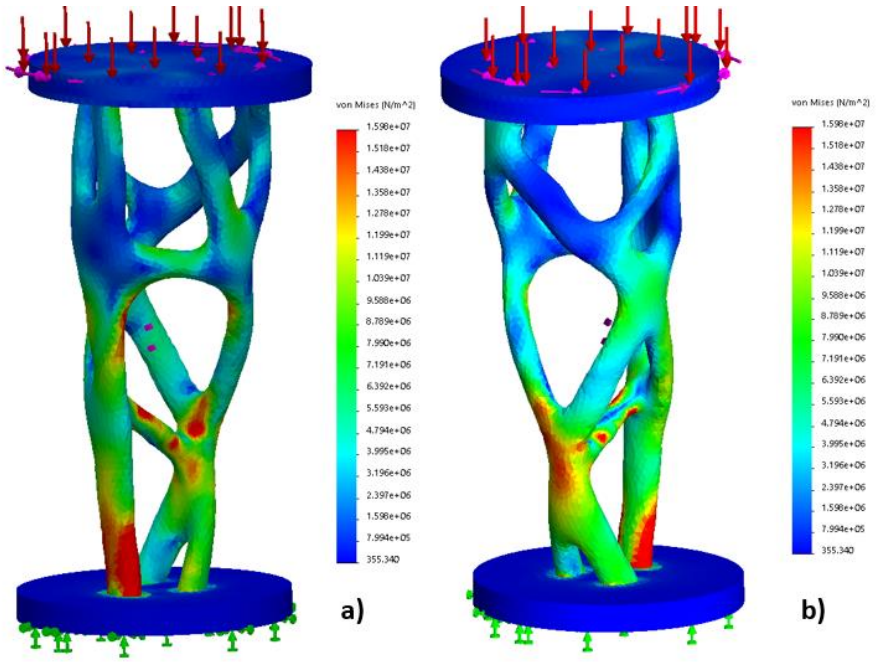

Figure 6.10. Finite Element Analysis of Pylon under ISO standard 10328:2006 compressive and torsional loads. A maximum stress of 16 MPa was found. A) Anterior view and B) posterior view.

6.4.2. Experimental Results

Mechanical testing results show the importance of selecting appropriate printing parameters and materials. Figure 6.11 demonstrates the mechanical testing set-up for the ankle foot complex using angled blocks mounted to a Universal Testing System (Instron 3367, Norwood, MA, US).

Figure 6.11. Mechanical testing of the 3D printed prosthetic feet (unfilled nylon) was achieved using angled HDPE blocks, 15 degrees for toe loading and 20 degrees for heel loading, on an Instron 3367 Universal Testing System.

The maximum deformation of the prosthetic feet varied significantly based on loading condition (heel or toe) and material (PA645, carbon fiber filled PA, or PC). A load-displacement curve for the chopped carbon fiber filled nylon is shown in Figure 6.12. In this case, the PACF feet were loaded to 4480 N, the ultimate static test force prescribed for an athletic 100 kg individual. The significant difference in displacement is a typical for prosthetic feet, due to the

difference in the lever arm between the neutral axis running up the center of the ankle and the toe or heel. This is verified through CAD simulations in Figure 6.7.

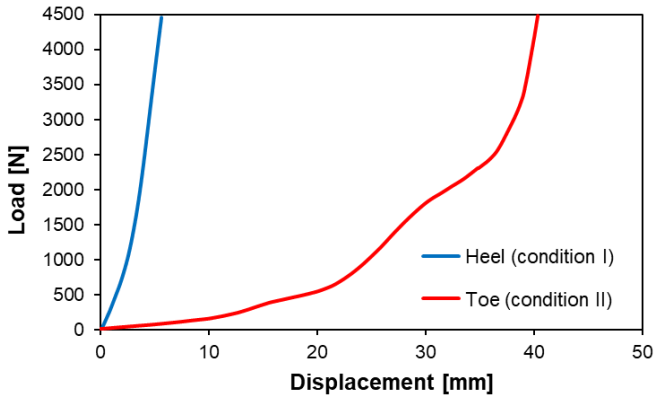

Figure 6.12. Load-displacement curve for heel (condition I) versus toe (condition II) loading of prosthetic feet printed out of chopped carbon fiber nylon. Due to the design of prosthetic feet, the toe displaces significantly more at any given load.

Material selection has a significant effect on the load-displacement behavior of the ankle-foot complex as exemplified in Figure 6.13. For ultimate heel loading (condition I), PC feet deformed the least at 4.7-5.0 mm, PACF feet deformed 5.7 mm, and PA645 feet deformed the most at 9.8-10.8 mm. For ultimate toe loading (condition II), PA645 feet deformed the least at 23.0-25.2 mm and PACF feet deformed 35.9 mm, while PC foot showed the most deformation across all loads up to its failure load of 2750 N.

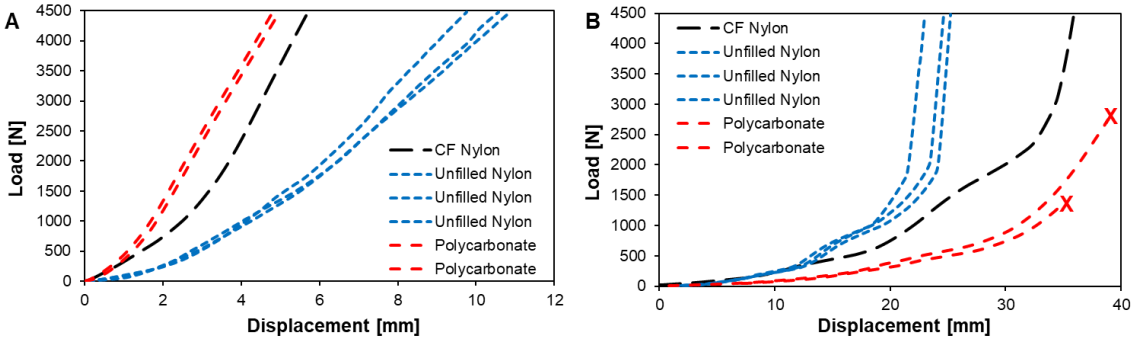

Figure 6.13. Load-displacement curves for carbon-fiber filled nylon, unfilled nylon, and polycarbonate 3D printed feet tested in A) heel (condition I) and B) toe (condition II) loading.

Due to the viscoelastic properties of thermoplastic materials, the ankle-foot complex shows a strain rate dependent loading curve. At low loading rates, the material will displace more for any given load. It is important to note that the gait cycle leads to loading rates between 100-250 N/s, which will lead to a non-equilibrium mechanical behavior. In fact, the ISO 10328 standard specifies that mechanical testing must be performed in this loading rate range [16]. However, as demonstrated in Figure 6.14B, the displacement-controlled load frame utilized in this study is not able to provide smooth loading at a rate of 100 N/s. For this reason, all testing was done at rates of 1 mm/s and 5 mm/s for heel and toe loading, respectively.

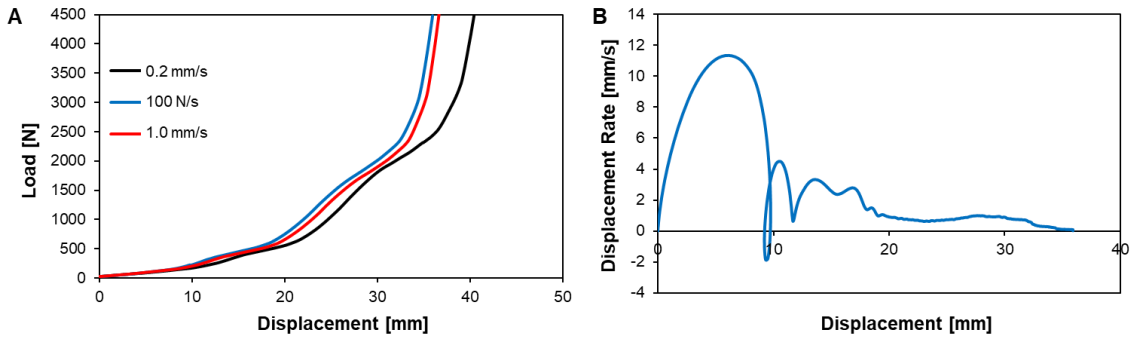

Figure 6.14. A) Displacement rate effect for prosthetic feet printed from chopped carbon fiber nylon. B) Displacement rate achieved for a 100 N/s loading rate. The ISO 10328 standard specifies a loading rate between 100-250 N/s, which is difficult for displacement-controlled load-frames.

To test the viscoelastic behavior of the unfilled nylon, the ankle-foot complex was loaded to 4480 N, held for 30 s, and unloaded. After a resting period of five-minutes, the loading cycle was repeated. Three runs are shown in Figure 6.15. Comparing this to cyclic loading done over 100 cycles in Figure

6.16, the resting period significantly reduced the residual deformation (memory-effect).

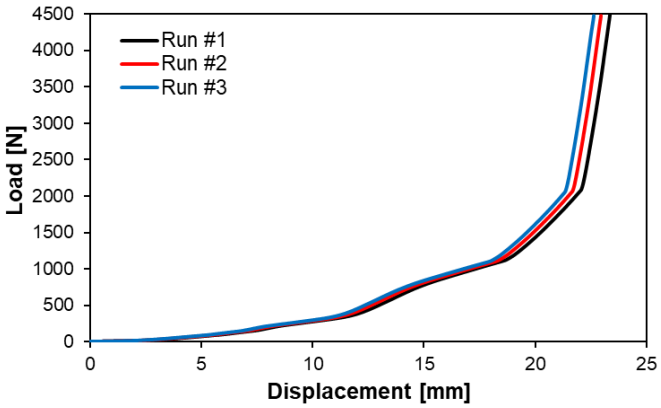

Figure 6.15. Toe loading (condition II) of the same Nylon 645 prosthetic foot with five-minute resting periods between each test. Compared to a cyclic test with no rest period, relatively little deformation memory remains after the resting period.

The stored energy of the ankle-foot complex is equal to the area under the curve. The area of the rising curve minus the area of the decreasing curve is equal to the energy loss during the gait cycle. In the case of prosthetic feet, where a quick energy release is desired, a small difference is optimal. Figure 6.16 demonstrates the mechanical behavior of 3D printed ankle-foot complexes across 100 loading-unloading cycles, between 50 N to 1330 N. As expected, cyclic tests of the heel show significantly less deformation across all cycles compared to cyclic toe loading. The significant differences between an ankle-foot complex printed with fiber-filled vs. unfilled nylon clearly illustrates the difference in viscoelastic properties between carbon fiber filled and unfilled nylons. Adding reinforcing, even chopped or non-continuous, fibers enables a spring-like behavior and reduces the viscoelastic properties intrinsic to nylon. For carbon fiber filled nylon, a much lower memory effect is observed resulting in a greater

portion of the stored energy being returned during the dynamic gait cycle. In addition, tighter grouping of the 1, 5, 10, 30, 50, and 100 cycle loading curves indicates fewer cycles are necessary to reach equilibrium behavior. For a prosthetic foot, this behavior is important so it can maintain its behavior over many gait cycles without losing integrity or energy capture and return characteristics.

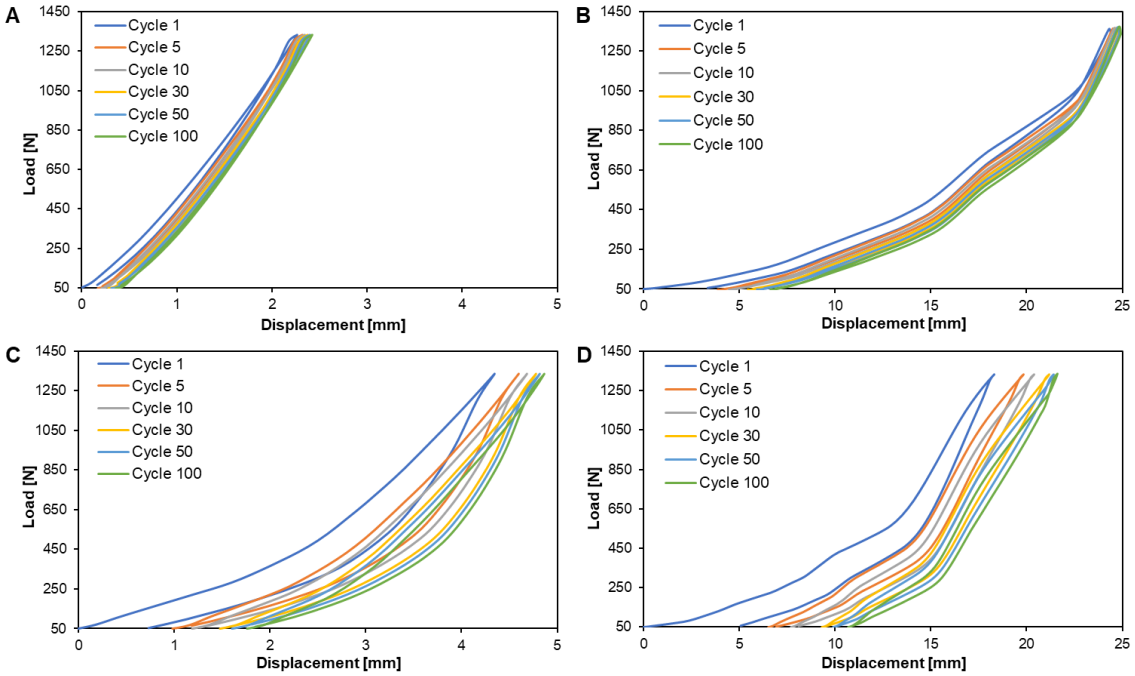

Figure 6.16. Load-displacement curves showing the cyclic testing of 3D printed prosthetic feet for A,B) carbon fiber filled nylon and C,D) unfilled nylon. A,C) Heel loading (condition I) and B,D) toe loading (condition II) curves show different behavior due to the longer forefoot blade than heel blade. Loading to unloading curves are shown for cycles 1, 5, 10, 30, 50, and 100.

The failure behavior is shown in Figure 6.17, with A) simulation results, B) experimental results, and C) fracture surfaces. As expected, the areas of tensile stress concentration predicted by simulations closely match the failure locations from experiments. For toe loading, tensile stress accumulates on the posterior surface of the curved ankle and is likely exacerbated by the layer lines. However,

based on fracture surface analysis, fracture occurs across layers along a tortuous path. This fracture behavior indicates good interlayer bonding and a behavior approaching that of a dense isotropic thermoplastic. These findings support our hypothesis that the use of correct 3D printing parameters and environmental control, such as a heated printer chamber, can produce strong prosthetic devices and/or components.

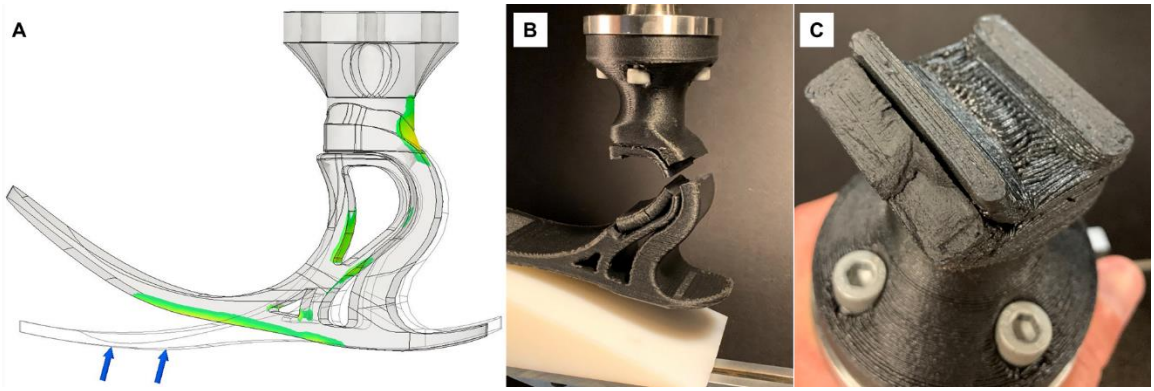

Figure 6.17. A) Simulation of the prosthetic foot using isotropic mechanical properties from the filament manufacturer that highlights stress concentrations at the back of the ankle, within the 'D-shaped' support, and bottom of the foot-blade. B) Fracture locations from a toe loading (condition II) mechanical test match predicted points of stress concentration from simulation results. C) The fracture surface shows both trans- and inter-layer crack propagation, indicating good layer bonding.

Compared with other low-cost thermoplastic prosthetic feet [265], the LIMBER ankle-foot complex was significantly stronger. Filled and unfilled nylon feet passed ultimate strength loading in both heel and toe loading conditions, while polycarbonate feed passed proof loading but failed before ultimate loading was achieved.

6.4.3. Validation with a Patient Fitting

Patient D. Zam was fitted with a unibody transtibial prosthetic device of the invention. Alignment was assessed in anterior and lateral planes with the patient standing, Figure 6.18. For proper TKA alignment, the trochanter (hip), knee, and ankle points must fall along a vertical line when standing. To quantify the benefits of the present unibody transtibial prosthetic device, a comparison of weight, cost, and time of design were made against a patient's existing prosthetic device. Weight comparison between the devices revealed a 55% weight reduction from the conventional prosthetic, which weighed 4 pounds, to the present device weighing only 1.8 lbs. Lighter weight devices reduce metabolic cost during activity and are often reported to be more comfortable. Time of design and manufacture was compared between the two design methodologies. Total traditional transtibial prosthetic leg time for design and manufacture was estimated at 14 days. This estimate includes measurements (1 Day), mold creation (3 Days), socket creation (6 Days), and assembly and alignment (4 Days). In comparison, the present unibody design and manufacture time is 16 hours, which consists of data acquisition (1 Hour), design time (3 Hours), and printing time (12 Hours).

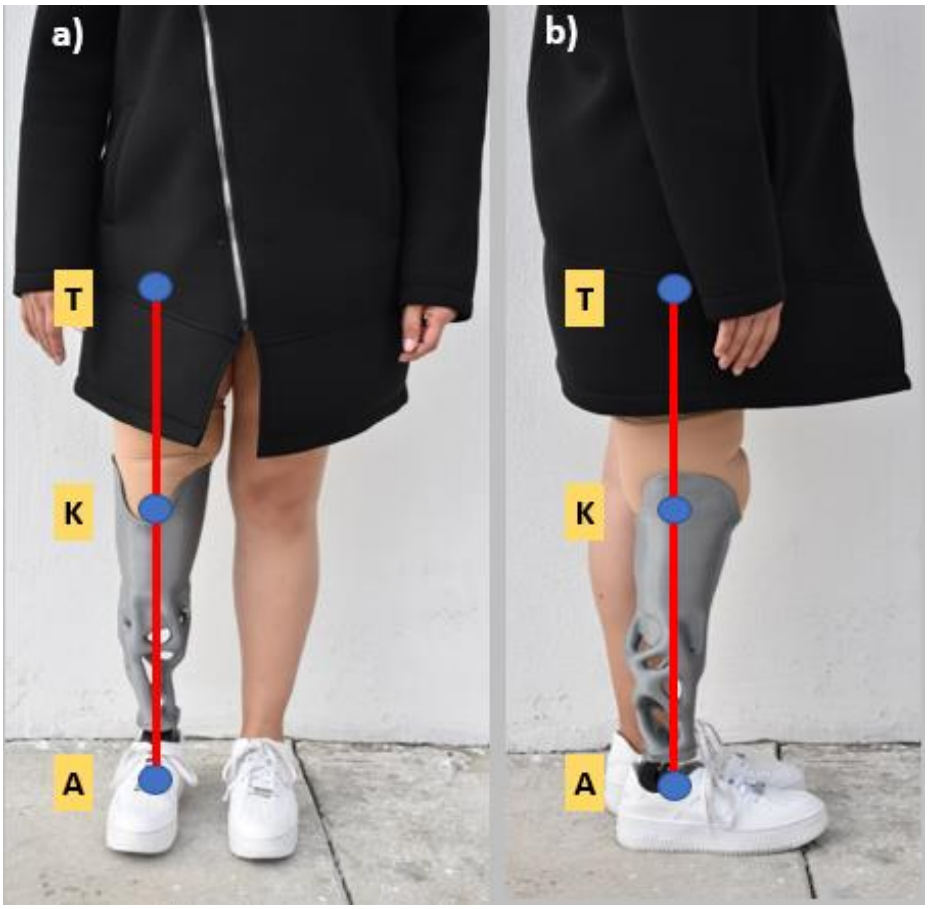

Figure 6.18. Trochanter-knee-ankle (TKA) alignment shown for patient D. Zam. wearing the 3D printed UniLeg prosthesis. A) Anterior view and B) lateral view.

6.5. Summary

6.5.1. Conclusion

The LIMBER workflow presents a rapid and scalable solution for the production of affordable, personalized prosthetic devices. Our mission is to solve the worldwide prosthetic accessibility crisis to improve quality of life for the millions of amputees in need.

Through mechanical testing and field testing in partnership with the Rotary foundation, the LIMBER UniLeg was demonstrated to be safe and functional. In

comparison with traditional prosthetic devices, we lowered the average cost, weight, and time of production by 95%, 55%, and 95%, respectively. The foot-ankle complex met or exceeded loading requirements specified in ISO 10328. Maximum loads achieved were 8 kN for heel loading and 15 kN for toe loading. A total of 1,000 cycles were successfully demonstrated under P5 cyclic loading conditions, with a load cycle between 50 N to 1330 N. These tests indicate our material selection and manufacturing process should create safety prosthetic limbs.

The LIMBER UniLeg fills the gap in available lower-limb prostheses through several key features: (1) our novel design workflow aligns and blends the socket, pylon, and foot-ankle complex into a single piece that retains alignment from scan data through the design phase and manufacturing process; (2) we 3D print using the fused filament fabrication (FFF) technique, which uses low-cost feedstock material compared to other additive techniques such as stereolithography and multi-jet fusion; (3) we have a novel design that provides multi-axial dynamic gait performance without the use of joints or sliding surfaces that reduce durability; and (4) our device is an endoskeletal system to enable post-fabrication alignment and fit adjustment through thermoforming.

To tackle the worldwide prosthetic accessibility crisis, a two-fold approach is needed that both provides affordable devices while also not requiring an on-site highly skilled prosthetist to sculpt, fit, or align the device. Current lower-limb devices cannot fill this gap because they are either expensive and require on-site

prosthetists or have limited comfort and functionality and the amputee won't wear the device. The LIMBER UniLeg is a scalable solution that will provide affordable and personalized prosthetic care to amputees that don't have access to highly skilled prosthetists.

6.5.2. Next Steps

The patent-pending LIMBER UniLeg has been successfully demonstrated with five patients in the US and MX. An additional eight patients have been scanned and will receive legs in July, 2022. Figure 6.19 shows a printed leg on the custom high-temperature 3D printer with active chamber heating developed for this research. Figure 6.20 shows three happy patients who received UniLegs.

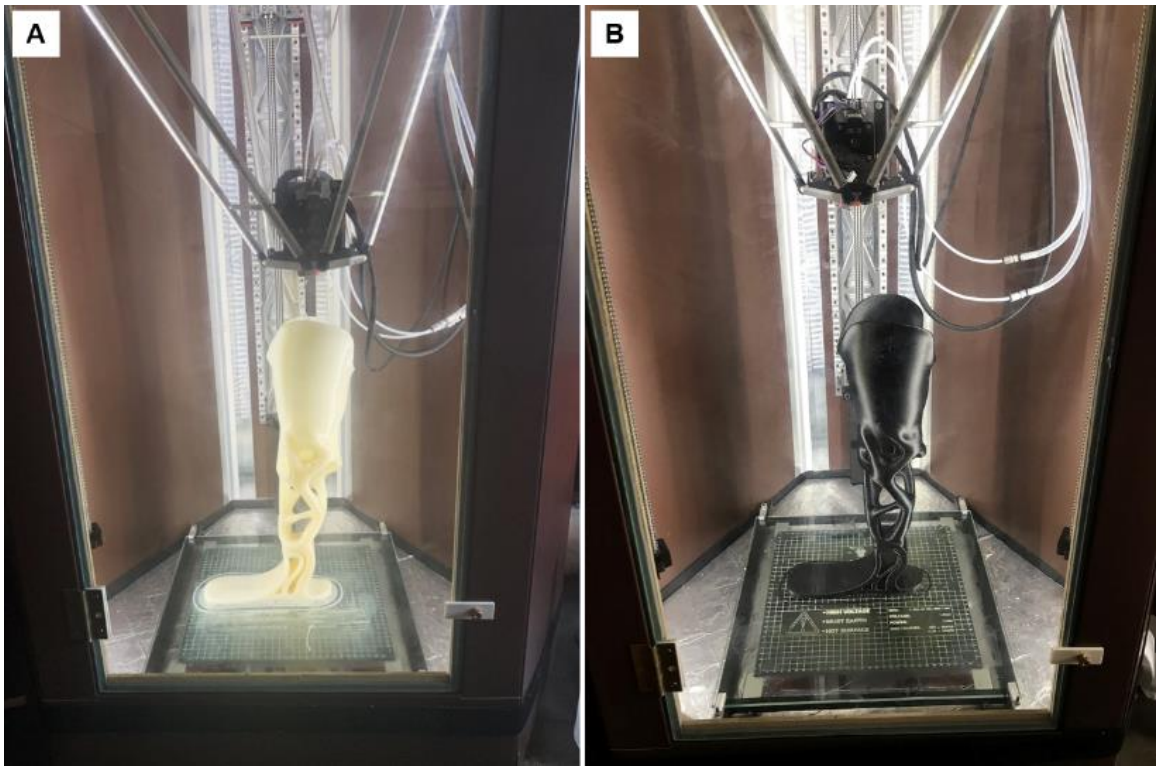

Figure 6.19. UniLeg printed in A) PA645 and B) PACF on the custom developed 3D printer.

Figure 6.20. Three patients wearing the LIMBER UniLeg.

Next steps include multi-material designs and smart devices that include smart actuators with intelligence through sensory feedback. Figure 6.21 demonstrates one of the many possibilities that multi-material 3D printing can offer. For example, printing an ankle-foot complex with a mixture of filled and unfilled nylon enables ultra-personalization of every device to tune the gait response for each patient's needs.

Figure 6.21. Multi-material printing enables to fabrication of the ankle-foot complex with tailored load-displacement response and energy return. Carbon fiber filled nylon is stiffer and springier than unfilled nylon, and the spatial tailoring of each material will enable enhanced functionality.

The device shown in Figure 6.22 is a new research direction the LIMBER project is studying with the goal of creating an adaptable socket through soft actuators controlled through feedback loops and sensors. This will enable the socket to adjust to accommodate the volume fluctuations that the residual limbs of amputees, both new and mature, experience.

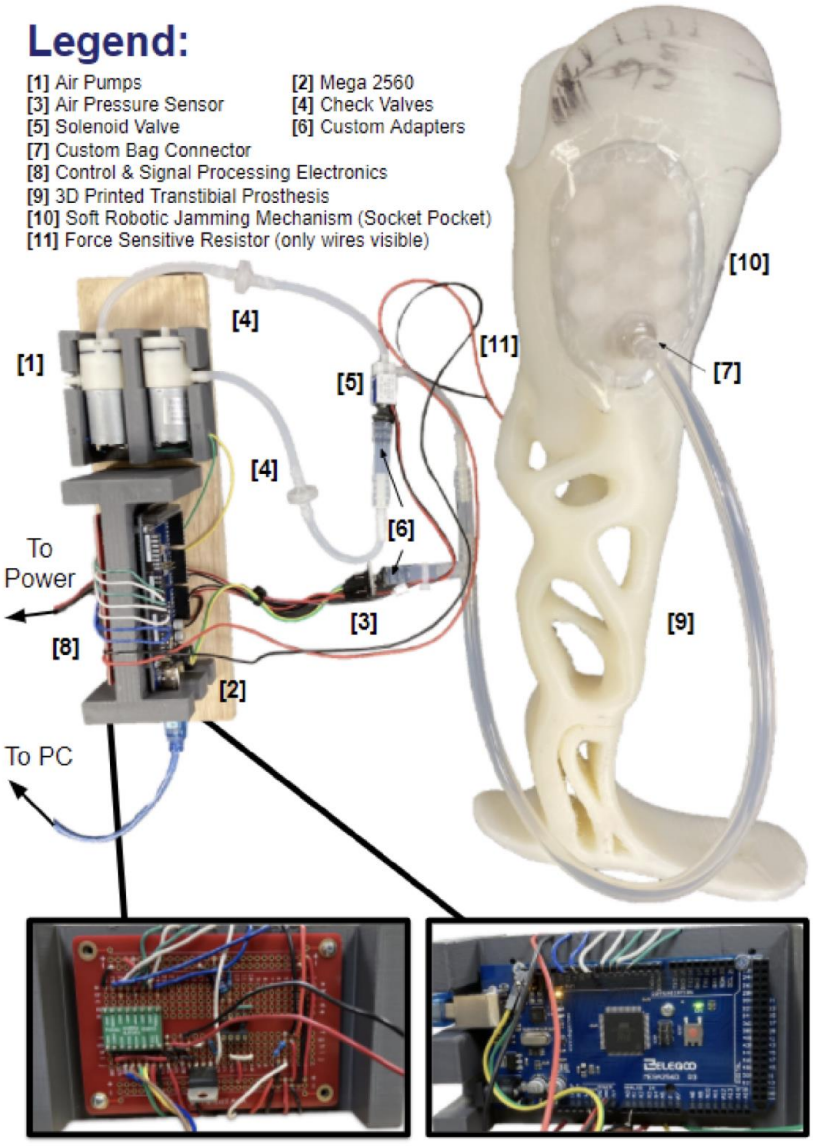

Figure 6.22. The smart socket enables to modification of the LIMBER UniLeg to include pressure sensors and soft jamming materials to improve fit and comfort.

6.5.3. Acknowledgement

Chapter 6, in part, is currently being prepared for submission for publication of the material. J. Pelz, L. De Vivo, H. Barrack, and F. Kuester. The dissertation author was the primary investigator and author of this paper.

Chapter 6, in part, is a reprint of material that was submitted: J. Pelz, L. De Vivo, H. Barrack, F. Kuester “PCT/US22/11939 - UNIBODY ENDOSKELETAL TRANSTIBIAL PROSTHETIC DEVICES AND DIGITAL FABRICATION WORKFLOW,” Patent Council Treaty, 2022. The dissertation author is an inventor and the primary author of this patent.

Chapter 6, in part, is also a reprint of material that has been published: L. De Vivo, J. Pelz, J. Mendoza, H. Barrack, F. Kuester, “Towards 3D Printing of a Monocoque Transtibial Prosthesis using a Bio-Inspired Design Workflow,” Rapid Prototyping Journal, 2021. The dissertation author was the co-primary investigator of this paper and helped prepare the original and final drafts.

APPENDIX

Appendix A: Scale of Segregation MATLAB Script

Appendix A.1. User Guide

To use the MATLAB script, a high-resolution SEM image with sufficient contrast between phases is necessary. This script uses a binary thresholding script, and therefore can only handle two phases. First, the image name should be updated. Next, the image magnification should be changed to match the value on the electron micrograph. For different microscopes and software, the magnification value may not produce identical pixel scales, so care should be taken to confirm pixel dimensions match using the imtool (img1) measuring capabilities. Next, the pix_count can be changed based on user preference (recommended values are 50,000-300,000). Next, r_steps should be updated to roughly match the largest expected inclusion diameter. If the correlogram doesn't approach the x-axis, r_steps should be increased to a larger value.

Appendix A.2. MATLAB Script

```
%%Read in images and display
img1 = imread('Image name goes here');
imtool(img1)

%% Pixel to Particle size
%img_zoom = input('Enter magnification: ');
img_zoom = 150;
pix_count = 50000;
pix_i = size(img1,2);
pix_j = size(img1,1);
pix_j = round(pix_j - (pix_j*0.068)); % to remove SEM info bar at image bottom
pixelSize = (207346/img_zoom)/pix_i; %[microns] for input magnification
pixels_SiC = 0.71/pixelSize;
```

```
pixels_B4C = 3.61/pixelSize;

%% Convert to B&W
%img1_BW = rgb2gray(img1);
img1_BW = img1;

%% Crop off info bar
img1_BW_C = imcrop(img1_BW,[0 0 pix_i pix_j]);

%% Calculate Grayscale Histogram
%figure
%imhist(img1_BW_C)
thresholdLevel = graythresh(img1_BW_C); %[1]
img1_Binary = imbinarize(img1_BW_C,thresholdLevel); %[1]
%imtool(img1_Binary);
figure
imshow(img1_Binary)
%imshowpair(img1_BW_C,img1_Binary,'montage')
%[1] Otsu, N., "A Threshold Selection Method from Gray-Level Histograms."
IEEE Transactions on Systems, Man, and Cybernetics. Vol. 9, No. 1, 1979, pp.
62–66.

%% Scale of Segregation - method 1
%method (c) in Danckwerts
X1 = pix_i*pixelSize;
J1 = sum(img1_Binary,2);
a_avg = mean(img1_Binary,'all');
J_var1 = mean((J1 - a_avg*X1).^2,'all');
a_diff = img1_Binary - a_avg;
a_var = mean((a_diff).^2,'all');
S1 = J_var1/(2*X1*a_var);
%[2] Danckwerts, P.V., "The definition and measurement of some characteristics
of mixtures," Appl. Sci. Res. A, 3:279-296, 1952.

%% Scale of Segregation - method 2

%Finding R(r): coefficient of correlation
%For an imperfect mixture, R(r) will be greater than 0 for small values of r,
becasue points close together will often be in the same clump.
r_steps = round(min(pix_i,pix_j)/10);
a1 = zeros(1,pix_count); %center pixels
```

```
a2 = zeros(r_steps,pix_count,4); %pixels branching out 0, 270, 180, 90 directions
a3 = zeros(r_steps,pix_count,4); %pixels branching out 315, 225, 135, 45
directions = sqrt(2) * distance
r1 = 0;
r2 = 1:r_steps;
r3 = r2.*sqrt(2);
R2 = zeros(1,r_steps);
R3 = zeros(1,r_steps);
correlogram = zeros(r_steps*2+1,2);
correlogram_sort_adjusted = zeros(r_steps*2+1,2);

i_1 = randi(pix_i-(2*r_steps),1,pix_count); %only generate pixels in a central
rectangle of image so out of bound pixels are not analyzed during r_steps
j_1 = randi(pix_j-(2*r_steps),1,pix_count);
i_1 = i_1+r_steps;
j_1 = j_1+r_steps;

grayImage = 255 * uint8(img1_Binary);
RGB = cat(3, grayImage, grayImage, grayImage); %create an RBG image that
can be used to de-bug


for x = 1:pix_count
    a1(1,x) = img1_Binary(j_1(1,x),i_1(1,x)); %analyze center pixels
          RGB(j_1(1,x),i_1(1,x),1) = 255;
          RGB(j_1(1,x),i_1(1,x),2) = 0;
          RGB(j_1(1,x),i_1(1,x),3) = 0;

    for y = 1:r_steps
        a2(y,x,1) = img1_Binary(j_1(1,x),i_1(1,x)+y); %angle = 0 degrees
              RGB(j_1(1,x),i_1(1,x)+y,1) = 255;
              RGB(j_1(1,x),i_1(1,x)+y,2) = 0;
              RGB(j_1(1,x),i_1(1,x)+y,3) = 0;
        a3(y,x,1) = img1_Binary(j_1(1,x)-y,i_1(1,x)+y); %angle = 45 degrees
              RGB(j_1(1,x)-y,i_1(1,x)+y,1) = 255;
              RGB(j_1(1,x)-y,i_1(1,x)+y,2) = 0;
              RGB(j_1(1,x)-y,i_1(1,x)+y,3) = 0;
        a2(y,x,2) = img1_Binary(j_1(1,x)-y,i_1(1,x)); %angle = 90 degrees
              RGB(j_1(1,x)-y,i_1(1,x),1) = 255;
              RGB(j_1(1,x)-y,i_1(1,x),2) = 0;
              RGB(j_1(1,x)-y,i_1(1,x),3) = 0;
```

```
        a3(y,x,2) = img1_Binary(j_1(1,x)-y,i_1(1,x)-y); %angle = 135 degrees
            RGB(j_1(1,x)-y,i_1(1,x)-y,1) = 255;
            RGB(j_1(1,x)-y,i_1(1,x)-y,2) = 0;
            RGB(j_1(1,x)-y,i_1(1,x)-y,3) = 0;
        a2(y,x,3) = img1_Binary(j_1(1,x),i_1(1,x)-y); %angle = 180 degrees
            RGB(j_1(1,x),i_1(1,x)-y,1) = 255;
            RGB(j_1(1,x),i_1(1,x)-y,2) = 0;
            RGB(j_1(1,x),i_1(1,x)-y,3) = 0;
        a3(y,x,3) = img1_Binary(j_1(1,x)+y,i_1(1,x)-y); %angle = 225 degrees
            RGB(j_1(1,x)+y,i_1(1,x)-y,1) = 255;
            RGB(j_1(1,x)+y,i_1(1,x)-y,2) = 0;
            RGB(j_1(1,x)+y,i_1(1,x)-y,3) = 0;
        a2(y,x,4) = img1_Binary(j_1(1,x)+y,i_1(1,x)); %angle = 270 degrees
            RGB(j_1(1,x)+y,i_1(1,x),1) = 255;
            RGB(j_1(1,x)+y,i_1(1,x),2) = 0;
            RGB(j_1(1,x)+y,i_1(1,x),3) = 0;
        a3(y,x,4) = img1_Binary(j_1(1,x)+y,i_1(1,x)+y); %angle = 315 degrees
            RGB(j_1(1,x)+y,i_1(1,x)+y,1) = 255;
            RGB(j_1(1,x)+y,i_1(1,x)+y,2) = 0;
            RGB(j_1(1,x)+y,i_1(1,x)+y,3) = 0;
    end
end

R1 = (mean((a1(1,:)-a_avg).*(a1(1,:)-a_avg)))/(a_var);

for x = 1:r_steps
    R2(1,x) = (mean((a1(1,:)-a_avg).*(a2(x,:,:)-a_avg),'all'))/(a_var);
    R3(1,x) = (mean((a1(1,:)-a_avg).*(a3(x,:,:)-a_avg),'all'))/(a_var);
end

compile_R = [R2,R3];
compile_R(1,r_steps*2+1) = R1;
compile_r = [r2,r3];
compile_r(1,r_steps*2+1) = 0;
compile_r_adjusted = compile_r*pixelSize;

for x = 1:r_steps*2+1
    correlogram(x,1) = compile_r_adjusted(1,x);
    correlogram(x,2) = compile_R(1,x);
end
```

```
[correlogram_sort,index] = sortrows(correlogram,1); %sort by distance
maintaining index relations

for x = 1:r_steps*2+1 %chop off values less than 0 for calculating Scale of
Segregation
    correlogram_sort_adjusted(x,1) = correlogram_sort(x,1);
    if correlogram_sort(x,2) >= 0
       correlogram_sort_adjusted(x,2) = correlogram_sort(x,2);
   end
end

S2 = trapz(correlogram_sort_adjusted(:,1),correlogram_sort_adjusted(:,2));

%figure
%plot(correlogram_sort(:,1),correlogram_sort(:,2))

figure
plot(correlogram_sort_adjusted(:,1),correlogram_sort_adjusted(:,2),'r','LineWidth',
2)
set(gca,'fontname','arial')
xlabel('r [um]','fontweight','bold','fontsize',12)
ylabel('R(r)','fontweight','bold','fontsize',12)

% figure
% imshow(RGB)
```

REFERENCES

[1] K.J. Hemker, M. Chen, J.W. McCauley, Shock-Induced Localized Amorphization in Boron Carbide, Science (80-.). 299 (2003) 1563–1566. https://doi.org/10.1126/science.1080819.

[2] B. Malmal Moshtaghioun, A.L. Ortiz, D. Gómez-García, A. Domínguez-Rodríguez, Toughening of super-hard ultra-fine grained B4C densified by spark-plasma sintering via SiC addition, J. Eur. Ceram. Soc. 33 (2013) 1395–1401. https://doi.org/10.1016/j.jeurceramsoc.2013.01.018.

[3] M.A. Meyers, A.Y.M. Lin, P.Y. Chen, J. Muyco, Mechanical strength of abalone nacre: Role of the soft organic layer, J. Mech. Behav. Biomed. Mater. 1 (2008) 76–85. https://doi.org/10.1016/j.jmbbm.2007.03.001.

[4] A. 52900:2015, Standard Terminology for Additive Manufacturing – General Principles – Terminology, ASTM Int. i (2015) 1–9. https://doi.org/10.1520/F2792-12A.2.

[5] T. Chartier, C. Chaput, F. Doreau, M. Loiseau, Stereolithography of structural complex ceramic parts, J. Mater. Sci. (2002). https://doi.org/10.1023/A:1016102210277.

[6] J. Christian Nelson, N.K. Vail, J.W. Barlow, J.J. Beaman, D.L. Bourell, H.L. Marcus, Selective Laser Sintering of Polymer-Coated Silicon Carbide Powders, Ind. Eng. Chem. Res. (1995). https://doi.org/10.1021/ie00044a017.

[7] Y.C. Hagedorn, N. Balachandran, W. Meiners, K. Wissenbach, R. Poprawet, SLM of net-shaped high strength ceramics: New opportunities for producing dental restorations, 22nd Annu. Int. Solid Free. Fabr. Symp. - An Addit. Manuf. Conf. SFF 2011. (2011) 536–546.

[8] P. Kunchala, K. Kappagantula, 3D printing high density ceramics using binder jetting with nanoparticle densifiers, Mater. Des. 155 (2018). https://doi.org/10.1016/j.matdes.2018.06.009.

[9] E.A. Griffin, D.R. Mumm, D.B. Marshall, Rapid prototyping of functional ceramic composites, Am. Ceram. Soc. Bull. (1996).

[10] T. Wang, B. Derby, Ink-jet printing and sintering of PZT, J. Am. Ceram. Soc. (2005). https://doi.org/10.1111/j.1551-2916.2005.00406.x.

[11] E. Peng, D. Zhang, J. Ding, Ceramic Robocasting: Recent Achievements, Potential, and Future Developments, Adv. Mater. 30 (2018) 1–14. https://doi.org/10.1002/adma.201802404.

[12] V.K. Balla, S. Bose, A. Bandyopadhyay, Processing of bulk alumina ceramics using laser engineered net shaping, Int. J. Appl. Ceram. Technol. (2008). https://doi.org/10.1111/j.1744-7402.2008.02202.x.

[13] J. Pelz, N. Ku, M. Meyers, L. Vargas-Gonzalez, Additive Manufacturing Utilizing a Novel In - Line Mixing System for Design of Functionally Graded Ceramic Composites, 2019.

[14] L. Gabriele, D.V. Nicoloso, J. Pelz, Towards 3D printing of a monocoque transtibial prosthesis using a bio-inspired design work fl ow, 11 (2021) 67–80. https://doi.org/10.1108/RPJ-06-2021-0136.

[15] O.R. Orlovskaya, Nina, M. Lugovy, V. Subbotin, DESIGN AND MANUFACTURING B4C-SiC LAYERED CERAMICS FOR ARMOR APPLICATIONS, Ceram. Armor Armor Syst. (2003). https://doi.org/10.1002/9781118406793.ch5.

[16] ISO, Prosthetics - Structural testing of lower-limb prostheses - Requirements and test methods, ISO 103282016. 3 (2016).

[17] L. Vargas-Gonzalez, R.F. Speyer, J. Campbell, Flexural strength, fracture toughness, and hardness of silicon carbide and boron carbide armor ceramics, Int. J. Appl. Ceram. Technol. 7 (2010) 643–651. https://doi.org/10.1111/j.1744-7402.2010.02501.x.

[18] S. Das, W. Ronan, H.N.G. Wadley, V.S. Deshpande, Penetration of confined ceramics targets, Extrem. Mech. Lett. 18 (2018) 45–57. https://doi.org/10.1016/j.eml.2017.11.001.

[19] A. Krell, E. Strassburger, Order of influences on the ballistic resistance of armor ceramics and single crystals, Mater. Sci. Eng. A. 597 (2014) 422–430. https://doi.org/10.1016/j.msea.2013.12.101.

[20] W.D. Callister, Materials science and engineering: An introduction (2nd edition), Mater. Des. (1991). https://doi.org/10.1016/0261-3069(91)90101-9.

[21] E. Medvedovski, Ballistic performance of armour ceramics: Influence of design and structure. Part 1, Ceram. Int. 36 (2010) 2103–2115. https://doi.org/10.1016/j.ceramint.2010.05.021.

[22] S. Zhao, J.C. LaSalvia, B. Kad, C.E. Wehrenberg, K.D. Behler, B.A. Remington, M.A. Meyers, Directional amorphization of boron carbide subjected to laser shock compression, Proc. Natl. Acad. Sci. 113 (2016) 12088–12093. https://doi.org/10.1073/pnas.1604613113.

[23] M.A. Meyers, B. Kad, C.E. Wehrenberg, R. Flanagan, E.N. Hahn, K. More, B.A. Remington, R. Cauble, S. Zhao, Shock-induced amorphization in silicon carbide, Acta Mater. 158 (2018) 206–213. https://doi.org/10.1016/j.actamat.2018.07.047.

[24] L. Chen, H. Quan, S. Zhao, W. Yang, M. Meyers, C. Wehrenberg, B. Kad, K. More, J. LaSalvia, Y. Opachi, E. Hahn, B. Remington, Shock-induced Amorphization in Covalently Bonded Solids, EPJ Web Conf. 183 (2018)

03027. https://doi.org/10.1051/epjconf/201818303027.

[25] G.C. Farlow, C.W. White, H. Naramoto, C.J. McHargue, B.R. Appleton, J.M. Williams, The amorphization of ceramics by ion beams, Mater. Sci. Eng. 69 (2003) 123–127. https://doi.org/10.1016/0025-5416(85)90382-9.

[26] S. Yarmolenko, J. Shih, M. Chheda, J. Sankar, O. Radchenko, N. Orlovskaya, M. Lugovy, V. Subbotin, J. Adams, Robust design and manufacturing of ceramic laminates with controlled thermal residual stresses for enhanced toughness, J. Mater. Sci. 40 (2005) 5483–5490. https://doi.org/10.1007/s10853-005-1923-x.

[27] M.I. Lopez, P.E. Meza Martinez, M.A. Meyers, Organic interlamellar layers, mesolayers and mineral nanobridges: Contribution to strength in abalone (Haliotis rufescence) nacre, Acta Biomater. 10 (2014) 2056–2064. https://doi.org/10.1016/j.actbio.2013.12.016.

[28] W. Yang, B. Gludovatz, E.A. Zimmermann, H.A. Bale, R.O. Ritchie, M.A. Meyers, Structure and fracture resistance of alligator gar (Atractosteus spatula) armored fish scales, Acta Biomater. 9 (2013) 5876–5889. https://doi.org/10.1016/j.actbio.2012.12.026.

[29] V.R. Sherman, H. Quan, W. Yang, R.O. Ritchie, M.A. Meyers, A comparative study of piscine defense: The scales of Arapaima gigas, Latimeria chalumnae and Atractosteus spatula, J. Mech. Behav. Biomed. Mater. 73 (2017) 1–16. https://doi.org/10.1016/j.jmbbm.2016.10.001.

[30] W. Yang, I.H. Chen, B. Gludovatz, E.A. Zimmermann, R.O. Ritchie, M.A. Meyers, Natural flexible dermal armor, Adv. Mater. 25 (2013) 31–48. https://doi.org/10.1002/adma.201202713.

[31] C. an Wang, Y. Huang, Q. Zan, H. Guo, S. Cai, Biomimetic structure design - a possible approach to change the brittleness of ceramics in nature, Mater. Sci. Eng. C. 11 (2000) 9–12. https://doi.org/10.1016/S0928-4931(00)00133-8.

[32] R.P. Wilkerson, B. Gludovatz, J. Watts, A.P. Tomsia, G.E. Hilmas, R.O. Ritchie, A study of size effects in bioinspired, “nacre-like”, metal-compliant-phase (nickel-alumina) coextruded ceramics, Acta Mater. 148 (2018) 147–155. https://doi.org/10.1016/j.actamat.2018.01.046.

[33] M.P. Rao, A.J. Sánchez-Herencia, G.E. Beltz, R.M. McMeeking, F.F. Lange, Laminar ceramics that exhibit a threshold strength, Science (80-.). 286 (1999) 102–105. https://doi.org/10.1126/science.286.5437.102.

[34] M. Lugovy, V. Slyunyayev, N. Orlovskaya, G. Blugan, J. Kuebler, M. Lewis, Apparent fracture toughness of Si3N4-based laminates with residual compressive or tensile stresses in surface layers, Acta Mater. 53 (2005) 289–296. https://doi.org/10.1016/j.actamat.2004.09.022.

[35] C.B. Carter, G. Norton, Ceramic Materials: Science and Engineering, 1st ed., Springer, 2007. https://doi.org/10.1007/978-1-4614-3523-5.

[36] V.L. Wiesner, J.P. Youngblood, R.W. Trice, Room-temperature injection molding of aqueous alumina-polyvinylpyrrolidone suspensions, J. Eur. Ceram. Soc. 34 (2014) 453–463. https://doi.org/10.1016/j.jeurceramsoc.2013.08.017.

[37] S. Tariolle, C. Reynaud, F. Thévenot, T. Chartier, J.L. Besson, Preparation, microstructure and mechanical properties of SiC-SiC and B 4C-B4C laminates, J. Solid State Chem. 177 (2004) 487–492. https://doi.org/10.1016/j.jssc.2003.02.007.

[38] N. Travitzky, A. Bonet, B. Dermeik, T. Fey, I. Filbert-Demut, L. Schlier, T. Schlordt, P. Greil, Additive manufacturing of ceramic-based materials, Adv. Eng. Mater. 16 (2014) 729–754. https://doi.org/10.1002/adem.201400097.

[39] M.L. Griffith, J.W. Halloran, Freeform Fabrication of Ceramics via Stereolithography, J. Am. Ceram. Soc. 79 (2005) 2601–2608. https://doi.org/10.1111/j.1151-2916.1996.tb09022.x.

[40] N. Oxman, S. Keating, E. Tsai, Functionally Graded Rapid Prototyping, Innov. Dev. Virtual Phys. Prototyp. (2012) 483–489. https://doi.org/10.1201/b11341-78.

[41] E. Atzeni, A. Salmi, Economics of additive manufacturing for end-usable metal parts, Int. J. Adv. Manuf. Technol. 62 (2012) 1147–1155. https://doi.org/10.1007/s00170-011-3878-1.

[42] S. Jauhar, K.M. Asthankar, A.M. Kuthe, Cost benefit analysis of Rapid Manufacturing in Automotive Industries, Adv. Mech. Eng. Its Appl. (2012).

[43] J.E. Smay, S.S. Nadkarni, J. Xu, Direct writing of dielectric ceramics and base metal electrodes, Int. J. Appl. Ceram. Technol. 4 (2007) 47–52. https://doi.org/10.1111/j.1744-7402.2007.02118.x.

[44] W. Li, A.J. Martin, B. Kroehler, A. Henderson, T. Huang, J. Watts, G.E. Hilmas, M.C. Leu, Fabricating Functionally Graded Materials by Ceramic On-Demand Extrusion with Dynamic Mixing, Proc. 29th Annu. Int. Solid Free. Fabr. Symp. – An Addit. Manuf. Conf. (2018) 1087–1099. http://sffsymposium.engr.utexas.edu/sites/default/files/2018/088 FabricatingFunctionallyGradedMaterialsbyCeram.pdf.

[45] T.J. Ober, D. Foresti, J.A. Lewis, Active mixing of complex fluids at the microscale, Proc. Natl. Acad. Sci. U. S. A. 112 (2015) 12293–12298. https://doi.org/10.1073/pnas.1509224112.

[46] D.T. Nguyen, T.D. Yee, N.A. Dudukovic, K. Sasan, A.W. Jaycox, A.M. Golobic, E.B. Duoss, R. Dylla-Spears, 3D Printing of Compositional Gradients Using the Microfluidic Circuit Analogy, Adv. Mater. Technol. 4

(2019) 1–7. https://doi.org/10.1002/admt.201900784.

[47] G. V. Franks, C. Tallon, A.R. Studart, M.L. Sesso, S. Leo, Colloidal processing: enabling complex shaped ceramics with unique multiscale structures, J. Am. Ceram. Soc. 100 (2017) 458–490. https://doi.org/10.1111/jace.14705.

[48] J.A. Lewis, Colloidal Processing of Ceramics, J. Am. Ceram. Soc. 83 (2000) 2341–2359. https://doi.org/10.1111/j.1151-2916.2000.tb01560.x.

[49] L.M. Rueschhoff, Novel Ceramic Near-Net Shaped Processing, (2017).

[50] F. F. Lange, Powder Processing Science and Technology for Increased Reability, J. Am. Ceram. Soc., 1989, 72, 3–15. 72 (1989) 3–15.

[51] J. Zhou, Y. Zhang, J.K. Chen, Numerical simulation of random packing of spherical particles for powder-based additive manufacturing, J. Manuf. Sci. Eng. Trans. ASME. 131 (2009) 0310041–0310048. https://doi.org/10.1115/1.3123324.

[52] H.M. Chan, Layered ceramics: Processing and mechanical behavior, Annu. Rev. Mater. Sci. 27 (1997) 249–282. https://doi.org/10.1146/annurev.matsci.27.1.249.

[53] S.L. Morissette, J. a Lewis, J. Cesarano, D.B. Dimos, T.Y. Baer, Solid freeform fabrication of aqueous alumina-poly(vinyl alcohol) gelcasting suspensions, J. Am. Ceram. Soc. 83 (2000) 2409–2416. https://doi.org/10.1111/j.1151-2916.2000.tb01569.x.

[54] L. Rueschhoff, W. Costakis, M. Michie, J. Youngblood, R. Trice, Additive Manufacturing of Dense Ceramic Parts via Direct Ink Writing of Aqueous Alumina Suspensions, Int. J. Appl. Ceram. Technol. 13 (2016) 821–830. https://doi.org/10.1111/ijac.12557.

[55] M. Faes, H. Valkenaers, F. Vogeler, J. Vleugels, E. Ferraris, Extrusion-based 3D printing of ceramic components, Procedia CIRP. 28 (2015) 76–81. https://doi.org/10.1016/j.procir.2015.04.028.

[56] J. Liao, H. Chen, H. Luo, X. Wang, K. Zhou, D. Zhang, Direct ink writing of zirconia three-dimensional structures, J. Mater. Chem. C. 5 (2017) 5867. https://doi.org/10.1039/c7tc01545c.

[57] D. Zhang, E. Peng, R. Borayek, J. Ding, Controllable Ceramic Green-Body Configuration for Complex Ceramic Architectures with Fine Features, Adv. Funct. Mater. 29 (2019) 1–12. https://doi.org/10.1002/adfm.201807082.

[58] W.J. Costakis, L.M. Rueschhoff, A.I. Diaz-Cano, J.P. Youngblood, R.W. Trice, Additive manufacturing of boron carbide via continuous filament direct ink writing of aqueous ceramic suspensions, J. Eur. Ceram. Soc. 36 (2016) 3249–3256. https://doi.org/10.1016/j.jeurceramsoc.2016.06.002.

[59] S. Eqtesadi, A. Motealleh, F.H. Perera, P. Miranda, A. Pajares, R. Wendelbo, F. Guiberteau, A.L. Ortiz, Fabricating geometrically-complex B4C ceramic components by robocasting and pressureless spark plasma sintering, Scr. Mater. 145 (2018) 14–18. https://doi.org/10.1016/j.scriptamat.2017.10.001.

[60] S. Arnold, J. Coltman, Design trade-offs for ceramic/composite armor materials, 1990.

[61] S. Bose, M. Roy, A. Bandyopadhyay, Recent advances in bone tissue engineering scaffolds, Trends Biotechnol. 30 (2012). https://doi.org/10.1016/j.tibtech.2012.07.005.

[62] S. Bose, D. Ke, H. Sahasrabudhe, A. Bandyopadhyay, Additive manufacturing of biomaterials, Prog. Mater. Sci. 93 (2018). https://doi.org/10.1016/j.pmatsci.2017.08.003.

[63] L.C. Hwa, S. Rajoo, A.M. Noor, N. Ahmad, M.B. Uday, Recent advances in 3D printing of porous ceramics: A review, Curr. Opin. Solid State Mater. Sci. 21 (2017) 323–347. https://doi.org/10.1016/j.cossms.2017.08.002.

[64] T.M.G. Chu, D.G. Orton, S.J. Hollister, S.E. Feinberg, J.W. Halloran, Mechanical and in vivo performance of hydroxyapatite implants with controlled architectures, Biomaterials. 23 (2002) 1283–1293. https://doi.org/10.1016/S0142-9612(01)00243-5.

[65] S. Bose, S. Vahabzadeh, A. Bandyopadhyay, Bone tissue engineering using 3D printing, Mater. Today. 16 (2013) 496–504. https://doi.org/10.1016/j.mattod.2013.11.017.

[66] J.T. Muth, P.G. Dixon, L. Woish, L.J. Gibson, J.A. Lewis, Architected cellular ceramics with tailored stiffness via direct foam writing, Proc. Natl. Acad. Sci. 114 (2017) 1832–1837. https://doi.org/10.1073/pnas.1616769114.

[67] C.-J. Bae, Integrally Cored Ceramic Investment Casting Mold Fabricated By Ceramic Stereolithography, 2008.

[68] F. Weng, C. Chen, H. Yu, Research status of laser cladding on titanium and its alloys: A review, Mater. Des. 58 (2014). https://doi.org/10.1016/j.matdes.2014.01.077.

[69] Y. Zhang, H. Sahasrabudhe, A. Bandyopadhyay, Additive manufacturing of Ti-Si-N ceramic coatings on titanium, Appl. Surf. Sci. 346 (2015) 428–437. https://doi.org/10.1016/j.apsusc.2015.03.184.

[70] V.K. Balla, P.P. Bandyopadhyay, S. Bose, A. Bandyopadhyay, Compositionally graded yttria-stabilized zirconia coating on stainless steel using laser engineered net shaping (LENS^{TM}), Scr. Mater. 57 (2007) 861–864. https://doi.org/10.1016/j.scriptamat.2007.06.055.

[71] H.M. Wang, C.M. Wang, L.X. Cai, Wear and corrosion resistance of laser clad Ni2Si/NiSi composite coatings, Surf. Coatings Technol. 168 (2003). https://doi.org/10.1016/S0257-8972(03)00240-8.

[72] X. Xu, J. Han, C. Wang, A. Huang, Laser Cladding of Composite Bioceramic Coatings on Titanium Alloy, J. Mater. Eng. Perform. 25 (2016). https://doi.org/10.1007/s11665-015-1868-4.

[73] W. Gao, Y. Zhang, D. Ramanujan, K. Ramani, Y. Chen, C.B. Williams, C.C.L. Wang, Y.C. Shin, S. Zhang, P.D. Zavattieri, The status, challenges, and future of additive manufacturing in engineering, CAD Comput. Aided Des. 69 (2015) 65–89. https://doi.org/10.1016/j.cad.2015.04.001.

[74] C.B. Carter, M.G. Norton, Ceramic materials: Science and engineering, 2013. https://doi.org/10.1007/978-1-4614-3523-5.

[75] D. Richerson, W. Lee, Applications and Processing of Ceramics, in: Mod. Ceram. Eng., 2006.

[76] H. Le Ferrand, Magnetic slip casting for dense and textured ceramics: A review of current achievements and issues, J. Eur. Ceram. Soc. 41 (2021). https://doi.org/10.1016/j.jeurceramsoc.2020.08.030.

[77] J. Yang, J. Yu, Y. Huang, Recent developments in gelcasting of ceramics, J. Eur. Ceram. Soc. 31 (2011). https://doi.org/10.1016/j.jeurceramsoc.2010.12.035.

[78] F. Klocke, Modern approaches for the production of ceramic components, J. Eur. Ceram. Soc. 17 (1997) 457–465. https://doi.org/10.1016/S0955-2219(96)00163-X.

[79] M.L. Griffith, J.W. Halloran, Freeform Fabrication of Ceramics via Stereolithography, J. Am. Ceram. Soc. (2005). https://doi.org/10.1111/j.1151-2916.1996.tb09022.x.

[80] J.S. Pelz, N. Ku, W.T. Shoulders, M.A. Meyers, L.R. Vargas-Gonzalez, Multi-material additive manufacturing of functionally graded carbide ceramics via active, in-line mixing, Addit. Manuf. (2020). https://doi.org/10.1016/j.addma.2020.101647.

[81] T.D. Ngo, A. Kashani, G. Imbalzano, K.T.Q. Nguyen, D. Hui, Additive manufacturing (3D printing): A review of materials, methods, applications and challenges, Compos. Part B Eng. 143 (2018) 172–196. https://doi.org/10.1016/j.compositesb.2018.02.012.

[82] E. Sachs, M. Cima, J. Cornie, Three-Dimensional Printing: Rapid Tooling and Prototypes Directly from a CAD Model, CIRP Ann. - Manuf. Technol. 39 (1990) 201–204. https://doi.org/10.1016/S0007-8506(07)61035-X.

[83] A. Zocca, P. Colombo, C.M. Gomes, J. Günster, Additive Manufacturing of Ceramics: Issues, Potentialities, and Opportunities, J. Am. Ceram. Soc. 98

(2015) 1983–2001. https://doi.org/10.1111/jace.13700.

[84] A. Krell, S. Schädlich, Nanoindentation hardness of submicrometer alumina ceramics, Mater. Sci. Eng. A. 307 (2001). https://doi.org/10.1016/S0921-5093(00)01818-9.

[85] C.Y. Yap, C.K. Chua, Z.L. Dong, Z.H. Liu, D.Q. Zhang, L.E. Loh, S.L. Sing, Review of selective laser melting: Materials and applications, Appl. Phys. Rev. 2 (2015). https://doi.org/10.1063/1.4935926.

[86] H. Kodama, JPS56144478A: Stereoscopic Figure Drawing Device, 1980.

[87] Hideo Kodama, Automatic method for fabricating a three- dimensional plastic model with photo- hardening polymer, Rev. Sci. Instrum. 52 (1981).

[88] C.W. Hull, APPARATUS FOR PRODUCTION OF THREE-DMENSONAL OBJECTS BY STEREOLITHOGRAPHY, 4,575,330, 1984.

[89] T. Gornet, T. Wohlers, History of Additive Manufacturing, in: Wohlers Rep., Wohlers Report, 2014: pp. 1–34. https://doi.org/10.1617/s11527-011-9818-6.

[90] C.R. Deckard, J.J. Beaman, J.F. Darrah, METHOD FOR SELECTIVE LASER SINTERING WITH LAYERWISE CROSS-SCANNING, 1986. https://doi.org/US005485919A.

[91] W.E. Masters, US4665492A: Computer automated manufacturing process and system, 1987. https://doi.org/10.1016/0736-5845(87)90060-3.

[92] M. Feygin, Apparatus and method for forming an integral object from laminations, US Pat. 4,752,352. (1988).

[93] M. Feygin, B. Hsieh, Laminated object manufacturing: A simpler process, in: Proc. 2nd Solid Free. Fabr. Symp., 1991.

[94] S.S. Crump, APPARATUS AND METHOD FOR CREATING THREE-DIMENSIONAL OBJECTS, 1989.

[95] E. Sachs, J. Haggerty, M. Cima, P. Williams, THREE-DIMENSIONAL PRINTING TECHNIQUES, 1989. https://doi.org/US005485919A.

[96] J.P. Kruth, Material Incress Manufacturing by Rapid Prototyping Techniques, CIRP Ann. - Manuf. Technol. (1991). https://doi.org/10.1016/S0007-8506(07)61136-6.

[97] J.-P. Kruth, M.C. Leu, T. Nakagawa, Progress in Additive Manufacturing and Rapid Prototyping, CIRP Ann. 47 (1998) 525–540. https://doi.org/10.1016/S0007-8506(07)63240-5.

[98] B. Van der Schueren, J. Geling, Parts to go, Prototyp. Technol. Int. (1998) 48–52.

[99] S.J. Rock, C.R. Gilman, A New SFF Process for Functional Part Rapid

Prototyping and Manufacturing: Freeform Powder Molding, Solid Free. Fabr. Symp. Proc. (1995) 80–87.

[100] J.-C. Wang, H. Dommati, S.-J. Hsieh, Review of additive manufacturing methods for high-performance ceramic materials, Int. J. Adv. Manuf. Technol. 103 (2019) 2627–2647. https://doi.org/10.1007/s00170-019-03669-3.

[101] A.J. Allen, I. Levin, S.E. Witt, Materials research & measurement needs for ceramics additive manufacturing, J. Am. Ceram. Soc. (2020). https://doi.org/10.1111/jace.17369.

[102] J.W. Halloran, Ceramic Stereolithography: Additive Manufacturing for Ceramics by Photopolymerization, Annu. Rev. Mater. Res. 46 (2016) 19–40. https://doi.org/10.1146/annurev-matsci-070115-031841.

[103] M.L. Griffith, J.W. Halloran, Stereolithography of ceramics, Int. SAMPE Tech. Conf. (1995).

[104] M.L. Griffith, J.W. Halloran, Ultraviolet Curing of Highly Loaded Ceramic Suspensions for Stereolithography of Ceramics, Solid Free. Fabr. Symp. (1994).

[105] M.L. Griffith, J.W. Halloran, Freeform fabrication of ceramics via stereolithography, J. Am. Ceram. Soc. (1996). https://doi.org/10.1111/j.1151-2916.1996.tb09022.x.

[106] M.L. Griffith, J.W. Halloran, Scattering of ultraviolet radiation in turbid suspensions Prediction of ceramic stereolithography resin sensitivity from theory and measurement of diffusive photon Scattering of ultraviolet radiation in turbid suspensions, J. Appl. Phys. (1997). https://doi.org/10.1063/1.1980531.

[107] R. Garg, R.K. Prud'homme, I.A. Aksay, F. Liu, R.R. Alfano, Absorption length for photon propagation in highly dense colloidal dispersions, J. Mater. Res. 13 (1998) 3463–3467. https://doi.org/10.1557/JMR.1998.0472.

[108] C. Hinczewski, S. Corbel, T. Chartier, Ceramic suspensions suitable for stereolithography, J. Eur. Ceram. Soc. (1998). https://doi.org/10.1016/s0955-2219(97)00186-6.

[109] K. Zhang, R. He, G. Ding, X. Bai, D. Fang, Effects of fine grains and sintering additives on stereolithography additive manufactured Al2O3 ceramic, Ceram. Int. 47 (2021) 2303–2310. https://doi.org/10.1016/j.ceramint.2020.09.071.

[110] K. Zhang, R. He, G. Ding, C. Feng, W. Song, D. Fang, Digital light processing of 3Y-TZP strengthened ZrO2 ceramics, Mater. Sci. Eng. A. 774 (2020) 138768. https://doi.org/10.1016/j.msea.2019.138768.

[111] M. Schwentenwein, J. Homa, Additive manufacturing of dense alumina

ceramics, Int. J. Appl. Ceram. Technol. (2015). https://doi.org/10.1111/ijac.12319.

[112] U. Scheithauer, E. Schwarzer, T. Moritz, A. Michaelis, Additive Manufacturing of Ceramic Heat Exchanger: Opportunities and Limits of the Lithography-Based Ceramic Manufacturing (LCM), J. Mater. Eng. Perform. (2018). https://doi.org/10.1007/s11665-017-2843-z.

[113] G. Mitteramskogler, R. Gmeiner, R. Felzmann, S. Gruber, C. Hofstetter, J. Stampfl, J. Ebert, W. Wachter, J. Laubersheimer, Light curing strategies for lithography-based additive manufacturing of customized ceramics, Addit. Manuf. 1 (2014). https://doi.org/10.1016/j.addma.2014.08.003.

[114] G. Ding, R. He, K. Zhang, C. Xie, M. Wang, Y. Yang, D. Fang, Stereolithography-based additive manufacturing of gray-colored SiC ceramic green body, J. Am. Ceram. Soc. (2019). https://doi.org/10.1111/jace.16648.

[115] G. Ding, R. He, K. Zhang, M. Xia, C. Feng, D. Fang, Dispersion and stability of SiC ceramic slurry for stereolithography, Ceram. Int. 46 (2020) 4720–4729. https://doi.org/10.1016/j.ceramint.2019.10.203.

[116] G. Ding, R. He, K. Zhang, N. Zhou, H. Xu, Stereolithography 3D printing of SiC ceramic with potential for lightweight optical mirror, Ceram. Int. 46 (2020) 18785–18790. https://doi.org/10.1016/j.ceramint.2020.04.196.

[117] E. Zanchetta, M. Cattaldo, G. Franchin, M. Schwentenwein, J. Homa, G. Brusatin, P. Colombo, Stereolithography of SiOC Ceramic Microcomponents, Adv. Mater. 28 (2016) 370–376. https://doi.org/10.1002/adma.201503470.

[118] X. Wang, F. Schmidt, D. Hanaor, P.H. Kamm, S. Li, A. Gurlo, Additive manufacturing of ceramics from preceramic polymers: A versatile stereolithographic approach assisted by thiol-ene click chemistry, Addit. Manuf. 27 (2019) 80–90. https://doi.org/10.1016/j.addma.2019.02.012.

[119] P. Colombo, G. Mera, R. Riedel, G.D. Sorarù, Polymer-derived ceramics: 40 Years of research and innovation in advanced ceramics, J. Am. Ceram. Soc. 93 (2010) 1805–1837. https://doi.org/10.1111/j.1551-2916.2010.03876.x.

[120] Z.C. Eckel, C. Zhou, J.H. Martin, A.J. Jacobsen, W.B. Carter, T.A. Schaedler, Additive manufacturing of polymer-derived ceramics, Sci. Mag. Res. Reports. 351 (2016) 58–62.

[121] M.R. O'Masta, E. Stonkevitch, K.A. Porter, P.P. Bui, Z.C. Eckel, T.A. Schaedler, Additive manufacturing of polymer-derived ceramic matrix composites, J. Am. Ceram. Soc. 103 (2020) 6712–6723. https://doi.org/10.1111/jace.17275.

[122] G. Liu, Y. Zhao, G. Wu, J. Lu, Origami and 4D printing of elastomer-derived ceramic structures, Sci. Adv. 4 (2018) 1–11. https://doi.org/10.1126/sciadv.aat0641.

[123] H. Chen, X. Wang, F. Xue, Y. Huang, K. Zhou, D. Zhang, 3D printing of SiC ceramic: Direct ink writing with a solution of preceramic polymers, J. Eur. Ceram. Soc. 38 (2018) 5294–5300. https://doi.org/10.1016/j.jeurceramsoc.2018.08.009.

[124] A.N. Chen, J.M. Wu, K. Liu, J.Y. Chen, H. Xiao, P. Chen, C.H. Li, Y.S. Shi, High-performance ceramic parts with complex shape prepared by selective laser sintering: a review, Adv. Appl. Ceram. 117 (2018) 100–117. https://doi.org/10.1080/17436753.2017.1379586.

[125] K. Subramanian, N. Vail, J. Barlow, H. Marcus, Selective laser sintering of alumina with polymer binders, Rapid Prototyp. J. (1995). https://doi.org/10.1108/13552549510086844.

[126] A. Gahler, J.G. Heinrich, J. Günster, Direct laser sintering of Al2O3-SiO2 dental ceramic components by layer-wise slurry deposition, J. Am. Ceram. Soc. 89 (2006) 3076–3080. https://doi.org/10.1111/j.1551-2916.2006.01217.x.

[127] H. Yves-Christian, W. Jan, M. Wilhelm, W. Konrad, P. Reinhart, Net shaped high performance oxide ceramic parts by Selective Laser Melting, Phys. Procedia. 5 (2010) 587–594. https://doi.org/10.1016/j.phpro.2010.08.086.

[128] J. Wilkes, Y.C. Hagedorn, W. Meiners, K. Wissenbach, Additive manufacturing of ZrO2-Al2O3 ceramic components by selective laser melting, Rapid Prototyp. J. (2013). https://doi.org/10.1108/13552541311292736.

[129] M. Greulich, M. Greul, T. Pintat, Fast, functional prototypes via multiphase jet solidification, Rapid Prototyp. J. (1995). https://doi.org/10.1108/13552549510146649.

[130] M. Mapar, D.Q. Zhang, Z.H. Liu, W.Y. Yeong, C.K. Chua, B.Y. Tay, O. Geramifard, S. Maleksaeedi, F.E. Wiria, Preparation and flowability characterization of ceramic powders for Selective Laser Melting, in: High Value Manuf. Adv. Res. Virtual Rapid Prototyp. - Proc. 6th Int. Conf. Adv. Res. Rapid Prototyping, VR@P 2013, 2014. https://doi.org/10.1201/b15961-50.

[131] U. Lakshminarayan, S. Ogrydiziak, H.L. Marcus, Selective Laser Sintering of Ceramic Materials, in: Int. Solid Free. Fabr. Symp., 1990. https://doi.org/T2MG7GC58.

[132] N.K. Vail, J.W. Barlow, Effect of Polymer Coatings as Intermediate Binders on Sintering of Ceramic Parts, in: Solid Free. Fabr. Proc., 1991: pp. 195–

204.

[133] J.C. Nelson, N.K. Vail, J.W. Barlow, Laser Sintering Model for Composite Materials, in: Solid Free. Fabr. Symp., 1993.

[134] D.M. Gureev, R. V. Ruzhechko, I. V. Shishkovskiĭ, Selective laser sintering of PZT ceramic powders, Tech. Phys. Lett. (2000). https://doi.org/10.1134/1.1262811.

[135] R.S. Evans, D.L. Bourell, J.J. Beaman, M.I. Campbell, RAPID MANUFACTURING OF SILICON CARBIDE COMPOSITES, Rap. (2004) 228–235.

[136] K. Shahzad, J. Deckers, J.P. Kruth, J. Vleugels, Additive manufacturing of alumina parts by indirect selective laser sintering and post processing, J. Mater. Process. Technol. 213 (2013). https://doi.org/10.1016/j.jmatprotec.2013.03.014.

[137] K. Liu, Y. Shi, C. Li, L. Hao, J. Liu, Q. Wei, Indirect selective laser sintering of epoxy resin-Al2O 3 ceramic powders combined with cold isostatic pressing, Ceram. Int. 40 (2014) 7099–7106. https://doi.org/10.1016/j.ceramint.2013.12.043.

[138] P. Bertrand, F. Bayle, C. Combe, P. Goeuriot, I. Smurov, Ceramic components manufacturing by selective laser sintering, Appl. Surf. Sci. 254 (2007). https://doi.org/10.1016/j.apsusc.2007.08.085.

[139] J.W. Halloran, Freeform fabrication of ceramics, Br. Ceram. Trans. 98 (1999) 299–303. https://doi.org/10.1179/096797899680633.

[140] J.E. Fromm, NUMERICAL CALCULATION OF THE FLUID DYNAMICS OF DROP-ON-DEMAND JETS., IBM J. Res. Dev. (1984). https://doi.org/10.1147/rd.283.0322.

[141] E. Sachs, M. Cima, J. Cornie, D. Brancazio, J. Bredt, A. Curodeau, T. Fan, S. Khanuja, A. Lauder, J. Lee, S. Michaels, Three-Dimensional Printing: The Physics and Implications of Additive Manufacturing, CIRP Ann. - Manuf. Technol. (1993). https://doi.org/10.1016/S0007-8506(07)62438-X.

[142] A. Butscher, M. Bohner, N. Doebelin, S. Hofmann, R. Müller, New depowdering-friendly designs for three-dimensional printing of calcium phosphate bone substitutes, Acta Biomater. (2013). https://doi.org/10.1016/j.actbio.2013.07.019.

[143] J. Yoo, K.M. Cho, W.S. Bae, M. Cima, S. Suresh, Transformation-toughened ceramic multilayers with compositional gradients, J. Am. Ceram. Soc. (1998). https://doi.org/10.1111/j.1151-2916.1998.tb02291.x.

[144] M. Lanzetta, E. Sachs, Improved surface finish in 3D printing using bimodal powder distribution, Rapid Prototyp. J. (2003). https://doi.org/10.1108/13552540310477463.

[145] J.A. Gonzalez, J. Mireles, Y. Lin, R.B. Wicker, Characterization of ceramic components fabricated using binder jetting additive manufacturing technology, Ceram. Int. (2016). https://doi.org/10.1016/j.ceramint.2016.03.079.

[146] P. Karandikar, M. Watkins, A. McCormick, B. Givens, M. Aghajanian, Additive manufacturing (3D printing) of ceramics: Microstructure, properties, and product examples, Ceram. Eng. Sci. Proc. 38 (2018) 175–190. https://doi.org/10.1002/9781119474746.ch17.

[147] J.H. Song, M.J. Edirisinghe, J.R.G. Evans, Formulation and multilayer jet printing of ceramic inks, J. Am. Ceram. Soc. (1999). https://doi.org/10.1111/j.1151-2916.1999.tb02253.x.

[148] P.F. Blazdell, J.R.G. Evans, M.J. Edirisinghe, P. Shaw, M.J. Binstead, The computer aided manufacture of ceramics using multilayer jet printing, J. Mater. Sci. Lett. 14 (1995). https://doi.org/10.1007/BF00455415.

[149] W.D. Teng, M.J. Edirisinghe, Development of ceramic inks for direct continuous jet printing, J. Am. Ceram. Soc. (1998). https://doi.org/10.1111/j.1151-2916.1998.tb02443.x.

[150] K.A.M. Seerden, N. Reis, J.R.G. Evans, P.S. Grant, J.W. Halloran, B. Derby, Ink-Jet Printing of Wax-Based Alumina Suspensions, J. Am. Ceram. Soc. (2001). https://doi.org/10.1111/j.1151-2916.2001.tb01045.x.

[151] B. Derby, N. Reis, Inkjet Printing of Highly Loaded Particulate Suspensions, MRS Bull. (2003). https://doi.org/10.1557/mrs2003.230.

[152] N. Reis, C. Ainsley, B. Derby, Ink-jet delivery of particle suspensions by piezoelectric droplet ejectors, J. Appl. Phys. (2005). https://doi.org/10.1063/1.1888026.

[153] G.N. HOWATT, R.G. BRECKENRIDGE, J.M. BROWNLOW, Fabrication of Thin Ceramic Sheets for Capacitors, J. Am. Ceram. Soc. 30 (1947) 237–242.

[154] G.N. HOWATT, Method of producing high dielectric high insulation ceramic plates, 1952.

[155] A.R. Rodriguez, J. Cronin, Process for manufacturing multilayer ceramic capacitors, 1966.

[156] C. Griffin, J. Daufenbach, S. McMillin, Solid Freeform Fabrication of Functional Ceramic Components Using a Laminated Object Manufacturing Technique, Solid Free. Fabr. Conf. (1994) 17–25. https://doi.org/10.1002/ana.23630.

[157] D. Klosterman, R. Chartoff, B. Priore, N. Osborne, G. Graves, A. Lightman, G. Han, S. Pak, J. Weaver, Structural Composites via Laminated Object Manufacturing LOM., Solid Free. Fabr. Symp. Proc. (1996).

[158] T. Himmer, T. Nakagawa, H. Noguchi, Stereolithography of ceramics, Solid Free. Fabr. Symp. 42 (1997).

[159] D. Klosterman, R. Chartoff, G. Graves, N. Osborne, B. Priore, Interfacial characteristics of composites fabricated by laminated object manufacturing, Compos. Part A Appl. Sci. Manuf. (1998). https://doi.org/10.1016/S1359-835X(98)00088-8.

[160] S.J. Rodrigues, R.P. Chartoff, D.A. Klosterman, M. Agarwala, N. Hecht, Solid Freeform Fabrication of Functional Silicon Nitride Ceramics By Laminated Object Manufacturing, in: Proc. Solid Free. Fabr. Symp., 2000.

[161] M. Steinau, N. Travitzky, T. Zipperle, P. Greil, Functionally graded ceramics derived from preceramic polymers, in: Ceram. Trans., 2010. https://doi.org/10.1002/9780470880630.ch8.

[162] C.M. Gomes, C.R. Rambo, A.P.N. De Oliveira, D. Hotza, D. Gouvêa, N. Travitzky, P. Greil, Colloidal processing of glass-ceramics for laminated object manufacturing, J. Am. Ceram. Soc. 92 (2009). https://doi.org/10.1111/j.1551-2916.2009.03035.x.

[163] J. Park, M.J. Tari, H.T. Hahn, Characterization of the laminated object manufacturing (LOM) process, Rapid Prototyp. J. (2000). https://doi.org/10.1108/13552540010309868.

[164] K.P. Karunakaran, S. Dibbi, P.V. Shanmuganathan, D.S. Raju, S. Kakaraparti, Efficient stock cutting for laminated manufacturing, CAD Comput. Aided Des. (2002). https://doi.org/10.1016/S0010-4485(01)00087-2.

[165] L. Weisensel, N. Travitzky, H. Sieber, P. Greil, Laminated Object Manufacturing (LOM) of SiSiC composites, Adv. Eng. Mater. (2004). https://doi.org/10.1002/adem.200400112.

[166] J.A. Lewis, Direct ink writing of 3D functional materials, Adv. Funct. Mater. 16 (2006) 2193–2204. https://doi.org/10.1002/adfm.200600434.

[167] T.A. Baer, J. Cesarano III, P. Calvert, Recent developments in freeform fabrication of dense ceramics from slurry deposition, Solid Free. Fabr. Proceedings, Sept. 1997. (1997).

[168] M.K. Agarwala, A. Bandyopadhyay, R. van Weeren, A. Safari, S.C. Danforth, N.A. Langrana, V.R. Jamalabad, P.J. Whalen, Fused Deposition of Ceramics: Rapid Fabrication of Structural Ceramic Components, Am. Ceram. Soc. Bull. 11 (1996) 60–65.

[169] M.K. Agarwala, A. Bandyopadhyay, R. Van Weeren, Fused Deposition of Ceramics (FDC) for Structural Silicon Nitride Components, in: Proc. Solid Free. Fabr. Symp., 1996.

[170] M.K. Agarwala, V.R. Jamalabad, N.A. Langrana, A. Safari, P.J. Whalen,

S.C. Danforth, Structural quality of parts processed by fused deposition, Rapid Prototyp. J. 2 (1996). https://doi.org/10.1108/13552549610732034.

[171] D. Kupp, H. Eifert, M. Greul, M. Kunstner, Rapid prototyping of functional metal and ceramic components by the multiphase jet solidification (MSJ) process, Proc. Solid Free. Fabr. Symp. (1997).

[172] J. Cesarano, S. Grieco, Robocasting: A New Technique for the Freeform Fabrication of Near-Net-Shape Ceramics, Mater. Technol. (1997). https://doi.org/10.1080/10667857.1997.11752736.

[173] J. Cesarano III, I.A. Aksay, A. Bleier, Stability of Aqueousa Al203 Suspensions with Poly(methacrylic acid) Polyelectrolyte, J. Am. Ceram. Soc. 71 (1988) 250–255.

[174] M.A. Jafari, W. Han, F. Mohammadi, A. Safari, S.C. Danforth, N. Langrana, A novel system for fused deposition of advanced multiple ceramics, Rapid Prototyp. J. (2000). https://doi.org/10.1108/13552540010337047.

[175] S. Iyer, J. Mcintosh, A. Bandyopadhyay, N. Langrana, A. Safari, S.C. Danforth, R.B. Clancy, C. Gasdaska, P.J. Whalen, Microstructural characterization and mechanical properties of Si3N4 formed by fused deposition of ceramics, Int. J. Appl. Ceram. Technol. 5 (2008) 127–137. https://doi.org/10.1111/j.1744-7402.2008.02193.x.

[176] M. Allahverdi, S.C. Danforth, M. Jafari, A. Safari, Processing of advanced electroceramic components by fused deposition technique, J. Eur. Ceram. Soc. (2001). https://doi.org/10.1016/S0955-2219(01)00047-4.

[177] G. Franchin, L. Wahl, P. Colombo, Direct ink writing of ceramic matrix composite structures, J. Am. Ceram. Soc. 100 (2017) 4397–4401. https://doi.org/10.1111/jace.15045.

[178] E. Feilden, C. Ferraro, Q. Zhang, E. García-Tuñón, E. D'Elia, F. Giuliani, L. Vandeperre, E. Saiz, 3D Printing Bioinspired Ceramic Composites, Sci. Rep. (2017). https://doi.org/10.1038/s41598-017-14236-9.

[179] B.P. Croom, A. Abbott, J.W. Kemp, L. Rueschhoff, L. Smieska, A. Woll, S. Stoupin, H. Koerner, Mechanics of nozzle clogging during direct ink writing of fiber-reinforced composites, Addit. Manuf. 37 (2021) 101701. https://doi.org/10.1016/j.addma.2020.101701.

[180] J.W. Kemp, A.A. Diaz, E.C. Malek, B.P. Croom, Z.D. Apostolov, S.R. Kalidindi, B.G. Compton, L.M. Rueschhoff, Direct ink writing of ZrB2-SiC chopped fiber ceramic composites, Addit. Manuf. 44 (2021) 102049. https://doi.org/10.1016/j.addma.2021.102049.

[181] F. Niu, D. Wu, G. Ma, S. Zhou, B. Zhang, Effect of second-phase doping on laser deposited Al2O3 ceramics, Rapid Prototyp. J. (2015). https://doi.org/10.1108/RPJ-12-2014-0167.

[182] J. V Tompkins, R. Laabi, B.R. Birmingham, H.L. Marcus, Advances in Selective Area Laser Deposition of Silicon Carbide, in: Solid Free. Fabr. Symp., 1994.

[183] K.J. Jakubenas, Y.L. Lee, M.S. Shaarawi, H.L. Marcus, J.M. Sanchez, Selective area laser deposition of titanium oxide, Rapid Prototyp. J. (1997). https://doi.org/10.1108/13552549710176699.

[184] J. Fessler, a Nickel, G. Link, Functional gradient metallic prototypes through shape deposition manufacturing, Proc. Solid Free. Fabr. Symp. (1997) 521–528. http://utwired.engr.utexas.edu/lff/symposium/proceedingsArchive/pubs/Manuscripts/1997/1997-61-Fessler.pdf.

[185] J.E. Crocker, L.C. Sun, H. Ansquer, L.L. Shaw, H.L. Marcus, “Processing and characterization of SALDVI ceramic structures,” Solid Free. Fabr. Proceedings, August 1999. (1999).

[186] F. Niu, D. Wu, G. Ma, J. Wang, M. Guo, B. Zhang, Nanosized microstructure of Al2O3-ZrO2 (Y2O3) eutectics fabricated by laser engineered net shaping, Scr. Mater. 95 (2015). https://doi.org/10.1016/j.scriptamat.2014.09.026.

[187] Y. Hu, H. Wang, W. Cong, B. Zhao, Directed Energy Deposition of Zirconia-Toughened Alumina Ceramic: Novel Microstructure Formation and Mechanical Performance, J. Manuf. Sci. Eng. (2020). https://doi.org/10.1115/1.4045626.

[188] Y. Hu, F. Ning, W. Cong, Y. Li, X. Wang, H. Wang, Ultrasonic vibration-assisted laser engineering net shaping of ZrO2-Al2O3 bulk parts: Effects on crack suppression, microstructure, and mechanical properties, Ceram. Int. 44 (2018). https://doi.org/10.1016/j.ceramint.2017.11.013.

[189] Z. Liu, F. Ning, W. Cong, Q. Jiang, T. Li, H. Zhang, Y. Zhou, Energy consumption and saving analysis for laser engineered net shaping of metal powders, Energies. 9 (2016). https://doi.org/10.3390/en9100763.

[190] S. Yan, D. Wu, F. Niu, G. Ma, R. Kang, Al2O3-ZrO2 eutectic ceramic via ultrasonic-assisted laser engineered net shaping, Ceram. Int. 43 (2017). https://doi.org/10.1016/j.ceramint.2017.08.165.

[191] M. Golt, L.R. Vargas-Gonzalez, J. Sietins, C. Moorehead, V. Blair, Additive Manufacturing in Ceramics: Current Status, Capability Gaps, and Paths Forward, 2018.

[192] W.G. Fahrenholtz, Reactive processing in ceramic-based systems, Int. J. Appl. Ceram. Technol. 3 (2006). https://doi.org/10.1111/j.1744-7402.2006.02059.x.

[193] A.B. Peters, D. Zhang, A. Hernandez, M.C. Brupbacher, D.C. Nagle, T.

Mueller, J.B. Spicer, Selective Laser Sintering in Reactive Atmospheres: Towards In-Situ Synthesis of Net-Shaped Carbide and Nitride Ceramics, Addit. Manuf. 45 (2021) 102052. https://doi.org/10.1016/j.addma.2021.102052.

[194] J. Schmidt, L. Brigo, A. Gandin, M. Schwentenwein, P. Colombo, G. Brusatin, Multiscale ceramic components from preceramic polymers by hybridization of vat polymerization-based technologies, Addit. Manuf. 30 (2019) 100913. https://doi.org/10.1016/j.addma.2019.100913.

[195] D.A. Anderegg, H.A. Bryant, D.C. Ruffin, S.M. Skrip, J.J. Fallon, E.L. Gilmer, M.J. Bortner, In-situ monitoring of polymer flow temperature and pressure in extrusion based additive manufacturing, Addit. Manuf. (2019). https://doi.org/10.1016/j.addma.2019.01.002.

[196] S. Clijsters, T. Craeghs, S. Buls, K. Kempen, J.P. Kruth, In situ quality control of the selective laser melting process using a high-speed, real-time melt pool monitoring system, Int. J. Adv. Manuf. Technol. 75 (2014) 1089–1101. https://doi.org/10.1007/s00170-014-6214-8.

[197] T. Fang, M.A. Jafari, S.C. Danforth, A. Safari, Signature analysis and defect detection in layered manufacturing of ceramic sensors and actuators, Mach. Vis. Appl. 15 (2003). https://doi.org/10.1007/s00138-002-0074-1.

[198] D. Hagen, J.J. Beaman, D. Kovar, Selective laser flash sintering of 8-YSZ, J. Am. Ceram. Soc. 103 (2020) 800–808. https://doi.org/10.1111/jace.16771.

[199] Sigma-Aldrich, Methyl Cellulose Product Information Sheet, Saint Louis, Missouri, 1997.

[200] C.A. Schneider, W.S. Rasband, K.W. Eliceiri, NIH Image to ImageJ: 25 years of image analysis, Nat. Methods. (2012). https://doi.org/10.1038/nmeth.2089.

[201] P. V. Danckwerts, The definition and measurement of some characteristics of mixtures, Appl. Sci. Res. Sect. A. 3 (1952). https://doi.org/10.1007/BF03184936.

[202] S.C. Blair, P.A. Berge, J.G. Berryman, Using two-point correlation functions to characterize microgeometry and estimate permeabilities of sandstones and porous glass, J. Geophys. Res. B Solid Earth. 101 (1996). https://doi.org/10.1029/96jb00879.

[203] C1326-13(2018) Standard Test Method for Knoop Indentation Hardness of Advanced Ceramics, West Conshohocken, PA, 2018. https://doi.org/10.1520/C1326-13R18.

[204] B.H. Toby, R.B. Von Dreele, GSAS-II : the genesis of a modern open-

source all purpose crystallography software package , J. Appl. Crystallogr. 46 (2013) 544–549. https://doi.org/10.1107/s0021889813003531.

[205] J. ITO, M. IWATSUKI, T. FUKASAWA, Reinvestigation of crystallographic data and X-ray diffraction data of silicon carbide for polytype identification purposes., Bunseki Kagaku. (2011). https://doi.org/10.2116/bunsekikagaku.42.8_445.

[206] A.L. Hannam, P.T.B. Shaffer, Revised X-ray diffraction line intensities for silicon carbide polytypes, J. Appl. Crystallogr. 2 (1969) 45–48. https://doi.org/10.1107/s0021889869006510.

[207] O. Sologub, Y. Michiue, T. Mori, Boron carbide, B13-x C2-y (x = 0.12, y = 0.01), Acta Crystallogr. Sect. E Struct. Reports Online. 68 (2012) 1–6. https://doi.org/10.1107/S1600536812033132.

[208] P.T.B. Shaffer, The SiC phase in the system SiCB4CC, Mater. Res. Bull. 4 (1969) 213–219. https://doi.org/10.1016/0025-5408(69)90058-0.

[209] N. Otsu, THRESHOLD SELECTION METHOD FROM GRAY-LEVEL HISTOGRAMS., IEEE Trans Syst Man Cybern. SMC-9 (1979). https://doi.org/10.1109/tsmc.1979.4310076.

[210] T. Li, E. Al Olevsky, M.A. Meyers, The development of residual stresses in Ti6Al4V-Al3Ti metal-intermetallic laminate (MIL) composites, Mater. Sci. Eng. A. 473 (2008) 49–57. https://doi.org/10.1016/j.msea.2007.03.069.

[211] M. Lugovy, N. Orlovskaya, K. Berroth, J. Kuebler, Macrostructural engineering of ceramic-matrix layered composites, Compos. Sci. Technol. 59 (1999) 1429–1437. https://doi.org/10.1016/S0266-3538(98)00183-3.

[212] F. Thévenot, Boron carbide—A comprehensive review, J. Eur. Ceram. Soc. 6 (1990) 205–225. https://doi.org/10.1016/0955-2219(90)90048-K.

[213] J.J. Swab, Recommendations for Determining the Hardness of Armor Ceramics, Int. J. Appl. Ceram. Technol. (2005). https://doi.org/10.1111/j.1744-7402.2004.tb00173.x.

[214] J.W. Matthews, A.E. Blakeslee, Defects in epitaxial multilayers, J. Cryst. Growth. (1974). https://doi.org/10.1016/s0022-0248(74)80055-2.

[215] T.J. Gosling, S.C. Jain, J.R. Willis, A. Atkinson, R. Bullough, Stable configurations in strained epitaxial layers, Philos. Mag. A Phys. Condens. Matter, Struct. Defects Mech. Prop. 66 (1992) 119–132. https://doi.org/10.1080/01418619208201517.

[216] J.H. van der Merwe, Structure of epitaxial crystal interfaces, Surf. Sci. 31 (1972) 198–228. https://doi.org/10.1016/0039-6028(72)90261-0.

[217] G.W. HOLLENBERG, G. WALTHER, The Elastic Modulus and Fracture of Boron Carbide, J. Am. Ceram. Soc. 63 (1980) 610–613.

https://doi.org/10.1111/j.1151-2916.1980.tb09845.x.

[218] D.T. Livey, P. Murray, Surface Energies of Solid Oxides and Carbides, Am. Ceram. Soc. 39 (1956).

[219] S.R. Levine, E.J. Opila, M.C. Halbig, J.D. Kiser, M. Singh, J.A. Salem, Evaluation of ultra-high temperature ceramics for aeropropulsion use, J. Eur. Ceram. Soc. 22 (2002). https://doi.org/10.1016/S0955-2219(02)00140-1.

[220] I.G. Crouch, Body armour – New materials, new systems, Def. Technol. 15 (2019). https://doi.org/10.1016/j.dt.2019.02.002.

[221] M.A. Meyers, Dynamic Behavior of Materials, 1994. https://doi.org/10.1002/9780470172278.

[222] S. Zhao, B. Kad, B.A. Remington, J.C. Lasalvia, C.E. Wehrenberg, K.D. Behler, M.A. Meyers, Directional amorphization of boron carbide subjected to laser shock compression, Proc. Natl. Acad. Sci. U. S. A. 113 (2016) 12088–12093. https://doi.org/10.1073/pnas.1604613113.

[223] K.S. Ravichandran, Thermal residual stresses in a functionally graded material system, Mater. Sci. Eng. A. 201 (1995). https://doi.org/10.1016/0921-5093(95)09773-2.

[224] S. Hasanov, S. Alkunte, M. Rajeshirke, A. Gupta, O. Huseynov, I. Fidan, F. Alifui-Segbaya, A. Rennie, Review on additive manufacturing of multi-material parts: Progress and challenges, J. Manuf. Mater. Process. 6 (2022). https://doi.org/10.3390/jmmp6010004.

[225] H. Horii, S. Nemat-Nasser, Compression-induced microcrack growth in brittle solids: Axial splitting and shear failure, J. Geophys. Res. 90 (1985). https://doi.org/10.1029/jb090ib04p03105.

[226] M.F. Ashby, S.D. Hallam (Née Cooksley), The failure of brittle solids containing small cracks under compressive stress states, Acta Metall. 34 (1986). https://doi.org/10.1016/0001-6160(86)90086-6.

[227] B. Paliwal, K.T. Ramesh, An interacting micro-crack damage model for failure of brittle materials under compression, J. Mech. Phys. Solids. 56 (2008). https://doi.org/10.1016/j.jmps.2007.06.012.

[228] S. Suresh, T. Nakamura, Y. Yeshurun, K. -H Yang, J. Duffy, Tensile Fracture Toughness of Ceramic Materials: Effects of Dynamic Loading and Elevated Temperatures, J. Am. Ceram. Soc. 73 (1990). https://doi.org/10.1111/j.1151-2916.1990.tb07613.x.

[229] A.G. EVANS, K.T. FABER, Crack-Growth Resistance of Microcracking Brittle Materials, J. Am. Ceram. Soc. 67 (1984). https://doi.org/10.1111/j.1151-2916.1984.tb18842.x.

[230] G. Ravichandran, G. Subhash, Critical Appraisal of Limiting Strain Rates for Compression Testing of Ceramics in a Split Hopkinson Pressure Bar, J. Am. Ceram. Soc. 77 (1994). https://doi.org/10.1111/j.1151-2916.1994.tb06987.x.

[231] Split-Hopkinson Pressure Bar Testing of Ceramics, in: Mech. Test. Eval., ASM International, 2018: pp. 497–504. https://doi.org/10.31399/asm.hb.v08.a0003299.

[232] W.W. Chen, B. Song, Split Hopkinson (Kolsky) Bar: Design, Testing and Applications., 2013.

[233] J.J. Swab, W. Chen, J. Hogan, H. Liao, C. Lo, S. Mates, C. Meredith, J.J. Pittari, R. Rhorer, G.D. Quinn, Dynamic Compression Strength of Ceramics: What was Learned from an Interlaboratory Round Robin Exercise?, J. Dyn. Behav. Mater. 7 (2021). https://doi.org/10.1007/s40870-020-00264-6.

[234] W. Chen, G. Subhash, G. Ravichandran, Evaluation of Ceramic Specimen Geometries Used in a Split Hopkinson Pressure Bar, Dyn. Behav. Mater. 1 (1994) 193–210.

[235] A. International, ASTM C1161 - Standard Test Method for Flexural Strength of Advanced Ceramics at Ambient Temperature, ASTM Int. (2013).

[236] P. Patel, J. Swab, M. Staley, G. Quinn, Indentation Size Effect (ISE) of Transparent AION and MgAl2O4, 2006.

[237] L. Farbaniec, J. Hogan, J. McCauley, K. Ramesh, Anisotropy of Mechanical Properties in a Hot-Pressed Boron Carbide, Int. J. Appl. Ceram. Technol. 13 (2016) 1008–1016. https://doi.org/10.1111/ijac.12585.

[238] J.J. Swab, C.S. Meredith, D.T. Casem, W.R. Gamble, Static and dynamic compression strength of hot-pressed boron carbide using a dumbbell-shaped specimen, J. Mater. Sci. 52 (2017) 10073–10084. https://doi.org/10.1007/s10853-017-1210-7.

[239] A. Cieza, P. Kleinitz, M. Mallick, S. Mishra, Z. Mirza, A. Pupulin, H. Sakr, E. Tebbut, A.J. Vasquez, Standards for Prosthetics and Orthotics. Part 1: Standards, 2017.

[240] K. Ziegler-Graham, E.J. MacKenzie, P.L. Ephraim, T.G. Travison, R. Brookmeyer, Estimating the Prevalence of Limb Loss in the United States: 2005 to 2050, Arch. Phys. Med. Rehabil. 89 (2008). https://doi.org/10.1016/j.apmr.2007.11.005.

[241] A. Sahu, R. Sagar, S. Sarkar, S. Sagar, Psychological effects of amputation: A review of studies from India, Ind. Psychiatry J. 25 (2016). https://doi.org/10.4103/0972-6748.196041.

[242] A Manual of Orthopaedic Terminology, 2015. https://doi.org/10.1016/c2012-0-07633-8.

[243] C.L. McDonald, S. Westcott-McCoy, M.R. Weaver, J. Haagsma, D. Kartin, Global prevalence of traumatic non-fatal limb amputation, Prosthet. Orthot. Int. (2020). https://doi.org/10.1177/0309364620972258.

[244] F. Paradisi, A.S. Delussu, S. Brunelli, M. Iosa, R. Pellegrini, D. Zenardi, M. Traballesi, The conventional non-articulated SACH or a multiaxial prosthetic foot for hypomobile transtibial amputees? A clinical comparison on mobility, balance, and quality of life, Sci. World J. 2015 (2015). https://doi.org/10.1155/2015/261801.

[245] H. Houdijk, D. Wezenberg, L. Hak, A.G. Cutti, Energy storing and return prosthetic feet improve step length symmetry while preserving margins of stability in persons with transtibial amputation, J. Neuroeng. Rehabil. 15 (2018). https://doi.org/10.1186/s12984-018-0404-9.

[246] N.P. Fey, G.K. Klute, R.R. Neptune, The influence of energy storage and return foot stiffness on walking mechanics and muscle activity in below-knee amputees, Clin. Biomech. 26 (2011) 1025–1032. https://doi.org/10.1016/j.clinbiomech.2011.06.007.

[247] A. H., Finite Element based Model of Modified Niagara Foot and its Effect on Stiffness, Int. J. Comput. Appl. 134 (2016). https://doi.org/10.5120/ijca2016907837.

[248] G.R. Colborne, S. Naumann, P.E. Longmuir, D. Berbrayer, Analysis of mechanical and metabolic factors in the gait of congenital below knee amputees. A comparison of the SACH and Seattle feet, Am. J. Phys. Med. Rehabil. 71 (1992). https://doi.org/10.1097/00002060-199210000-00004.

[249] S. Summit, Additive manufacturing of a prosthetic limb, in: Rapid Prototyp. Biomater. Princ. Appl., 2014. https://doi.org/10.1533/9780857097217.285.

[250] W. Layman, METHOD OF DIGITALLY CONSTRUCTING A PROSTHESIS, 2014.

[251] T.G. Valenti, Experience with endoflex: A monolithic thermoplastic prosthesis for below-knee amputees, J. Prosthetics Orthot. 3 (1990). https://doi.org/10.1097/00008526-199000310-00012.

[252] Y. Akutsu, Instalimb, ZDNet Japan. (2022). https://japan.zdnet.com/article/35182786/.

[253] D.M. Sengeh, H. Herr, A variable-impedance prosthetic socket for a transtibial amputee designed from magnetic resonance imaging data, J. Prosthetics Orthot. 25 (2013). https://doi.org/10.1097/JPO.0b013e31829be19c.

[254] G. Pirouzi, N.A. Abu Osman, A. Eshraghi, S. Ali, H. Gholizadeh, W.A.B.

Wan Abas, Review of the socket design and interface pressure measurement for transtibial prosthesis, Sci. World J. 2014 (2014). https://doi.org/10.1155/2014/849073.

[255] M. Al Muderis, W. Lu, J.J. Li, Osseointegrated Prosthetic Limb for the treatment of lower limb amputations, Unfallchirurg. 120 (2017). https://doi.org/10.1007/s00113-016-0296-8.

[256] J.T. Cantrell, S. Rohde, D. Damiani, R. Gurnani, L. DiSandro, J. Anton, A. Young, A. Jerez, D. Steinbach, C. Kroese, P.G. Ifju, Experimental characterization of the mechanical properties of 3D-printed ABS and polycarbonate parts, Rapid Prototyp. J. 23 (2017). https://doi.org/10.1108/RPJ-03-2016-0042.

[257] M. Ramesh, K. Panneerselvam, Materials Today : Proceedings Mechanical investigation and optimization of parameter selection for Nylon material processed by FDM, Mater. Today Proc. 46 (2021) 9303–9307. https://doi.org/10.1016/j.matpr.2020.02.697.

[258] P. Parandoush, D. Lin, A review on additive manufacturing of polymer-fiber composites, Compos. Struct. 182 (2017). https://doi.org/10.1016/j.compstruct.2017.08.088.

[259] N. van de Werken, H. Tekinalp, P. Khanbolouki, S. Ozcan, A. Williams, M. Tehrani, Additively manufactured carbon fiber-reinforced composites: State of the art and perspective, Addit. Manuf. 31 (2020) 100962. https://doi.org/10.1016/j.addma.2019.100962.

[260] G.D. Goh, Y.L. Yap, S. Agarwala, W.Y. Yeong, Recent Progress in Additive Manufacturing of Fiber Reinforced Polymer Composite, Adv. Mater. Technol. 4 (2019) 1–22. https://doi.org/10.1002/admt.201800271.

[261] X. Tian, T. Liu, C. Yang, Q. Wang, D. Li, Interface and performance of 3D printed continuous carbon fiber reinforced PLA composites, Compos. Part A Appl. Sci. Manuf. 88 (2016). https://doi.org/10.1016/j.compositesa.2016.05.032.

[262] V. Shanmugam, D. Joel, J. Rajendran, K. Babu, S. Rajendran, A. Veerasimman, U. Marimuthu, F. Berto, S. Ramakrishna, The mechanical testing and performance analysis of polymer-fibre composites prepared through the additive manufacturing, Polym. Test. 93 (2021) 106925. https://doi.org/10.1016/j.polymertesting.2020.106925.

[263] S.Y. Fu, B. Lauke, Y.W. Mai, Science and engineering of short fibre reinforced polymer composites, 2009. https://doi.org/10.1533/9781845696498.

[264] M.A. Caminero, J.M. Chacón, I. García-Moreno, J.M. Reverte, Interlaminar bonding performance of 3D printed continuous fibre reinforced thermoplastic composites using fused deposition modelling, Polym. Test.

68 (2018). https://doi.org/10.1016/j.polymertesting.2018.04.038.

[265] J.S. Jensen, H.B. Treichl, Mechanical testing of prosthetic feet utilized in low-income countries according to ISO-10328 standard, Prosthet. Orthot. Int. 31 (2007) 177–206. https://doi.org/10.1080/03093640701210986.